DOCTORAL THESIS

Digital radiography: Image Acquisition and Scattering Reduction in X-ray imaging

Author:
Elena MARIMÓN MUÑOZ

A thesis submitted in fulfilment of the requirements for the degree of Engineering Doctorate

in the

Centre for Digital Entertainment
Media School, Bournemouth University

January 28, 2019

Copyright Statement

Abstract

Since the discovery of the X-rays in 1895, their use in both medical and industrial imaging applications has gained increasing importance. As a consequence, X-ray imaging devices have evolved and adapted to the needs of individual applications, leading to the appearance of digital image capture devices. Digital technologies introduced the possibility of separating the image acquisition and image processing steps, allowing their individual optimization. This thesis explores both areas, by seeking the improvement in the design of the new family of Varex Imaging CMOS X-ray detectors and by developing a method to reduce the scatter contribution in mammography examinations using image post-processing techniques.

During the CMOS X-ray detector product design phase, it is crucial to detect any shortcomings that the detector might present. Image characterization techniques are a very efficient method for finding these possible detector features. This first part of the thesis focused in taking these well-known test methods and adapt and optimize them, so they could act as a red flag indicating when something needed to be investigated. The methods chosen in this study have proven to be very effective in finding detector shortcomings and the designs have been optimised in accordance with the results obtained. With the aid of the developed imaging characterization tests, new sensor designs have been successfully integrated into a detector, resulting in the recent release into the market of a new family of Varex Imaging CMOS X-ray detectors.

The second part of the thesis focuses in X-ray mammography applications, the gold standard technique in breast cancer screening programmes. Scattered radiation degrades the quality of the image and complicates the diagnosis process. Anti-scatter grids, the main scattering reduction technique, are not a perfect solution. This study is concerned with the use of image post-processing to reduce the scatter contribution in the image, by convolving the output image with kernels obtained from simplified Monte Carlo simulations. The proposed semi-empirical approach uses three thickness-dependant symmetric kernels to accurately estimate the environment contribution to the breast, which has been found to be of key importance in the correction of the breast-edge area. When using a single breast thickness-dependant kernel to convolve the image, the post-processing technique can over-estimate the scattering up to 60%. The method presented in this study reduces the uncertainty to a 4-10% range for a 35 to 70 mm breast thickness range, making it a very efficient scatter modelling technique.

The method has been successfully proven against full Monte Carlo simulations and mammography phantoms, where it shows clear improvements in terms of the contrast to noise ratio and variance ratio when the performance is compared against images acquired with anti-scatter grids.

Acknowledgements

I would like to express my most sincere gratitude to my official and not so official supervisors, Philip A. Marsden, Hammadi Nait-Charif and Oliver Díaz Montesdeoca, for their support, time, patience and enthusiasm that kept me motivated all these years. Special thanks also goes to the Centre for Digital Entertainment, Bournemouth University, University of Bath and Dexela Ltd. and, of course, to all the people behind these institutions, who gave me this opportunity for which I will always be grateful.

Gratitude is extended, with no particular order, to Unitive Design and Analysis, Tony Sedivy and FilmLight Ltd. for sharing their servers, to the medical physics departments of Barts NHS Trust and of the University Hospital Parc Taulí (specially to Amy Rose, Mandy Price and Eduard Bardaji for aiding me in the acquisition of the clinical data), to Mark Williams and Andrew Polemi from the University of Virginia and to John Hazelwood and all the other people that helped me with the udders experiment. With special mention to Phil's parents and Alex for sharing their freezer space for months.

Last but not least, to my family, friends and all the people with whom I had helpful discussions, great time and laugh - Thanks!

Contents

List of Figures

List of Tables

List of Abbreviations

1D	one dimension
2D	two dimensions
3D	three dimensions
α-Se	amorphous Selenium
α-Si	amorphous Silicon
AAPM	American Association of Physicists in Medicine
ABP	Animal By-Product
aC	amorphous Carbon
ACR	American College of Radiology
ADC	Analogue to Digital Converter
AEC	Automatic Exposure Control
Ag	Silver
ALARP	As Low As Reasonably Practicable
APS	Active Pixel Sensor
ASP	Analogue Signal Processor
AutoPIA	Automatic Phantom Image Analysis
BI-RADS	Breast Imaging Reporting and Data System
CAD	Computer-Aided Diagnosis
CB	Cone Beam
CCD	Charge-Coupled Device
CDE	Centre for Digital Entertainment
CDMAM	Contrast Detail MAMmography
CMOS	Complementary Metal-Oxide Semiconductor
CNR	Contrast to Noise Ratio
CR	Computed Radiography
CsI	Cesium Iodine
CsI:Tl	Thallium activated Cesium Iodine
CT	Computer Tomography
DAK	Detector Air Kerma
DBT	Digital Breast Tomosynthesis
DCC	Detail Compacted Contrast
DCIS	Ductal Carcinoma In Situ
DDS	Delta Double Sampling
DQE	Detective Quantum Efficiency
DN	Digital Number
DSNU	Dark Signal Non-Uniformity
EM	ElectroMagnetic
ESF	Edge Spread Function
fASKS	Fast Adaptive Scatter Kernel Superposition
Fcc	Fractional concavity
FD	Fractal Dimension

FF	Fourier Factor
FFT	Fast Fourier Transform
FOP	Fibre Optic Plate
FOV	Field Of View
FPN	Fixed Pattern Noise
FWC	Full Well Capacity
Gadox	GADolinium OXysulfide ceramic screen
GOS	Gadolinium Oxysulfide ceramic Screen
GPS	General Particle Source
HCR	High Contrast Resolution
HRT	Hormone Replacement Therapy
HVL	Half Value Layer
IEC	International Electrotechnical Commission
LHS	Left Hand Side
lp	line pairs
LSF	Line Spread Function
MC	Monte Carlo
Mo	Molybdenum
MRE	Mean Radial Extent
MRI	Magnetic Resonance Imaging
MTF	Modulation Transfer Function
MV	Mean Variance
N/A	Not Applicable
NHS	National Health Service
NNPS	Normalised Noise Power Spectrum
NPS	Noise Power Spectrum
PMMA	Polymethyl methacrylate or acrylic or perspex
PRNG	Pseudo-Random Number Generator
PB	Pencil Beam
PPS	Passive Pixel Sensor
PRNU	Photo-Response Non-Uniformity
PSF	Point Spread Function
PSP-CR	Photostimulable Storage Phosphor Computed Radiography
QC	Quality Control
Rh	Rhodium
RHS	Right Hand Side
ROI	Region Of Interest
RQA	Radiation Quality
SEM	Standard Error of the Mean
SF	Scatter Fraction
SI	Spiculation Index
SID	Source to Imager Distance
SNR	Signal to Noise Ratio
SPID	Support Paddle to Imager Distance
SPR	Scatter to Primary Ratio
SPSF	Scatter Point Spread Function
StD	Standard Deviation
TFT	Thin-Film Transistor
UCL	University College London

Vr.	Variance ratio
W	Tungsten
WHO	World Health Organization

Chapter 1

Introduction

This chapter provides an introduction to the thesis, including a brief description of digital radiography and the project overview and motivations. The structure of the thesis is then defined and the achievements and major contributions are presented at the end.

1.1 Introduction to the field

The use of X-rays in medicine started right after their discovery in 1895. Wilhelm Conrad Roentgen observed a fluorescent glow of some crystals when he was working with a cathode-ray tube in a nearby area. A Crookes, or cathode-ray, tube is a partially evacuated glass bulb where a high voltage can be applied in between the two metal electrodes that are placed at both ends. The electrons are generated by the ionization of the residual air by the applied voltage. They are then attracted towards the positive electrode (anode) creating an electron beam, or cathodes rays. When the beam hits the anode or the glass wall with enough kinetic energy, X-rays are generated. The phenomenon observed by Roentgen was possible thanks to the penetrating nature of the X-rays: the photons that were generated in the tube ended up interacting with the crystals of the nearby table. (Turner, 1995; Bushberg et al., 2012)

The interest that the discovery of the X-rays generated in the scientific and medical community was immediate. Their use in medicine dates as early as 1896 with radiographic systems based in simple single-emulsion glass plates. By the 1920s, the systems evolved into screen-film radiography, where the detector was formed by a cassette containing one or two screens and a film. Screen-film, or conventional radiography, became the predominant radiographic method for most part of the 20th century. It was not until the late 1990s that digital technology started to take over in the radiography and mammography market. (Bushberg et al., 2012)

Digital radiography uses digital image capture devices. It allows the user to preview the image and avoids the costly processing steps of conventional radiography. The most important feature, however, is the possibility of dividing the process into three steps: image

acquisition, image processing and image display. The physical separation of the acquisition process and the processing of the raw image allows their individual optimization, leading to improvements in image quality:

1.1.1 Image acquisition: Digital X-ray detectors

As a result of the very positive response to the advent of digital radiography, different technologies have been developed and are available for use in hospitals and industry. The wide range of choice in digital radiography has led to more specialised devices, allowing the possibility of defining different imaging requirements for different medical procedures, i.e. which organ to be imaged, which details are more important, the possibility of accounting for body motion, etc. Chest radiography, for example, requires a large detector size (being $43\ \mathrm{cm}$ x $43\ \mathrm{cm}$ the standard size) and relatively high energies. Mammography needs high spatial resolution in order to detect microcalcifications, a lower energy range (25-30 keV) and a small pixel size (between 25 and 70 µm preferrably). While cardiology needs high frame rates, as the system must follow the motion of the heart (Hoheisel, 2006).

By the optimization of the X-ray systems either the image quality can be improved or the radiation dose minimized, following the ALARP principle that stablishes that the ionizing radiation has to be kept "As Low As Reasonable Practicable" (Bushberg et al., 2012). Due to the damaging effects that radiation has on the living tissue, a trade-off between image quality and delivered dose has always to be found and dedicated X-ray equipment and imaging technologies can help to find the best possible outcome.

The main digital radiography technologies currently available are Thin-Film Transistor (TFT) based detectors, Charge Couple Devices (CCD), Complementary Metal Oxide Semiconductors with Active Pixel Sensors (CMOS APS). As these technologies can target different applications, a critical performance study is necessary in order to allow the end user to make an objective decision when choosing the device.

The basic imaging performance of X-ray detector systems can be characterized by the study of the resolution, efficiency, noise and contrast. A series of parameters can be measured in order to assess the characteristics of the detector and, therefore, can be used to compare between technologies and industries and/or to find design problems. Some of these parameters are the response curve, dynamic range, signal to noise ratio, photon transfer curve, modulation transfer function, noise power spectrum and detective quantum efficiency.

1.1.2 Image processing: Scattering reduction in mammography

Image processing algorithms manipulate raw radiographies in order to adapt them to the radiologist's requirements. These algorithms are designed to optimize the quality of the output, minimizing the degradation of the image and avoiding the introduction of artefacts that might lead to misdiagnosis. There are many different types of algorithms, indeed each manufacturer or system typically has their own, and they are focused on solving particular issues that the raw images present for the application chosen.

In mammography applications, new scatter reduction techniques based on image post-processing have been emerging in the last years. A mammography test requires good contrast, good resolution, low dose and large dynamic range (NHS, 2016). The breast is composed of soft tissue, fat, blood vessels and it may have calcifications or tumours. Some of these tissues have very similar composition, therefore a X-ray scan must be sensitive to small differences in order to obtain enough contrast to distinguish them.

Scattered radiation limits the quantitative usefulness of radiographic images by degrading the contrast and "signal-to-noise" ratio and decreasing the dynamic range. Therefore, the presence of scatter reduces the quality of the image and affects the diagnosis of low contrast lesions (Boone and Cooper, 2000; Cooper et al., 2000; Ahn, Cho, and Jeon, 2006; Ducote and Molloi, 2010). In addition to the risk of misdiagnosis, X-ray scatter also causes underestimation in the measurement of the attenuation coefficients and the thickness estimation (Ahn, Cho, and Jeon, 2006; Ducote and Molloi, 2010).

To reduce the scattered radiation in mammography the most widespread technique, at the moment, is the use of anti-scatter grids. Anti-scatter grids are, however, an incomplete solution that ends up adding complexity and cost to the mammography process. Although they help to improve the quality of the image they also attenuate primary radiation, leading to an increase in the delivered dose (up to a factor of 3) (Krol et al., 1996; Wang et al., 2015; Binst et al., 2015). The limitations of the anti-scatter grids combined with the introduction of new mammography screening techniques that do not allow the use of grids, such most digital breast tomosynthesis systems, justify the interest and increase in research for new post-processing scatter reduction techniques.

1.2 Project overview

This EngD thesis presents the work undertaken in collaboration with Dexela Ltd. (Varex Imaging London, former PerkinElmer Medical Imaging London), the Centre for Digital Entertainment (CDE), Bournemouth University and University of Bath. The project is

based in the field of digital radiography, focusing more specifically on detector characterization of CMOS X-ray detectors and on studying image post-processing techniques for scatter reduction in mammography applications.

For the last five years PerkinElmer Medical Imaging first and Varex Imaging London now, has been developing new products to include to their family of CMOS digital X-ray detectors. The main components of a CMOS X-ray detector are a scintillator, i.e. to convert the X-rays into light photons, a CMOS sensor and electronics. The new engineering programme included a close interaction in the sensor development process, technology that was previously acquired from a third-party company. Integral to this development process is a tight regime of testing and performance verification and evaluation. New testing procedures had to be defined for the purposes of design optimisation and product qualification. Most of the research done in the image characterization part of this thesis has focused on this task, which is a critical input into the design cycle.

Although radiographic image quality testing is a well-known subject, it is usually focused in final product characterization. There is little information about image characterization during the product design phase, as it is not in the private companies' interest to share this kind of information. The main challenge has been to adapt well-known test methods to try to identify detector or sensor issues, while mapping those issues to their root cause. This step is necessary to complete and challenge the initial modelling of the sensor performance, done during the first stages of the design cycle. The optical response evaluation is a crucial test stage of the sensor development and it is achieved thanks to a close collaboration between the imaging, sensor design and engineering teams.

Each detector prototype must be challenged in terms of image quality, to obtain a final product that is suitable for medical or industrial applications and competitive in the market. The image characterization process closes the design loop.

The final image, however, is always delivered to the user after a certain amount of image processing on the raw image. The second part of this thesis is based on the image processing side of digital radiography, focusing on scattering reduction in mammography. Scattering is produced when the original trajectory of the X-ray particle is deviated as a consequence of the photon interaction with matter. It is important to minimise this effect, as it causes an increase in noise in the acquired image. The idea behind this study is to reduce the scatter component of an acquired mammogram using post-processing techniques, aiming to obtain equal or better image quality to the one obtained with the use of anti-scatter grids. The main objective is to determine if anti-scatter grids can be made redundant.

Anti-scatter grids are currently the main method for scatter reduction in mammography applications; the motivation behind getting rid of them is multiple. The main advantage being the possibility of reducing the dose delivered to the patient, i.e. the grid absorbs

approximately 20% of the primary (non-scattered) beam so the dose needs to be increased to maintain a good image quality. In the same way, the scattered radiation is not completely absorbed, 30 to 60% will still be transmitted to the detector (Wang et al., 2015). Moreover, they are an expensive addition to the mammography system and either they appear in the image, introducing an additional post-processing step to remove the pattern, or the system needs to include an additional mechanism to move the grid around its central position, making it invisible to the eye but increasing its size and price (Wang et al., 2015; Ahn, Cho, and Jeon, 2006; Binst et al., 2015; Krol et al., 1996).

1.3 Industrial Partner

Varex Imaging Corporation is a X-ray imaging solution provider that covers medical to industrial applications. The extensive catalogue of products includes X-ray tubes, flat panel digital detectors, high-voltage connectors, X-ray collimators, ionization chambers, mammography paddles, solid state automatic exposure control systems and buckies for digital imaging.

Varian Medical Systems created Varex Imaging Corporation as a "spin-off" company in January 2017. Varex Imaging completed the acquisition of the medical imaging branch of PerkinElmer in May 2017, the area of the company that was in charge of developing, manufacturing and selling digital X-ray detectors.

The CMOS flat panel detectors are currently being developed in Dexela Ltd, Varex Imaging - London. Dexela Ltd was founded in 2005 as a software and X-ray detector Medical Imaging Company and was acquired in June 2011 by PerkinElmer, adding CMOS technology to the company's medical and industrial imaging portfolio.

1.4 Structure of the thesis

This thesis is divided into seven chapters, including the present introduction. As it is an EngD thesis, the project covers two research topics that were of interest of the industrial partner, both under the area of digital radiography: Chapters 2 and 3 focus on image characterization analysis for the CMOS X-ray detector design phase. Chapters 4, 5 and 6 look into using image post-processing techniques for reduction of scattered radiation in mammography. The conclusions of the findings and future work suggestions are presented in Chapter 7. Chapters 2 to 6 are explained below.

- **Chapter 2** starts with a theoretical background introduction about X-rays photons to help in the interpretation of the results obtained in subsequent chapters. The

chapter follows with a description of the available digital X-ray detector technologies and introduces the methods for performing a complete detector evaluation using image characterization techniques.

- In **Chapter 3** the image characterization techniques previously introduced in Chapter 2 are adapted and optimized to find sensor and detector shortcomings in the design phase of CMOS X-ray detectors. The chapter describes the process of method optimization, giving examples of the failures found in the prototype evaluation and their root causes.

- **Chapter 4** introduces the topic of scatter reduction in mammography applications. It presents some initial background information about breast cancer, mammography screening programmes and the mammography X-ray systems used for breast cancer detection. It continues with a description of the contribution of the scatter radiation in an image and presents the different alternatives to the anti-scatter grids available for scatter estimation, including physical detection methods and simulated techniques. Finally, the system contribution to the scatter is evaluated in order to identify the key areas that need to be carefully controlled in the study presented in the following chapters.

- The point spread function (PSF) post-processing technique, based on the convolution of the output image with a set of scatter kernels, is the scattered reduction method chosen in this study. **Chapter 5** explains the simulation process, starting with an introduction to Geant4 (the chosen simulation tool-kit) and includes an overview of the experimental set up and validation of the simulations and geometry chosen. The proposed scatter correction method is then introduced, describing the optimisation process and the robustness analysis that was carried out in this study by comparing the results against full Monte Carlo simulations.

- **Chapter 6** expands the validation of the chosen methodology to clinical images obtained with real mammography systems where the grid has been removed. The results obtained with a series of mammography phantoms are challenged against the images acquired with the use of an anti-scatter grid. A one to one comparison between processed grid-less and grid images is performed for each of the examples.

1.5 Achievements and major contributions

1.5.1 Image characterization techniques

Prototypes of CMOS X-ray detectors under development have been been challenged in terms of image quality. Image characterization methods were adapted and optimized for

the task of finding design shortcomings that needed to be fixed before the product was finalised and released into the market.

The techniques defined in this research project have been key to the development of a new family of CMOS X-ray detectors that are being released by Dexela Ltd. (Varex Imaging Corporation - London). The project required to work in close contact with a multinational engineering team, providing them with the imaging science that they required during the design cycle.

These test methods have a foundation in well-known image analysis techniques, but additional tools had to be developed to stretch the performance limits of these state-of-the-art custom, wafer-scale image sensor designs. The techniques adopted have been implemented in the company's quality system to be used in the image quality evaluation of future products.

1.5.2 Scatter estimation in mammography

A convolution based post-processing technique has been chosen as scatter estimation method in this study. The scatter image is the convolution result of the input image with a point spread function (PSF) kernel. The primary image can then be calculated by just subtracting the scatter to the input image.

It was established that, in order to account for variations in the image, the use of a single symmetric PSF for the convolution of the whole image was not a viable solution. The main sources of discrepancies found were introduced by the scatter produced outside the breast area, i.e. background scatter produced mainly by the compression paddle, the thickness variation introduced by the angle of the X-ray beam at the edge of the breast and, in a smaller amount, the thickness reduction of the breast-edge area.

The proposed semi-empirical model accounts for the described discrepancies by introducing three additional kernels: two for estimating the background contribution to the breast and one for the thickness variations of the breast-edge. It was also seen that for breasts thinner than 50 mm the background contribution was enough to reduce the uncertainty to less than 5%. For thicker breasts, the three kernels were necessary and the discrepancy introduced by the model increased with the thickness, up to 10% for 70 mm thick breasts.

The final model was tested with a range of phantoms in clinical mammography systems and the resulting images were compared with images acquired with an anti-scatter grid. The results obtained were very positive, indicating that the technique has a lot of potential. Although limitations were found, this semi-empirical method is relatively fast, easily optimised, verified and extendible.

1.5.3 List of Publications

The following publications have resulted from the work published in this thesis:

- Elena Marimon, Hammadi Nait-Charif, Asmar Khan, Philip A. Marsden and Oliver Diaz. Detailed Analysis of Scatter Contribution from Different Simulated Geometries of X-ray Detectors. *In Proc. of IWDM, LNCS 9699, pp. 203-210, 2016.*
- Elena Marimon, Hammadi Nait-Charif, Asmar Khan, Philip A. Marsden and Oliver Diaz. Scatter reduction for grid-less mammography using the convolution-based image post-processing technique. *In Proc. of SPIE Medical Imaging 10132, 10132-4D, 2017.*

Chapter 2

X-ray systems

This chapter defines the theory behind digital X-ray systems. It starts giving some background information about the X-ray spectrum and defining the main widespread digital X-ray detector technologies. The chapter finishes with an introduction to image quality characterization and detector evaluation.

2.1 X-rays

X-rays form part of the high frequency end of the electromagnetic spectrum, see Figure 2.1. They are considered ionising radiation as their energy is high enough to liberate an electron from an atom, creating and ion pair and causing the atom to be positively charged.

The discovery of the X-rays in 1895 by Roentgen can be considered as the starting point of ionizing radiation in physics. X-rays can traverse most objects, including human tissue, characteristic that makes them very useful in medical applications. In fact, their use in medicine started within six months after their discovery; they were used at the frontline in battlefields to help locate bullets in injured soldiers. From 1913, when a X-ray tube was designed to allow the use of high voltages, the improvements in the image quality were enough to start being used extensively in medicine (Reed, 2011).

X-rays can be produced when a beam of electrons strikes a target of high atomic number, e.g. Tungsten. Most of these electrons, up to 99 %, interact with the target's orbital electrons, mainly producing heat but also, in smaller proportions, characteristic radiation if the interaction occurs in the inner orbitals K and L shells. The remaining < 1 % interacts with the atomic nuclei of the target, producing a continuous poly-energetic X-ray spectrum known as bremsstrahlung. (Turner, 1995; Dowsett, Kenny, and Johnston, 2006; Knoll, 2010).

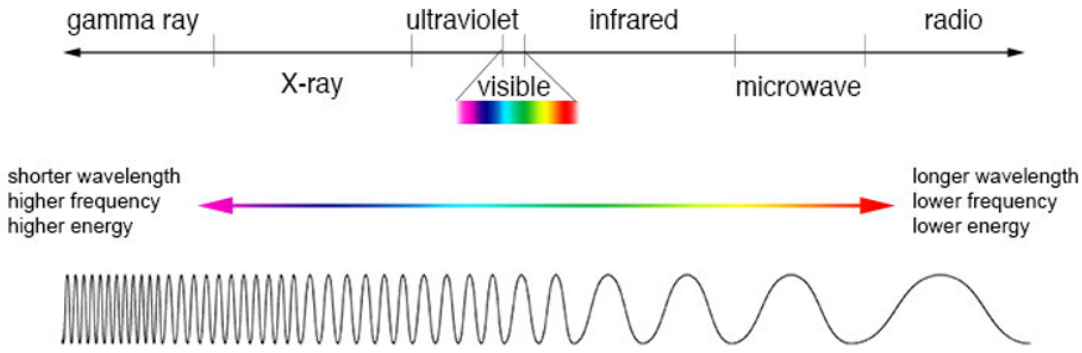

Figure 2.1: Schematic of the Electromagnetic (EM) spectrum. This figures shows that the X-ray photons and the visible or ultraviolet photons are both EM radiation of different energies, frequencies or wavelengths. The figure was taken from the NASA website (NASA, 2015).

2.1.1 Bremsstrahlung radiation

The bremsstrahlung is caused when the electrons pass close to the atomic nuclei of the target and are deflected from their initial path by the nuclear coulomb field. The change of velocity causes them to lose energy in the form of electromagnetic radiation. The X-rays emitted in this process form the Bremsstrahlung (or braking radiation) (Turner, 1995).

This type of radiation forms the continuous X-ray spectrum, with a spread of energies that go from a maximum value, i.e. all the electron's energy is transformed into a X-ray photon, to a minimum energy value, i.e. the electron is slightly deflected. The middle X-ray energies are produced when the electrons suffer several deflections, creating X-ray photons of varied energies. (Dowsett, Kenny, and Johnston, 2006)

2.1.2 Characteristic radiation

If the electron kinetic energy is sufficient, an atomic electron from inner orbitals (K, L, M) of a high atomic number target can be ejected. When electrons from higher shells fill the inner vacancies, discrete X-ray photons are produced, with energies equal to the binding energy, i.e. the energy difference between the two shells. (Turner, 1995; Dowsett, Kenny, and Johnston, 2006; Knoll, 2010)

The X-ray photons produced in this interaction have discrete energies that depend on the binding energy of the target material, so they are characteristic to the material chosen. The characteristic X-ray photons are named after the shell with the vacancy (K, L, ...) and a sub-index indicating the shell that gives the electron (L, M, ...), e.g. K_α, K_β, L_α, L_β, where α and β correspond to the L and M shells or the M and N shell, respectively. Figure 2.2 illustrates three examples of X-ray spectra, K_α, K_β peaks can be seen at energies

59.3 and 67.2 keV for tungsten, at 17.5 and 19.5 keV for molybdenum and at 20.2 and 22.7 keV for rhodium, respectively. The outer the orbit where the vacancy is created, the lower the energy of the X-ray photon and the higher the probability of being absorbed by the X-ray tube housing or filtration. (Turner, 1995; Dowsett, Kenny, and Johnston, 2006).

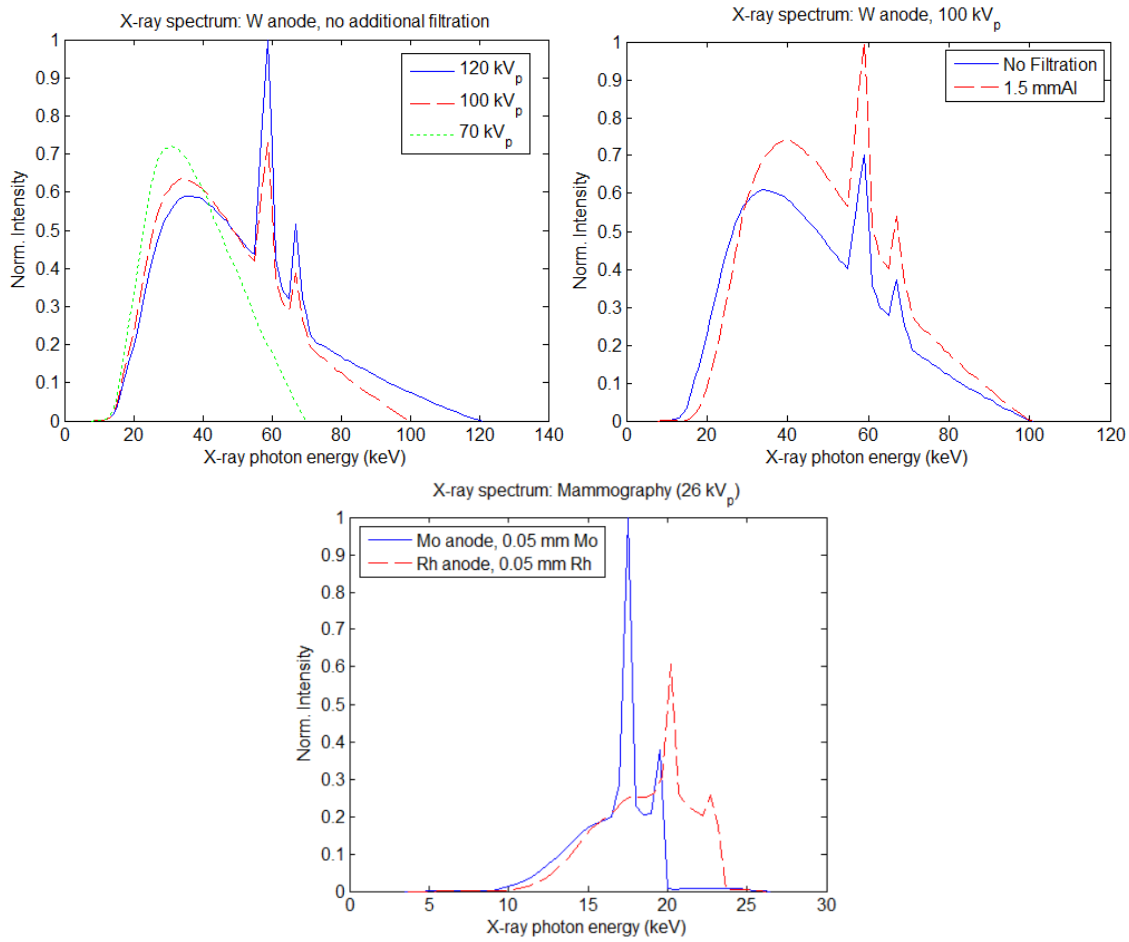

Figure 2.2: X-ray spectrum at three peak voltages (top-left). 100 kVp X-ray spectrum with and without external filtration (top-right). 26 kVp mammography X-ray spectrum with Molybdenum and Rhodium anode/filter combinations.

The X-ray spectrum is a superimposition of the bremsstrahlung and characteristic radiations. For the production of the final spectrum, the choice of the X-ray tube voltage, the anode material (target) and the filtration is crucial, and varies between applications, (Turner, 1995; Dowsett, Kenny, and Johnston, 2006).

2.1.3 X-ray tube characteristics

Voltage

A X-ray tube is formed by an enclosure sealing a cathode and an anode under high vacuum conditions. The electrons are emitted from the cathode, a heated tungsten filament, and accelerated towards the anode in a strong electric field, that is produced by a large potential difference. The spectrum produced is directly related with the electron's kinetic energy and, therefore, with the X-ray tube voltage. The maximum energy will delimit the bremsstrahlung spectrum while the characteristic spectrum will be seen only if the electrons have enough kinetic energy to remove an electron from the inner orbital of the target.

The choice of voltage determines the X-ray penetration and image quality: higher contrast is achieved using low kilovoltages, e.g. being able to distinguish subtle soft tissue differences in mammography applications, while higher voltages, which produce X-rays with increased overall energy, have higher penetration levels needed in general radiography applications.

Target

The anode material needs to have a high atomic number, as heavy nuclei cause stronger electron deflections and are more efficient in producing Bremsstrahlung radiation. The material needs high melting points, as 99+% of the electron's energy is converted into heat, and their contribution to the characteristic radiation needs to be taken into account and balanced with housing and additional filtrations.

The most common target materials are tungsten and molybdenum, with binding energies at the K shell of 69.5 and 59.3 keV, and 20.0 and 17.3 keV respectively.

Filtration

The beam filtration is needed for removing the lower X-ray energies (reducing the patient dose) and "hardening" the beam by increasing the effective energy, e.g. acting as a high-pass filter. The choice of filtration depends on the application. For general radiography, the most common material is aluminium, which has a very low K-edge (1.6 keV), i.e. K-edge is the binding energy of the electrons situated in the innermost shell of an atom. For higher energy medical exams, such as Computed Tomography (CT), a combination of aluminium and copper (8.0 keV) is used. For mammography, however, metals with higher K-edge are needed, as they remove unneeded higher energy photons, e.g. Molybdenum (20.0 keV) or Rhodium (23.2 keV), as well as the lower X-ray energies.

2.2 Photon interaction with matter

When the X-ray beam passes through an absorber, the incident photons can be transmitted without interacting with the material, totally absorbed or scattered from their original direction. The beam is attenuated, i.e. its intensity is reduced, as a consequence of these interactions.

The interactions of the X-ray beam with matter take place at the atomic level and can involve collisions with the electrons (photoelectric effect and scattered radiation) or with the nuclei (pair production). For nuclear interaction the incident photon needs to have a very high energy (E > 1.022 MeV) in comparison with the energies used in diagnostic imaging (20 to 150 keV), as illustrated in Figure 2.3. Therefore only the electron interactions are going to be discussed in this work, i.e. photoelectric effect and coherent and incoherent scattering. (Turner, 1995; Dowsett, Kenny, and Johnston, 2006; Knoll, 2010)

2.2.1 Photoelectric effect

In the photoelectric absorption, the incident photon loses all its energy in the interaction with the atom. One electron is ejected (photoelectron), as illustrated in Figure 2.4, with energy equal to the incident photon minus the electron binding energy and the energy given to the recoiling atom (energy that can usually be neglected). This interaction only affects electrons with high binding energy, i.e. K-shell and (sometimes) L-shell, in order to satisfy both the conservation of energy and of momentum. (Dowsett, Kenny, and Johnston, 2006)

The probability of a photoelectric effect event decreases with the photon energy and increases with the target's atomic number, $\propto \frac{Z^3}{E^3}$. Therefore, its contribution is very strong at low diagnostic energies, i.e. mammography. (Turner, 1995)

The energy given to the photoelectron is usually completely deposited in the absorber, contributing to the radiation dose, as the range of the electron is short and interacts in the surrounding atoms. The photoelectric effect is the major contribution to dose in the tissue. (Dowsett, Kenny, and Johnston, 2006)

2.2.2 Coherent or elastic scattering

Coherent scattering takes place when the incident photon undergoes a change in direction without transferring energy or ionizing the atom. The scatter can happen with bound electrons (Rayleigh scattering) or with loosely bound electrons (Thomson scattering). In the diagnostic energy range, only 10% of the photon interaction events are due to elastic scattering. (Turner, 1995; Dowsett, Kenny, and Johnston, 2006)

Rayleigh scattering

Rayleigh scattering events are more important at low incident photon energies for targets with high atomic numbers. Its probability is proportional to $\propto \frac{Z^2}{E}$. (Turner, 1995; Dowsett, Kenny, and Johnston, 2006)

2.2.3 Inelastic (Compton) scattering

This interaction takes place with loosely bound electrons. The incident photon, of energy E_1, interacts with the electron which is ejected with energy e and at an angle ϕ. The photon is scattered at an angle θ and energy $E_2 = E_1 - e$, as depicted in Figure 2.4. The energy received by the Compton electron and the direction of the scattered photon is related to the incident photon energy; as the incident photon's energy increases, the energy fraction given to the electron increases and a forward scatter angle is favoured. (Turner, 1995; Dowsett, Kenny, and Johnston, 2006)

The probability to have a Compton scattering event slightly decreases with the energy and is independent on the atomic number, $\propto \frac{1}{E}$.(Dowsett, Kenny, and Johnston, 2006)

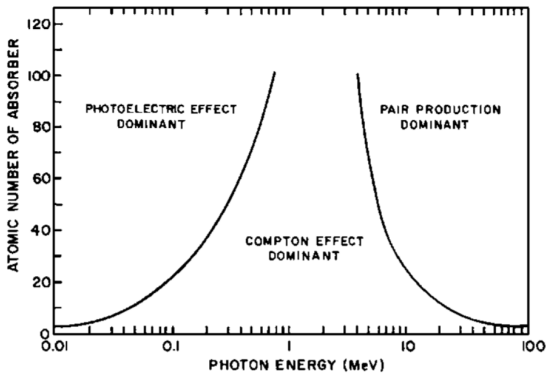

Figure 2.3: The plot shows the range of importance of the three principal X-ray modes of interaction as a function of the photon energy and target's atomic number. Image taken from (Hendee and Ritenour, 2002).

2.2.4 Image formation

The final image is formed by the photons that are absorbed by the X-ray detector. Those photons can be the ones that have been transmitted without interacting along the path (useful information) or scattered photons that increase the noise in the image. The objects that are placed in between the X-ray beam and the imager are shown in the final image because of the difference in the photon intensity, as each material attenuates the beam differently.

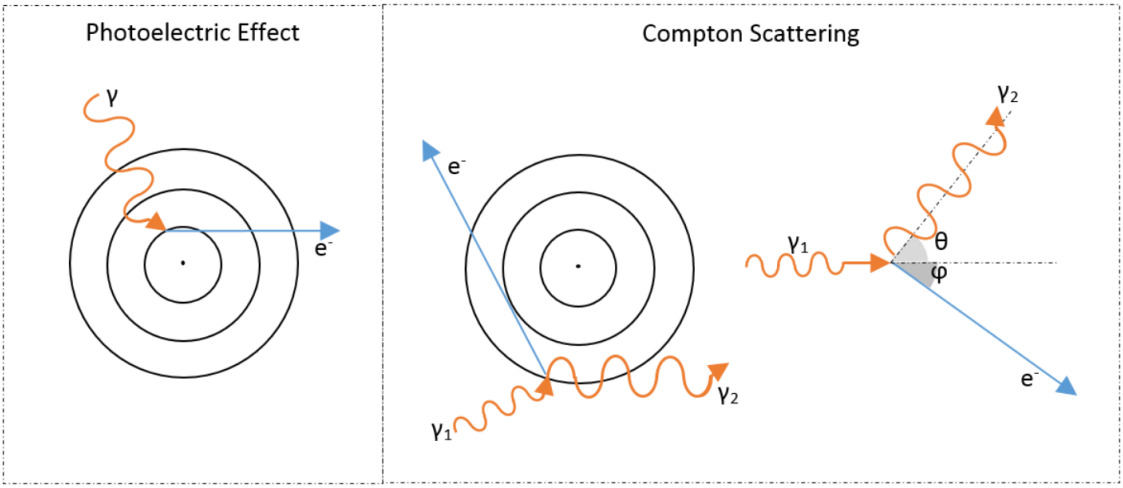

Figure 2.4: Schematics of the Photoelectric Effect interaction (left) and the Compton scattering process (right). In the image the photons are referred as γ and the electrons as e^- .

The initial beam intensity (I_0) is reduced as the photon beam passes through different absorbers, following the exponential law (Turner, 1995; Dowsett, Kenny, and Johnston, 2006):

$$I = I_0 e^{-\mu x} \tag{2.1}$$

where, x is the thickness of the absorber and μ is the linear attenuation coefficient.

The value of the attenuation coefficient depends on the absorber's density and atomic number, but also on the energy of the beam. Equation 2.1 is valid for describing the attenuation of a mono-energetic beam. An energy dependant formula would be needed for describing the poly-energetic process:

$$I = \int_{E_{min}}^{E_{max}} I_0(E) e^{-\mu(E)x} \tag{2.2}$$

At a given energy, it is possible to write μ as a combination of the linear attenuation coefficients of all the X-ray interaction processes (photoelectric, Compton and elastic scattering in the diagnostic imaging range), see equation 2.3.

$$\mu = \mu_{PE} + \mu_{Comp} + \mu_{Ray} \tag{2.3}$$

It is also possible to write it as a sum of the coefficients of different absorbers, see equation 2.4 (Dowsett, Kenny, and Johnston, 2006).

$$\mu = \sum_i w_i \mu_i \tag{2.4}$$

where, w_i is a weighting factor to account for the proportion of each material (i).

The energy dependency of the linear attenuation coefficients is shown in Figure 2.5 for several materials that can be found in medical X-ray imaging applications.

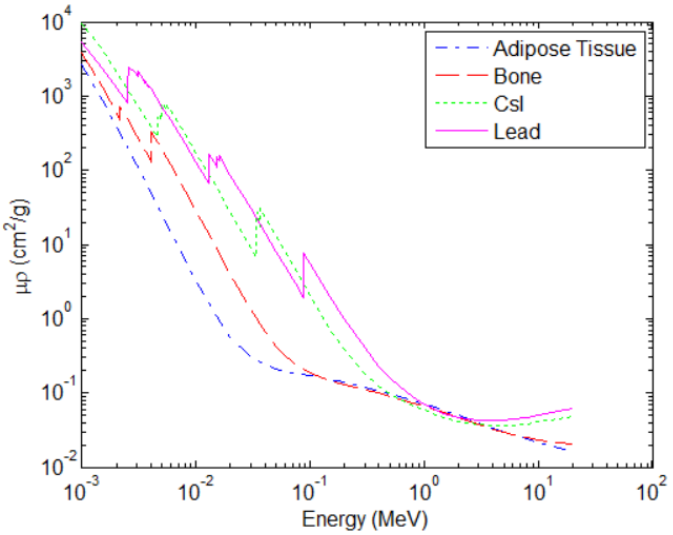

Figure 2.5: Plot showing the dependency of the mass attenuation coefficient (linear attenuation coefficient divided by the density of the material) with the photon energy. The plot shows curves for different materials (adipose tissue, bone, CsI scintillator material and lead). The data was taken from NIST, (NIST, 2004).

2.3 Digital X-ray detectors

The performance of radiography scanners has improved in recent decades, with the development of X-ray equipment and recording systems. In the earlier stages, non-dedicated detectors and industrial film-based detectors were used. Consequently, the contrast in the images was low and the radiation dose delivered to the patient was high, between 50-100 times larger than the average doses currently delivered in mammography, for example (Barnes and Frey, 1993).

Nowadays, more dedicated equipment is used and two main recording systems are available: film-screen and digital radiography detectors. In this section, both methods are explained and their main characteristics compared. In order to address this comparison, a series of parameters have to be defined:

- Signal-to-Noise Ratio (SNR): It is the ratio between the intensity of the signal and the noise at a given region of interest (ROI). The higher the SNR, the better the image quality obtained (James, 2004).
- Dynamic Range: It is the ratio between the maximum signal that the detector can read and the signal equivalent to the noise of the detector (Muller, 1999).
- Spatial Resolution: It is the parameter that describes the ability of an imaging system to individually discriminate two adjacent high-contrast objects.
- Modulation Transfer Function (MTF): It is the measurement of the spatial resolution in the spatial frequency domain.
- Detective Quantum Efficiency (DQE): It is the quantity that measures the efficiency with which the information is transferred from the imaging system to the final displayed image, allowing to quantify how good the imaging system is (James, 2004).

The terms described above are some of the parameters needed to assess the quality of the images. They will be defined further in Section 2.5.

Digital radiography was introduced in the mid-1980s and, with increasing popularity, is currently taking over the conventional film-screen radiography market in all radiographic applications (Bansal, 2006).

The main characteristic and advantage of digital radiography is the separation of image acquisition, image processing and image display. This allows the individual optimization of these three steps, avoiding the compromise in the performance that would be needed otherwise (Muller, 1999; Noel and Thibault, 2004).

Other advantages are a wider dynamic range, increased linearity, higher contrast resolution and higher DQE. This allows either to reduce the delivered dose to the patient maintaining the SNR or to improve the image quality, compensating for the lower spatial resolution that digital systems typically have (James, 2004; Muller, 1999). All these improvements, together with easier processing and data storage, management and visualization, and the possibility of increasing the scope of medical applications, such as in computer-aided diagnosis (CAD) or three-dimensional mammography, makes digital radiography the best system for radiographic screening (James, 2004; Muller, 1999).

There are also drawbacks to a digital radiography system. In addition to the lower image resolution observed, there is a possibility of introducing image artefacts during the processing stage, increasing the number of false positive diagnoses. Although some of the artefacts can be corrected, like the non-uniformity in the response, there are others which are difficult to avoid, e.g. dead areas in the images caused by the gap between two image sensors when they are joined together to make a large area detector. The detector itself can also lead to problems, if the detector field of view is not large enough to cover the

absorber, for example. Finally, there are also some minor disadvantages such as the need of multiple monitors of large dimensions, with large contrast resolution and high luminescence, that increases the price of the system (although it also introduces a powerfull tool by allowing the reader to zoom in or change the image contrast if needed). Monitors are needed to allow radiologists to review the mammograms in an easy way and to allow the comparison between different images at the same time and with high speed (Muller, 1999).

As mentioned above, manufacturers have adopted different approaches and introduced several detector technologies into the market, each of them capable of producing high-quality performance. The main technologies that are currently available are film-screen, photostimulable storage phosphor computed radiography (PSP CR) and solid state detectors, including thin film transistor, i.e. TFT: Amorphous silicon (α-Si) or amorphous selenium (α-Se), CCD and CMOS detectors. Newer technologies that have not been widely adapted yet, such as photon-counting detectors, will not be discussed in this chapter.

2.3.1 Screen-Film

In general, film-screen cassettes consist of a film emulsion layer located between two fluorescent screens and loaded into a light-tight cassette. The fluorescent screens, made of scintillator material, convert the incident X-ray photons into visible or ultraviolet photons that are detected by the film (for a presentation of the differences between types of Electromagnetic (EM) radiation, in particular the X-ray and visible or ultraviolet radiation, refer to Figure 2.1). The film is a sheet of thin plastic with a photosensitive silver halide emulsion coated onto both sides and it is the part of the detector that forms the latent image when the detector is exposed with the X-rays, i.e. it records the X-ray intensity pattern. The final image is obtained by chemically processing of the film, reducing the silver halide into metallic silver grains (Bushberg et al., 2012).

For mammography applications, this configuration is changed to a one sided high definition screen, used as a back screen, in contact with a single emulsion film, which acts simultaneously as an image acquisition detector, as a storage medium and as a display device (Muller, 1999). This combination reduces the light diffusion, which is one of the main causes of blurring (Barnes and Frey, 1993).

The choice of the type of film and screen, the processing conditions (i.e. chemical formulation of the solutions employed), the time of exposure, the dose employed and even the ambient conditions (temperature or humidity) will affect the performance of the detector (Barnes and Frey, 1993). It is, therefore, very important to choose correctly between materials and ways of operations, to optimize the outcome.

The principal advantage of film-screen imaging systems is its excellent spatial resolution. The films are also physically handled, allowing the radiographer to display more than one image at the same time, for comparative analysis, and can be stored for long periods of time suffering almost no degradation. The detectors can be large and have continuos sensitive surfaces and are directly sensitive to the impact of the X-ray beam (Muller, 1999; Noel and Thibault, 2004).

On the other hand, the main drawback is in the image quality; film-screen systems usually have low SNR and low dynamic range. There is a compromise between the spatial resolution and the detection efficiency of the X-ray image and between the dynamic range and the contrast resolution that limits the quality of the images. Moreover, the film layer is fragile and cannot be duplicated without loss of quality (Muller, 1999; Noel and Thibault, 2004). In applications such as mammography, conventional film-screen imaging is not precise enough, missing approximately 10% of the breast cancers that can be detected by physical examinations (Muller, 1999).

2.3.2 Photostimulable storage phosphor computed radiography (PSP-CR)

In this system the screen-film combination is replaced by a storage phosphor imaging plate, also contained inside a cassette. Irradiation excites electrons in the phosphor and the crystalline structure traps them, keeping them stable until the exposure is finished. The number of excited electrons is proportional to the intensity of the beam so, after the exposure, the phosphor plate can be processed and the pattern of the absorbed X-rays read. In the processing step, the phosphor plate is inserted into a reader and scanned by a laser of appropriate wavelength. The phosphor plate can be reused after the residual latent image is erased (James, 2004; Noel and Thibault, 2004).

The main advantage that CR systems have over full digital radiography systems, is the lower investment cost required, as it is possible to re-purpose existing conventional radiography systems just by changing the screen and film of the cassettes by the CR phosphor plates. However, if new installations are required, the cost difference between CR and other digital mammography systems stops being significant. On the other hand, CR needs higher dose to obtain an acceptable image quality, mainly due to lower overall DQE and to the impossibility of changing and optimizing the exposure parameters (Bick and Diekmann, 2007).

2.3.3 Thin-film transistor (TFT) based detectors or Active Matrix Flat Panel Imagers

TFT panels have been used extensively for medical imaging applications since the 1990s. There are two main types: Amorphous Silicon and Amorphous Selenium detectors, which are indirect and direct conversion detectors, respectively.

2.3.3.1 Amorphous silicon-based technology

Amorphous silicon (α-Si) detectors are indirect conversion detectors, the X-rays are converted into visible light photons by a scintillator, usually a layer of thallium-activated caesium iodide (CsI:Tl). The scintillator plate is combined with an array of photodiodes and a thin film transistor (TFT) made with amorphous silicon material, which converts the photons into electronic charges before the analogue-to-digital conversion is performed, see Figure 2.6-left (James, 2004; Noel and Thibault, 2004).

These detectors, also called integrated area detectors, have favourable spatial resolution, good DQE and the images can be obtained in relatively short sequences. However, a reduction of the pixel size is difficult, as it reduces the DQE and increases the required dose exposure to the patient (James, 2004; Bick and Diekmann, 2007). A minimum size of 100 µm is the typical value, although manufacturers have been recently releasing α-Si detectors with smaller pixel size, e.g. 83 µm - Varex Imaging, for mammography applications.

2.3.3.2 Amorphous selenium-based technology

The detector consists of a thin layer of photoconductive material, amorphous selenium (α-Se), deposited on an imaging plate and with a uniform positive charge applied on the surface. The incident X-ray photons strike the surface of the material freeing electrons. The partial discharge produced has the form of a charge distribution pattern, as it is related to the local radiation exposure. The latent image can then be read out and digitalized, resulting in an unprocessed radiography, see Figure 2.6-right (James, 2004; Noel and Thibault, 2004).

The main advantage of this technology over other digital radiography systems is the direct conversion of the X-rays into electrical charge. This allows the avoidance of scintillation noise, sharpness reduction and conversion losses characteristic of indirect X-ray detectors, i.e. when X-ray photons are converted into light and light into electrical charge. Direct conversion detectors have lower noise and a higher degree of sharpness, so they generally have good DQE values. The main drawbacks are longer image lag and ghosting (James, 2004).

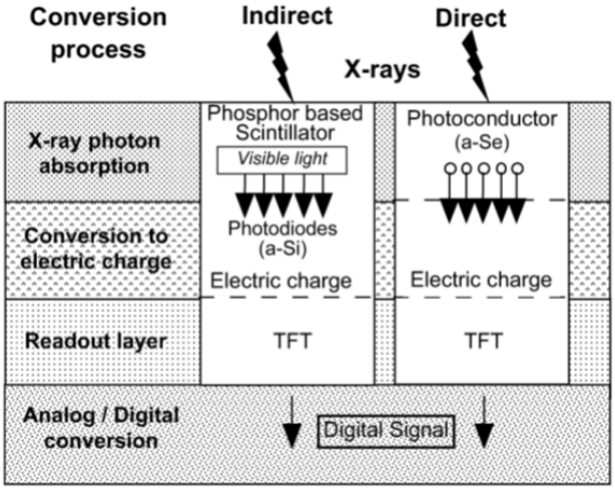

Figure 2.6: Image obtained from A. Noel and F. Thibault (Noel and Thibault, 2004). The figure shows the schematic of both the direct conversion α-Se TFT (right) and the indirect conversion α-Si TFT (left) detectors. It shows the main characteristics of both detectors and the detection process.

The main advantages of these two types of TFT-based detectors are their high performance, radiation hardness and the possibility of achieving large active areas, making them a good choice for general radiography applications.

However, these detectors have high read noise, which results in a reduction of the DQE at low doses. They suffer from ghosting, an excess of image lag and baseline drifts (caused by the amorphous structure) at high frame rates and the pixel size is too large for some applications, usually restricted to 100-130 µm (Konstantinidis et al., 2013).

2.3.4 Charge Couple Device (CCD)

A CCD is another type of indirect solid-state detector. A scintillator, usually CsI:Tl, is used to convert the X-rays into visible photons. Optical focusing devices, such as lenses or fibre optics, are typically used for demagnification in order to match the scintillator size with the CCD size and, finally, a silicon CCD chip is used to detect the light photons, converting them into electronic signal and digitizing them. A schematic of a CCD chip can be seen in Figure 2.7-middle.

When the light strikes the pixel, electron-hole pairs are formed and the electrons are constrained to an area by electrostatic forces. Figure 2.7-left shows the pixel structure with the typical 3 electrode structure. The charge is then moved down the columns (Full Frame Readout method, see Figure 2.7-right) to the readout row using voltage sign changes, then it is moved out from that row, amplified and digitized. (Farman and Farman, 2005; Evans, Workman, and Payne, 2002)

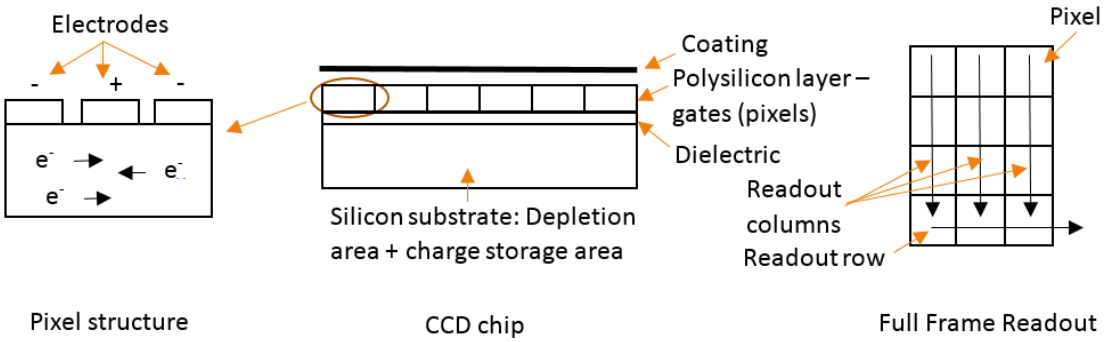

Figure 2.7: From left to right: Typical 3 electrodes pixel structure, CCD chip layout and typical Full Frame Readout schematics.

CCDs have a wide dynamic range (65-70 dB), a low fixed-pattern noise, high light sensitivity, high spatial resolution and a 100% Fill Factor with full frame readout technology. They also present a linear response, small pixel sizes (<=25um), high SNR and, therefore, high image quality.

The main disadvantage of this technology is the size limitation of the sensor, being usually limited to 5x5 cm^2 and significantly increasing the cost with the size. The small active area combined with the impossibility to increase the pixel size reduces the applications that the CCD technology can target. It can achieve high frame rates but the read noise increases with it, limiting its performance for CT, tomosynthesis or fluoroscopy applications. It also requires relatively high power and it is susceptible to temperature changes and radiation damage. The demagnification mentioned above, however, is the major concern as the light collection efficiency is affected and it can also lead to geometric distortion, light scattering and bad coupling efficiency. Special care has to be taken in the demagnification process to minimize these effects (Konstantinidis et al., 2012; Konstantinidis et al., 2013).

The introduction of CMOS technology to the market has progressively taken over the CCD market. This technology is now considered obsolete.

2.3.5 Complementary Metal Oxide Semiconductor (CMOS) imagers

CMOS based X-ray detectors are another type of indirect solid-state detectors. CMOS technology used for image sensors was introduced around the 1960s, but it did not become competitive until the 1990s, early 2000s for medical applications. The first generation of CMOS sensors were based on passive pixel arrays (PPS), but the performance was not comparable to the image quality of the CCD technology. The second generation, named CMOS Active Pixel Sensors (APS), presented lower readout noise and higher speed, improving stability. Due to the high performance of this new generation, the ongoing research has been focused on the APS technology (Bigas et al., 2006).

2.3.5.1 CMOS image sensor

The general architecture of a CMOS image sensor consists of a pixel matrix array selected a row at a time by row select logic. A pixel is addressed when the column and row decoder is active. The pixel is read out when the signal is buffered by an amplifier and the value is sent to vertical column busses that connect the selected row of pixels to a group of Analogue Signal Processors (ASP). The sampled signal is held in a Sample-and-Hold (S/H) capacitor that is connected to each column bus and then is exported from the chip by an output amplifier, see Figure 2.8 (Bigas et al., 2006; Fossum and Member, 1997; Tan, 2013).

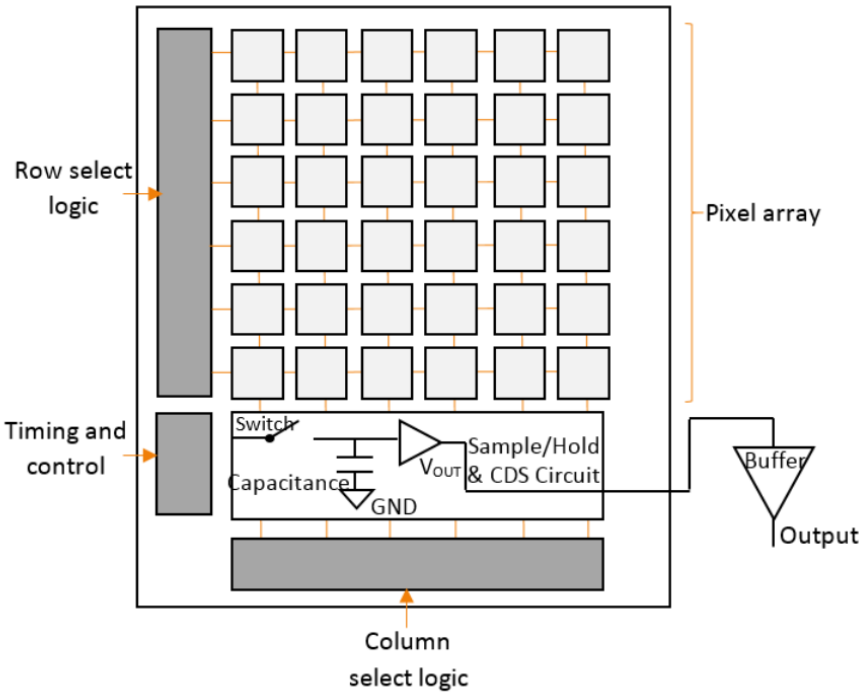

Figure 2.8: Overall CMOS architecture showing the pixel array, the row and column decoders and the analogue signal processors (S/H, CDS Capacitors and Amplifiers). This image is a modified version of the CMOS architecture schematic from (Fossum and Member, 1997; Tan, 2013).

While the PPS pixel structure consists of a photodiode and a pass (access) transistor, the APS approach introduces an active amplifier (source follower) within the pixel structure. This leads to a reduction in the capacitance and, therefore, reduction in the readout noise and increase of the Dynamic Range and the SNR.

The most common pixel type in radiography is the 3T (three transistor) pixel, formed by a photodiode, which is composed of a reverse-biased p-n junction, and three transistors: a reset transistor (RST), a source follower transistor (SF) and a row selector transistor (RS). The schematic of a 3T pixel is illustrated in Figure 2.9.

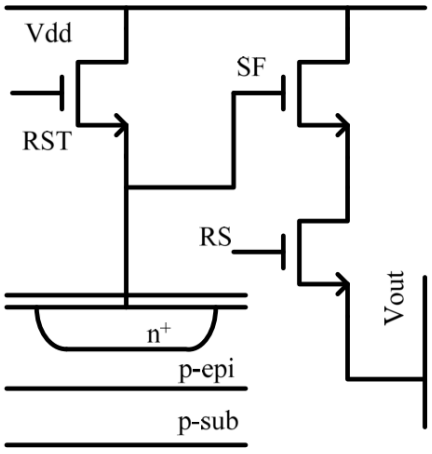

Figure 2.9: CMOS 3T Pixel schematic. Image obtained from (Tan, 2013).

Before the exposure, the photodiode capacitor is charged to a reset voltage through the RST. During the exposure, the RST is turned off and the capacitor gets discharged as the photo-generated electrons are integrated. Therefore, a bright pixel will have lower analogue signal voltage than a dark pixel.

After the exposure, the voltage signal level is read out, the pixel is reset, a new exposure is started and the reset voltage of the second frame is read out. Both voltages are sequentially transferred to the S/H capacitance in a CDS circuit. The signal level is subtracted from the voltage level in order to reduce the fixed pattern noise (FPN), the kTC noise of the photodiode capacitance and the 1/f noise. However, as the sampling process, called delta double sampling (DDS), uses voltages from two different frames the kTC noise is not eliminated and it becomes the main limiting factor in the 3T performance (Tan, 2013).

The CMOS APS technology presents a cost-effective radiographic detector with low power consumption and very fast image acquisition due to its random pixel addressing capability. It is possible to achieve large active pixel areas using stitching and tiling technologies and medium size pixel pitch, around 50 to 100 µm. The performance at high frame rates is good, as the column parallel read out reduces the read noise. The low read noise leads to high DQE values at low exposures and it is possible to avoid blooming and smearing effects, features that limit the performance of CCDs.

The main drawbacks compared with CCDs, are a reduced sensitivity to incident light (due to low fill factor and quantum efficiency), lower dynamic range, which is limited by the photosensitive-area size, the integration time, stochastic noise and high fix pattern noise (Konstantinidis et al., 2013; Bigas et al., 2006).

2.3.5.2 CMOS APS X-ray detector

Since CMOS based X-ray detectors are indirect solid-state detectors, a scintillator plate is required to convert the incident X-rays into light. Despite the relatively high radiation tolerance of CMOS sensors, a Fibre Optic Plate (FOP) is typically placed between the scintillator and the sensor with the objective of absorbing the X-ray photons that are not converted in the scintillator. See schematic below, Figure 2.10: The X-rays pass through the Carbon Cover and are converted into light photons by the scintillator, which is pressed firmly against the Fibre Optic Plate in order to eliminate air gaps. The FOP, bonded to the CMOS sensor, absorbs the remaining X-rays while also guiding the light photons that are detected by the sensor. Finally, the output signal is processed and digitalized in ancillary electronics.

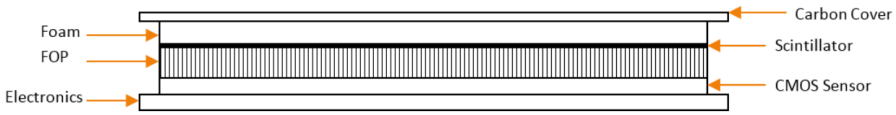

Figure 2.10: CMOS APS X-ray detector schematic.

2.3.6 Scintillator technology

Scintillator screens are materials that, when traversed by an X-ray beam, X-ray photons are absorbed and light photons of a specific wavelength are emitted. When radiation passes through a material, the atoms become excited and light is emitted when electrons return to their ground state. If the emission takes place inmediatly after the absorption, the scintillation process is called fluorescence. On the other hand, if the emission is delayed, due to the presence of metastable states, the process is called phosphorescence. Phosphorescence can occur after some microseconds up to hours. It is important to minimize this effect as it contributes to an increase in noise in the image reducing the quality of the acquired image (Knoll, 2010; Turner, 1995).

The main characteristics that an ideal scintillator material would have are (Farman et al., 2005; Farman et al., 2006):

- Linear light output with the deposited energy.
- High density and atomic number. This leads to high X-ray absorption, improving the spatial resolution and protecting the sensor from radiation damages
- High light output
- Transparency to its own fluorescent radiation
- Appropriate wavelength matching the sensor quantum efficiency curve

- Short decay time without phosphorescence
- Low cost
- Mechanical and chemical ruggedness

Unfortunately, a material with all the above properties does not exist. The most common materials used in X-ray detectors are Thallium-activated structured Caesium Iodide crystals (CsI:Tl) and Gadolinium Oxysulfide (GOS or Gadox) ceramic screens.

CsI:Tl scintillators are grown in a needle-like columnar structure, perpendicular to a substrate (usually carbon or aluminium). The light is channelled to the sensor when the scintillation fluorescence direction is within the acceptance cone of the CsI light guide. If the angle is bigger, the light is scattered to neighbour needles until the incident angle is acceptable to be channelled (Moy, 1998). A general restriction of scintillator materials is their thickness: a thick material leads to a higher X-ray absorption but, at the same time, substantially increases the light scattering and image blur. The needle structure of CsI scintillators reduces the light scattering, allowing an increase of the thickness of the screen without losing spatial resolution quality. This material emits green light and has a response time in the region of 1 to 3 ms (Farman et al., 2005). It has one of the highest scintillation yields and, for the energies used in diagnostic imaging, the number of optical photons emitted per absorbed X-ray is large (>1000) (Granfors and Aufrichtig, 2000). It also has high detectability, due to the K-absorption edge of the Iodine and Caesium, 33.2 keV and 36.0 keV respectively (Konstantinidis et al., 2013). For all these reasons, this material is widely used in X-ray diagnostic imaging.

Gadox screens, $Gd_2 0_2 S$:Tb, present high efficiency (a response time between 1 and 3 ms) green light emission (peak around 545 nm) and a main absorption edge at 50 keV. It is a very stable and easily handled material (Farman et al., 2005). Its main drawbacks are the thickness limitation (the light scatter increases considerably with the thickness due to its unstructured nature) and the deep notch in sensitivity right at the peak of the X-ray beam spectrum for radiography diagnosis applications (Farman et al., 2006). Although CsI:Tl screens are a better option, the low cost of Gadox screens makes them a good alternative for some applications.

2.4 General design requirements for the next generation of detectors

The objective of acquiring images for medical use is to achieve an accurate diagnosis. The last word about the quality of the image is given by the radiologists, who are the subjective receptors. However, there are a series of parameters that define the performance of the X-ray detector and have to be optimized before the product is released.

Any ideal detector would have:

- No dark current, i.e. no electrons generated and collected without light input
- Infinite dynamic range
- 100% of quantum efficiency, i.e. ratio of incident photons to converted electrons equal to 1
- 100% of fill factor
- No fixed pattern noise, i.e. no non-uniformities on dark current generation or pixel response, threshold variations or gain and offset differences
- No sensor noise
- High frame rate
- High resolution
- High signal to noise ratio
- High sensitivity
- No power consumption
- Linear response
- Radiation hardness
- Choice of active area (length)
- Choice of pixel size
- Absence of image lag or ghosting

The limitations present in every sensor technology make it impossible to achieve this ideal case. But in order to develop a product that can be sold in the medical market, the manufacturers have to optimize these parameters to obtain a minimum quality standard, e.g. low dark current, noise and power consumption and high dynamic range, quantum efficiency, frame rate, resolution and sensitivity.

Each digital detector technology has a series of strengths and weaknesses that can be referred to the parameters described above. The choice of technology will be decided depending on the desired medical application and, therefore, the performance optimization will be affected by the targeted requirements.

The most restrictive parameters, that are decisive when choosing between technologies, are shown in the Table 2.1. Some parameters, like the fixed pattern noise or the linearity,

can be corrected in firmware or software and others, like the spatial resolution, can be improved with the choice of scintillator, so they were not taken into account in the table.

Table 2.1: The table shows the expected performance of the four main digital radiography technologies in comparison with the response of an ideal detector. Highlighted in red are the main restrictions the technologies have.

Parameters	Ideal	α-Se	α-Si	CCD	CMOS-APS
Dynamic Range	Infinite	Wide	Wide	Wide	Restricted
Fill Factor	100%	100%	Restricted	100%	Restricted
Read Noise [1][2]	None	*High*	*High*	*Variable with mode*	Low
Frame rate [1]	Infinite	*Low*	*Low*	*Low*	High
Power consumption	None	High	High	High	Low
Radiation Hardness	Yes	Yes	Yes	No	Yes (FOP use)
Size [3]	Large	Large	Large	*Small*	Medium
Pixel size [2]	Small/ Medium	Medium	*Large/ Medium*	Small	Medium

[1] CT, tomography or fluoroscopy applications require high frame rate and low read noise.
[2] Mammography applications require a small or medium pixel size and low read noise. The most adopted technology in mammography is α-Se.
[3] General radiography applications require a large/medium detector active area.

From Table 2.1 it can be seen how the CCD technology is not acceptable for CT, tomography or fluoroscopy applications due to the reduction in the frame rate needed to keep a low read noise. The most widespread technologies for this application are the α-Si and α-Se sensors; however, the possibility of bonding several sensors together, increasing the active area, and the low read noise of the CMOS sensors is helping this technology to become competitive in these markets.

The large active area of α-Si and α-Se X-ray detectors makes them the leading technology for general radiography. CMOS sensors on the other hand have taken over CCD sensors in mammography applications, although the dominant technology still is the α-Se Flat Panel.

2.5 Detector evaluation

When a sensor is being developed, after the technology and application have been decided, its response has to be optimised and its limitations minimised. Due to the complicated structure of the sensor, it is very difficult to simulate the performance of the detector

with high accuracy. This leads to a series of sensor versions that have to be tested against the product specifications. The quality of the image characterization tests will define the quality of the final product, so it is critical for the manufacturer to cover all the possible errors that the sensor might encounter before freezing the design.

2.5.1 Electro-optical performance

2.5.1.1 Noise

Noise is a variation in the pixel value of an acquired image that is not caused by the original object. There are many factors that contribute to the final noise observed in an image and they have to be minimized in order to improve the image quality. The main noise sources in a digital detector are:

Electronic Temporal Noise: In electronic detectors, it is the flow of electrons that conveys the output signal. These electrons can be produced by the input signal or be artificially introduced, causing electronic noise (Hoheisel, 2006).

The electronic temporal noise is composed of (Konstantinidis et al., 2012):

- **Read noise**: It is mainly comprised of pixel source follower noise and it is not function of the signal.
- **Reset** or **kTC noise**: It appears due to the uncertainty of the capacitor's amount of charge after it has been charged through a resistor.
- **Thermal noise**: It is generated in resistors and MOS transistors.
- **1/f noise** or **flicker noise**: It is a low frequency noise that appears in MOS transistors.
- **Dark current shot noise**: It is the statistical variation on the amount of electrons generated in dark (without light input).
- **ADC quantization noise**: Analogue to Digital convertors produce discrete output levels. Therefore, some analogue inputs give the same output value.
- **Phase noise**: It comes from external sources rather than being caused in the sensor, e.g. power supply.

Temporal noise is especially problematic at low signal levels, in particular when the noise-electrons are added to the system before the amplification circuits (Bushberg et al., 2012).

Input Signal Noise: Photon shot noise, or quantum noise, is the variation of the number of X-ray photons detected. These counting statistics follow the Poisson distribution and it can be approximated to the normal or Gaussian distribution if the variance (σ^2) is assumed to be equal to the mean number of photons detected, N. Therefore, the noise is equal to the square root of N and the relative noise, i.e. noise to signal ratio, shows how an increase of the number of detected photons lead to a reduction of the noise (Bushberg et al., 2012). The total photon shot noise is a mixture of both, X-ray photon shot noise and, in less proportion, scintillated photon shot noise.

Fixed Pattern Noise (FPN): FPN, also called structured noise, refers to two parameters: the dark signal non uniformity (DSNU) and the photo response non uniformity (PRNU). The DSNU noise is the offset between pixels in a dark image, i.e. no illumination level, at a specific temperature and exposure time. The PRNU is the response variation between pixels under illumination.

The FPN is usually caused by the read out channels of pixelated detectors, although dust or imperfections in the sensor can also contribute to the noise. CMOS detectors, for example, have parallel read out channels with their own amplification circuits, so they cannot be perfectly matched with respect each other, creating a different offset and gain response between pixels (Bushberg et al., 2012).

The main advantage of the FPN is that it is a correlated non-stochastic noise, i.e. relatively constant in time, so the gain and offset factors of each pixel can be characterized and the image corrected. The gain and offset correction algorithm is described in equation 2.5,

$$I_{\text{corr}} = g\frac{I_{\text{raw}} - I_{\text{offset}}}{I_{\text{gain}} - I_{\text{offset}}} \tag{2.5}$$

where,

$g =$ Mean Pixel Value of the offset corrected gain image, $I_{\text{gain}} - I_{\text{offset}}$

$I_{\text{raw}} =$ Raw image to correct

$I_{\text{offset}} =$ Offset or dark image, acquired with no illumination. Usually 20 dark images are averaged

$I_{\text{gain}} =$ Gain or flat image, typically acquired at a similar illumination level that the image to correct

All the images have to be taken using the same exposure time. It is recommended to collect the I_{offset} and I_{gain} images at regular time intervals to account for temperature or position variations (Bushberg et al., 2012; Konstantinidis et al., 2012)

2.5.1.2 Conversion Gain

The Conversion Gain gives the conversion factor to transform the digital numbers (DN), i.e. count unit (ADC) given by the detector which is meaningless by itself, to electrons.

A way of calculating it is following the mean-variance analysis, described by (Konstantinidis et al., 2012):

$$\sigma_S^2 = G\bar{S} + \sigma_R^2 \tag{2.6}$$

where,

σ_S^2 is the total measured temporal noise (signal independent and dependent). The way of calculating this variable is acquiring a number (N) of images at a constant signal level and quantifying the temporal variation of each pixel around its averaged value. The mean of the resulting 2D matrix gives the total measured temporal noise.

σ_R^2 is the signal independent read noise in $[\mathrm{DN}^2]$

$\bar{S}$ is the signal level in $[\mathrm{DN}^2]$

G is the conversion gain in $[\mathrm{DN}/e^-]$

Plotting the total measured temporal noise versus the signal level and fitting the straight area of the curve will lead to the Conversion Gain (slope of the curve) and the signal independent read noise (y-intercept).

2.5.1.3 Full Well Capacity (FWC)

The FWC is the maximum electronic charge that each pixel's photodiode sense node can accommodate before the pixel is saturated.

It can be obtained using the mean-variance analysis of the conversion gain calculation, by multiplying the conversion gain with the mean signal level that corresponds to the higher variance level, without previously subtracting the dark level (Konstantinidis et al., 2012).

2.5.1.4 Dynamic Range

The dynamic range is the ratio between the largest and smallest value of the signal. It is given by the ratio between the FWC and the read noise. It can be described by the equation below, 2.7 (Konstantinidis et al., 2012; Zanella, 2002).

$$\mathrm{DR}[dB] = 20 \log \frac{\mathrm{FWC}[e^-]}{\sigma_R^2[e^-]} \tag{2.7}$$

2.5.2 X-ray performance

2.5.2.1 Contrast Resolution

Contrast resolution is a measurement of the imaging system's ability to detect subtle changes in the grey scale, i.e. structures that cause small changes in the signal intensity that are difficult to be distinguished from the background.

The SNR is a parameter used for the evaluation of the contrast resolution. It measures the ratio between the signal integrated over an object of interest, i.e. sum of the pixel signal amplitude (for pixel i: $(x_i - \bar{x}_{bg})$), and the noise background (σ_{bg}). Therefore, the SNR studies the integrated signal, obtained from a ROI that encloses the object, divided by the noise, see Figure 2.11. This metric describes how well an object can be observed by including its size and shape, while being independent of its distribution, i.e. it does not require the signal to be homogeneous. (Bushberg et al., 2012).

The SNR can be described as:

$$\mathrm{SNR} = \sum_i \frac{(x_i - \bar{x}_{bg})}{\sigma_{bg}} \tag{2.8}$$

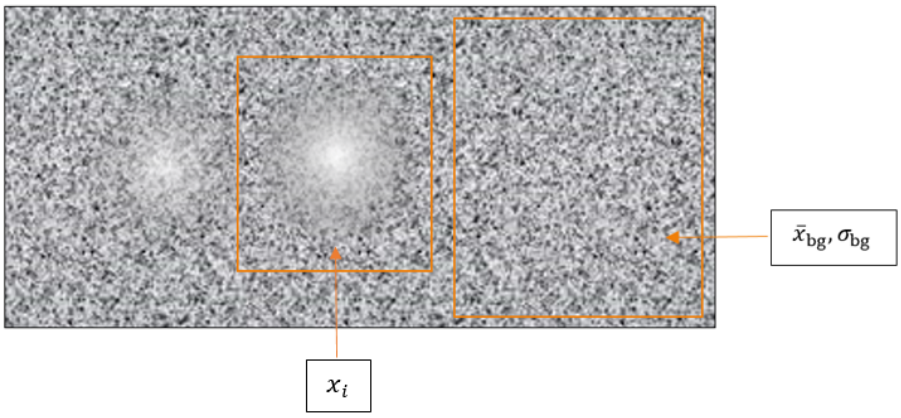

Figure 2.11: Example of a non-homogeneous bright object and the parameters needed for the Signal to Noise Ratio (SNR) calculation. The idea of the image was obtained from (Bushberg et al., 2012).

2.5.2.2 Spatial Resolution: Modulation Transfer Function

The spatial resolution is a measure of the smallest object that can be resolved in an imaging system, describing the level of detail that can be appreciated in an acquired image or the minimum separation distance needed between two high-contrast objects to be discriminated by the imaging system (Bushberg et al., 2012). For digital systems, the lower limit to the size that can be resolved is equal to the pixel size. However, smaller objects can be detected if the signal amplitude is enough to affect the grey scale value of that pixel, i.e. high-contrast objects. Although the pixel size is the lowest limit achievable there are other factors that can restrict further the spatial resolution.

The modulation transfer function (MTF) is a metric that describes the spatial resolution in the spatial frequency domain; this method gives more accurate and objective results than the resolution or line pair phantoms. Conceptually, if an image system is stimulated spatially with a pure sinusoidal wave of frequency f and amplitude 1, it will produce another sinusoidal wave with same frequency but lower contrast, i.e. amplitude smaller than 1, due to the system resolution losses. When the Fourier transform of the resulting signal is calculated, a peak at frequency f and height equal to the amplitude of the wave will be obtained. If instead of one pure sinusoidal wave, the input signal is formed by more than one wave, the Fourier transform will separate the result for each frequency. The curve evolving each one of the frequency peaks will result in the MTF curve. This process is illustrated in Figure 2.12.

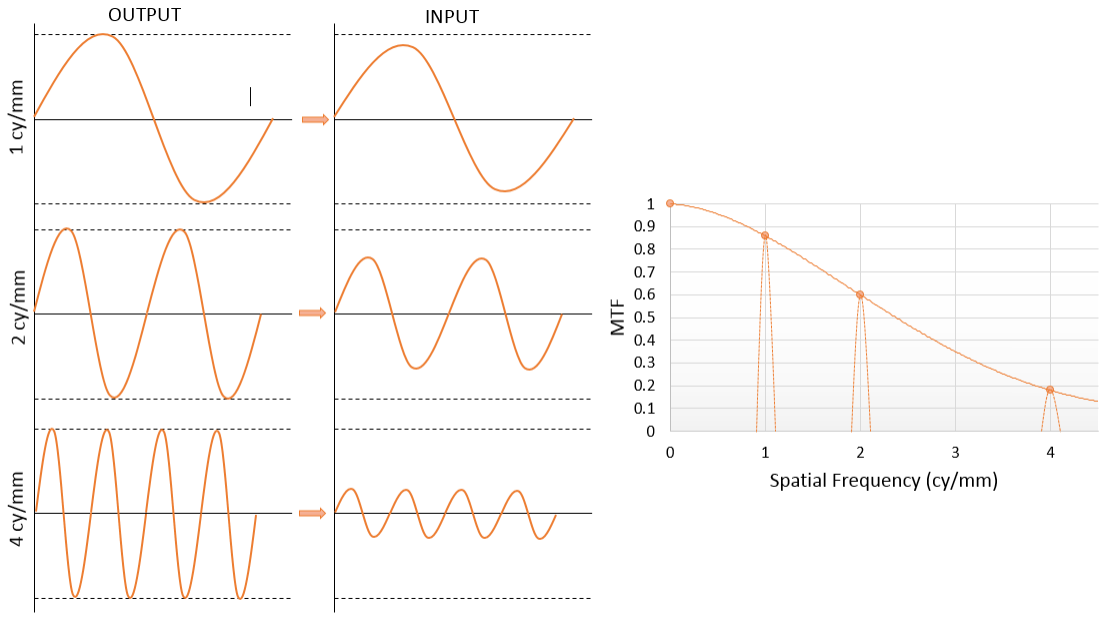

Figure 2.12: Description of the effect that the imaging system has over pure sinusoidal profile (left) and visual explanation of how the MTF is obtained (right).

The MTF values are between 0 and 1, where 1 means a complete transmission of the object's contrast to the output image and 0 means no transmission of the contrast. High spatial resolution results in an improvement of image sharpness and a better detection of small details (very useful in analysis of microcalcifications, for example). Therefore the MTF is desired to be as high as possible for all frequencies.

While the MTF describes the spatial resolution in the frequency domain, there are three other functions that help to define it in the spatial domain: point spread function (PSF), line spread function (LSF) and edge spread function (ESF):

- The PSF is the 2D response of the system to a point source that is, approximately, five to ten times smaller than the pixel pitch.
- The LSF describes the response of the system to a test device that has a narrow slit (1D).
- The ESF is the response of the detector to a sharp edge (1D). A straight edge is the easier device to make, so the MTF is usually obtained from a measurement of the ESF.

There is a direct relationship between these four parameters, see equations 2.9, 2.10 and 2.11, so it is possible to choose the simplest and easier function to measure and calculate the MTF.

$$\mathrm{LSF}(x) = \int_{y=-\infty}^{\infty} \mathrm{PSF}(x, y)dy \tag{2.9}$$

$$\mathrm{ESF}(x) = \int_{y=-\infty}^{\infty} \mathrm{LSF}(x')dx' \tag{2.10}$$

$$\mathrm{MTF}(f) = \mathrm{FFT}(\mathrm{LSF}(\mathrm{x})) \tag{2.11}$$

The MTF evaluation is very sensitive to the measurement acquisition method, the analysis process and the measurement settings. The International Electrotechnical Comission created the documents: "IEC 62220-1: Medical Electrical Equipment - Characteristics of Digital X-ray Imaging Devices - Part 1: Determination of the Detective Quantum Efficiency", (IECP, 2007b), and "IEC 62220-1-2: Medical Electrical Equipment - Characteristics of Digital X-ray Imaging Devices - Part 1-2: Determination of the Detective Quantum Efficiency – Detectors used in mammography", (IECP, 2007a), in order to standardise and control the MTF measurement method, reducing the number of variables that hinders the comparison between systems.

E. Samei, J.T. Dobbins and N. T. Ranger, (Samei et al., 2006), made a study of the relationship between three different methods used for MTF estimation, two developed before the international standard and the IEC 62220-1 method, aiming to find a relationship that would allow the comparison of results in the literature.

In their study, they also included an analysis of the impact of different measurement settings in the MTF results. They found that there is very little difference between the MTF measurement in the horizontal and vertical directions, with exception of slot-scanning systems. That the presence of external collimators affect the final measurement of the MTF between a 4.0%±0.9% and 7.0%±0.9%, for external apertures and internal beam collimators respectively, and that a misalignment between the edge and the axis of the X-ray beam does not introduce significant changes in the MTF estimates.

Their evaluation concluded that the method introduced by the IEC standard, using an opaque edge test device for measuring the ESF, gives lower MTF measurements. The averaged relative differences up to the Nyquist frequency, i.e. highest frequency that allows the full reconstruction of the signal, was found to be 5.2%±0.2% when compared with a method using a slit test device for calculating directly the LSF, method that was introduced by Dobbins et al. (Dobbins et al., 1995), and 2.0%±0.2% when compared to a method using a translucent edge test device, introduced by Samei et al. (Samei, Flynn, and Reimann, 1998).

2.5.2.3 Noise Power Spectrum

The Noise Power Spectrum (NPS) is a parameter that quantifies the spectral decomposition of the noise variance of an image as a function of the spatial frequency (Monnin et al., 2007; Konstantinidis, 2011). It is a way of quantifying the noise "texture", i.e. two images can have the same variance but a different frequency dependence of the noise. The NPS gives a more accurate description of the noise by measuring the effect that the image system has on the noise input (Hoheisel, 2006).

The 2D NPS is described by equation 2.12 (IECP, 2007b):

$$\mathrm{NPS}(u,v) = \frac{\Delta x \Delta y}{M N_x N_y} \sum_{i=1}^{M} |\mathrm{FFT}\left[I(x_i, y_i) - S(x_i, y_i)\right]|^2 \tag{2.12}$$

where,

(u, v) are the spatial frequencies in the horizontal (x-axis) and vertical (y-axis) directions, respectively.

Δx and Δy are the pixel sizes in the x-axis and y-axis respectively. Note that $\Delta x = \Delta y$ for squared pixels.

$N_x N_y$ is the Region of Interest (ROI) size, 256 x 256 pixel^2 if the analysis method followed is the IEC 62220-1 (IECP, 2007b).

M is the number of ROIs per frame.

I(x,y) is the flat field image.

S(x,y) is the correction applied to each captured image to compensate the presence of background trends and non-linearity.

The NPS curve is constant as a function of spatial frequency for uncorrelated or white noise, i.e. the noise value of one pixel is independent of its neighbours. However, it typically decreases with the spatial frequency when the noise is correlated, i.e. there is noise leak into adjacent elements (Bushberg et al., 2012).

2.5.2.4 Detective Quantum Efficiency (DQE)

The DQE metric describes the ability that an imaging system has to capture information over a range of spatial frequencies. It expresses the efficiency with which the detector uses the input signal (incident X-ray photons) to form the image, i.e. how effectively the system uses the available input quanta (Monnin et al., 2007; Konstantinidis, 2011).

The DQE depends on the noise generated by the detector and its spatial resolution, so it gives a measure of the SNR, the contrast resolution and the dose efficiency (Noel and Thibault, 2004; Smith, 2003). An ideal detector would have a DQE equal to 1 for all spatial frequencies, while a real detector has values between 0 and 1, typically decreasing with increases of the spatial frequency, as a consequence of the degradation of the SNR between the output and the input signals(Konstantinidis, 2011; Noel and Thibault, 2004; Smith, 2003). Therefore, improvements in the DQE results in better image quality while keeping the dose received by the patient constant, or even decreasing it. The DQE is given by equation 2.13

$$\mathrm{DQE} = \frac{\mathrm{SNR}^2_{\mathrm{Out}}}{\mathrm{SNR}^2_{\mathrm{In}}} = \frac{\mathrm{MTF}(f)^2}{\frac{\phi}{k_a} k_a \,\mathrm{NNPS}(f)} \tag{2.13}$$

where,

$\mathrm{SNR}^2_{\mathrm{Out}} = \frac{\mathrm{MTF}(f)^2}{\mathrm{NNPS}(f)}$. The NNPS, Normalized Noise Power Spectrum, is already a measure of the variance and does not need to be squared.

$\mathrm{SNR}^2_{\mathrm{In}} = \frac{\phi}{k_a} k_a$ is the fluence per exposure ratio, $\frac{\phi}{k_a}$, multiplied by the exposure kerma (in µGy).

There are different ways of calculating the fluence per exposure ratio. The International Standard IEC 62220-1 gives a photon-counting approximation, assuming that an ideal detector behaves like an ideal photon counter. It can be calculated following the equation 2.14 (Konstantinidis et al., 2012).

$$\frac{\phi}{k_a} = \int_0^{kV} \phi_{\mathrm{norm}}(E) \frac{WQ}{(\frac{\mu_{en}(E)}{\rho})_{\mathrm{air}} E e 10^8} dE \tag{2.14}$$

where,

$\phi_{\mathrm{norm}}(E)$ is the normalized spectrum.

$W = 33.97[\mathrm{eV/ionpair}]$ is an accurate value for X-rays in dry air, (Konstantinidis et al., 2012).

$Q = 2.5810^4[C/Kg/R]$ is the charge liberated in air by one R.

$e = 1.602210^{-19}[C]$ is the electronic charge.

As mentioned, the standard gives a photon-counting approximation. For energy integrating detectors it is possible to perform an energy-weighted calculation of the fluence per exposure ratio. However, previous studies mentioned by Konstantinidis et al. ((Konstantinidis et al., 2012)) proved that the difference at radiation quality RQA-5 (explained below) is less than 3%, decreasing further for lower voltage spectra.

The International Standard dictates the DQE assessment at different radiation qualities, which correspond to different radiographic applications. The measurement settings and the photon-counting approximation vary with each radiation quality; the IEC 62220-1-2 document provides the radiation qualities for mammography (RQA-M) while the IEC 62220-1 document gives radiation qualities RQA3 (paediatrics), RQA5 (general radiography) and RQA7 (higher energy applications), among others.

2.6 Chapter summary and discussion

This chapter presented a critical review of the theory behind digital X-ray detector technologies. To set the basic knowledge needed to understand the concepts that will be introduced in this thesis, the chapter started with a theoretical introduction of X-ray production, photon interaction with matter and X-ray image formation.

The main widespread digital X-ray detector technologies such as TFT panels, i.e. α-Se and α-Si, CCDs or CMOS were then introduced, including their general design requirements and comparing them against the performance of an ideal X-ray detector.

The chapter finished giving detailed information about the techniques and parameters involved in the evaluation and quality control of X-ray panels. It was defined that a characterization exercise needs to focus in the study of the electro-optical performance of the detector as well as its response to incoming photons. Therefore, the chapter explained the theory behind the different types of noise (e.g. electronic temporal noise, input signal noise and fix pattern noise), introduced the concept of conversion gain, dynamic range and contrast resolution, and gave the theoretical background and analysis methods needed for measuring the MTF (for spatial resolution analysis), NPS (for noise structure analysis) and DQE (gold standard that describes the ability that the imaging system has to capture the incoming information).

The parameters explained in this section allow to fully characterize the performance of a detector and set the basis for the comparison between technologies and manufacturers.

Chapter 3

Characterization of CMOS X-ray detectors

This chapter has been excised for industrial IP confidentiality reasons.

Chapter 4

Scatter Reduction

This chapter introduces the second part of the thesis. It begins with some background information about breast cancer and mammography systems. It continues with a mathematical interpretation of the scatter distribution in an image to then focus in defining the different grid-less scatter reduction methodologies available for mammography applications.

4.1 Mammography

4.1.1 Breast anatomy

The femmale mammary gland lies partly on the ribs and partly on the pectoralis muscle, a large fan-shaped muscle that covers the chest and stretches up into the armpit. The breast is formed by three different type of tissue: glandular, fibrous and fatty tissue, surrounded by a thin skin layer. The glandular tissue is composed by 15-20 lobes, each of which is formed by lobules, smaller gland structures that radiate around the nipple and produce milk in nursing women. Each lobule opens into small ducts that join together to form the excretory or lactiferous ducts. Towards the centre of the breast, these ducts form dilatations, lactiferous sinus, that act as milk reservoir which, at the same time, are connected to the nipple by narrow ducts (Seeley, Stephens, and Tate, 1998; Waugh et al., 2014; Kopans, 2007). An illustration of the structure of the breast can be seen in Figure 4.1.

The lobes are supported by the fibrous tissue and covered by adipose tissue, which gives the breast its form. The breast is supplied with blood with the thoracic branches of the axillary artery, the internal mammary and intercostal arteries and the axillary and mammary veins. The lymphatic channels run towards the armpit, passing through the lymph nodes, which are in charge of filtering the germs contained in the lymph.(Seeley, Stephens, and Tate, 1998)

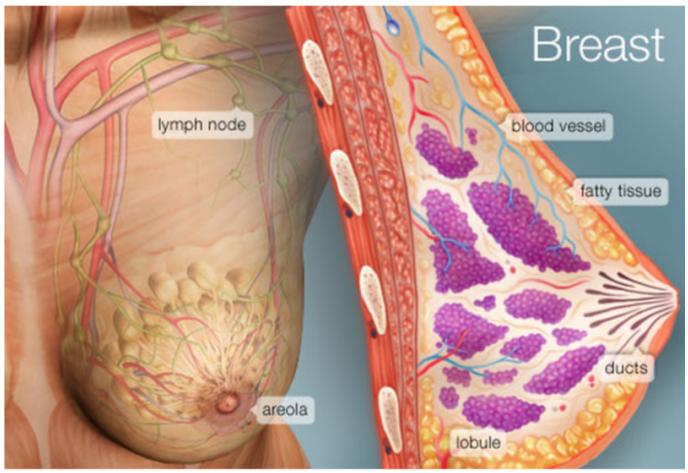

Figure 4.1: The figure shows the structure of the breast (WebMed, 2014).

4.1.2 Breast cancer

Cancer is the term used to describe a group of diseases whose common characteristic is the transformation of a normal cell into one that behaves dangerously for the human body. Among females, breast cancer is the leading cancer-related cause of death globally. There are approximately 1.7 million new breast cancer cases per year worldwide, representing 25 % of all cancers in women, (World Cancer Research Fund International, 2015). In the UK, one in eight women will be diagnosed with breast cancer during their lifetime (McPherson, Steel, and Dixon, 2000; Tobias and Hochhauser, 2009; Torre et al., 2016).

90% of breast tumours are benign, being fibroadenomas the most common type. Although they can be formed any time after puberty, most incidences happen nearing the menopause (Waugh et al., 2014). Malignant tumours appear in the epithelial cells that line the terminal duct lobular unit, they can be classified as non-invasive, i.e. carcinoma in situ (DCIS), or invasive. In the first type, the cancer cells are found inside the milk ducts and have not spread, this accounts for 1/5 of the diagnosed women. In the invasive carcinomas case (4/5), the cancer grows out of the milk ducts and into the surroundings of the breast. If untreated, most will spread to other parts of the body (metastasis) (McPherson, Steel, and Dixon, 2000; NHS, 2016).

Tumours can be classified by their shape. Benign masses have, in general, well-defined contours and are round or oval in shape, while malignant masses have an irregular outline. The lesion classification is done by identifying factors that can be used to describe the lesion and help with the diagnosis, such as Compactness (C), Fourier Factor (FF), Fractal Dimension (FD), Fractional concavity (Fcc), or Spiculation Index (SI) (Rangayyan and Nguyen, 2005). Once the tumour is detected a biopsy is needed to confirm the diagnosis.

In order to reduce the uncertainty and standardize the diagnosis in mammography, the American College of Radiology (ACR) developed, published and registred in 1992 a radiographic tool called BI-RADS (Breast Imaging Reporting and Data System) (Sickles, 2013). The BI-RADS atlas helps to describe, classify and categorise the findings and it has been widely adopted in clinical practice throughout the world and in screening programmes in the US and Europe (Timmers et al., 2012).

The causes of breast cancer are not completely understood. However, there are different factors that have been linked with an increase of the probability of developing breast cancer (NHS, 2016; Dixon, 2012; Waugh et al., 2014; Tobias and Hochhauser, 2009):

Age: The risk of developing breast cancer increases with age, up to 8 in 10 breast cancer cases are developed in women that are over 50 years old.

Previous diagnosis of breast cancer: Women who have developed breast cancer in one mammary gland have higher probability of developing a new breast cancer.

Previous diagnosis of a benign breast lump: Benign changes in breast tissue may increase the risk in developing future breast cancer. Some examples are: atypical ductal hyperplasia - cells growing abnormally in ducts; or lobular carcinoma in situ - abnormal cells inside the breast lobes.

Family history: Although most breast cancer cases do not run in families, some genes that can be passed on from a parent to their child are associated with an increase in the breast cancer risk, i.e. BRCA1, BRCA2, TP53 and CHEK2 . Up to 10% of breast cancers cases in Western countries are due to genetic predisposition .

Oestrogen - Menarche, menopause and breast feeding: Oestrogen is a female hormone that can stimulate breast cancer cells and cause them to grow. Therefore, a higher oestrogen exposure level might slightly increase the risk of breast cancer, for example in cases of late menopause, late or non offspring breastfeeding or a menarche age of 12 years or younger.

In addition, studies have shown a protective effect for those women who have their children at an early age. This effect is seen in those women who have a full-term pregnancy with an age of 32 years or less, being more clear if the pregnancy takes place before 25 years old.

Breast density: This effect is not fully known. One of the possible explanations is the increase of lobules, i.e. glandular tissue that contains higher concentration of breast cells, which increase the number of cells that can become cancerous.

Lifestyle and health: Breast cancer is more frequent in women suffering from obesity, especially after the menopause, as being overweight causes more oestrogen to be produced.

Alcoholics are also more likely to develop breast cancer. In fact, studies show that there are three more cases for every 200 women if these women drink two alcoholic drinks a day.

Exercise has been proved to have a protective effect. A reduction of breast cancer incidence can be observed just with 30 minutes of exercise per week.

Radiation: X-rays, Computed Tomography (CT) scans or previous radiotherapy treatments, like the treatment of Hodgkin lymphoma, may increase the risk of breast cancer very slightly.

Hormone Replacement Therapy (HRT): This treatment is associated with an increased risk. Patients treated with combined HRT for 10 years show an increase of 19 cases for every 1000 women.

Contraceptive pill: Research shows a slight increase in women that take contraceptive pills. The risk starts decreasing the moment the woman stops taking the contraceptive pill. After 10 years the risk is back to normal.

Although there are no definite conclusions, studies suggest that maintaining a healthy lifestyle, i.e. healthy weight, regular exercise, low intake of saturated fat and alcohol, can reduce the risk of developing breast cancer by as much as a third (NHS, 2016).

More extreme measures can be considered for women that are in a high-risk group, such as performing a mastectomy, which can reduce the risk up to 90 %, or the use of medication, e.g. tamoxifen, anastroxole or raloxifene. These are not ideal solutions as it implies undergoing major and invasive surgery or taking medication with many side effects, some as serious as osteoporosis, blood clots or uterine cancer (NHS, 2016). For each individual case it will be necessary to balance the risk and benefits of the treatment.

In any case, if a breast cancer is developed, an early diagnosis can improve the outcome of the treatment, increasing the chances of survival and reducing the need of a mastectomy

or chemotherapy. For this reason, breast cancer awareness is very important; it is key to be familiarised with the symptoms and seek medical opinion if they appear. The first noticeable effects of breast cancer are usually the presence of a lump or thickened breast tissue. It is important to note that breast pain is not a symptom. Some indications can be (NHS, 2016):

- Change in size or shape of the breast(s)
- Change in appearance of the nipple(s)
- Nipple discharge
- Nipple rash
- Lump or swelling of one of the armpits
- Dimpling on the breast skin

However, a breast cancer in an early stage does not usually show any symptoms. For that reason, after a certain age and to increase the chances of early detection, some countries implement regular breast screening programmes.

4.1.3 Screening

Screening is the procedure of checking for the presence of potential health disorders in an asymptomatic population group (National Cancer Institute, 2015; WHO, 2014).

It is not possible to carry out screening programmes for all types of diseases, for example some health disorders cannot be detected before causing a symptom and some screening programmes present more disadvantages than benefits to the overall population. Therefore, screening programmes are limited to specific types of diseases, to certain population groups and/or to people with specific genetic risks.

To be considered valid, a screening programme needs to take the following aspects into consideration (Tobias and Hochhauser, 2009; WHO, 2014):

- Sensitivity of the test: It needs to be able to detect early stages of the disease and have a low index of false-positive results.
- Usefulness: The disease has to be treatable and curable if detected in an early stage.
- Incidence of the disease: The disease has to be common and have a high incidence to justify the programme.

Breast cancer is considered a suitable disease for a screening programme. It has high incidence in women population, there are high risk groups and it is easy to examine. Mammography is the only breast screening programme that has proved to be cost-effective so far. Several studies have shown that while self-examination does not show improvements in the mortality rate, there is approximately 20 % of relative mortality reduction, for patients over 50 years old, when a mammogram is done every two or three years (Tobias and Hochhauser, 2009; Whitman et al., 2006). However, the World Health Organization (WHO) (WHO, 2014) warns that, for mammography being an effective solution, the screening programme has to be implemented in an "organized population-based": the programme has to be of high standard, targeted at all the population at risk and the whole screened group needs to benefit equally of the screening, diagnosis and treatment services. Programmes that lack the necessary quality control, are opportunistic or not population-based can cause more harm than benefits and should not be implemented.

Younger women that have higher-than-average risk of breast cancer, might be referred for genetic testing and, if appropriate, for yearly MRI scans or mammograms, depending on age and level of risk. An ultrasound or a MRI scan will be performed if the woman has dense breast tissue, as lesions are harder to spot. (NHS, 2016)

Mammography screening programmes have a narrow balance of benefits and harm, especially in younger and older women. The risks or drawbacks that need to be taken into consideration are, among others (NHS, 2016; WHO, 2014):

- Prevention: Breast screening is only used for diagnostic purposes, it does not prevent the development of the cancer and may not be of much help if the cancer is at an advanced stage.
- Over-diagnosis: some women will be diagnosed and treated for a breast cancer that would have never caused them harm.
- False-positive/distress: 1 every 25 women will be called back for further assessment. From those, only the 25 % will be diagnosed, causing unnecessary worry to the rest 75 %.
- False-negatives: Missed tumours cause false security and delay in the diagnosis. The risk of false-negatives increase for dense breasts and young women.
- Radiation: A mammogram is a type of X-ray scan, which involves the use of ionizing radiation. However, the dose delivered in a mammogram is low, e.g. 5.5 times lower than the yearly dose received from natural background radiation, and the benefits of an early diagnosis outweigh the risk of having an X-ray scan performed.

There have been many studies published lately in favour and against mammography screening programmes, showing a significant uncertainty in the results and presenting

estimates that vary greatly between studies (Welch and Passow, 2014; Nikola and Peter, 2014; Miller et al., 2012). Reviews of observational studies entail a risk of bias in the interpretation of the available evidence, while specific trials can be outdated, not reflecting current practices and providing wrong estimates, (WHO, 2014).

The statistics presented by the National Health Service (NHS) and Cancer Research UK (NHS, 2016) show that while screening saves 1 every 200 women screened, 3 every 200 will be misdiagnosed and treated. This translates into 1300 lives saved and 4000 misdiagnosis per year in the UK; for every one woman saved, 3 will be diagnosed with a cancer that would never have become life-threatening. However, even if over-diagnosis is of great concern for policy-makers, qualitative research has shown that women see it as less personally relevant than a possible under-diagnosis (WHO, 2014).

In the UK, the NHS Breast Screening Programme was set up by the Department of Health in 1988. This programme was pioneering in the world, and currently performs around one and a half million mammograms each year (NHS, 2016). Women aged 50-70 are invited for breast cancer screening every three years, although at the moment the NHS is preparing a trial for extending their screening period to 47-73 years old women. The recommendation given by the WHO (WHO, 2014) is to keep mammography screening programmes in those countries that can guarantee an organized population-based programme. Their recommendation is to image women between 50 and 69 years old with a frequency of two years. Therefore, the benefits of the mammography screening are still considered to be higher than the shortcomings. The implementation of a risk-based stratification screening protocol is currently being studied, where the type of breast imaging modality is chosen based on the risk of each specific woman.

4.1.4 Technology and geometry

4.1.4.1 Mammography X-ray systems

The breast is composed of very similar soft tissues (fat, glandular or fibrous tissue), in opposition to conventional radiography applications where air, bone and soft tissue have very different attenuation properties. For this reason, mammography examinations are done using low energy X-rays, i.e. 25-30 keV, in the range that is most sensitive to small differences in tissue attenuation, where the effect of Compton scatter is minimum and the photoelectric effect is dominant, as illustrated in Figure 4.2.

In addition to the low energy photons, the contrast is maximized by selecting the right anode/filter material combination. The most typical materials used are combinations of Molybdenum (Mo), Tungsten (W), rhodium (Rh) or, in case of large breasts, Silver (Ag). Refer to Figure 4.3 for a comparison of Mo/Mo and Rh/Rh X-ray spectrum.

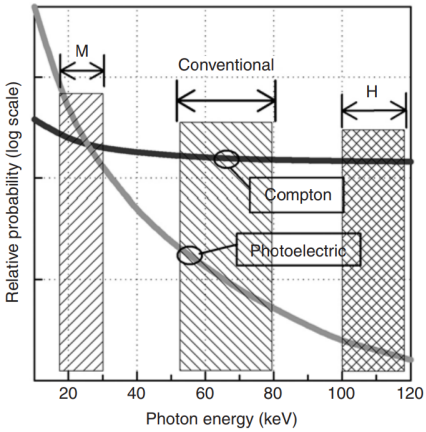

Figure 4.2: The figure shows the probability of photoelectric and Compton interactions as a function of the energy; highlighting the typical energy ranges for mammography examinations (M), conventional radiography and the high range examinations (H). The figure was taken from (Dowsett, Kenny, and Johnston, 2006).

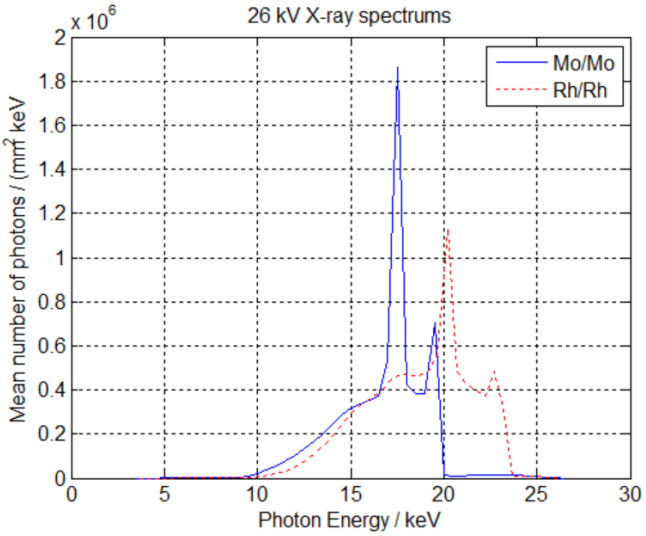

Figure 4.3: 26 kV X-ray spectrum for Mo/Mo (blue continued curve) and Rh/Rh (red dotted curve)anode/filter combinations. The Siemens online tool for the simulation of X-ray Spectra was used to obtain the data (Siemens, 2018).

A mammography system is comprised, from top to bottom, of: X-ray tube, additional filtration, collimator, breast compression paddle, support paddle, and X-ray detector. The typical geometry can be seen in Figure 4.4 and the typical parameters used in mammography examinations can be found in Table 4.1.

The image is formed by the photons that arrive at the X-ray detector sensor. Due to the low energy that is needed in mammography, the photon transmission is low, i.e. for 5cm breast thickness and a practical kilovoltage level of 28kV the transmitted photon fraction is around 20% (Dowsett, Kenny, and Johnston, 2006). As breast density increases, the

transmission decreases and the scatter radiation increases.

Table 4.1: The table shows the typical dimension values and material types of the geometry of digital mammography systems. Most of the parameters depend on the manufacturer and/or the breast thickness of the patient, the values shown in the table are only indicative.

Simulation Parameters		Value/Range	Material	Ref.
Anatomy	Breast Thickness	20-80 mm		4
Geometry	SID [1]	650-660 mm		5, 6
	SPID [2]	15-20 mm		4, 6
	Compression paddle	2-3 mm thick	Polycarbonate	5, 6
	Support paddle	2.5-3.5 mm thick	Carbon fibre	5
	Divergence angle	Up to 8 deg.		7
	Anode/Filter		Mo/Mo, Mo/Rh, W/Rh, W/Ag [3]	4
Settings	Energy	24-35 kVp (2-8 cm breast thickness)		4

[1] SID = Source to Imager Distance
[2] SPID = Support Paddle to Imager Distance
[3] Mo=Molybdenum, Rh=Rhodium, W=Tungsten, Ag=Silver
[4] (Boone et al., 2000)
[5] (Sechopoulos et al., 2007b)
[6] (Leon, Brateman, and Wagner, 2014)
[7] (Boone and Cooper, 2000)

For this reason, breast compression is key to improve image quality and reduce the dose delivered to the patient. With the compression, the breast tissue is more homogeneously distributed, the thickness becomes constant towards the centre of the breast and there is scatter reduction. In addition, low energy photons are absorbed in the paddle, hardening the beam and reducing the dose absorbed in the breast. Therefore, the image resolution and subject contrast are considerably improved (Dowsett, Kenny, and Johnston, 2006).

4.1.4.2 Mammography X-ray detectors

The improvements that radiography examinations have undergone in the last 50 years have been especially significant in mammography. The first mammography systems made use of non-dedicated equipment, that gave low contrast images and a dose 50 to 100 higher than the delivered in current mammography systems (Barnes and Frey, 1993).

Dedicated mammography equipment started to be developed in 1972, with the first screen-film combination coupled into a plastic vacuum bag. A few years later, mammography film-screen cassettes with a single emulsion layer were introduced into the

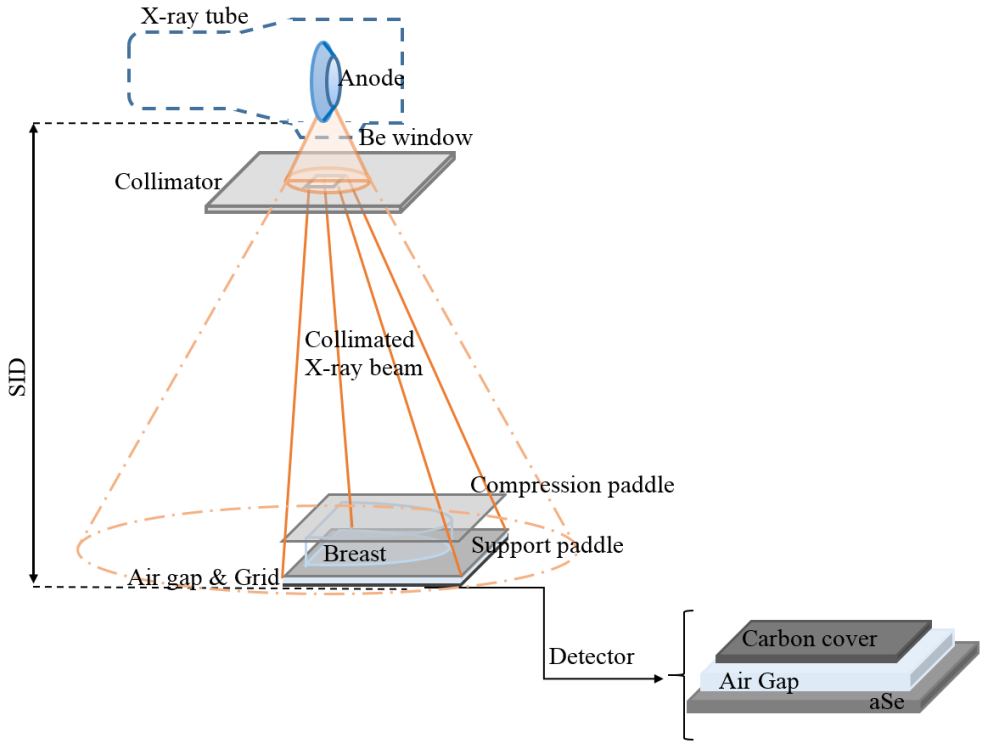

Figure 4.4: Schematic of a Mammography X-ray system with an α-Se detector.

market and finally, in the late 1980s, digital mammography started to overcome its drawbacks and became competitive (Barnes and Frey, 1993; Muller, 1999; Bick and Diekmann, 2007).

Digital mammography solved some of the issues that film-screen mammography presented, compensating for the lower spatial resolution of these systems. Improvements in the dynamic range, the contrast resolution, the DQE values and a reduction of the delivered dose to the patient, in combination with the possibility of separate image processing and data management, make digital mammography the best system for breast cancer screening at present (Muller, 1999; Bick and Diekmann, 2007; James, 2004). Improvements in the diagnosis are of particular importance among women under the age of 50 years, women with dense breasts and premenopausal or perimenopausal women, (Pisano et al., 2005). Different digital mammography technologies are available in the market, see Figure 4.5. For more information about these technologies see Chapter 2.

Computed Radiography (CR) was the first digital imaging system to be used for mammography in the early 1980s. It was a desirable choice as it makes use of a cassette that can be integrated in old screen-film systems, a characteristic that made it a very cost-effective solution, even though the performance is similar to screen-film technology. When compared with other digital mammography techniques, CR has lower MTF, SNR and DQE, leading to lower cancer detection rates, particularly for ductal carcinoma in situ (DCIS).

The main system currently used in mammography is α-Se Flat Panel detectors, followed by α-Si Flat Panel detectors. CMOS and photon-counting detectors have recently been adopted into mammography examinations, while CCDs have fallen into disuse. See Figure 4.5 for more information, (Smith, 2003; Yaffe and Mainprize, 2004; James, 2004; Diffey, 2015; Peters et al., 2016).

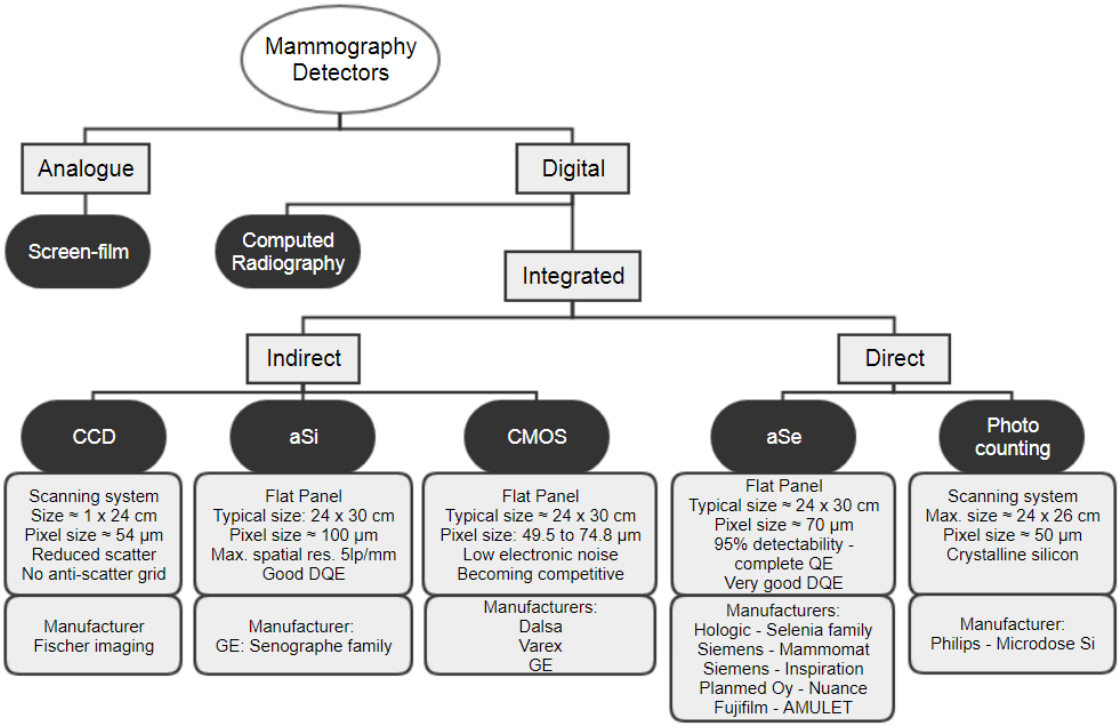

Figure 4.5: Diagram including all the technologies available for X-ray mammography. The main characteristics and manufacturers of the integrated digital X-ray detectors are included in the figure.

4.2 Techniques for scatter estimation

4.2.1 Overview

Scatter photons appear in the final image as misplaced events, adding to image noise and reducing image contrast. Although the probability of a Compton scatter event is highest at low photon energies, i.e. probability $\propto \frac{1}{E}$ see Figure 4.2, the majority of low-energy scattered photons are absorbed within the paddles and the patient, not contributing to the final image (Dowsett, Kenny, and Johnston, 2006).

Even though the scattered photons arriving to the detector are minimised by the choice of low photon energies and the optimisation of the X-ray tube and filters, scattering is still one of the main challenges remaining in digital X-ray mammography as it reduces

the quantitative usefulness of the mammogram and affects the diagnosis of malignant lesions (Boone and Cooper, 2000; Ducote and Molloi, 2010; Wang et al., 2015). The most wide spread scatter-reduction technique makes use of anti-scatter grids, i.e. a device that geometrically rejects the majority of the scattered photons. As stated in Chapter 1, anti-scatter grids are not an ideal solution and present important limitations. This has lead to the emergence of image post-processing scatter reduction methods to be used as an alternative to the anti-scatter grids.

A digital X-ray detector produces an image from the accumulation of events that hit individual pixels. Each of these events can be attributed either to the primary X-ray beam, that has passed through the body with no directional change, or to scattered radiation. Therefore, a radiographic image at a given pixel (x,y), I(x,y), can be described as the sum of a primary image, P(x,y), and a scatter image, S(x,y):

$$I(x, y) = P(x, y) + S(x, y). \tag{4.1}$$

The two dimensional description of the scatter can be seen as a low-pass filtered primary image (Ducote and Molloi, 2010; Love, 1987):

$$S(x, y) = P(x, y) * f(x, y), \tag{4.2}$$

where, f(x,y) is an unknown filtering kernel. However, as P(x,y) is unknown, and the determination of which is the principal objective of this study, it is not possible to use it to calculate S(x,y). To address this problem, different authors use different methods:

- Love and Kruger, (Love, 1987), obtain P(x,y) by approximating S(x,y) to:

  $$S(x, y) \approx I(x, y) * h(x, y), \tag{4.3}$$

  where, h(x,y) is a different low-pass filter kernel that has also to be determined.

  P(x,y) can be estimated by subtracting the scatter image to the output image:

  $$P(x, y) = I(x, y) - S(x, y), \tag{4.4}$$

  $$P(x, y) \approx I(x, y) - I(x, y) * h(x, y). \tag{4.5}$$

- Ducote and Molloi, (Ducote and Molloi, 2010), propose to work in the frequency domain to avoid the approximation step introduced in the method above. Their technique uses image deconvolution in order to decouple the convolution of the scatter component with the primary component:

  $$I(x, y) = P(x, y) + S(x, y) = P(x, y) * g_s(x, y) \tag{4.6}$$

where, g_s is the redefined convolution kernel that maps both the scatter and the primary components. The primary component can then be isolated if the Fast Fourier Transform (FFT) is applied:

$$\mathrm{FFT}(I(x,y)) = \mathrm{FFT}(P(x,y) * g_s(x,y)), \tag{4.7}$$

$$\mathrm{FFT}(I(x,y)) = \mathrm{FFT}(P(x,y)) \cdot \mathrm{FFT}(g_s(x,y)) \tag{4.8}$$

$$\mathrm{FFT}(P(x,y)) = \frac{\mathrm{FFT}(I(x,y))}{\mathrm{FFT}(g_s(x,y))} \tag{4.9}$$

$$P(x,y) = \mathrm{FFT}^{-1}\,\frac{\mathrm{FFT}(I(x,y))}{\mathrm{FFT}(g_s(x,y))} \tag{4.10}$$

where, FFT^{-1} is the inverse Fast Fourier Transform.

There are various parameters for quantifying the scattered radiation, the most common ones are are the scatter to primary ratio (SPR) and the scatter fraction (SF), defined in 4.11 and 4.12:

$$\mathrm{SPR} = \frac{S}{P} \tag{4.11}$$

$$\mathrm{SF} = \frac{S}{S+P} \tag{4.12}$$

where S and P are, respectively, the integrated energy of scattered radiation and the integrated energy of the primary radiation that strikes the region of interest (Boone and Cooper, 2000).

Another unit is the mean radial extent (MRE) that helps to characterize the spreading of the input signal in a pencil beam geometry, when the X-ray beam is simplified to a normally incident delta function (Leon, Brateman, and Wagner, 2014).

The main objective of this study is to find a primary image P(x,y) that is similar or better to the image that would have been obtained with the anti-scatter grid. If that is achieved, the possibilities of introducing artefacts with the grid removal post-processing methods would disappear, the dose delivered to the patient could be potentially reduced while recovering some of the image contrast (Wang et al., 2015).

The accuracy of the post-processing scatter correction depends strongly on the model chosen. An inaccurate simulation will lead to inaccurate corrections, obtaining suboptimal improvements or even artefacts in the image (Leon, Brateman, and Wagner, 2014). The scatter correction methods can be divided between physical and simulated methodologies. Within the physical techniques it is possible to find the edge spread methodology, the beam stop methodology, the scatter medium reposition methodology and the slat methodology. The simulated techniques are divided here into full Monte Carlo (MC) simulations and scatter convolution methods. The differences between the aforementioned

methods can be found in the next subsections.

4.2.2 Physical methods

4.2.2.1 Edge spread methodology

This method uses a lead edge device placed on top of a scatter medium, e.g. PMMA, which is on top of the detector surface and facing the X-ray beam. One image is acquired with the entire set up (primary-and-scatter image) and another image keeping the same geometry, see Figure 4.6-left, but without the scatter material (primary image).

From the acquired images it is possible to plot an intensity profile across the edge, Figure 4.6-right. In the primary-and-scatter image plot, the plateau (A in the figure) is composed by primary and scattered radiation (P+S), while the points B and C are $P + \frac{S}{2}$ and $\frac{S}{2}$ respectively, always that the length and width of the area not covered by the lead is greater than twice the effective radial range of the scatter. Point C is not 0 due to the scattered radiation signal "leaking" across the edge.

If the P image is subtracted from the S+P image, after normalization, the difference results in separate measurements of the scatter and primary radiation. The final plots can be then differentiated to obtain the scatter line spread function (LSF), that gives the scatter profile. (Leon, Brateman, and Wagner, 2014).

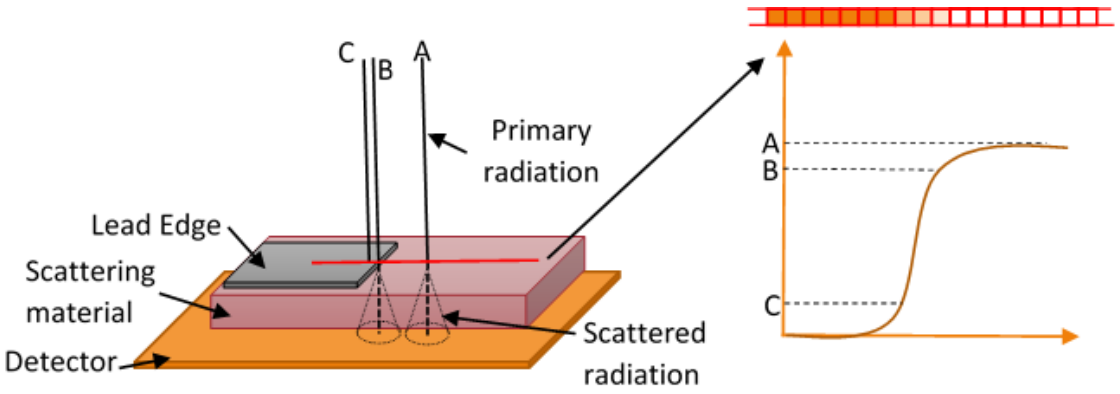

Figure 4.6: On the left the figure shows the geometry of the edge spread method, a lead edge is placed on top of the scatter material and an image is acquired. The right image shows an example of the intensity profile across the edge needed to calculate the scattering contribution.

4.2.2.2 Beam stop methodology

A series of annulus disks with inner holes of different diameters are placed between the beam and a scattering material, i.e. phantom, placed in front of a detector, see Figure 4.7.

The signal under the disk is measured as close as possible to the inner hole and the signal is plotted against the disk diameter. The scatter signal can be calculated by extrapolating to a 0 mm diameter disk. The SPR is obtained by comparing the scatter signal and an open field measurement, i.e. measurement without the disk. (Boone and Cooper, 2000).

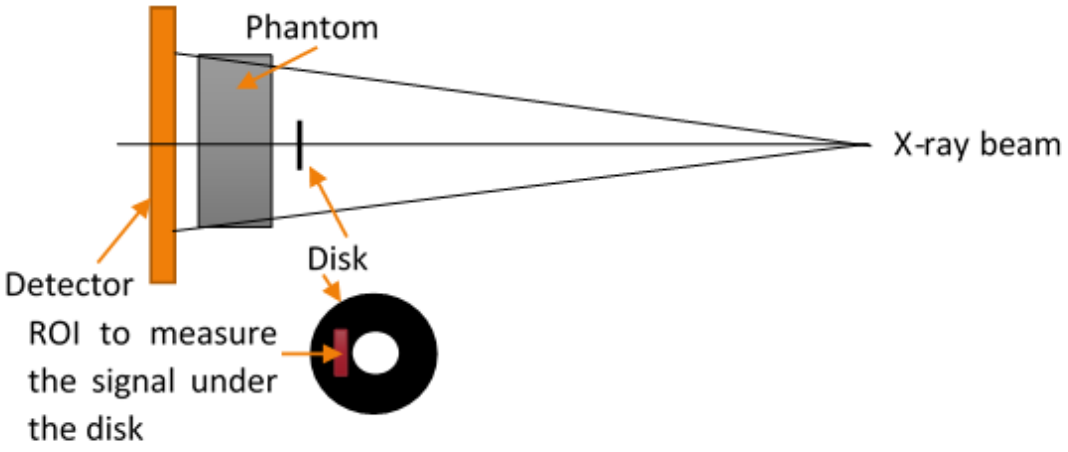

Figure 4.7: The image shows the geometry of the beam stop method and the disk region of interest (ROI) that is usually selected.

The extrapolation technique can be a source of ambiguity as it requires an assumption about the point spread function (PSF) shape. This might lead to a bias in the final results. Moreover, it does not give information about the spatial distribution of the scatter, which is useful when developing algorithms to correct for it (Cooper et al., 2000).

4.2.2.3 Scatter medium reposition methodology

This method was created to try to overcome the problems arising from the extrapolation function in the beam stop methodology. The SPR is calculated by subtracting a primary image (P) from an image that combines primary and scattered radiation (I).

Image I can be obtained by placing a lead sheet with a hole in it (a few centimetres of diameter) on top of the detector and a phantom on top of the lead, leaving a few centimetres air gap. The distance from the detector to the source must be large, i.e. a couple of metres, limiting the usefulness of this methodology.

Moving the phantom closer to the X-ray focal spot while keeping the rest of the geometry constant will give image P, see Figure 4.8, i.e. when the air gap is large, only a small amount of scattered radiation is recorded (Boone and Cooper, 2000). S can be estimated as $I - P$.

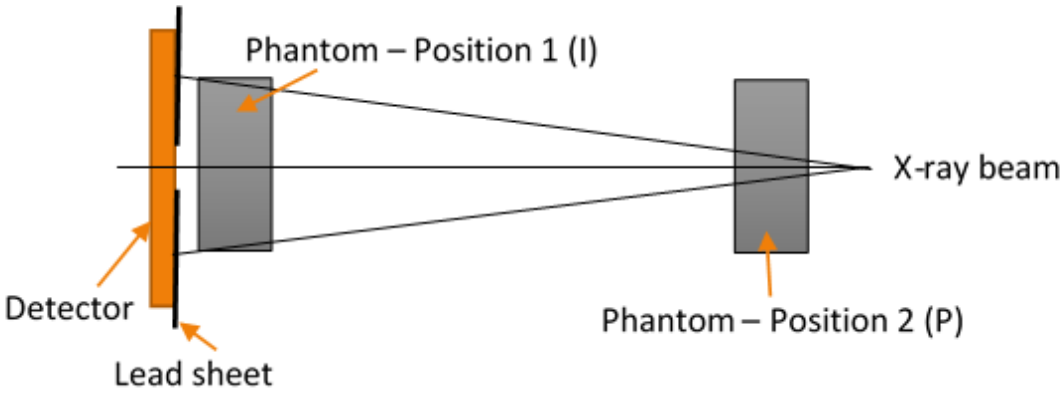

Figure 4.8: The image shows the geometry of the scatter medium reposition method with the two possible positions of the phantom (named position 1 (I) and position 2 (P) in the image.

4.2.2.4 Slat methodology

This method gives the SPR measurement across the image. A narrow steel slat is centred with the X-ray beam and placed in-between the beam and the phantom-detector combination, see Figure 4.9. Two images, one without and one with the slat in place, have to be acquired. The first one gives the primary and scattered image (I). The shadow created by the slat in the second image gives the scatter (S). The SPR can be obtained by subtracting the images and evaluating the shadowing area (Boone and Cooper, 2000).

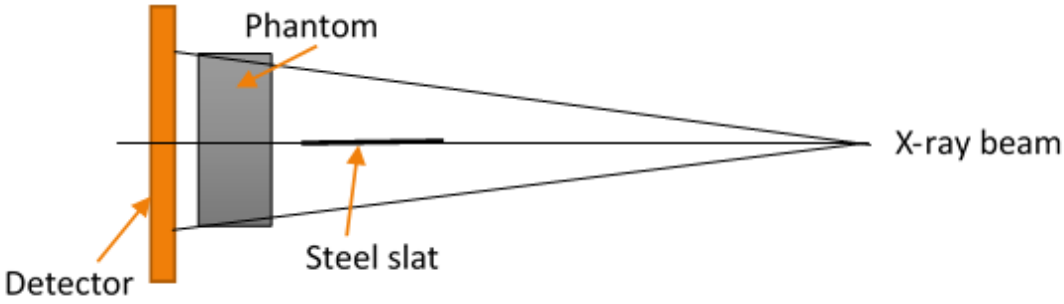

Figure 4.9: The image shows the geometry of the slat method where a steel slat is placed parallel to the X-ray beam and perpendicular to the phantom and the detector in order to study the SPR measurement across the image.

For scatter estimation, the physical methods described above usually stand as more convincing solutions than methods that make use of simulations, due to the synthetic nature of the latter. However, physical methods suffer from experimental biases and have not been proven to give better results, e.g. the ambiguity introduced when extrapolating to zero millimetres of diameter in the beam stopper method (Boone and Cooper, 2000). Moreover, some of these methods also require a direct measurement of the scatter signal,

increasing the delivered radiation dose to the patient, or need specific configurations for the medical examination (Ducote and Molloi, 2010; Seibert and Boone, 2006).

4.2.3 Simulations

4.2.3.1 Monte Carlo simulations (MC)

Direct MC simulations give very accurate values of the scatter and primary contributions and are conceptually simpler than the rest of the methods, (Boone and Cooper, 2000). However, if the scattering reduction is intended to be extended to all medical examinations, it would be necessary to implement one simulation per examination, as they are strongly dependent on the geometry and the part of the body being imaged. Moreover, these simulations are computationally expensive as reported by Díaz et al. (Díaz et al., 2012).

For all these reasons, full MC simulations are usually adopted purely for data verification and methodological validation purposes (Boone and Cooper, 2000).

4.2.3.2 Scatter convolution methodology

Convolution-based digital filtration techniques are based on the idea that the scatter in the system is spatially diffuse. Thus it can be approximated to a two-dimensional low-pass convolution filter of the primary image, as seen in equation 4.2 (Ducote and Molloi, 2010). As explained below, these 2D low pass filters can be obtained with simulations (point spread function) or adopting pre-defined kernel shapes:

Point spread function kernels:

PSF kernels are obtained from simplified MC simulations where the X-ray beam is a normally incident delta function, i.e. the X-ray tube is simulated following the narrow pencil beam method as a monochromatic point source (Boone and Cooper, 2000; Sechopoulos et al., 2007b; Díaz et al., 2014). This method is useful for the accurate assessment of the SPR for small apertures and large field of views, as it reduces the computation time (Boone and Cooper, 2000).

The programme computes the point spread function (PSF) of scattered radiation for a specific spectrum or for different energy steps, e.g. 1 keV steps from a 9.5 to 31.5 keV range (Sechopoulos et al., 2007b). For this last option the monochromatic data, stored in a precomputed library, is combined to form the desired X-ray spectra for each individual case. Once the PSF is obtained, it can be convolved with the field of view (FOV) in order to obtain the scatter distribution (Boone et al., 2000).

Results from MC simulations show that the PSF distribution can be taken as rotationally symmetric (Ahn, Cho, and Jeon, 2006). However, the assumption of symmetry can be argued against. Wang et al. (Wang et al., 2015) suggest that it would be better to adapt the kernel to local variations in object thickness and attenuation. The authors say that asymmetric kernels give better results than symmetric kernels, especially in areas close to the edge of the breast, where the symmetric ones tend to over-correct the scatter signal. The idea behind the asymmetric kernels is to account for elevated or depressed scatter due to thinner or thicker neighbouring regions, respectively. Wang et al. propose a fast adaptive scatter kernel superposition method (fASKS) in the frequency domain.

Moreover, if the kernel is chosen spatially invariant, it will risk overestimation of scattering around the edge area of the breast, leading to up to 50% of discrepancies when compared with pure Monte Carlo simulations (Díaz et al., 2012).

Pre-defined shaped kernels:

The kernel, h(x,y), used to convolve the output image can be calculated following the point spread function method, as explained above, or it can be a pre-defined low-pass filter kernel. Authors like Love (Love, 1987), Ducote and Molloi (Ducote and Molloi, 2010) or Boone and Seibert (Boone and Seibert, 1988) used this last option in their studies.

Love and Kruger (Love, 1987) studied four generic kernel shapes, 2D boxes, pyramid, Gaussian and exponential profiles, limiting their investigation to closed form functions to simplify the process and allow reproducibility. They used kernels that were functionally separable in the x and y directions, so instead of applying a 2D convolution they applied two consecutive 1D convolutions in order to speed up the process. Their study focused on finding the optimal kernel shape and size and their findings suggested that an exponential shape gave slightly better results when the size was big enough, i.e. 75 x 75 pixel kernel.

Ducote and Molloi (Ducote and Molloi, 2010), and Boone and Seibert (Seibert and Boone, 2006; Boone and Seibert, 1988) made use of a radially symmetric scattering kernel in order to have a better approximation to physical reality. The formula that describes the kernel used by Ducote and Molloi has a first term with a delta function, that represents the mapping of the primary component, and a second term that is a function of the scatter fraction (SF) and the scatter radial extent or the mean propagation distance (k):

$$g_{si}(r) = \frac{\delta(r)}{r} + \frac{SF}{(1-SF)2kr} e^{\frac{-r}{k}} \tag{4.13}$$

To obtain the values of the SF and k both Ducote and Molloi, and Boone and Seibert used the beam stopping physical method.

The studies made with pre-defined shaped kernel shapes were always combined with the use of anti-scatter grids, so they were focused on further reductions in the scatter. Therefore, the results in the absence of an anti-scatter grid could be completely different to the ones presented in the papers above. In fact, a recently published paper by Leon and Wagner, (Leon, Brateman, and Wagner, 2014), combines the kernel shape proposed by Ducote and Molloi with the simulated PSF method, which they use to calculate the SF and the mean propagation distance (MRE). They applied this method with and without an anti-scatter grid and studied different dependencies, like breast glandularity, size and thickness, or X-ray spectra. Their results show a perfect fit between the kernel shape and the grid data. However, when applied to grid-less measurements, the reported PSF form turned out to be less accurate, and they found that a bi-exponential PSF shape would be a better fit. Their explanation is related to the Compton scattering contribution: The grid scatter absorption makes coherent scattering to dominate over the Compton scattering. However, the Compton contribution becomes larger when the grid is not used, and so the bi-exponential equation accounts for both factors.

The 2D low pass filters, independently of how they have been obtained, can be assumed to be shift invariant, i.e. the same kernel is used to convolve the whole image, or can be optimised in shape and size and operated on a pixel by pixel basis (Ducote and Molloi, 2010; Ahn, Cho, and Jeon, 2006).

Size optimization can be performed by selecting a kernel with radial dependency, as explained in the Ducote and Molloi method. These authors also present a way of taking into account the breast thickness variations using a look up table with kernels calculated at different thicknesses, $g_s(t)$, for example using 1mm steps. After the mammogram is acquired, the apparent breast thickness can be estimated in a pixel by pixel basis, using a set of binary masks illustrating all corresponding pixels from 0 to maximum thickness in steps of 1 mm. Each mask is then convolved with its corresponding kernel and n partial primary images are obtained. The primary image is finally obtained by adding all the partial images (Ducote and Molloi, 2010).

Ahn et al. (Ahn, Cho, and Jeon, 2006) present a different algorithm to account for the thickness contribution, also creating a look up table with the PSF simulated as a function of the thickness. They later use them to correct the image in a pixel by pixel basis: starting from pixel (0,0) the thickness is estimated and the image is convolved with the PSF of the corresponding thickness; the process is repeated for all pixels. Their algorithm also takes into account possible errors in the thickness estimation, as they report that the scattering affects the estimations when using general algorithms for dual-energy imaging. They propose an iterative method that recalculates the thickness estimation with the scattered corrected image obtained from the first iteration. The iteration stops when a pre-defined optimisation value is achieved.

Convolution-based techniques do not require a direct measurement of the scatter signal, thus there is no further increase in the radiation dose. As they are applied after the image acquisition, it is possible to use them in the emerging imaging technique digital breast tomosynthesis (DBT) since both, 2D mammography and DBT, have a very similar set up (Ducote and Molloi, 2010; Seibert and Boone, 2006). Their main limitation is in the simulation itself: geometry idealisation or oversimplification will lead to over or underestimation of the scatter contribution (Díaz et al., 2014).

In addition, the manufacturer Siemens has recently introduced a software-based scatter correction for grid-less mammography acquisitions, Mammomat Inspiration PRIME (Binst et al., 2015). They affirm that the dose delivered to the patient can be significantly reduced.

4.3 Scattering dependencies

The dependencies on the distribution of the scatter, in the absence of an anti-scatter grid, have been largely studied in the literature, (Dowsett, Kenny, and Johnston, 2006; Ducote and Molloi, 2010; Cooper et al., 2000; Sechopoulos et al., 2007b; Díaz et al., 2014; Feng et al., 2014; Boone et al., 2000; Highnam, Brady, and Shepstone, 1998; Highnam et al., 2010; Gonzalez Trotter et al., 2002; White, Martin, and Darlison, 1977; Díaz, 2013; Sechopoulos, 2007). The way most of the authors carry out this study is by modifying the PSF simulations, e.g. modifying the X-ray beam energies to study the energy dependency, simulating different breast phantoms changing breast glandularity or thickness, varying the air gaps or changing the shape and size of the field of view (FOV) are some examples (Boone et al., 2000). The parameters generally studied are:

4.3.1 X-ray energy:

The method used by Boone et al., (Boone et al., 2000), calculates mono-energetic PSFs from 5 to 120 keV in 1keV increments and then weights them using the poly-energetic X-ray spectra. The authors found that the scatter properties are approximately constant at the energy range used in diagnostic mammography. The maximum scatter to primary ratio (SPR) relative difference when comparing 40kVp and 22kVp energies (obtained with a Mo/Mo anode/filter combination) was found for a 6 cm breast thickness (12.7%). The difference was reduced to 7% for a 4cm breast thickness, 1% for 2cm and to 2% for 8cm. Similar results were found by Sechopoulos et al. (Sechopoulos et al., 2007b).

4.3.2 Position in the field of view (FOV)

Boone et al., (Boone et al., 2000), found that the SPR depends strongly on the position within the FOV, being maximum in the centre of the breast and dropping off towards the edges, due to the amount of scattering material in nearby regions.

4.3.3 Air gap

Again Boone et al., (Boone et al., 2000), found that the PSF shape depends on the air gap, i.e. space between the support paddle and the detector surface. The PSF values in the central area decrease with the increase of the air gap while the curve fall off becomes less steep. Therefore, the air gap contributes to the spread of the scatter; the thicker the air gap, the larger the area affected.

Diaz et al., (Díaz et al., 2012; Díaz et al., 2014), introduce a second air gap contribution, present between the lower curved breast edge and the detector. The authors believe that the extended path length of the photons have an important contribution in the discrepancies that appear close to the breast edge, reported when using a spatial invariant kernel. It is therefore important to correct for this contribution, as the scattered photons do not encounter the same attenuation path and scattering than the ones that go through the centre of the breast. In cases where the breast is simulated, the breast curvature is a known parameter. However, if this correction is to be applied to clinical data, the breast curvature will need to be estimated during the examination (Díaz et al., 2012).

4.3.4 Breast thickness

It has been found that the SPR is nearly linear as a function of breast thickness. The slope of this function being dependent on the air gap and the selected FOV diameter (Boone et al., 2000; Seibert and Boone, 2006; Sechopoulos et al., 2007b).

It is therefore essential to estimate the breast thickness with accuracy. The compression thickness that is reported by the mammography unit can be used as an initial reference measurement but the thickness calibration is sometimes inaccurate, and the breast thickness changes towards the periphery. A software based algorithm to calculate the thickness is recommended for obtaining reliable results (Leon, Brateman, and Wagner, 2014; Highnam, Brady, and Shepstone, 1998; Mawdsley et al., 2009).

The breast compression in general mammography allows the achievement of a relatively constant breast thickness, excluding the periphery where the thickness decreases. However, the pressure applied to the compression paddles ends up deforming them and creating a tilt in the area without breast (Mawdsley et al., 2009). This effect introduces variations in the breast thickness. If these variations are assumed to be negligible within the compressed breast, the thickness calculation is then reduced to an estimate of the averaged value, (Highnam, Brady, and Shepstone, 1998; Highnam et al., 2010; Gonzalez Trotter et al., 2002). However, this assumption introduces some errors that add up in the final scattering simulation. For this reason, some other authors calculate a pixel by pixel thickness map and use kernels that are a function of the thickness, K(t), (Mawdsley et al., 2009; Leon, Brateman, and Wagner, 2014).

4.3.5 Breast tissue composition

The study of the contribution of breast tissue composition has been commonly carried out by using phantoms with different glandular percentage, with 0, 50 and 100% being the most common choices. The literature presents very little dependency between SPR changes and breast composition, (Boone et al., 2000; Sechopoulos et al., 2007b), the major impact found to be in the apparent thickness calculation (Leon, Brateman, and Wagner, 2014). Due to the small glandular contribution it is possible to use a PSF simulated for a homogeneous breast (Sechopoulos et al., 2007b; Díaz et al., 2014). The scatter kernel can be calculated, for example, as the linear combination of the scatter response with 0% and 100% of glandularity (Díaz et al., 2014).

4.3.6 Detector cover plate, detector compression plate and breast support plate

The detector cover plate and the compression and breast support plates were found to have a significant contribution to the scattered signal (Sechopoulos et al., 2007b; Ducote and Molloi, 2010; Díaz et al., 2014), especially for thicker breasts, i.e. 5-7cm, close to the edges of the compressed breast. The reason, found by Sechopoulos et al. (Sechopoulos et al., 2007b) and studied further by Diaz et al. (Díaz et al., 2014), was related to the scattering contribution of the plates in the area without breast tissue. Some of that scatter is detected under the shadow of the breast, producing a high contribution due to the absorption of the primary photons by the breast tissue. If the breast is thin enough, that absorption is decreased and the SPR is therefore reduced. This contribution can be precorrected by simulating the measurements at zero thickness (Ducote and Molloi, 2010). A more precise method, reported by Díaz et al. (Díaz et al., 2014), is to include the plates in the simulations. To account for the scattering contribution of the area without breast, i.e. system contribution, a second simulation can be done keeping the same geometry but

removing the scattering material, i.e. breast phantom. The system kernel will be applied to the areas outside the breast, while the breast kernel (that has been calculated taking the plates into account) is applied within the breast areas. However, an additional correction is needed. The scattered photons produced outside, but near, the breast, might be scattered towards the breast. In that case, the system scattered radiation will be attenuated by the breast tissue. In order to compensate for this effect, Diaz et al. proposed to weight the system kernel with a weight map, α, where $\alpha = 1$ outside the scattering material and $\alpha < 1$ when the beam passes through the breast. It is therefore very important not to exclude the plates in the simulation. If they are not taken into account the scatter can be underestimated by as much as 31% (Sechopoulos et al., 2007b; Díaz et al., 2014).

4.3.7 Source to image distance (SID)

The SID has been reported not to affect the scattered radiation distribution (Boone and Cooper, 2000).

4.3.8 Backscatter

Backscatter from the body or the detector can affect the scatter estimation, as reported by Sechopoulos et al. (Sechopoulos et al., 2007b).

4.3.9 Detector composition

The detectors are commonly simplified to a scintillator plate or an ideal geometry. Accounting for the scattering produced after the detector cover plate could lead to more precise SPR estimations, introducing an advantage when compared with the anti-scatter grid method (Marimon et al., 2016).

4.4 Chapter summary and discussion

This chapter introduces the second part of this thesis, focused in post-processing scatter reduction for mammography applications. The theoretical framework, necessary for the development of an adequate scatter reduction methodology, was developed in this chapter.

After an initial discussion about breast cancer, breast cancer screening programmes and mammography systems, a mathematical interpretation of the scatter contribution to the

image was defined and the most common techniques for scatter estimation were evaluated, i.e. physical and simulation methods, paying special attention to the scatter convolution methodology, as it will be the foundation of the technique developed and proposed in this thesis.

The chapter finished with a study of the scattering dependencies with the geometry of the system, evaluating how sensitive the scattering is to changes in the X-ray energy spectrum or in the dimensions and compositions of the different layers of the geometry, as encountered by the photon beam's path.

Chapter 5

PSF scatter reduction and validations

A post-processing scatter estimation methodology, which is based on scatter convolution using simulated point spread function kernels, is developed, optimised and validated (against full Monte Carlo simulations and previously published data) in this chapter.

5.1 Scatter convolution methodology

The point spread function (PSF) post-processing scatter reduction technique is the methodology chosen to estimate the scatter in this study. As explained in Chapter 4, this method assumes that the scatter in the system is spatially diffuse, thus it can be approximated by a two-dimensional low-pass convolution filter of the primary image. The scatter PSF (SPSF) filters, or scatter kernels, are calculated with a simplified MC simulation, by using a narrow pencil beam.

This methodology has proven to be accurate, non-invasive (in opposition to some of the physical scatter estimation methods, where the dose has to be increased or the system set up modified) and less time consuming that full Monte Carlo simulations. From the different options presented in Chapter 4, the author has chosen to follow Love's approximation, see equation 4.3 (Love, 1987), using a set of symmetric kernels with special emphasis on the treatment of the background scatter contribution to the breast, as a way of correctly estimating the scatter in the breast edge area of the image, easily overestimated.

5.2 Geant4 simulation tool-kit

There are several particle physics MC software packages available that allow the study of particle interactions with matter in the medical physics range, e.g. GEANT4, Penelope, FLUKA, EGSx/EGSnrc and MCNP/MCNPX, (Díaz, 2013). GEANT4, in particular, has been chosen by many authors, i.e Sechopoulos et al. (Sechopoulos, 2007; Sechopoulos et al., 2007b; Sechopoulos et al., 2007a), Feng et al. (Feng and Sechopoulos, 2011; Feng et al.,

2014), Wang et al. (Wang et al., 2015) and Diaz et al. (Díaz et al., 2012; Díaz, 2013; Díaz et al., 2014), as it is a free software supported by the European Organization for Nuclear Research (CERN), where it is possible to obtain active assistance, (Agostinelli et al., 2003; Díaz, 2013).

GEANT4 provides detector and physics modeling, simulating the interaction and passage of particles through matter. This simulation toolkit includes all aspects of the simulation process, i.e. the system geometry and materials, the fundamental particles of interest, including a tracking system of them and their interactions, the detector response, etc. (Agostinelli et al., 2003; Allison et al., 2006) . Although GEANT4 was initially designed for high energy physics, its object-oriented structure has allowed the adaptation to a wider range of energies, including medical physics, i.e. mammography, brachytherapy or hadron therapy, and radiation protection (Díaz, 2013).

When applied to mammography, GEANT4 has been validated in a number of publications. Sechopoulos (Sechopoulos, 2007) modified the code to simulate X-rays passing through only breast tissue, activating and deactivating the interaction process to study each individual case. That way, the attenuation coefficients were calculated and compared to the values reported by the National Institute of Standards and Technology (NIST) and by other authors finding excellent agreements in all cases. Feijó and Hoff, (Feijó Pery and Hoff, 2008), validated the software comparing results to previously published data. They report less than 5% difference between the compared values. Also Diaz, (Díaz, 2013), validated the toolkit with published and clinical data, arriving to the conclusion that GEANT4 is suitable for modelling X-ray mammography systems.

For the mentioned reasons, GEANT4 (version 10.01.p02) will be the toolkit used in this work.

5.2.1 Geant4 architecture

The Geant4 toolkit architecture is composed by a set of modules written in C++. It is the user's responsibility to build the application architecture, a characteristic that contributes to Geant4's flexibility. The Geant4 information has been obtained from the Geant4 user manuals published by CERN, (CERN, 2016; collaboration, 2016).

The main architecture structure can be seen in the diagram of Figure 5.1. A main() method, required to build the programme, is implemented by two manager classes, G4RunManager and G4UIManager. The run manager class controls the flow of the programme, manages the event loop(s) and the initialization procedures. Therefore, it has to receive all the information needed to build and run the simulation. The three main initialization classes directly set to the run manager are:

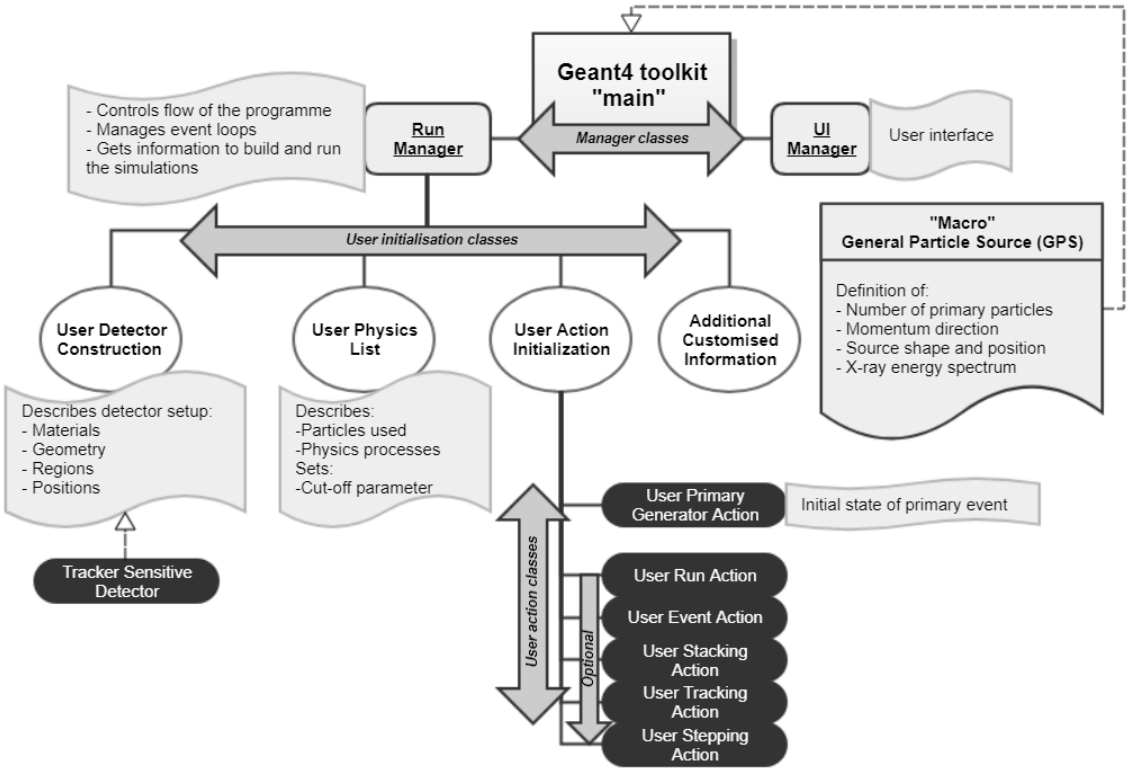

Figure 5.1: Diagram showing the main modules that form the architecture of Geant4.

5.2.1.1 G4VUserDetectorConstruction

In this class, the user defines the entire detector geometry, from the chemical elements to the distribution of the materials in the volume.

The detector construction needs:

- Definition of the chemical elements that compose the materials used in the simulation. The elements are defined by their atomic number and weight.

  e.g. elH = new G4Element("Hydrogen", "H", z=1., a=1.01*g/mole);

- Definition of the materials, either by using their chemical formula or their density and fractional mass of the components. The information needed to define the materials was taken from the NIST website (*NIST material composition [online]*).

  e.g. CsI = new G4Material("CsI",density=4.53*g/cm3,2);

  CsI->AddElement(elCs,1);

  CsI->AddElement(elI,1);

- Definition of the dimensions of the mother volume (or world).

- Definition of the materials:
  - Create a solid defining its dimensions and geometrical shape. The materials can have simple shapes as box/tube/cylinder/parallelepiped, or more complex designs, combining shapes or loading voxelised geometries.
  - Define a logical volume, where the solid is filled with the appropriate material composition.
  - Place the volume in the desired position in the world volume.
- Set sensitive detectors: Information of the interactions that occur within a volume will be provided if the volume is marked as sensitive. More information about the tracking is given below in the explanation of the TrackerSD class.

5.2.1.2 G4VUserPhysicsList

This class registers all the physics processes and all the particle types required in the simulation. It also defines a threshold on particle production, where no secondary particles are generated if they are unable to travel at least the cut-off range distance. In this study the cut-off threshold was chosen to be 1 mm.

The electromagnetic (EM) physics constructor chosen in this work is the "emstandard_opt4", which has been designed for applications that require higher accuracy of electrons, hadrons and ion tracking and uses the most accurate standard and low-energy models available, (CERN, 2017).

5.2.1.3 G4VUserActionInitialization

In this class the user defines the user action classes that are invoked during the run phase of the simulation. There is one mandatory class, the Primary Generator Action, and five additional classes that the user can decide to use, the Run Action, the Event Action, the Stacking Action, the Tracking Action and the Stepping Action.

The G4UserPrimaryGeneratorAction specifies how a primary event should be generated. The generation of the primary particles is done in the Primary Generator class.

Other modules used for the simulations of this work that are worth mentioning are:

5.2.1.4 TrackerSD

The tracker sensitive detector class allows to follow each individual particle as it passes through the sensitive volumes, tracking the interactions that the particle undergoes and saving any relevant information for the user, e.g. classify the particles in primary or scattered or quantify the energy deposited in the volume of interest.

In this study, the primary particles are X-ray photons and, therefore, they can either suffer a Compton, photoelectric or Rayleigh interaction or exit the sensitive volumes without interaction. The last sensitive layer corresponds to the sensor of the detector. The particle that has undergone any type of interaction before arriving to the sensor volume is classified as a scatter event, otherwise the particle is counted as a primary event.

If the mammography detector is considered ideal, all the particles that arrive to its surface are taken into account, and the interactions within the detector volume are not considered. If a more realistic geometry is needed, only those particles that suffer a Compton or photoelectric interaction in the sensor volume are taken into account and their position recorded; the particles will be recorded as scatter or primary events depending on the classification of the particle before interacting with the sensor, Figure 5.2 illustrates this process with a flowchart. In this study the use of one type of detector or another will be specified for each individual experiment.

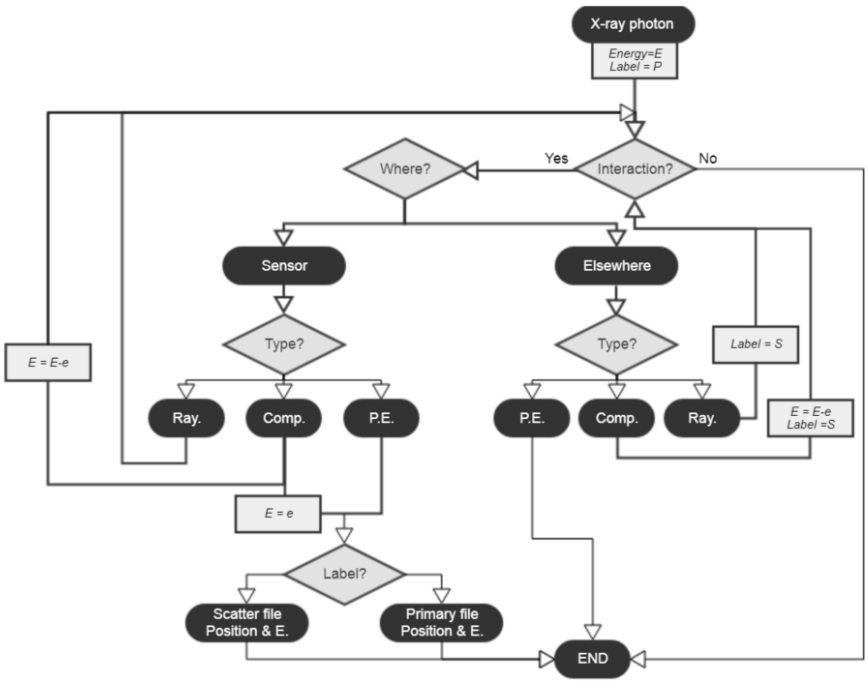

Figure 5.2: Flowchart of the X-ray photon tracking process. The scatter interactions, i.e. photoelectric (P.E.), Compton (Comp.) or Rayleigh (Ray.), and deposited energy of each X-ray photon is accounted up to the detector surface volume, where it is divided in Primary or Scatter type and sorted.

In the TrackerSD class, the position of the particles as they interact in the sensor volume are also recorded and exported to a file. There are different options as to the way the particles can be stored. The most precise method is to save the (x,y) coordinates of each particle. This option is, however, very expensive in terms of memory, and time, as many simulations need to be run to obtain values statistically significant. An intermediate solution is to sample the photons in an array, mimicking the pixel matrix of digital detectors. The full MC simulations executed in this study use this last option. For the pencil beam simulations the data storage can be simplified even further without compromising the final results, by assuming cylindrical symmetry and binning the energy into concentric annuli of radius equal to half the chosen pixel size.

5.2.1.5 Random Number Generator

Random numbers are sequences of numbers that must be produced by a random physical process and that cannot be predicted better than by random chance. Due to the difficulty to generate completely random numbers, MC simulation software tool-kits make use of pseudo-random number generators (PRNGs), which are produced by using a numerical algorithm based in a periodic cycle. An initial value, known as seed or key, that is defined in each cycle is used to determine the sequence of pseudo-random numbers.

Geant4 makes use of the HEPRandom module from CLHEP, a PRNG C++ class library for high-energy physics. The Random package uses well-known algorithms (or engines) to produce the pseudo-random numbers, the most common engines implemented in HepRandom are HepJamesRandom, DRand48Engine, MixMaxRng, RanluxEngine and Ranecu.

In this study, the engine selected was Ranecu, the one recommended by CERN (CERN, 2016; collaboration, 2016). This engine has a relatively long period, 2 x 10^{18}, providing reproducibility and good statistical properties (Díaz, 2013; Demchik, 2011). In Ranecu, the initialisation is carried out using a multiplicative congruential generator that uses the formula constants of L'Ecuyer. An index integrer, set by the execution time in seconds, is used to obtain two seeds from a seed table (collaboration, 2016).

5.2.1.6 General Particle Source (GPS) macros

The GPS class allows to specify the spectral, spatial and angular distribution of the primary source particles.

In this work, the GPS commands have been specified in a macro file, among the number of particles simulated, the visualization drivers and the amount of information displayed

(verbosity). The use of a macro file allows to avoid the compilation step every time the parameters are changed.

The source is placed on top of the volume (z direction) for all geometries, but its position in the horizontal plane (x-y) changes with the application. For a pencil beam geometry, a point source will be simulated, centred and perpendicular to the x-y plane. For full MC simulations, the position, shape and extension of the source will vary. The most common set up being a cone-beam, aligned with the chest-wall and collimated to the detector surface, as in realistic mammography geometries. In other examples, the cone-beam source can be centred with the horizontal plane and collimated to the detector surface, or a square shaped source of the same size than the detector surface can be simulated, where the photons are fired perpendicular to the x-y plane (photon shower). Figure 5.3 shows the different options used in this study.

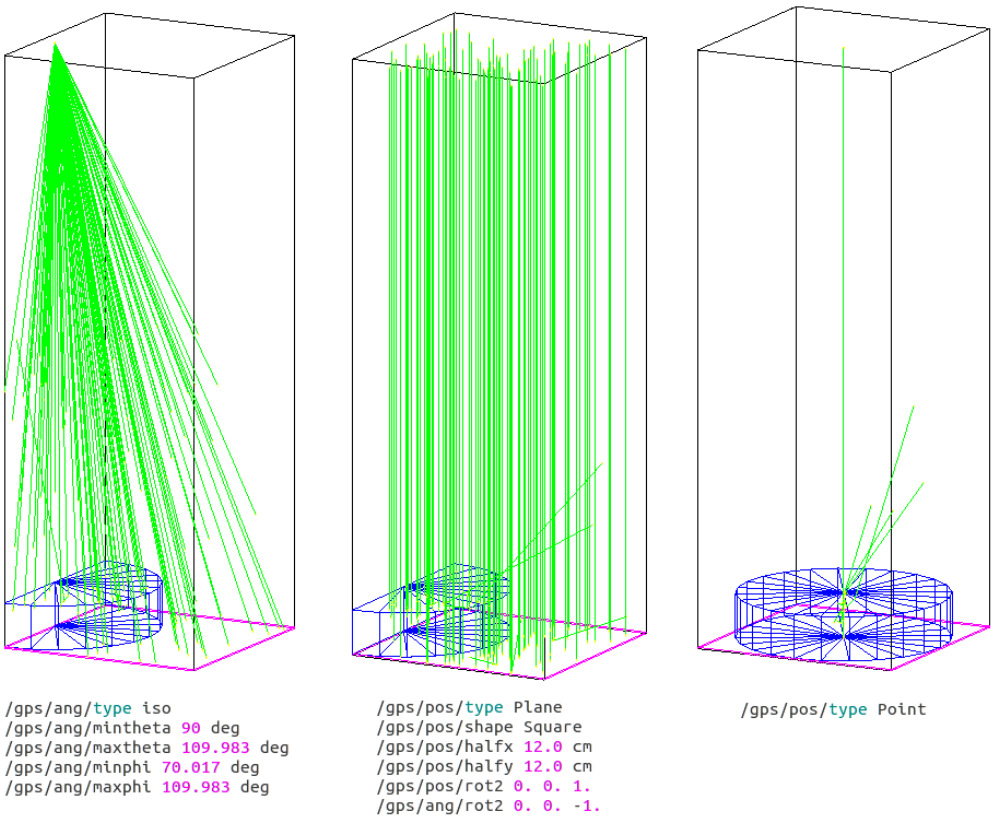

Figure 5.3: The figure shows the three beam shapes that have been used in this study: cone beam (left), photon shower (middle) and pencil beam (right). The image shows an OpenGL visualization a 100 particles Geant4 simulation.

This work makes use of polyenergetic X-ray beams that are given to the GPS macro file in a histogram form. The spectrum is generated using Boone's probability distributions of the photons from the energy spectra (Boone, Fewell, and Jennings, 1997), mathematically

attenuated by the different material layers, e.g. filtration or Beryllium window, and considering its half value layer (HVL). Some of the validations make use of mono-energetic X-ray beams. For this case, instead of the histogram the source has to be defined as "type Mono".

The visualization drivers are a key point in the geometry and GPS set up, to ensure that no mistake has been introduced in the process. In this study the software interface that is used is OpenGL, a module that enables direct visualization from GEANT4 of 2D and 3D volumes.

5.2.2 Number of simulations and uncertainties

The precision of the results is obtained by reducing the statistical uncertainty which is directly related with the number of simulations and the number of particles run per simulation. It is key to correctly choose the total number of particles used, i.e. number of simulations multiplied by the number of particles in each simulation. Too few will increase the uncertainty of the final results, while too many will imply a big computational strain. In this study, the number of particles per simulation was set to 10^9 and the number of simulations was adjusted accordingly to the needs of each particular case.

To select the right number, the uncertainties need to be evaluated. Due to the random behaviour of the X-ray photon interaction and to the large number of particles used, it is possible to describe the uncertainties with a Gaussian distribution (central limit theorem). The method used for the evaluation is the Standard Error of the Mean (SEM), the standard deviation of the sample mean (Sempau et al., 2001; Díaz et al., 2014). It is estimated by the standard deviation of the population, i.e. energy deposited, $q_i(x,y)$, divided by the size of the sample, i.e. number of simulations, N:

$$\mathrm{SEM} = \frac{\sigma}{\sqrt{N}}. \tag{5.1}$$

where,

$$\sigma = \sqrt{\frac{1}{N}\sum_{i=1}^{N}\left(q_i - \bar{q}\right)^2}, \tag{5.2}$$

$$\mu = \frac{1}{N}\sum_{i=1}^{N} q_i. \tag{5.3}$$

Additional ways to reduce the computational time, without compromising the statistical uncertainty, are increasing the sampling area, i.e. pixel size, or applying a smoothing spatial filter, such as a median filter, to the data.

The pixel size of a mammography X-ray detector is 70-75 µm. It has been found that to achieve a SEM lower than 1%, using this pixel size range and a pencil beam geometry, 15 to 20 simulations are needed. This number does not imply a big computational constraint and so the smoothing spatial filter does not need to be used in combination with the pencil beam geometry.

In full MC simulation applications, the number of simulations needed is increased considerably. This is because the beam is spread in a bigger area and the data sampling is restricted to an array ("pixelated") sampling, as it is not safe to assume spatial symmetry. As full MC simulations have been only used for validation applications, the aid of a bigger pixel size has been used when possible.

5.2.3 Preliminary validation

The first set of validations that were performed were aimed to validate the Geant4 code, to make sure the different classes described above were properly configured.

With this objective in mind, the American Association of Physicists in Medicine (AAPM) task group 195 presented a report with a series of Monte Carlo data sets to be used as a reference to validate different Monte Carlo simulations (Sechopoulos et al., 2015; AAPM, 2015). The report encompasses MC simulations of a variety of medical examinations, from half value layer calculations to dose calculation in computed tomography examples. The values given in case number 3 (Mammography and breast tomosynthesis) of the report are the ones used as a benchmark in this validation exercise.

The geometry followed included breast compression and support paddles, both made of 2 mm thick PMMA material, a semi-circular cylinder as breast phantom (46 mm thick, composed by 80/20% of adipose/glandular tissue and surrounded by a 2 mm thick skin layer) and a 13 mm air gap placed between the support paddle and an idealized detector surface. The Source to Image Distance (SID) was 660 mm. A patient body made of water was also included, adjacent to the breast phantom's chest wall side, and centred in the vertical direction with the breast phantom. Figure 5.4-left shows a diagram of the geometry.

A combination of two X-ray beams (cone and pencil beam) and two X-ray spectra (monoenergetic and polyenergetic) were used for the validation. To reduce the uncertainty, the spectrum values were the same as the ones used by the AAPM group, (AAPM, 2015). For each of the combinations, the primary radiation, Compton scattering, Rayleigh scattering and multiple scattering events were measured in 7 different regions of interest (ROIs), as described by (AAPM, 2015), see Figure 5.4-right. Table 5.1 gives the source

type, i.e. Cone Beam or Pencil Beam, and spectrum chosen for the four validations performed. Enough particles to produce Standard Error of the Mean (SEM) values equal or lower than 1% were run.

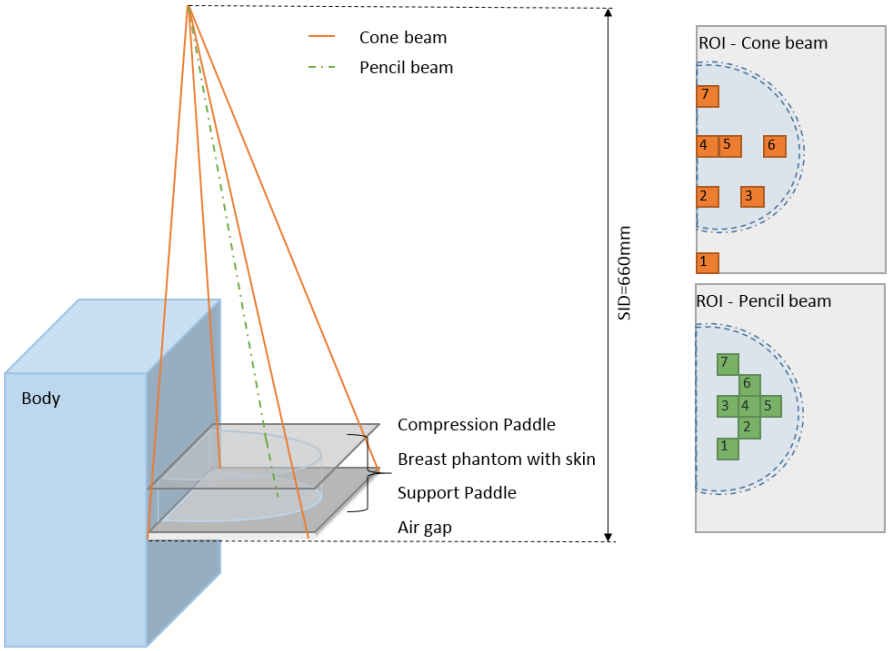

Figure 5.4: On the left: Diagram of the geometry used for the validation against the AAPM task group 195 report- Case 3, showing the shapes of the cone and pencil beams. On the right, a top view of the ROI sensitive areas, for a cone beam geometry (top) and pencil beam geometry (bottom).

Table 5.1: The table shows the four X-ray source/spectrum combinations used for the validation against the AAPM task group 195 - Case 3 report.

Validation	Source type	Spectrum
V1	Cone Beam	Mono-energetic (16.8 keV)
V2	Cone Beam	30 kVp Mo/Mo (HVL=0.3431 mmAl)
V3	Pencil Beam	Mono-energetic (16.8 keV)
V4	Pencil Beam	30 kVp Mo/Mo (HVL=0.3431 mmAl)

Table 5.2 shows the relative difference of both, Primary and Scatter deposited energies, between this study and the values reported by the AAPM task group 195 - Case 3. Figure 5.5 compares the Primary and Scatter results for the V3 validation, i.e. Mono-energetic PB case. The maximum discrepancy found is 1.59%, for the scatter energy of ROI 7 in validation V1.

For more details, see Appendix A. Table A.1 provides the energy data used in the calculations shown in Table 5.2. The scattering energy information is subdivided into Compton, Rayleigh and multiple events. In this case, the maximum discrepancies, up to 4%, were found for the Cone Beam geometries (V1 and V2), when accounting for the multiple scatter events. This might be related to discrepancies in the beam definition or the way the

particles are followed in the TrackerSD class. For the Pencil Beam geometry the agreement is better, with a minimum value of 98.1% and an average agreement of 99.7%. It is, therefore, safe to assume that the risk of using the Geant4 code is very small.

Table 5.2: The table shows the relative difference between this study and the AAPM task group 195 - Case 3, comparing the primary and scatter deposited energy (eV/ph) in 7 pre-defined ROIs for four X-ray source/spectrum combinations, i.e. V1 to V4.

eV/ph - Relative difference (%) against AAPM T.G. 195 Case 3					
ROI no.	**Type**	**V1**	**V2**	**V3**	**V4**
1	**Primary**	0.59	0.00	0.62	0.00
	Scattering	0.30	-0.90	0.19	-1.10
2	**Primary**	0.20	0.00	0.67	0.00
	Scattering	-1.50	-0.16	-1.19	-0.29
3	**Primary**	0.64	0.00	0.65	0.00
	Scattering	-1.47	-0.53	-0.95	-0.49
4	**Primary**	0.53	0.00	0.51	0.00
	Scattering	-0.74	-0.21	-0.73	-0.19
5	**Primary**	0.48	-0.08	0.77	-0.02
	Scattering	-0.85	-0.04	-0.70	-0.03
6	**Primary**	0.55	0.00	0.53	0.00
	Scattering	-1.31	-0.32	-0.54	-0.28
7	**Primary**	0.36	0.00	0.58	0.00
	Scattering	-1.59	-1.06	-1.18	-0.74

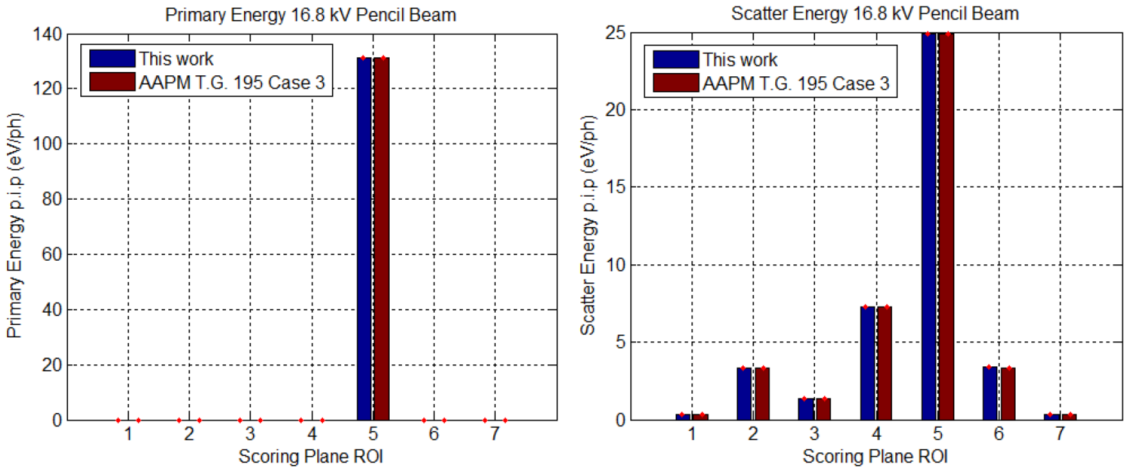

Figure 5.5: Comparison against the AAPM task group 195 - Case 3. The plots show the primary (left) and scatter (right) deposited energy in each of the 7 ROIs defined in the scoring plane. The scatter energy is the sum of the single Compton, single Rayleigh and multiple scatter events.

5.3 System Geometry

After the validation of the Geant4 code, the geometry of the simulations needs to be adapted to reproduce a realistic mammography system. This can be based either in a real geometry, used when acquiring clinical images, or in a full MC geometry, used to acquire synthetic images. For consistency purposes, and unless otherwise specified, the parameters used in the full MC geometries were based on the real clinical mammography system data.

Two manufacturers, providing different digital X-ray mammography detectors, have been used in the study: Varex Imaging Corporation (CMOS) and Hologic (α-Se). For system accessibility reasons, most of the images were acquired with the α-Se detector, specifically with two Hologic Selenia mammography systems: Lorad Selenia, hosted at Barts NHS trust (London), and Selenia Dimensions, hosted at the university hospital Parc Taulí (Sabadell, Spain). The images with the CMOS mammography detector were either simulated or acquired at Dexela Ltd (Varex Imaging - London) without being integrated in a mammography system, for logistical reasons. The geometry parameters of the α-Se systems have been defined in Table 5.3; a schematic of the geometry can be seen in Figure 5.6 for the two simulations that will be performed, i.e. full MC on the left and Pencil Beam on the right.

Table 5.3: The table shows the geometry parameters used in the experiments described in Chapters 5 and 6, when simulating a grid-less α-Se realistic mammography geometry.

Hologic Selenia α-Se [1]			
Simulation Parameters		**Thick. (mm)**	**Material**
Anatomy	Phantom	Variety of phantoms used. [2]	
	Body	The body was not included in the simulations.	
Geometry	Anode		Tungsten
	Filter	0.06	Rh or Ag
	SID	660-700	Air
	Compression paddle	2.54	Polycarbonate
	Support paddle	2.54	Carbon fibre
	Air gap	17.46	Air
	Detector cover	Private Info. [3]	Carbon fibre
	Detector air gap	Private Info. [3]	Air
	Detector sensor	Private Info. [3]	α-Se

[1] Lorad Selenia and Selenia Dimensions.
[2] The type of phantoms used are defined further in Chapter 6.
[3] The detector information was obtained via private communication with Hologic Inc.

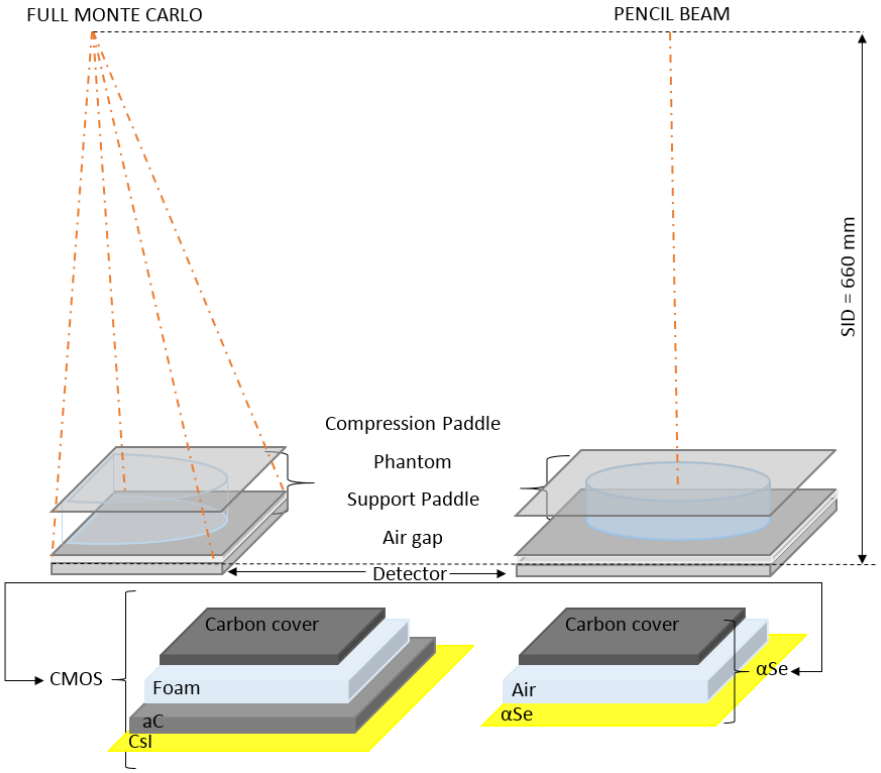

Figure 5.6: The figure shows a schematic of the general mammography geometries of the full Monte Carlo (left) and Pencil Beam (right) simulations used in Chapter 5 and 6.

5.3.1 Geometry and full MC validation

The geometry of the α-Se Hologic Lorad Selenia mammography system was validated by comparing an image acquired with the system and one simulated with a full Monte Carlo simulation.

The phantom chosen was a 5 mm thick squared aluminium sheet placed in between a 25 mm thick semi-cylindrical block of PMMA and it was aligned with the chest wall in the mammography system, as illustrated in Figure 5.6. The X-ray image acquired with the Selenia system is shown in Figure 5.7.

The real image is proportional to the energy deposited in the sensor. As the gain conversion factor is unknown, the backgrounds of the two images were made to match, and the full MC image was normalised accordingly. Figure 5.8 shows a plot comparing the intensity profiles of the real image and the normalised full MC image. The profile was drawn across the middle of the image in the horizontal direction, as shown by the yellow line in Figure 5.7.

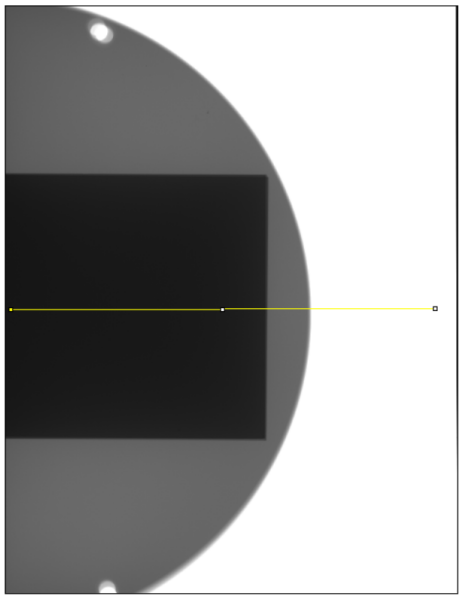

Figure 5.7: Image of a squared aluminium sheet embeded in a semi-cylindrical PMMA phantom, acquired with an α-Se Hologic Lorad Selenia system. In yellow, the line used to plot the intensity profile of the image.

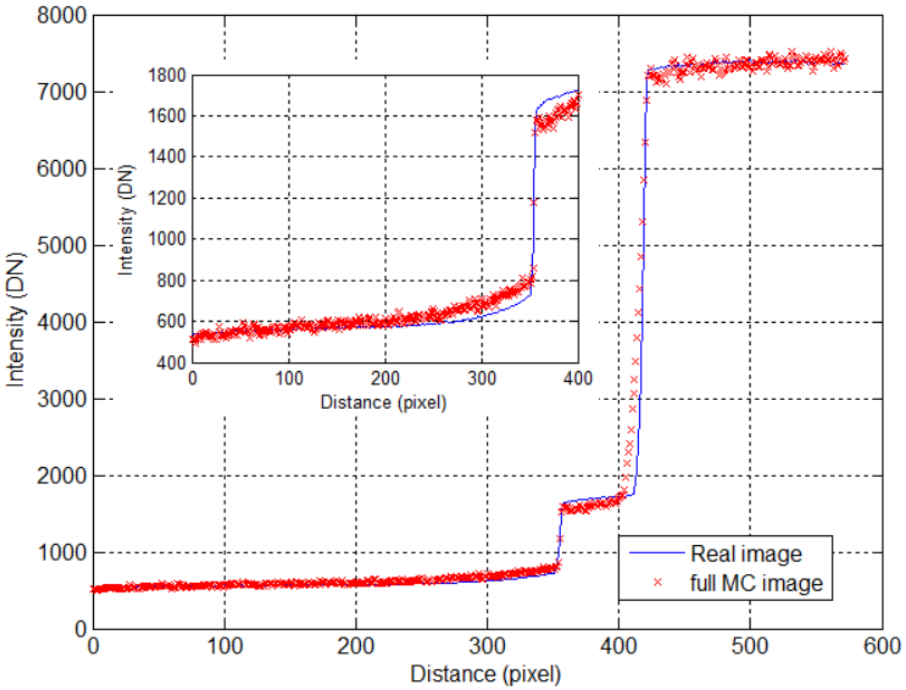

Figure 5.8: Plot showing the intensity profile comparison between the acquired real image and the synthetic image obtained by full Monte Carlo simulations.

As shown in the comparison made in Figure 5.8, the synthetic image that was obtained with a full MC simulation is a good representation of the real image. The main discrepancies seen in the profile comparison correspond to the area surrounding the boundary

between materials inside the phantom, showing a maximum discrepancy of 12%. This is due to the mismatch between the simulated and real phantom sizes and the introduction of a non-simulated air gap when the phantom changes from the PMMA plus aluminium area to a pure PMMA area.

It can be assumed that the results provided by the MC simulation developed in this work accurately reproduce the primary and scatter radiation distribution observed in the clinical images.

5.4 Kernel calculation

The energy and position of scatter and primary events at the detector's volume is the information generated by the simulations, once the Geant4 software is run. This information is enough to calculate the PSF kernel needed to convolve the image and, in consequence, to obtain the predicted scatter and primary images, as shown in equations 4.3 and 4.4.

The analysis of the simulations and image post-processing has been done with the aid of MATLAB software (R2013b, version 8.2 with image processing toolbox, version 8.3) and with ImageJ (version 1.47v).

To obtain the kernel, the method chosen uses a point spread function that is calculated from the scatter and primary information obtained with the pencil beam geometry. The scatter matrix gives information on the energy deposited per pixel, while the primary value comes from the central point where the pencil beam is pointed and gives the energy of all the particles that have not suffered any interaction before arriving to the sensor surface.

The kernel, or Scatter Point Spread Function (SPSF) is calculated by dividing the scatter matrix with the sum of the primary value and the total scatter energy (S_{TOT}):

$$\mathrm{SPSF}(x,y) = \frac{S(x,y)}{P(0,0) + S_{\mathrm{TOT}}} \tag{5.4}$$

where,

$$S_{\mathrm{TOT}} = \sum_x \sum_y S(x,y) \tag{5.5}$$

The term of the total scatter sum is added into the equation to compensate for the approximation of equation 4.3 (Boone and Cooper, 2000). If the correction was not to be added, the predicted scatter would be overestimated.

If the data is sampled into rings instead of pixels, by assuming isotropic symmetry as explained in section 5.2.1.4, the SPSF is simplified to a 1D problem, i.e. scatter vector, that needs to be sampled back to a 2D matrix. In order to create a vector independent of the pixel size, the SPSF(r) has to be divided by the area of the ring, $A_R(r)$. Then, when reconstructing the 2D matrix, each cell will have to be multiplied by the area of the pixel, A_P, and its values interpolated to each pixel, as illustrated in Figure 5.9.

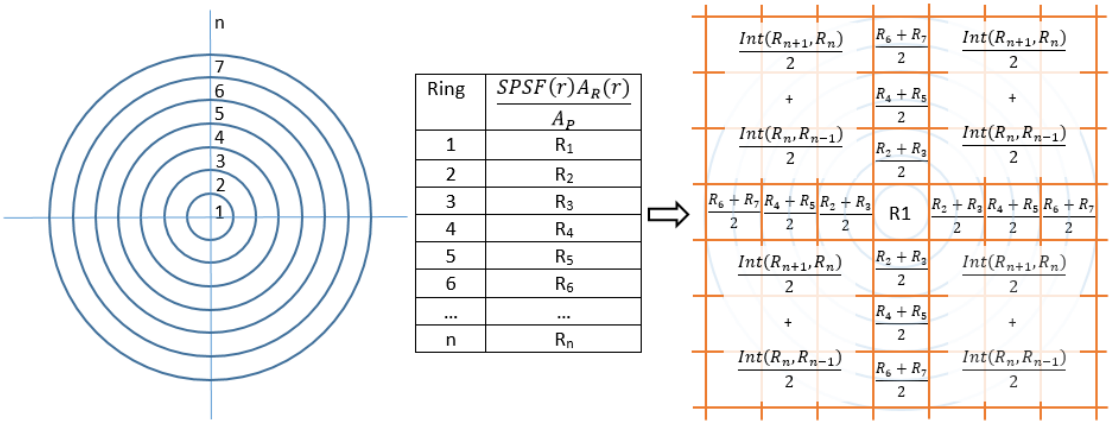

Figure 5.9: Schematic showing the ring sampling method (figure and table on the left), and the way the 2D kernel is calculated by interpolating the SPSF(r) values obtained from each ring (right). Int stands for Interpolation.

The Scatter to Primary Ratio (SPR) is an important figure to consider during the analysis of the scatter, for both, comparison and evaluation purposes. It is defined as the area under the SPSF(r) curve and represents the amount of total scatter fraction.

$$\mathrm{SPR} = \int_{r=0}^{r=r_{max}} \mathrm{SPSF}(r)dr \tag{5.6}$$

Plotting the SPR as a function of the radius permits to evaluate the distance at which the scatter contribution saturates, i.e. the SPR function arrives to a plateau, which allows to define the minimum size of the kernel. This is the distance at which the SPR function arrives to a plateau, and it is dependent on the geometry chosen, e.g. phantom thickness. An example of a 40 mm thick phantom using a simplified geometry, i.e. no compression or support paddles, can be seen in Figure 5.10. In this particular case, the minimum kernel size is 100 x 100 mm.

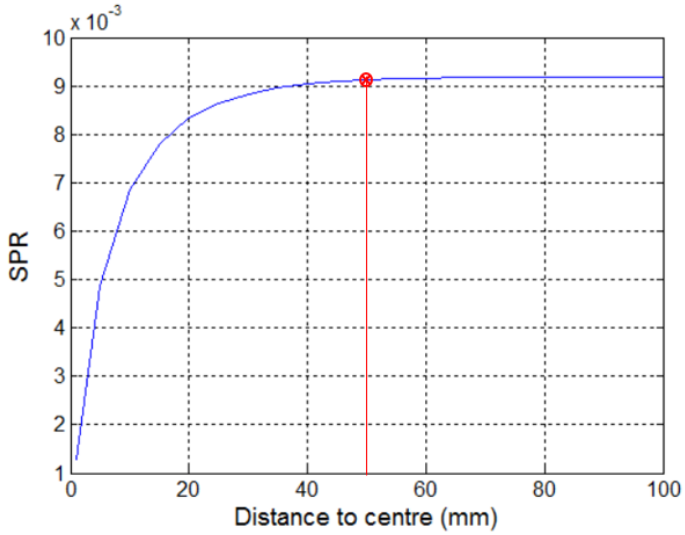

Figure 5.10: The plot shows the SPR (area under the SPSF curve) as a function of the distance to the centre. Showing the distance at which the scatter starts being negligible. In this particular chosen case, the kernel does not need to be bigger than 50 x 50 mm.

5.4.1 Kernel validation

5.4.1.1 SPR validation against published data

A simplified geometry used by previous authors for validation purposes (Sechopoulos et al., 2007b; Díaz et al., 2014), has been reproduced in order to validate the shape of the SPSFs as well as the total SPR, completing the preliminary validation of Section 5.2.3. This geometry is comprised of a cylindrical shaped phantom (116 mm of radius of different thicknesses and compositions), a 10 mm air gap between the lower surface of the phantom and the detector plane and an ideal image receptor. The pencil beam was pointed towards the centre of the phantom and a Mo/Mo energy spectrum of 26 keV was selected for all combinations. The data was recorded using the ring sampling method, see Figure 5.9.

The overall results, compared with the data published by Diaz (Díaz et al., 2014) and Sechopoulos (Sechopoulos et al., 2007b) are shown in Table 5.4. Figures 5.11 and 5.12 show plots of the different SPSF curves as a function of the distance, comparing the simulated data with data provided by Sechopoulos. The first plot, Figure 5.11, only shows the two extreme phantom compositions tested, 0% glandularity and water, as the curves are too close together to be able to visualise them properly in the same plot. Figure 5.12 includes the four thicknesses under study, in this last case the curves are more separated due to the greater thickness dependency of the SPSFs.

Overall, the agreement with previous published data is very good, with a maximum relative differences of 2.9% with Sechopoulos (5 cm thick, 100% glandular phantom) and 3.6% with Diaz (6 cm thick, 50% glandular phantom). These discrepancies could be related to differences in the material definition or in the Geant4 classes configuration, e.g. a different choice in the physics list.

The results show that the generated SPSFs can be used with confidence.

Table 5.4: The table shows eight phantom thickness and composition combinations used with a simplified geometry for the validation of the SPSF. The SPR values for a circular area of 100 mm radius are compared against Diaz et al. (Díaz et al., 2014) and Sechopoulos et al. (Sechopoulos et al., 2007b). The uncertainties for each case were kept below 1%.

		Area under the curve(SPR-100 mm rad)			**Difference(%)**	
Thick. (cm)	**Gland. (%)**	**Secho.**	**Diaz**	**This work**	**Vs. Secho.**	**Vs. Diaz**
5	0	$5.33x10^{-1}$	$5.23x10^{-1}$	$5.36x10^{-1}$	-0.6	2.5
5	50	$5.57x10^{-1}$	$5.40x10^{-1}$	$5.54x10^{-1}$	0.5	2.6
5	100	$5.92x10^{-1}$	$5.68x10^{-1}$	$5.75x10^{-1}$	2.9	1.2
5	Water	$5.91x10^{-1}$	$5.89x10^{-1}$	$5.94x10^{-1}$	-0.5	0.8
2	50	$2.44x10^{-1}$	$2.39x10^{-1}$	$2.43x10^{-1}$	0.4	1.7
4	50	$4.55x10^{-1}$	$4.41x10^{-1}$	$4.55x10^{-1}$	0.0	3.2
6	50	$6.63x10^{-1}$	$6.40x10^{-1}$	$6.63x10^{-1}$	0.0	3.6
8	50	$8.72x10^{-1}$	$8.43x10^{-1}$	$8.72x10^{-1}$	0.0	3.4

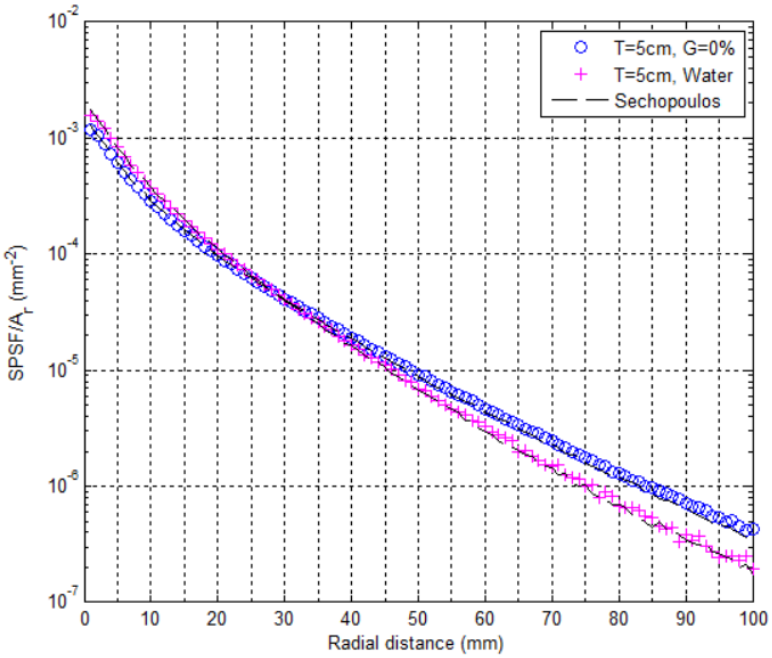

Figure 5.11: Plot showing the SPSF curve as a function of the distance for two different breast compositions, 100% adipose tissue and water. The results are compared against the data published by Sechopoulos (Sechopoulos et al., 2007b).

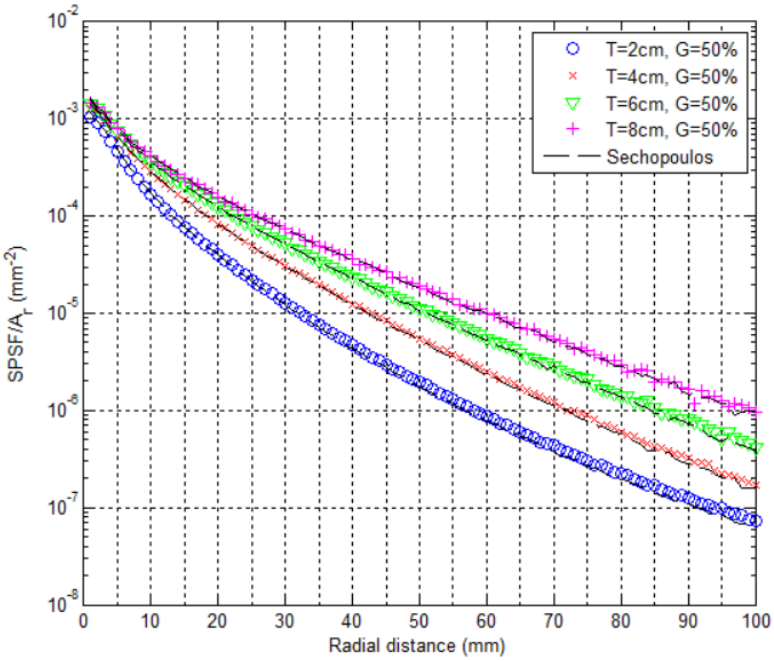

Figure 5.12: Plot showing the SPSF curve as a function of the distance for four breast thicknesses. The results are compared against the data published by Sechopoulos (Sechopoulos et al., 2007b).

5.4.1.2 Ring validation

The method to convert the 1D SPSF(r), obtained using the ring-sampling procedure, to a 2D kernel has been validated by comparing the final result against the kernel obtained with the pixel-sampling method. The geometry used for the comparison was the same one simulated in the previous validation, for a 5 cm thickness and 50% glandularity phantom using a Mo/Mo energy spectrum of 26 keV.

As expected, both kernels are identical, i.e. less than 0.2% of relative difference. Figure 5.13 shows the intensity profile across the centre of the kernel for kernels obtained pixelating the detector (dashed red curve) and using the ring method (circled blue curve). The statistical power of the ring method can be seen in the figure at high radial distances, where the pixelated detector option shows increasing noise due to the limited number of particles reaching the farther distances.

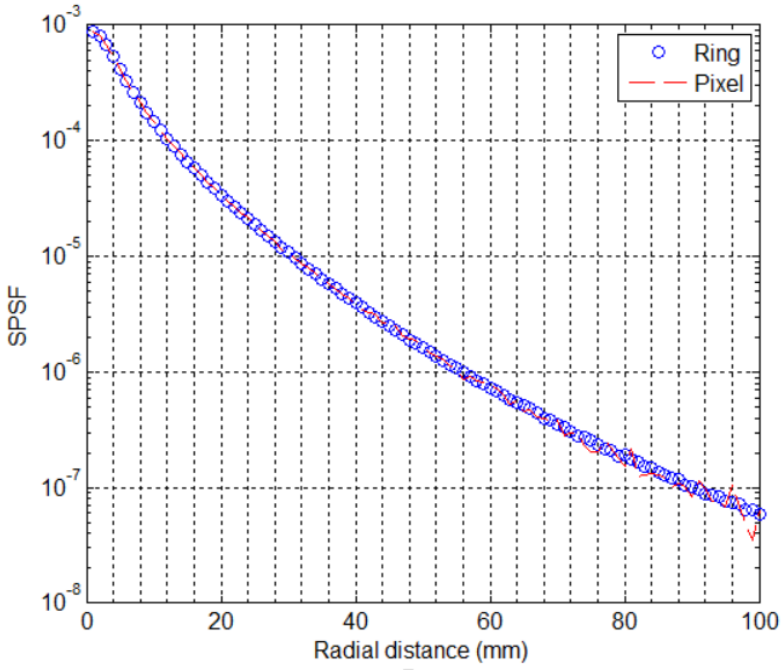

Figure 5.13: Intensity profile comparison between the two data sampling methods (pixelated and ring sampling). The improved statistics of the ring method can be seen at large radial distances, with a reduction in the fluctuation.

5.5 Convolution and analysis

The scatter and primary images can be predicted following equations 4.3 and 4.4. The scatter image (S) can be obtained by convolving the output image (I = P+S) with the appropriate scatter kernel. And the primary image (P), by subtracting to the image the calculated scatter (P = I-S).

There is a discussion in the literature about the amount and shape of the kernels needed to predict the primary image with accuracy. Some authors suggest the use of asymmetric kernels (Wang et al., 2015), while others use the same kernel to convolve the whole image (Ahn, Cho, and Jeon, 2006) or several thickness dependant kernels to account for the changes towards breast edge (Díaz et al., 2012), see Section 4.2.3 for more information.

An asymmetric kernel shape would help to properly treat the boundary between the object and the background. Using this approach, either the kernel is changed gradually to account for the changes in the geometry or a compromise is made and the kernel is modified at certain distances. In both cases, this solution implies a huge computational constraint, with the additional possibility of introducing image artefacts if the kernel is not changed pixel by pixel. Although this approach is more precise, it also has a higher

dependency with the simulated geometry, risking the introduction of errors if it is not properly computed.

The aim of this study is to find a simpler method, without the intrinsic complications of the asymmetric kernels but with good precision. The different options considered for the analysis are discussed below.

Unless specified otherwise, the geometry used in this study corresponds to the α-Se Hologic Lorad Selenia in combination with a realistic synthetic breast phantom, see Figure 5.6 and Table 5.3. For full MC simulations, the dimensions and shape of the breast phantom were based in the study published by Rodríguez-Ruiz et al. (Rodríguez-Ruiz, Agasthya, and Sechopoulos, 2017), where the shape of the compressed breast for mammography and breast tomosynthesis was characterised and modelled. For the simulation itself, the "PolyCone" volume available in Geant4 was chosen as a good approximation. Figure 5.14 shows an example of the breast phantom geometry and Table 5.5 gives the dimensions used for different thicknesses, all obtained with the aid of the Matlab code provided by Rodríguez-Ruiz. For simplification, the compression paddles were approximated to rigid and non-inclined paddles. The chosen breast composition was 30% glandular tissue, a value that approximately represents breasts of thickness 5-6 cm in women aged 50-64 (Dance et al., 2000; Yaffe et al., 2009). As shown in Section 4.3, changes in breast composition do not introduce large variations in the scattering estimation, therefore the chosen glandular percentage was kept constant for all the thicknesses studied. In addition, the phantom was surrounded by a 2 mm thick layer of skin and it was aligned with the chest wall.

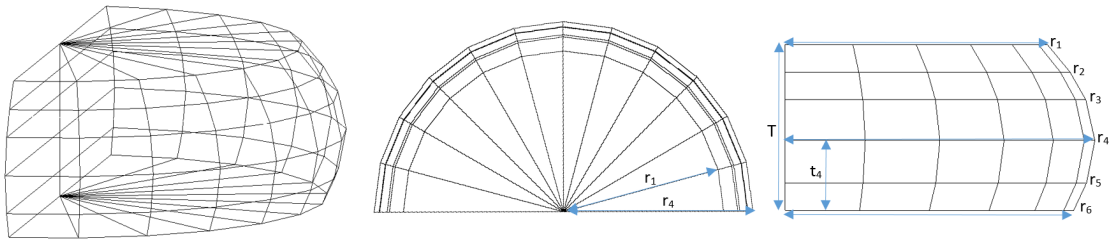

Figure 5.14: The figure shows different views of a simulated breast phantom that makes use of the "PolyCone" volume in Geant4.

For the pencil beam (PB) simulations the phantom kept the same composition and thickness to aid in the comparison against the full MC simulations. The phantom shape was modified to a cylinder and it was centred in the middle of the detector area, see Figure 5.6. A 50 mm breast phantom was chosen for the initial study. For statistic purposes, the pixel size was increased from 70 µm to 280 or 560 µm, depending on each particular case.

Table 5.5: Table with the dimensions (height and radius) of the simulated breast phantoms at five different thicknesses. The dimensions have been obtained following the study published by Rodríguez-Ruiz (Rodríguez-Ruiz, Agasthya, and Sechopoulos, 2017).

H (mm)	h_4 (mm)	r_1 (mm)	r_4 (mm)	r_6 (mm)
35	18.3	64.7	71.7	65.3
50	20.0	80.0	97.0	86.0
60	25.3	94.7	112.0	104.3
70	25	100	133	122
85	32.0	136.0	164.0	153.0

5.5.1 One kernel

The first option to consider is the use of only one symmetric kernel for the convolution analysis (specific to the phantom thickness). For this case, the PB simulation geometry would need to include the object of interest, centred with the pencil beam. To gain statistics, the pixel size of the full MC and PB images was increased to 280 µm, resulting in a 600 x 600 pixel^2 kernel that was used to convolve a 856 x 856 pixel^2 image.

There are two possibilities for performing the image convolution when using this approach. The kernel can be used to convolve the whole image, or the breast area can be masked from the background to force the kernel only to act in the region of interest. Both options present problems, especially close to the breast edge area:

- Using the whole image: Convolving the whole image leads to overestimation, starting 100 pixels after the chest-wall. When compared against the scatter obtained with a full MC simulation ("ground truth"), the predicted scatter is up to 2.6 times higher at the edge of the object, as shown in Figure 5.15.
- Using the phantom area: If the breast area is segmented from the background, the scatter originated in the phantom is underestimated up to 50% towards the edge of the phantom. Figure 5.16 shows the intensity profiles (across the centre of the phantom) of the predicted scatter and the scatter obtained with a full MC simulation ("ground truth").

The results obtained by using only one kernel to predict the scatter are far from being sensitive enough.

It is necessary to highlight the importance of accounting for the background contribution to the image (note that all area of the image that is outside the breast or phantom region is denominated background; the scattering proceeding from this area comes mainly from the compression and support paddles). An inappropriate background treatment can lead

to 50% of inaccuracies, as seen in Figures 5.15 and 5.16. This uncertainty would be even higher for thicker and denser breasts.

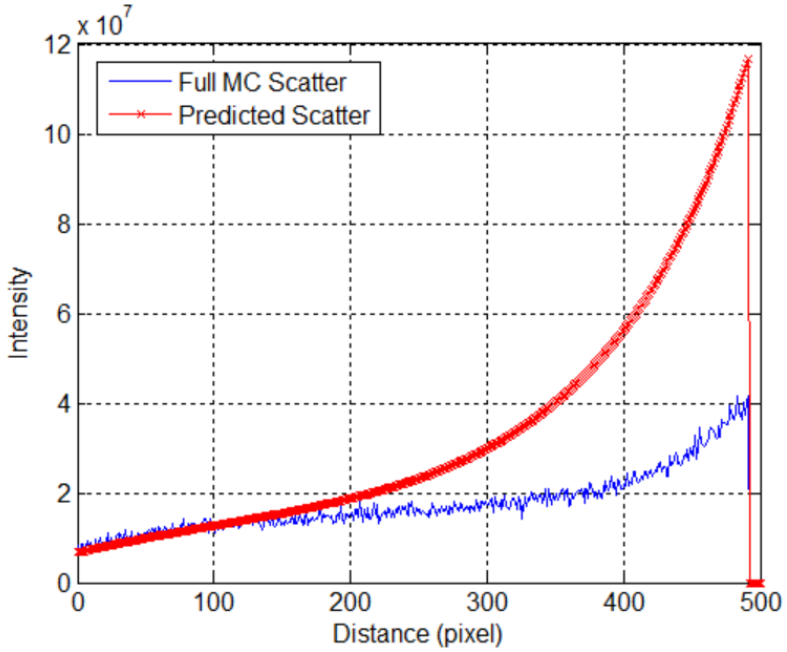

Figure 5.15: Intensity profile of the full MC scatter image (blue) and the predicted scatter image obtained from the convolution of the entire image with the phantom kernel (red).

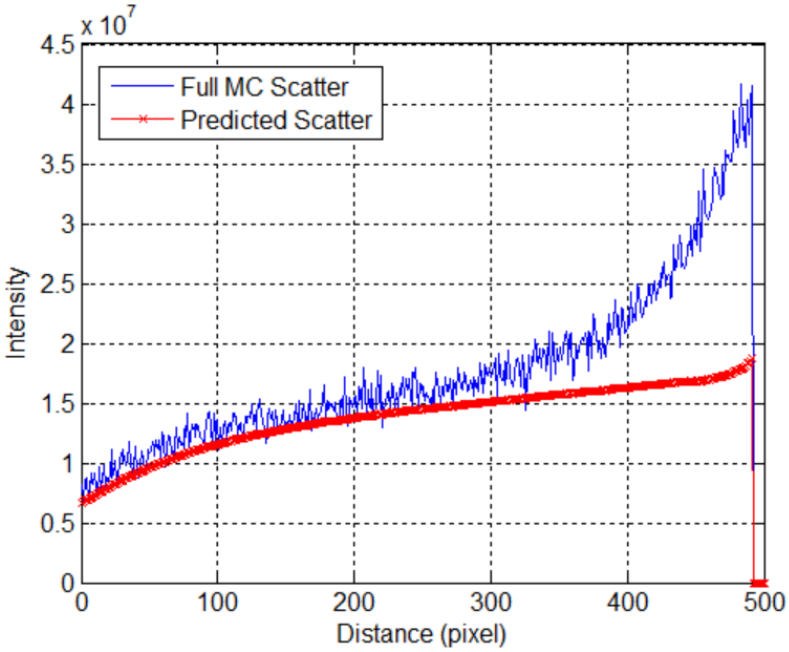

Figure 5.16: Intensity profile of the full MC scatter image (blue) and the predicted scatter image obtained from the convolution of the phantom when the background is set to zero (red).

5.5.2 Two kernels: Object and background

Considering the importance of the background contribution, shown in section 5.5.1, an alternative approach would be to treat each area of the image separately, using two different symmetric kernels to convolve them. To gain statistics, the pixel size of the full MC and PB images was increased to 280 µm, resulting in a 600 x 600 pixel^2 kernel that was used to convolve a 856 x 856 pixel^2 image.

The pencil beam geometry is simulated with the absence of the object to obtain the background kernel, as shown in Figure 5.17-right.

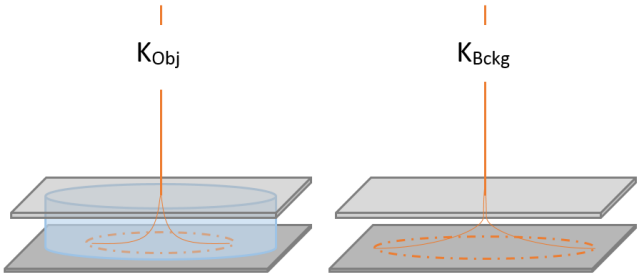

Figure 5.17: Schematic of the geometry used to calculate the object kernel (left) and the background kernel (right), differentiated only by the absence of the object.

During the processing step, a segmentation algorithm based on thresholding is applied to the image to separate both, object ($mask_O$) and background ($mask_B$), areas:

$$I(x,y) = I(x,y)\mathrm{mask_O}(x,y) + I(x,y)\mathrm{mask_B}(x,y) \tag{5.7}$$

$$I(x,y) = I_\mathrm{O}(x,y) + I_\mathrm{B}(x,y) \tag{5.8}$$

Each kernel is used to convolve its corresponding section of the image and then both results are added together to obtain the predicted scatter image, S:

$$S(x,y) = I_\mathrm{O}(x,y) * K_\mathrm{O}(x,y) + I_\mathrm{B}(x,y) * K_\mathrm{B}(x,y) \tag{5.9}$$

$$S(x,y) = S_\mathrm{O}(x,y) + S_\mathrm{B}(x,y) \tag{5.10}$$

Figure 5.18 shows the predicted and full MC ("ground truth") intensity profiles across the centre of the phantom, including as well the background and phantom contributions to the predicted scatter. It can be seen that right on the edge of the phantom (distance > 450 pixels) the predicted scatter is only slightly overestimated. The overestimation increases up to 9% towards the centre of the phantom and then decreases as the background contribution tends to zero, underestimating slightly the scatter towards the chest-wall.

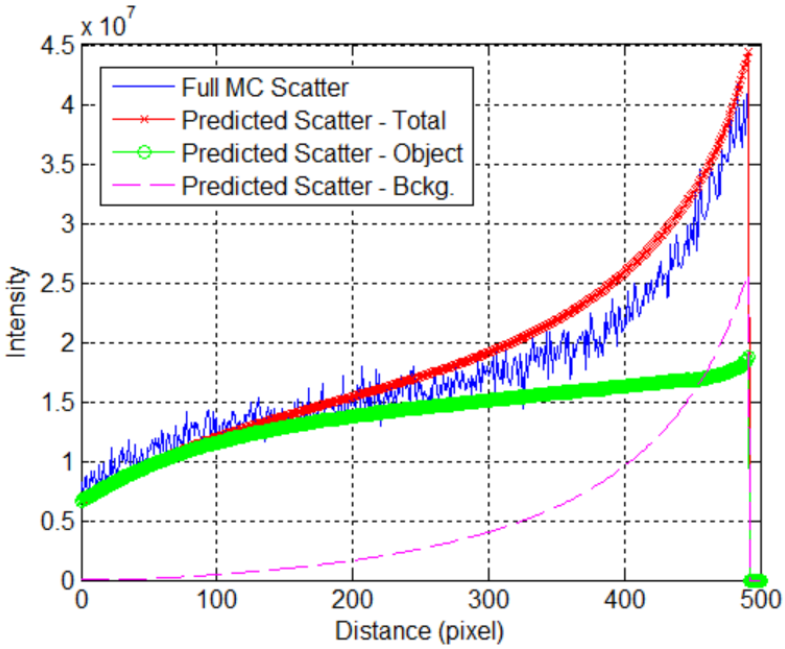

Figure 5.18: Intensity profile of the full MC scatter image (blue), the total predicted scatter image (red) and the object and background contribution to the predicted scatter (green and magenta respectively).

By convolving the image using two separate kernels instead of one, the discrepancy with the "ground truth" is approximately reduced from 50% to 10%. Although the two kernels approach shows a considerable improvement, further reduction of the discrepancies is desirable in order to improve the uniformity across the predicted primary image. Figure 5.19 shows both the full MC (left) and the processed (right) primary images. The non-uniformity of the processed image can be clearly seen in the darker area towards the phantom edge, where the primary image is underestimated due to the overestimation of the scatter.

Even though the background scatter contribution that arrives to the object is estimated correctly, this method oversimplifies the problem by assuming that the background and object absorption coefficients are equal. In reality, the photon absorption of the object is greater and, consequently, the path followed by the scatter photons is shorter. This leads to the 10% overestimation of the scatter seen in Figures 5.18 and 5.19. This effect, exaggerated for visualization purposes, is shown in Figure 5.20. The next section presents

the scatter estimation method proposed in this study, in which this observed issue is accounted for.

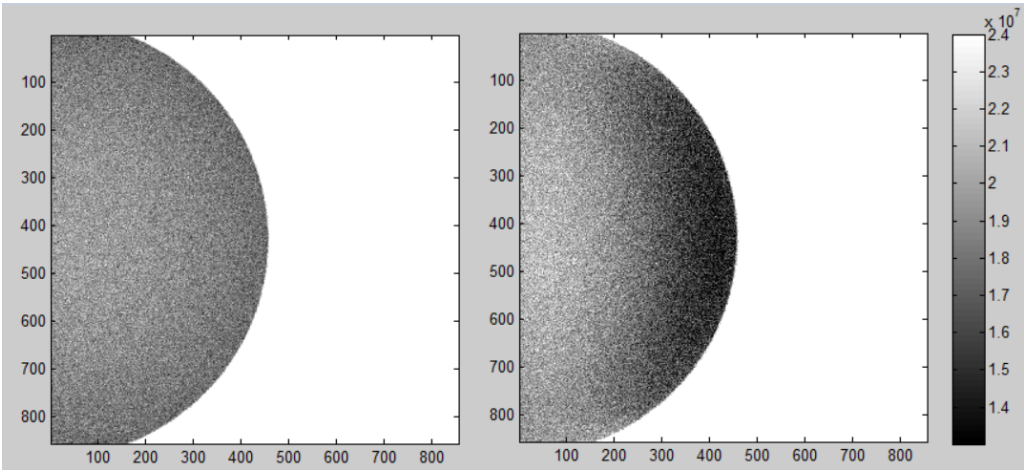

Figure 5.19: Full MC primary image (left) and predicted primary image obtained from the convolution with background and object kernels (right). The darker area of the predicted image indicates scatter overestimation.

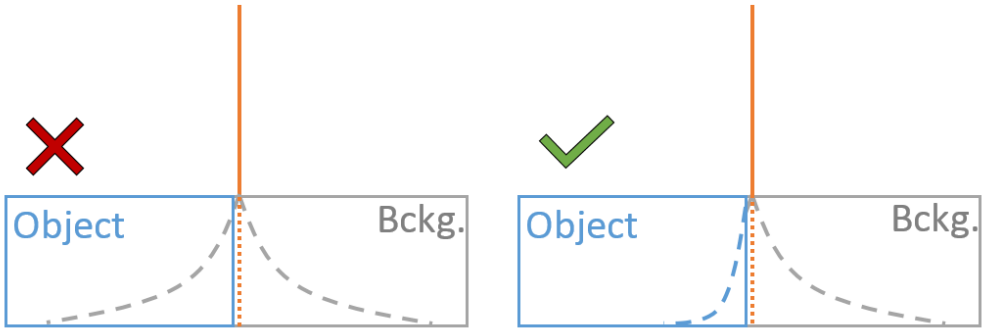

Figure 5.20: Schematic showing the scatter spreading in two media with different absorption coefficients. The incoming photon beam hits the background in an area close to the object. The two kernels method assumes that the scatter will spread equally (left figure); in reality the SPSFs will be asymmetric as the background and object absorption coefficients are different (right figure). The values are exaggerated for visualization purposes.

5.6 Proposed scatter reduction implementation

The method that has been chosen for scatter estimation in this study is a semi-empirical modification of the "two kernel" method, influenced by the theory behind the asymmetric kernels.

An abstracted schematic of the scatter distribution in the image is shown in Figure 5.21. The image illustrates the contributions to the scatter from the different areas of the image.

The method used in this study is based on the fact that the different scatter contributions are additive and, therefore, can be treated separately.

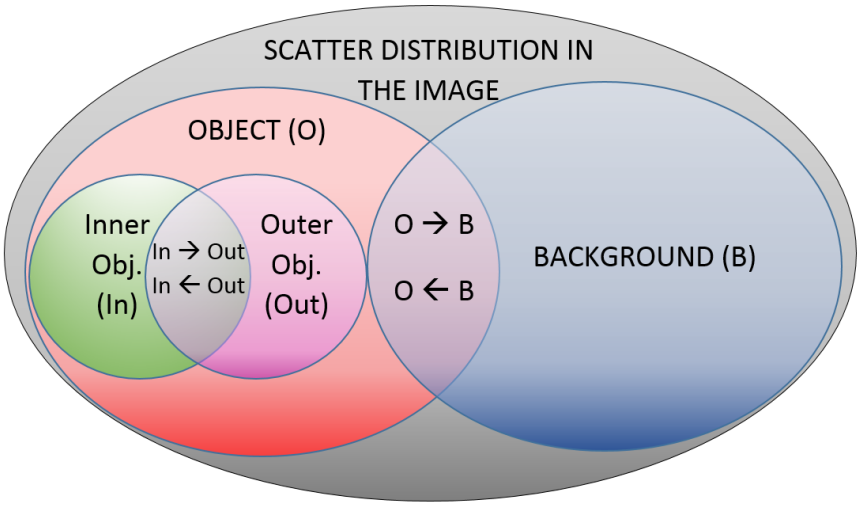

Figure 5.21: Abstracted schematic showing the scatter contribution of the different areas of the image to each other.

The chosen scatter estimation process consists in separating the scatter produced in the object and in the background, studying both contributions separately and accounting, when necessary, for differences in thickness within one same material or in absorption coefficients in the boundaries between objects. The robustness of the proposed method has been tested in this section by using different breast phantom thicknesses.

To gain statistics, the pixel size of the full MC and PB images was increased to 560 µm, resulting in a 500 x 500 pixel^2 kernel that was used to convolve a 650 x 650 pixel^2 image.

5.6.1 Background contribution to the object scattering

It is possible to further develop equation 5.10 by separating the contribution of each medium to itself and to the other medium, as shown in the equations 5.11 and 5.14. It is important to note that the convolution can produce non-zero values in those complementary areas of the image that were brought to zero by the masks; this is caused by the spread of the scatter contribution of the background to the object area and vice versa:

$$S_{\mathrm{O}}(x,y) = S_{\mathrm{O-O}}(x,y) + S_{\mathrm{B-B}}(x,y) \tag{5.11}$$

$$S_{\mathrm{O-O}}(x,y) = S_{\mathrm{O}}(x,y)\mathrm{mask}_{\mathrm{O}}(x,y) \tag{5.12}$$

$$S_{\mathrm{O-B}}(x,y) = S_{\mathrm{O}}(x,y)\mathrm{mask}_{\mathrm{B}}(x,y) \tag{5.13}$$

$$S_{\mathrm{B}}(x,y) = S_{\mathrm{B-B}}(x,y) + S_{\mathrm{B-O}}(x,y) \tag{5.14}$$

$$S_{\mathrm{B-B}}(x,y) = S_{\mathrm{B}}(x,y)\mathrm{mask}_{\mathrm{B}}(x,y) \tag{5.15}$$

$$S_{\mathrm{B-O}}(x,y) = S_{\mathrm{B}}(x,y)\mathrm{mask}_{\mathrm{O}}(x,y) \tag{5.16}$$

The components that are being under or overestimated (as mentioned in the previous section, i.e. two kernels: object and background) are the contributions from each area to the other one, $S_{O-B}(x,y)$ and $S_{B-O}(x,y)$.

When looking into the background to object contribution, the use of a pure background kernel results in an overestimation of the scatter, as the absorption coefficient of the object is larger than the background's (see Figures 5.18 and 5.19). In an opposite way, it could be possible to calculate a kernel that underestimates the scatter by placing a pencil beam hitting the background but surrounded by the object material, see Figures 5.22 and 5.23. In this case, the assumption is that the scatter is absorbed at the rate defined by the absorption coefficient of the object. While this is true when the beam is placed right next to the object, it is not true when the scatter has to travel through the background before arriving to the object, leading to scatter underestimation.

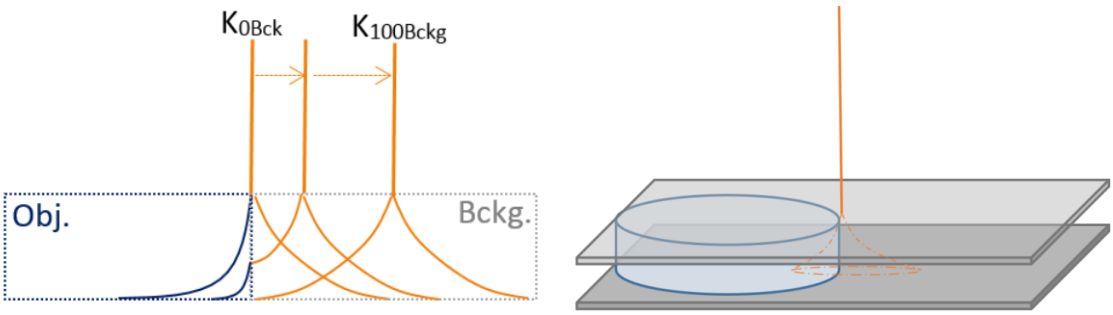

Figure 5.22: The figures show the difference in absorption between the object and the background for a pencil beam pointed to the background area.

The over and underestimation limits are defined by the two kernels described above, that will be named in this study k_{100B} and k_{0B}, see Figure 5.23 for a visual explanation of the geometry of these kernels. It is safe to assume the following conditions:

- Condition 1: the scatter values will be in between the over and underestimation limits, see Figure 5.22.
- Condition 2: the background contribution to the scatter at the edge of the object can be predicted by the pure background kernel, i.e. the kernel that is farthest away from the object as seen in Figure 5.22, k_{100B}.

- Condition 3: the background contribution to the scatter inside the object, towards the chest-wall, tends to be the one predicted by the background-object absorption kernel, i.e. the kernel that is placed next to the object as seen in Figure 5.22, k_{0B}.

The proposed method consists in combining the two scatter images, obtained from the convolution with kernels k_{100B} and k_{0B}, to predict the final scatter image. The explanation that follows will be focused in the background contribution to the object, as the main objective is to predict accurately the object scatter.

$$\left\{ \begin{array}{r} S_{100\mathrm{B-O}} = [I_{\mathrm{B}}(x,y) * K_{100\mathrm{B}}(x,y)]\mathrm{mask_O}(x,y) \\ S_{0\mathrm{B-O}} = [I_{\mathrm{B}}(x,y) * K_{0\mathrm{B}}(x,y)]\mathrm{mask_O}(x,y) \end{array} \right\} \Rightarrow S_{\mathrm{B\text{-}O}}$$

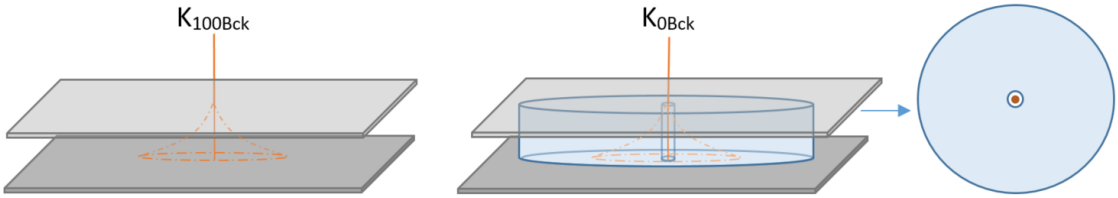

Figure 5.23: The figure shows the geometry used for obtaining the background kernels. On the left, the full background geometry (100%) is shown while the right shows the approximation used for the 0% background kernels.

For the image combination, a semi-empirical formula is adjusted to the intensity profile of the two scatter images. In mammography examinations the breast is aligned with the chest-wall, for that reason the adjustment process is done row by row (for an image displayed with the chest-wall side in the vertical direction). An additional correction will be introduced later to account for the top and bottom areas of the object.

For a given row, n, the intensity profile curves of the predicted scatter images calculated with the kernels K_{100B} and K_{0B} can be named, respectively, $f_n(x)$ and $g_n(x)$, where x is the column variable from the edge of the object (x=0) to the chest-wall (x=N, if N is the object width at the chosen row).

Considering the three conditions defined above:

- From condition 1: the wanted function $t_n(x)$, e.g. the S_{B-O} intensity profile of row n, is assumed to be a linear combination of $f_n(x)$ and $g_n(x)$:

$$t_n(x) = \alpha_n(x) f_n(x) + \beta_n(x) g_n(x) \tag{5.17}$$

  where, α(x) and β(x) are weighting factors.

- From condition 2: $t_n(0) = f_n(0) \Rightarrow \beta_n(0) = 0, \alpha_n(0) = 1$

- From condition 3: $t_n(N) = g_n(N) \Rightarrow \beta_n(N) = 1, \alpha_n(N) = 0$

Parameters α_n and β_n decrease and increase respectively with the distance to the breast edge (x). It was seen experimentally that it is possible to write β_n as being directly proportional to x, while assuming α_n to be inversely proportional to the distance led to scatter underestimation. Therefore, to account for the experimental data and for conditions $\alpha_n(0) = 1$, $\alpha_n(N) = 0$, $\beta_n(0) = 0$ and $\beta_n(N) = 1$, the parameters can be described as:

$$\alpha_n(x) = \frac{K_{\alpha 1}}{K_{\alpha 2} + x} \tag{5.18}$$

where, $K_{\alpha 1}$ has to be equal or very close to $K_{\alpha 2}$, to ensure that $\alpha_n(0) = 1$.

$$\beta_n(x) = K_\beta x \tag{5.19}$$

where, $1 > K_\beta > 0$. In particular, $K_\beta = \frac{1}{N}$, to ensure that $\beta_n(N) = 1$.

The constants $K_{\alpha 1}$ and $K_{\alpha 2}$ need to be adjusted across the image to obtain the final equation. For the adjustment phase, the scatter images obtained from full MC simulations were used as an aid to find the parameters, i.e. the "ground truth" results that the predicted scatter needs to match.

For the adjustment of the parameters, realistic mammography geometry and breast phantoms were used, as described at the beginning of section 5.5. The robustness of the method and the adjusted parameters, discussed at the end of the chapter, was tested by using different breast thicknesses and additional geometries. The most reproducible values found, that made the weighting factors independent of n, were $K_{\alpha 1} = 80$ and $K_{\alpha 2} = K_{\alpha 1} - 1$.

The equation adopted in this study is:

$$t_n(x) = \frac{80}{79 + x} f_n(x) + \frac{x}{N} g_n(x) \tag{5.20}$$

5.6.1.1 Additional correction: column to column

The method explained above makes use of a semi-empirical equation to calculate the scatter image in a row to row basis. The correction was applied in the horizontal direction because of the positioning of the object relative to the background. This correction would be enough if the object was rectangular, covering the image from top to bottom. However, the breast is not only curved but it is also smaller than the image in both vertical and horizontal directions. Therefore, even though the background contribution is larger in the horizontal direction, the vertical contribution needs to also be considered to avoid

the underestimation of the scatter around the top and bottom areas of the object-edge, Figure 5.24 illustrates the need of an additional correction for these areas.

The same equation can be used in the vertical direction correcting the top and bottom halves separately. The final image needs to have values in between the horizontal and vertical estimation.

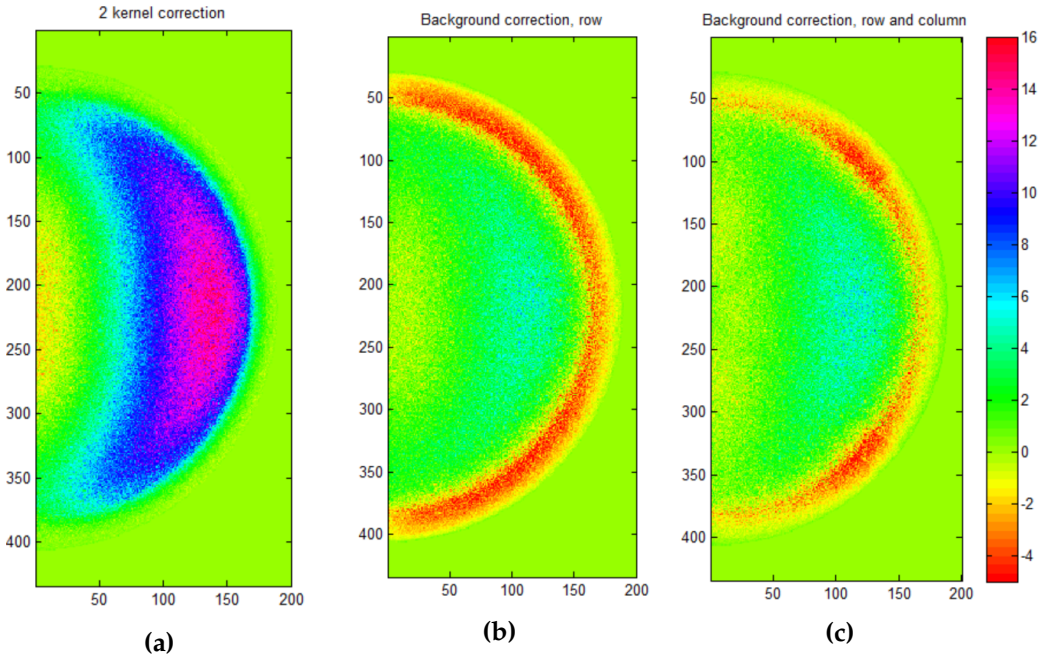

Figure 5.24: Relative difference between the predicted primary and the "ground truth" shown with three different scatter removal methods: using 2 kernels (A) and the background corrected method applied in the row direction (B) and in the row and column direction (C).

5.6.1.2 Object to background contribution

The method that is needed to calculate the object contribution to the scatter, S_{B-O}, is equivalent to the one described above, i.e. calculation of the background contribution to the object scatter, S_{O-B}. However, in this case, the upper and lower scatter limits are inverted: K_{100O} leads to the lower limit, as it assumes that the background absorption coefficient is higher than it is, and K_{0O} allows to obtain the upper limit.

A precise estimation of the background scatter is not within the goals of this study as the efforts have been made in removing the scatter in the object area with precision. For time optimization purposes, the background has been corrected following the method described in the subsection 5.5.2, using the background and object kernels only. On the other hand, the maximum phantom contribution to the background is around 10%, which is 35% lower than the background contribution to the object, so the impact of the correction is not as important.

5.6.2 Object scattering

Up to this point, a constant thickness assumption has been made when performing the phantom analysis. However, even if that was the case, at the edge of the breast the thickness decreases due to the breast curvature and the angle at which the X-ray beam arrives to the edge of the object creates a "shadow area", where the phantom thickness that the photons encounter is reduced gradually from the object thickness, T, to zero. This is illustrated in Figure 5.25.

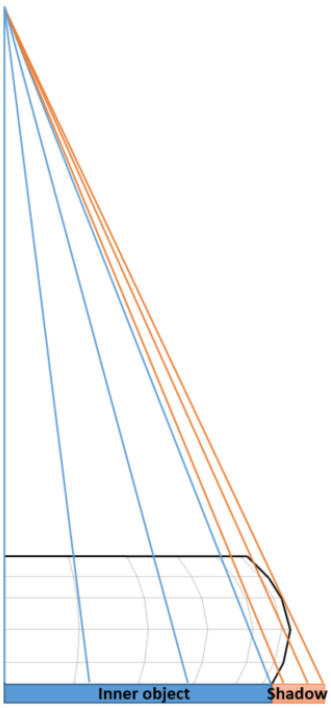

Figure 5.25: Schematic of the geometry showing the area where the breast thickness decreases from thickness T to 0 (named shadow area in the image). For visualization purposes the compression and support paddles and the detector have been removed from the schematic.

The use of a single kernel to correct the object area is an over-simplification that can lead to errors in the scattering prediction, not only in the edge but also in the neighbouring areas (where the predicted scatter will be overestimated due to a badly estimated contribution of the edge scatter). It has been found that the significance of the error introduced depends on the thickness of the phantom:

5.6.2.1 Thin breasts (T < 50 mm)

Experimentally, it has been seen that the change in breast thickness towards the edge of the breast does not introduce large errors in the simulations when only one kernel thickness is used.

In the area where the thickness decreases, i.e. shadow area, both the scatter produced and the percentage of photon absorption are reduced. Both variables seem to balance each other, reducing the introduction of errors. When this area is compared with the "ground truth", the maximum relative difference obtained for a 5 cm breast is $\pm$ 5%, reduced up to $\pm$ 3% for 3.5 cm breasts. As expected, the shadow area is the region of the image where the discrepancies are larger.

5.6.2.2 Thick breasts (T>50 mm)

As the breast phantom becomes thicker, the error introduced increases significantly, arriving to relative difference values of 45% for 85 mm breast thickness. A more detailed correction is needed in these cases.

For rigid compression paddles, with constant thickness in all the projected breast but the edge area, it is possible to find the position after which the breast thickness starts to decrease, by plotting an intensity profile of the unprocessed image (Primary + Scatter image). The constant and non-constant thickness regions can be differentiated using an intensity threshold and, therefore, can be analysed separately. As illustrated in Figure 5.26, the intensity profile increases rapidly towards the edge of the breast. The threshold needs to be chosen right before the profile increase starts.

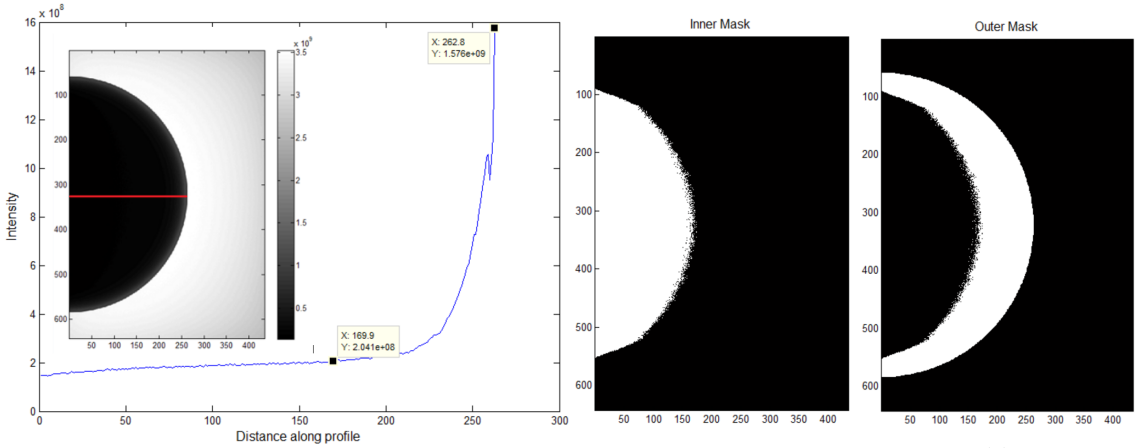

Figure 5.26: On the left (a) the intensity profile of the plot highlights the starting point of the breast thickness reduction. On the right (b and c), the figures show the inner and outer phantom masks obtained with the aid of the intensity profile.

The inner area of the phantom, of constant thickness, can be processed with one single kernel. To process the outer area there are two possibilities:

- Multiple kernel analysis: Calculate many kernels to account for the progressive change of thickness and convolute each area with its correspondent kernel thickness.
- Simplification: Find an equivalent thickness to represent the outer area. The space between the phantom and the support plate created by the thickness reduction is filled with air in this case.

The first option will give more accurate results, but at a high computational time cost, as it would be equivalent to the use of asymmetric kernels. Therefore, the second option has been the one chosen in this study, aiming to reduce to acceptable levels the error introduced by the simplification while reducing the computational time.

The method is similar to the one studied for the background: both areas will have their own scatter contribution and the scatter that arrives from the adjacent area, e.g. the scatter of the inner part of the phantom will be the sum of the inner scatter and the outer scatter contribution.

To compare the results with the full MC scatter image, the predicted background scatter needs to be subtracted to isolate the phantom contribution. Using the full MC as the benchmark result, it is possible to find empirically an equivalent thickness that gives an appropriate contribution from the outer to the inner area, see Figure 5.27. A 20% thickness reduction was found to give the better results, while being reproducible across different phantom thicknesses.

The equivalent thickness has been introduced to calculate the scatter contribution of the outer area of the breast to the inner area, but the calculation of the scatter in the outer region has not been included yet. The process to follow for this estimation is similar to the one introduced in the background-to-phantom scatter estimation, Section 5.6.1. However, in this case it is not necessary to use equation 5.20 as it is possible to simplify the method by making use of a polynomial fitting, using two well-known points and the inner scatter contribution profile:

- Inner object area: Defined by the equivalent thickness method introduced above.
- Boundary between the inner and the outer object area: The scattering at the outer profile starting point can be mapped from the inner profile end point.
- Breast edge: The breast edge corresponds to the thinner area of the outer section, it has been seen experimentally that it corresponds to the external 25% of the profile. The kernel that describes this area is obtained using a kernel with the beam hitting the maximum thickness but surrounded by background, i.e. 0 mm breast thickness.

It was proven experimentally that good results were obtained with a third order polynomial fit. An example illustrating this process is shown in Figure 5.28.

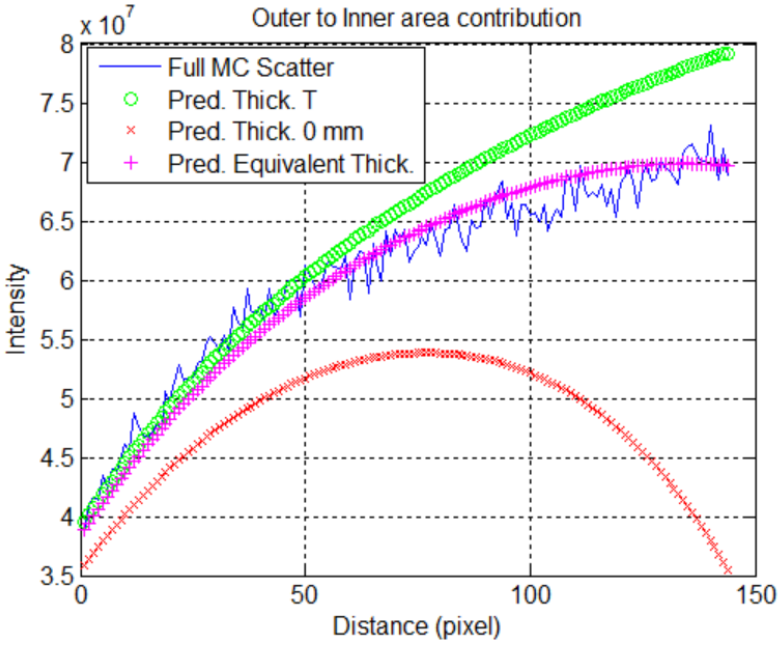

Figure 5.27: The figure illustrates the effect that the outer area of the phantom has in the scatter prediction of the inner area, considering four different cases: benchmark values (blue), 0 mm thick outer area (red), constant phantom thickness: outer = inner areas (green) and optimised equivalent outer thickness of 80% the phantom thickness (pink). All the cases include the support and compression paddles at constant distances.

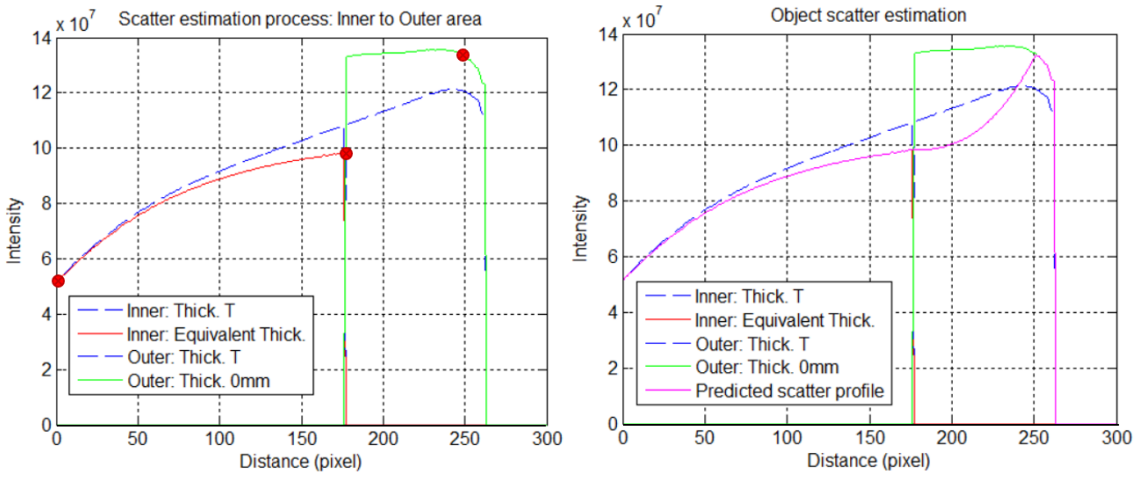

Figure 5.28: The plot on the left illustrates the procedure followed to estimate the scatter corresponding to the outer area of the object, marking the known points used for the polynomial adjustment. The plot on the right shows the adjusted profile.

5.6.3 Method robustness and convolution validation

Five different phantom thicknesses have been tested to validate and study the robustness of the proposed method. Two thin phantoms (35 and 50 mm) and three thick phantoms (60, 70 and 85 mm) were analysed. The scatter of the thinner phantoms was obtained using one kernel to evaluate the phantom scatter while the background contribution was analysed following the method explained in section 5.6.1. The thicker phantoms were analysed by dividing the breast in an outer and an inner area and using an equivalent breast thickness for the evaluation of the non-constant region, as explained in section 5.6.2.

5.6.3.1 Scatter estimation

Figures 5.29 and 5.30 show the relative difference between primary images, comparing the "ground truth", i.e. full MC simulated images, with the predicted image. On the left column, the positive values (blue/magenta colours) indicate scatter overestimation and the negatives (green/red colours) point to scatter underestimation. The plots on the right are the histograms of the images, showing the distribution of the data. Table 5.6 gives the mean value, the standard deviation and the maximum values of over and underestimation.

It is important to take into account the photon fluctuation in the simulated images; there is still some statistical uncertainty in the images used in the comparison, even though up to 80 simulations of 10^9 particles each were run for each of the full MC examples for a pixel size of 560 µm. In the examples evaluated, the fluctuation in the primary MC image goes from $\pm 1.5\%$ for 35 mm breast thickness up to $\pm 5\%$ for 85 mm. To take this into consideration, the maximum over and underestimation values of Table 5.6 have been corrected and the uncertainty values are included.

Table 5.6: Table showing the discrepancies between the predicted primary image and the "ground truth". For each thickness, the table gives the mean value, the standard deviation and the maximum under and overestimation (in %).

T (mm)	Mean (%)	STD (%)	Max. Underest. (%)	Max. Overest. (%)
35	-0.3	1.2	3.4 ± 1.5	2.8 ± 0.8
50	0.3	2.0	5.0 ± 3.3	4.8 ± 2.6
60	1.3	3.1	8.1 ± 5.2	5.6 ± 6.3
70	-0.4	3.3	8.1 ± 5.5	5.9 ± 5.1
85	-1.8	7.7	20.1 ± 14.5	23.0 ± 4.1

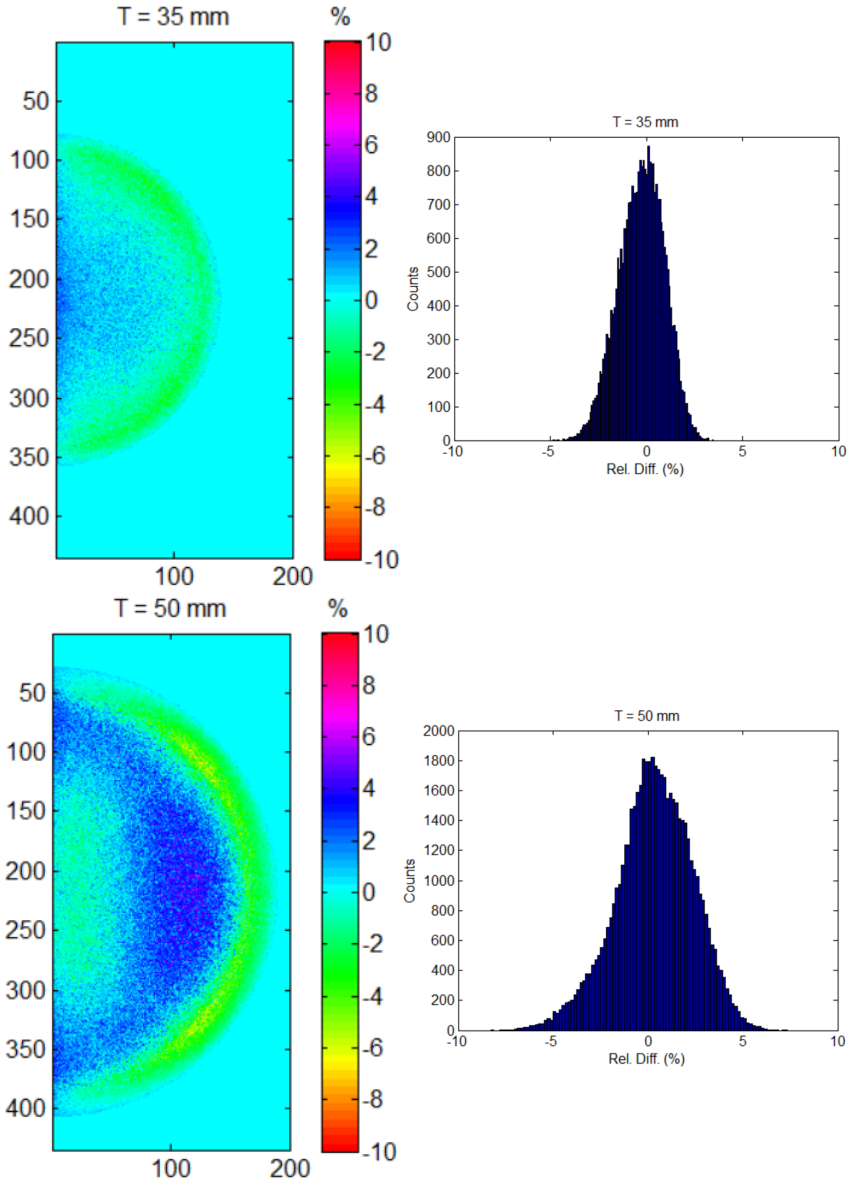

Figure 5.29: On the left, the plot shows the relative difference between the predicted primary image and the "ground truth" for thicknesses of 35 mm (top) and 50 mm (bottom). A histogram of the image distribution is shown on the right side.

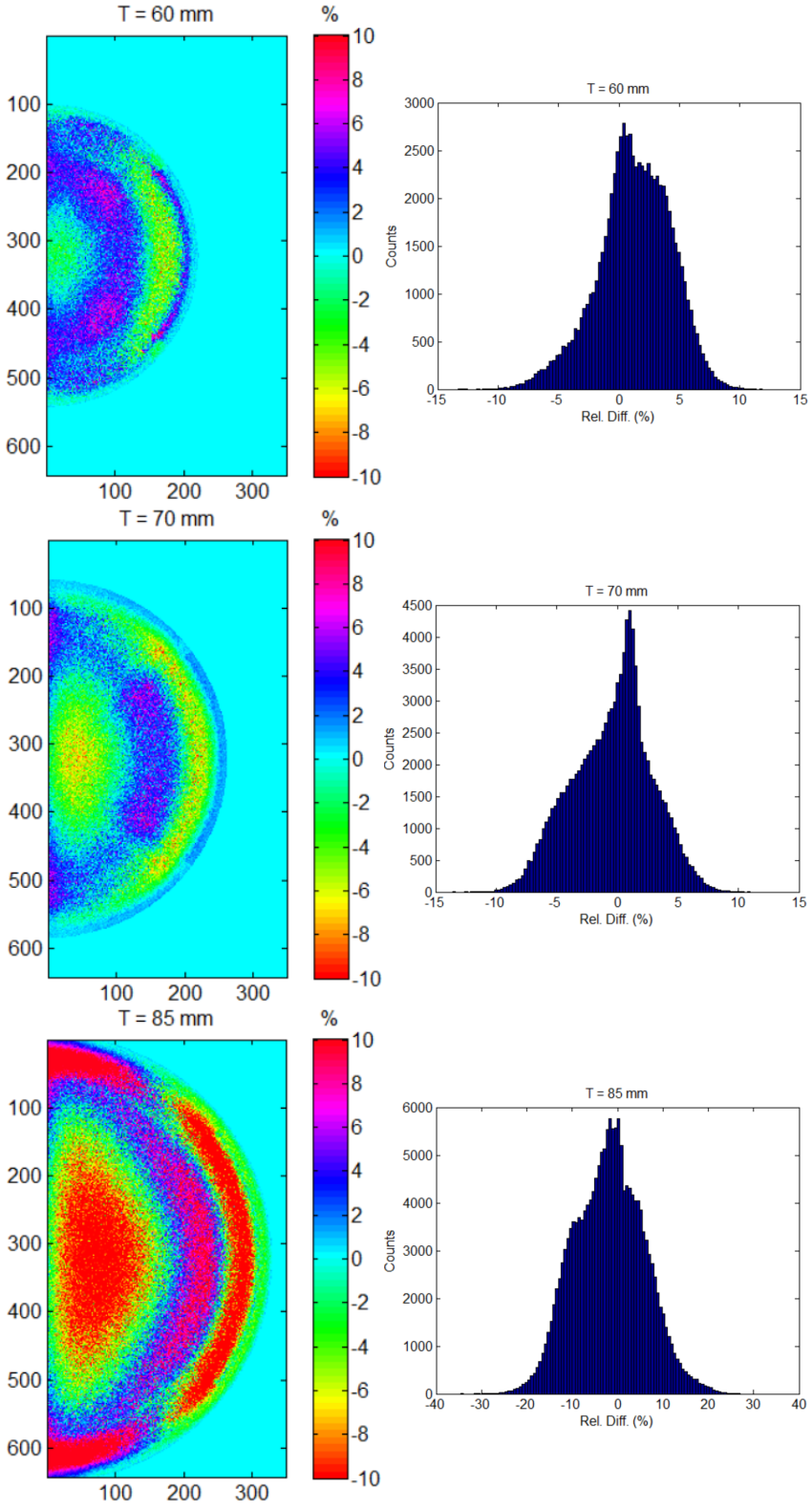

Figure 5.30: On the left, the plot shows the relative difference between the predicted primary image and the "ground truth" for thicknesses of 60 mm (top), 70 mm (centre) and 85 mm (bottom). A histogram of the image distribution is shown on the right side.

5.6.3.2 Method limitations and conclusion

The uncertainty introduced in the scatter estimation increases with the breast thickness. For thin breasts (up to 50 mm) the relative difference between the predicted primary image and the "ground truth" does not exceed 5%, which is considered a very good estimation. The error introduced increases up to 10% for thicker breasts (between 50 mm and 70 mm). The method correction is still considered to work properly. For breasts that are thicker than 70 mm the correction gets more complicated and the reproducibility starts to fail, i.e. for 85 mm the error introduced is around 20-25%. This is likely linked to the equivalent thickness simplification, see section 5.6.2.

To achieve better results the method would need to be modified. For breasts thicker than 70/75 mm it may be preferable the use of asymmetric kernels, in order to avoid a considerable increase in the manipulation of the image that would risk the introduction of image artefacts. For the rest of the cases, the results could be improved by modifying Equation 5.20 or evaluate alternative equations. For example, a thickness-dependent factor so the scatter estimation adapts better to changes in breast thickness, making the analysis less generic. In addition, future work will be needed to make the method more inclusive, evaluating its effectiveness and modifying it when necessary. For example:

- New research should focus in including inclined or flexible compression paddles.
- A modification of the method would also be required to include less common compressed breast shapes, i.e. the suggested method works under the condition that from the chest-wall to the breast-edge there are no "air/background" gaps. However, breasts that present dimple areas might present these gaps when compressed.

5.6.4 Method schematic

The proposed method for estimating the scatter radiation is described in the diagram of Figure 5.31, the schematic is a visual summary of the current section 5.6.

5.7 Chapter summary and discussion

The post-processing scatter estimation technique chosen in this thesis is based on the scatter convolution methodology, using as a kernel a point spread function simulated with simplified pencil beam Monte Carlo simulations. In this chapter the proposed scatter reduction technique was defined, optimised and validated against full MC simulations and previously published data.

The chapter started with an introduction to the chosen simulation tool-kit, i.e. Geant4, covering its general architecture, some of the specific adjustments made to adapt it to the needs of this study and validation against previous publications. It continued with a definition and validation of the system's geometry and kernel calculation. The validations against the simulation set up were essential to the study, as they reduced the possibility of introducing systematic errors in the kernel simulation, which would directly affect the estimation of the scatter. The agreements found indicated that it was safe to advance to the next step: the definition of the final methodology and estimation of the scatter and of the primary image.

Therefore, the second part of the chapter focused on the definition and optimisation of the scatter estimation methodology. Early results showed the need of an accurate treatment of the background contribution to the breast edge area, when background is considered to be all areas and material layers outside the phantom/breast. Accounting for differences in the absorption coefficients whenever there was a change of absorber, i.e. background to breast, was found to be key in the treatment of the breast edge.

The suggested study simplified the asymmetric kernel methodology to the use of three individual kernels for thin breasts (T < 50 mm) and five for thicker breasts (50 < T < 75 mm). In the latter case two additional kernels were needed to compensate for changes in the breast thickness, i.e. change in the materials that the photons encounter through their path across the breast edge. Validations against full MC simulations suggested agreements between the methods of 90-97%, for 75-35 mm thicknesses respectively.

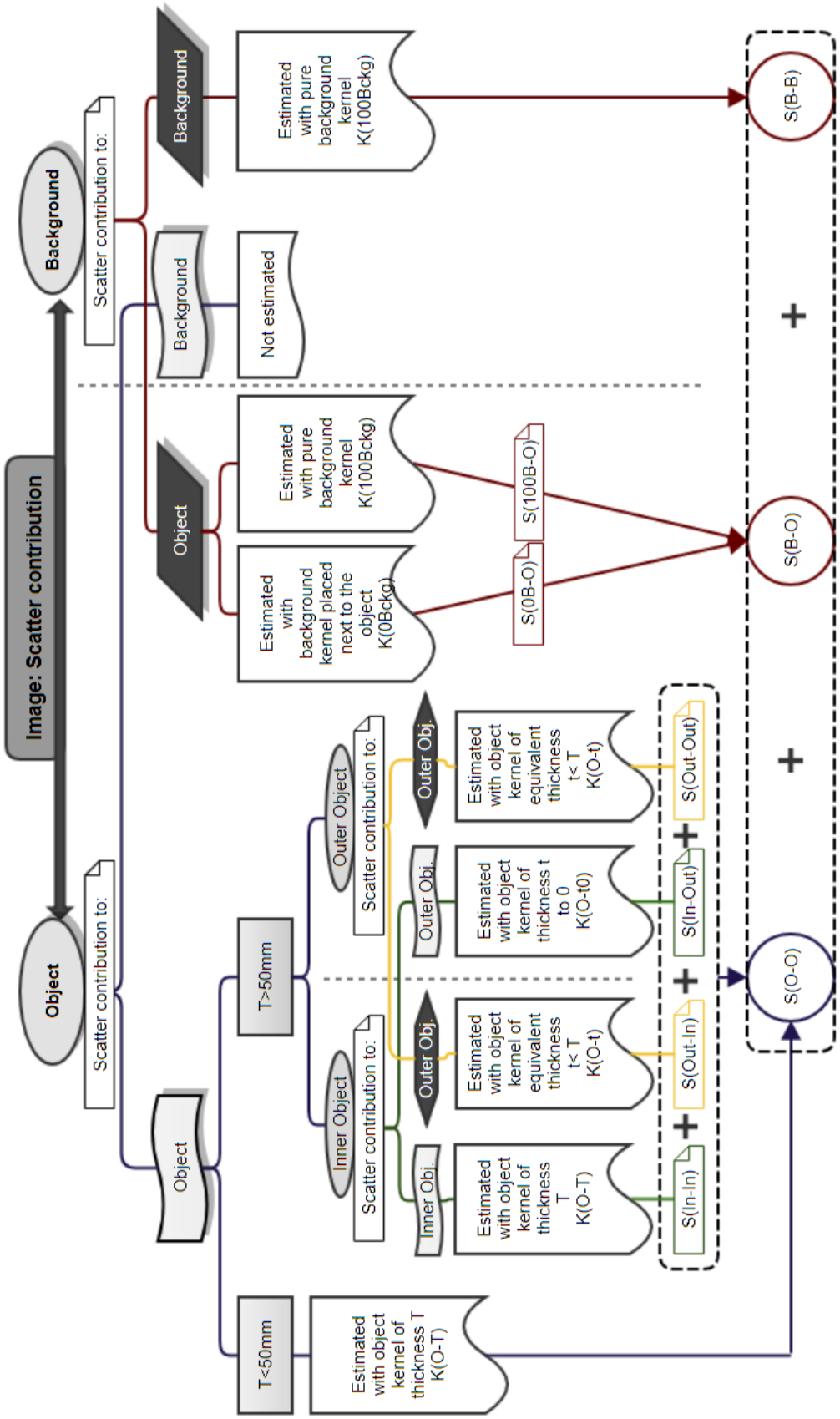

Figure 5.31: Diagram explaining the scatter contribution estimation method presented in this study, see section 5.6.

Chapter 6

PSF scatter reduction: Clinical evaluation with phantoms

The scatter estimation methodology developed previously is evaluated under clinical conditions in this chapter, testing its effectiveness against grid images acquired under the same conditions. A broad selection of clinical phantoms is used for this purpose.

6.1 Scatter estimation methodology

The post-process scattered radiation reduction method that has been chosen, see Section 5.6, assumes that the scattered radiation in the system can be approximated to two-dimensional low-pass filters of the primary image and can be calculated with the convolution between the input image and the filters. The filters, or kernels, are calculated using simplified Monte Carlo simulations where the incident beam is approximated by a delta function or narrow pencil beam.

The chosen scatter estimation method has been optimised in Chapter 5. To account for variations in the absorption coefficients within the system, i.e. background to breast boundary or thickness reduction towards the edge of the breast, the image is divided in two or three regions of interest, depending on the thickness of the breast. Each sub-image is analysed separately with its correspondent set of kernels, giving the scatter estimation of the analysed region and its contribution to the neighbouring areas. The final scatter image is obtained by adding together all the scatter sub-images. From there, the primary image can be calculated by subtracting the scatter image to the unprocessed (input) image, i.e. grid-less acquired image. The method work-flow can be seen in Figure 6.1.

In this chapter, the scatter reduction method is going to be further characterized and tested using two different technologies, i.e. α-Se and CMOS, with a wide range of clinical phantoms.

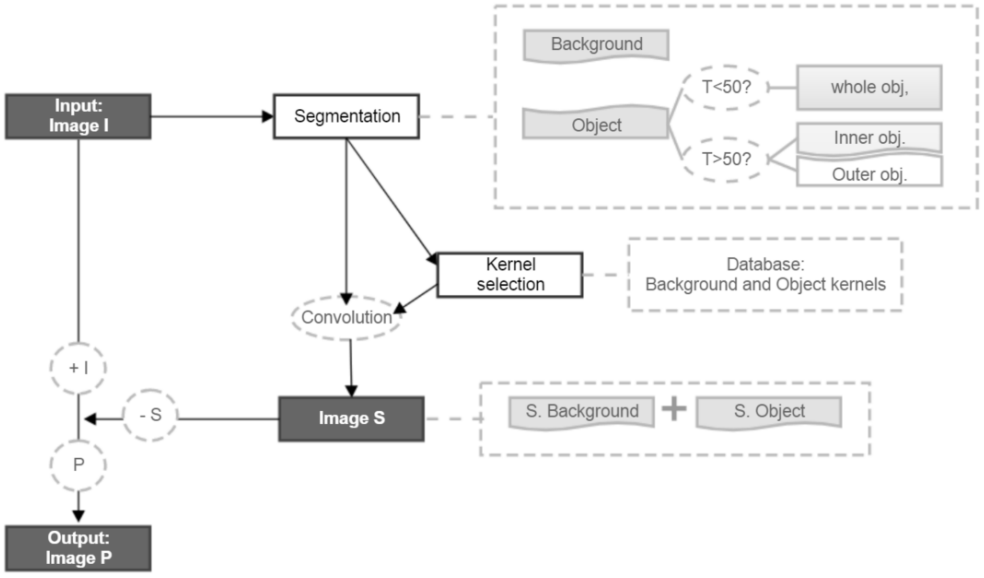

Figure 6.1: Schematic showing the work-flow of the scatter removal method chosen in this study.

6.2 Detector geometry: impact on the scatter contribution

This section looks into the impact that the detector geometry has on the scatter estimation, aiming to find if a simplification in the geometry will considerably affect the precision of the results.

This study has been made simulating CMOS-APS technology. The structure of CMOS X-ray detectors is comprised of a carbon cover, a piece of foam (simplified to an air gap), a CsI scintillator, and a fibre optic plate bonded to the CMOS sensor. The simulated system geometry also includes the compression and support paddles and air gap between the support paddle and the detector, see Figure 5.6-right. For simplification purposes, the interactions occurring after the X-rays are scintillated were not taken into account. The spectrum selected was a 30kVp Mo/Mo (HVL=0.3431 mmAl), 20 to 60 runs of 10^9 X-ray photons each were simulated, ensuring uncertainties lower than 1.5% in the simulated kernels, see section 5.2.2. Radial symmetry was assumed, given that the pencil beam hits a location far from the edges of the simulated phantom.

To evaluate the contribution of the detector geometry to the simulated kernels (PSF), three different detector set ups were compared:

- Case 1 - Ideal detector geometry: The detector is assumed to be an ideal X-ray sensitive surface. The stored energy values come from all X-ray photons that reach the detector surface.

- Case 2 - Simplified detector geometry: The detector is assumed to be only the scintillator plate (200 µm CsI on a 1.5 mm of amorphous Carbon (aC) substrate (*Scintillator plates - Hamamatsu photonics*)), placed right after an air gap of 13 mm. The stored energy values come from the X-ray photons that interact with the scintillator.
- Case 3 - Realistic detector geometry: The different layers of the detector down to the scintillator surface are considered and their contribution studied. From top to bottom, the layers of materials simulated after the 3 mm air gap are: a carbon cover, a second air gap (an approximation of the piece of foam) and a scintillator. See the CMOS detector structure defined in Figure 5.6. The stored energy values come from the X-ray photons that interact with the scintillator. The data was obtained via private communication with Varex Imaging.

The simplification seen in Case 2 is often found in the literature, in cases where the detector structure is unknown. To evaluate how effective this simplification is, Case 3 simulates a more realistic detector structure. For the three detector geometries described above, three breast thicknesses and three breast glandularity percentages - material composition obtained from Hammerstein et al. (Hammerstein et al., 1979) - were analysed. Table 6.1 shows all of the combinations under study. Data from experiment A (50 mm breast thickness, 20% glandularity) is taken as the reference values.

Table 6.1: The table shows the characteristics of the different experiments that have been studied. It specifies the breast thickness and glandularity of the phantom and the case number assigned to each combination.

Exp.	Breast Thickness (mm)	Glandularity (%)	Geometry: Cases 1, 2, 3
A	50	20	A.1, A.2, A.3
B	30	20	B.1, B.2, B.3
C	80	20	C.1, C.2, C.3
D	50	35	D.1, D.2, D.3
E	50	50	E.1, E.2, E.3

The figure of merit used for the analysis of the results was the total scatter to primary ratio (SPR), which corresponds to the area under the scatter point spread function (SPSF) curve and represents the amount of total scatter observed at each detector geometry, see equations 5.5 and 4.11.

Figure 6.2 shows the SPSF(r) normalised by the area, for Cases A.1, A.2 and A.3, plotting the spatial distribution of the scatter as a function of radial distance.

The area under the SPSF curve (SPR) allows the comparison of the total scatter contribution of the different experiments see Table 6.2. The SPR was measured using a maximum radial distance of 100 mm. The table also shows the ratio between Cases 1 and 3 and

Cases 2 and 3, giving an estimation of the change in the scattering between cases and experiments.

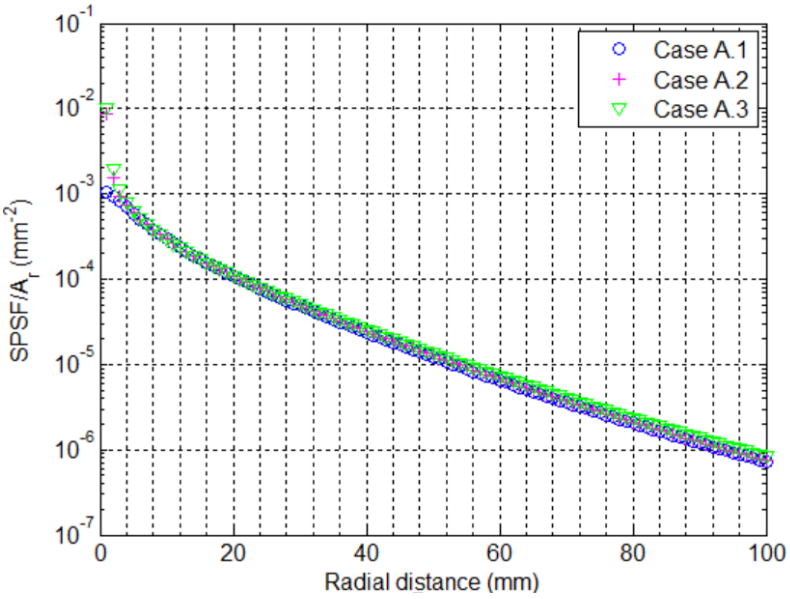

Figure 6.2: Plot showing the SPSF curve obtained when using an ideal detector (Case A.1), a scintillator plate (Case A.2) and a realistic detector geometry (Case A.3).

Table 6.2: The table shows the average SPR values and their uncertainty (in %) for the three detector geometries and the five experiments run (A-E), including also the ratios between C1-C3 and C2-C3.

Exp.	Total SPR (Error in %)			C1/C3	C2/C3
	Case 1	Case 2	Case 3		
A	0.60 (0.04)	0.64 (0.04)	0.67 (0.04)	0.90	0.95
B	0.40 (0.04)	0.43 (0.04)	0.46 (0.04)	0.86	0.94
C	0.92 (0.13)	0.97 (0.14)	1.00 (0.14)	0.92	0.97
D	0.61 (0.07)	0.65 (0.08)	0.68 (0.08)	0.90	0.95
E	0.62 (0.08)	0.66 (0.08)	0.69 (0.08)	0.90	0.95

Considering the overall scatter contribution (see Table 6.2), the total amount of scatter increases with additional layers of material. As expected, a more complex detector geometry presents higher SPR values. If Case 1 and Case 3 are compared, a discrepancy between 10-14% is found for the different experiments, while a discrepancy between 3-6% can be seen when comparing Cases 2 and 3. These results show that it is important to add the real detector information into the simulations. If the dimensions and component materials are unknown, simply adding the scintillator (substrate and CsI:Tl) to the geometry can improve the scatter simulation by 5-8%.

The changes in the ratio between the cases, as a function of variations in the glandularity or the thickness of the breast, can be seen in Figure 6.3. The figure shows the ratio (in %) between Case 1 and 2 and the reference experiment, i.e. Case 3.

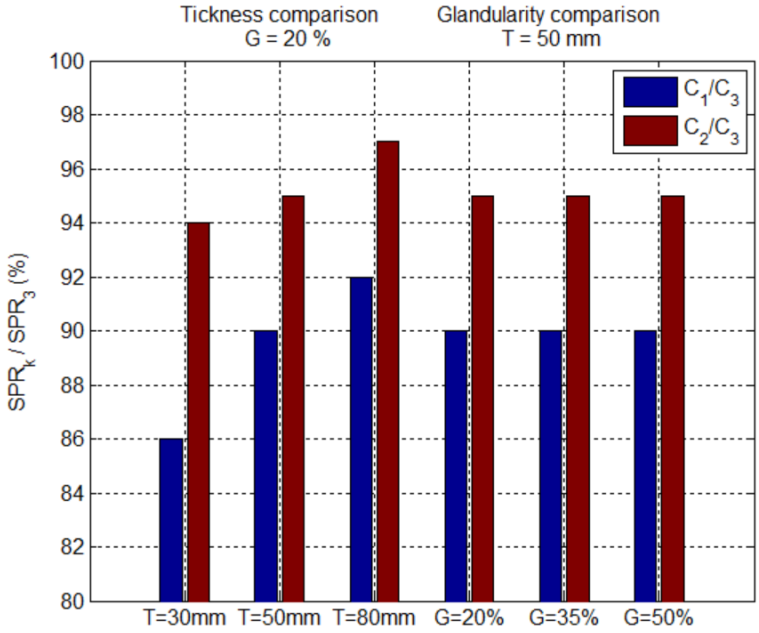

Figure 6.3: The plot shows the ratio between the ideal detector geometry C1 (and the scintillator plate geometry C2) and the more realistic geometry (C3) for different breast thicknesses (T, for a constant glandularity of 20%) and glandularity (G, for a constant thickness of 50 mm) combinations.

Changes in the breast thickness (experiment B) affect significantly the results obtained, being the thinner breasts the ones that are more influenced by the geometry of the detector. As thicker breast phantoms have greater contribution to the total SPR, the relative influence of the detector's geometry to the total SPR decreases. Glandularity variations do not seem to have a considerable effect on the ratio between the cases. This is in line with the literature, (Sechopoulos et al., 2007b; Boone et al., 2000).

6.3 Spatial resolution

MTF measurements have been chosen to quantitatively study the effect that the proposed post-processing scattering removal method has on the spatial resolution. A simulation study and a phantom evaluation study were performed for this purpose.

To carry out this evaluation, two MTF-Edge test devices have been used. The first phantom, DMam phantom from Leeds Test Objects, consisted of a straight 1 mm thick steel edge tilted 5 degrees and embedded in the middle of a 13.25 mm thick PMMA block. The low frequency MTF of this phantom is considerably reduced due to the scatter produced by the PMMA material. Therefore, if the image is scatter-corrected, the low frequency values of the MTF should be restored. The second edge test device was used as benchmark for comparison purposes; this device consisted of a Tungsten edge surrounded by

a plastic and lead frame, complying with the International Standard IEC 62220-1 guidelines, (IECP, 2007b).

The MTF was evaluated following the method presented by Buhr et al. (Buhr, Guenther-Kohfahl, and Neitzel, 2003), previously explained in Section **??**. As the phantom edge needed to be aligned with the X-ray source in order to get an accurate MTF reading, a non-mammography system was used. The image area was collimated to the phantom side, and the Source to Image Distance (SID = 150 cm) was chosen to be large enough to reduce the beam incident angle. The phantom was placed directly on top of the detector and no additional materials were included between the collimator and the phantom, i.e. no filtration, compression/support paddles or grid were used, Figure 6.4 shows an image of the set up. The voltage chosen was 40 kV, the lowest allowed by the system.

Figure 6.4: Experimental set up used for the MTF measurements, showing the X-ray tube and the Edge Test phantom placed on top of the detector. The SID was modified for visualization purposes.

This new set up was implemented in Geant4 and an ideal detector was assumed during the simulations, i.e. all the photons that arrived to the detector surface were detected and taken into account. The reason behind this decision was to facilitate the comparison

against the images taken with the benchmark phantom. MTF phantoms are used to measure the spatial resolution of the detector, which is reduced by the scattering produced in it. Accounting for this scattering would artificially increase the MTF values. The images were all acquired with a Dexela Ltd CMOS X-ray detector (Varex Imaging), the same type of detector that was previously simulated in the study of the geometry (see Section 6.2 and Figure 5.6).

A full MC study was made before performing the MTF analysis with the phantom images, to make sure that the processing did not compromise the study by the introduction of image artefacts. The simulations kept the same geometry as the clinical experiment when using the DMam phantom, i.e. edge embedded in PMMA. The MTF was measured in the full MC image (primary + scatter), in the full MC primary image and in the processed primary image, i.e. image that results from the convolution of the full MC image with the simulated kernels. The convolution method described in Chapter 5 had to be adapted to the structure of the MTF edge accounting in this occasion for the scatter contribution from the edge to the PMMA block, in addition to the PMMA to the edge contribution. A total of four kernels were used, according to the materials present in the geometry: steel and PMMA kernel, PMMA kernel, and the two kernels resulting from each material surrounded by the other, as explained in section 5.6.

For the three aforementioned cases, the MTF values, as a function of the spatial frequency, are shown in Figure 6.5 and Table 6.3.

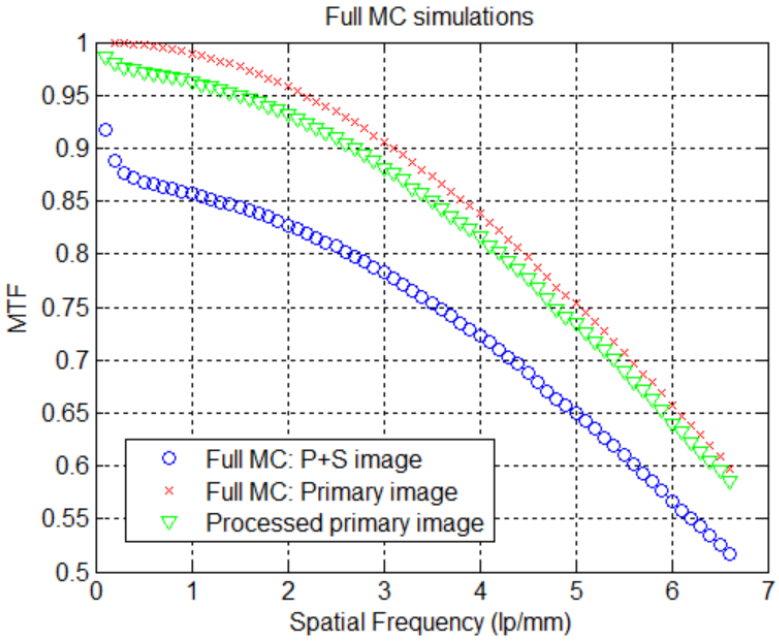

Figure 6.5: MTF curves acquired with the edge methodology, comparing the results obtained with full MC simulations, i.e. P+S and primary, and with the processed primary image.

Table 6.3: The table shows the MTF values at different spatial frequencies comparing the results obtained with full MC simulations, i.e. P+S and primary, and the processed primary image.

Spatial Freq. (lp/mm)	**MTF**		
	Full MC I (P+S)	Full MC P	Proc. P
0.1	0.92	1.00	0.99
0.5	0.87	1.00	0.97
1	0.86	0.99	0.96
1.5	0.84	0.98	0.95
2	0.83	0.96	0.93
3	0.78	0.91	0.88
4	0.72	0.84	0.82
5	0.65	0.75	0.73
6	0.57	0.66	0.64

Some observations that need to be highlighted from the results obtained with the full MC simulations are:

- The MTF values obtained with the full MC primary image are almost ideal, i.e. in digital detectors the MTF upper limit is defined by the pixel size, in form of the sinc-function. The lack of scattering proceeding from the detector, which would reduce the spatial resolution, explains the almost ideal results.
- The processed image highly improves the results obtained with the full MC P+S image. In average, the MTF results improve up to 12%.
- The processed image gives MTF results that are, in average, 3% lower than the MTF values obtained with the full MC primary image ("ground truth"). The precision achieved is very good, ruling out the introduction of artefacts and restoring almost perfectly the spatial resolution that was reduced by the scatter introduced by the PMMA block.

Any image artefact introduced by the convolution would have likely affected the shape or value of the MTF curve, e.g. increasing artificially the MTF results. As the results obtained with the simulation study did not introduce any of these issues, it was considered safe to proceed with the phantom evaluation. The measured MTF values, obtained with the unprocessed and processed DMam phantom images, i.e. PMMA-Edge, are compared with the "ground truth" in Figure 6.6 and Table 6.4.

As expected, the low frequency MTF values of the Dmam phantom are affected, up to 9%, by the scatter produced in the PMMA. The processing of the image successfully removes the scatter and restores the MTF curve to the detector real MTF values, i.e. "ground truth" values. In fact, the processing slightly improves the results obtained with the benchmark

phantom. The reason for this improvement lies in the geometry of the benchmark phantom. The design of the phantom introduces a 1 cm air gap between the tungsten edge and the detector, allowing the scatter produced in the edge to spread and, therefore, reducing the MTF values.

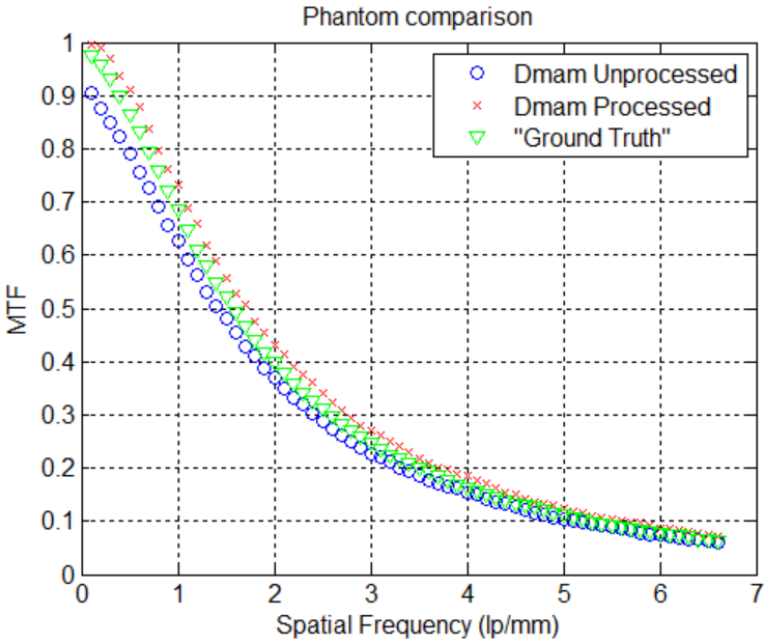

Figure 6.6: MTF curves comparing the results obtained with the two edge phantom images, i.e. unprocessed and processed DMam phantom and the IEC approved phantom (or "ground truth").

Table 6.4: The table shows the MTF values at different spatial frequencies comparing the results obtained with the two edge phantom images, i.e. unprocessed and processed DMam phantom and the IEC approved phantom (or "ground truth").

Spatial Freq. (lp/mm)	**MTF** Dmam Unproc.	Dmam Proc.	"Ground Truth"
0.1	0.91	0.99	0.98
0.5	0.79	0.91	0.87
1	0.63	0.73	0.68
1.5	0.48	0.56	0.52
2	0.37	0.43	0.40
3	0.23	0.27	0.25
4	0.15	0.19	0.16
5	0.10	0.12	0.11
6	0.07	0.09	0.08

6.4 Evaluation with phantoms designed for mammography

The impact that the selected scatter estimation method has in grid-less images has been evaluated in the two previous sections using CMOS X-ray detectors, the technology developed at the partner company Dexela Ltd (Varex Imaging Corporation). However, there are no Varex CMOS X-ray detectors currently being used for mammography applications. Due to the difficulty in finding a mammography system with an embedded CMOS detector, an alternative technology was sought. The medical physics department at Barts Health NHS trust (London, UK) and at the university hospital Parc Taulí (Sabadell, Spain) allocated time for continuing this study with one of their mammography systems. The technology chosen was α-Se. The Hologic Selenia Dimensions system at Parc Taulí hospital was used in combination with the CDMAM phantom (version 3.4); phantoms 010A from CIRS (*CIRS*) and TOR-MAS and TOR-MAM from Leeds Test Objects (*TOR-MAS*; *TOR-MAM*) were tested using the Hologic Lorad Selenia system available at Barts Health NHS trust, see Figure 6.7. The geometry of these systems was simulated to obtain the PB kernels, following the information provided in Section 5.3 and illustrated in Figure 5.6-right. The pixel size was kept at its real size, i.e. 70 µm, to analyse the images.

6.4.1 CDMAM

The CDMAM (Contrast Detail MAMography) phantom is a test object widely used for evaluating the detectability performance of mammography X-ray detectors. This contrast-detail phantom allows to assess the system ability to detect small lesions that have low contrast. The use of the CDMAM has been recommended in the European Protocol for digital mammography quality assurance, as one of the ways of describing the image quality of a X-ray system through contrast thresholding. (Grosjean and Muller, 2006; Díaz, 2013; Binst et al., 2015)

The CDMAM phantom consists of a 2 mm thick aluminium base that holds a matrix of gold discs and it is encased at the bottom of a 5 mm PMMA plate. Each cell of the matrix has two identical discs; the first one is always placed at the centre of the cell while the second one is randomly placed in one of the four quadrants, see Figure 6.8. The diameter and thicknesses of the discs decrease logarithmically, from 2.0 to 0.06 mm and 2.0 to 0.03 mm respectively, as the cells move across the rows and columns of the matrix (Díaz, 2013; Binst et al., 2015).

The analysis exercise consists in detecting the position of the disc inserts in a flat noisy background (Grosjean and Muller, 2006), starting with the cell that has thicker and bigger discs and moving row by row towards the thinner/smaller discs. The scoring can be made by a human reader or it can be automatized with a software. In this study the

Figure 6.7: Example of the experimental set up used in this study. The image corresponds to the Hologic Selenia system located at Barts NHS trust.

analysis has been performed with the CDCOM 1.6 automated scoring method (available at www.euref.com). The final results are normalised to the averaged human reader response, by multiplying with a given software-to-human ratio.

A set of images with and without grid were taken using different phantom thicknesses (20, 30, 40, 50 and 70 mm) and two energies per thickness. The two doses were chosen by the system's Automatic Exposure Control (AEC) when the grid was in use (AEC wG) and removed (AEC w/oG) from the system. The dose given without the grid was 45% lower in average. See Table 6.5 for details of the chosen X-ray settings per thickness.

PMMA blocks were added to the CDMAM phantom to increase its thickness, i.e. the phantom has an equivalent PMMA thickness of 10 mm. The CDMAM phantom was always placed at a fixed distance of the support paddle, i.e. 20 mm, to be in line with the experiment performed by Binst et al. (Binst et al., 2015). A 10 mm air gap between the phantom and the support paddle was left in the first case, where the total phantom

thickness was 20 mm, i.e. 10 mm of PMMA plus the CDMAM. As some of the disc inserts are smaller than the pixel size a total of eight images were acquired for each combination, shifting slightly the phantom in between measurements in order to reduce the possibility of the disc falling into the "dead" areas of the pixel.

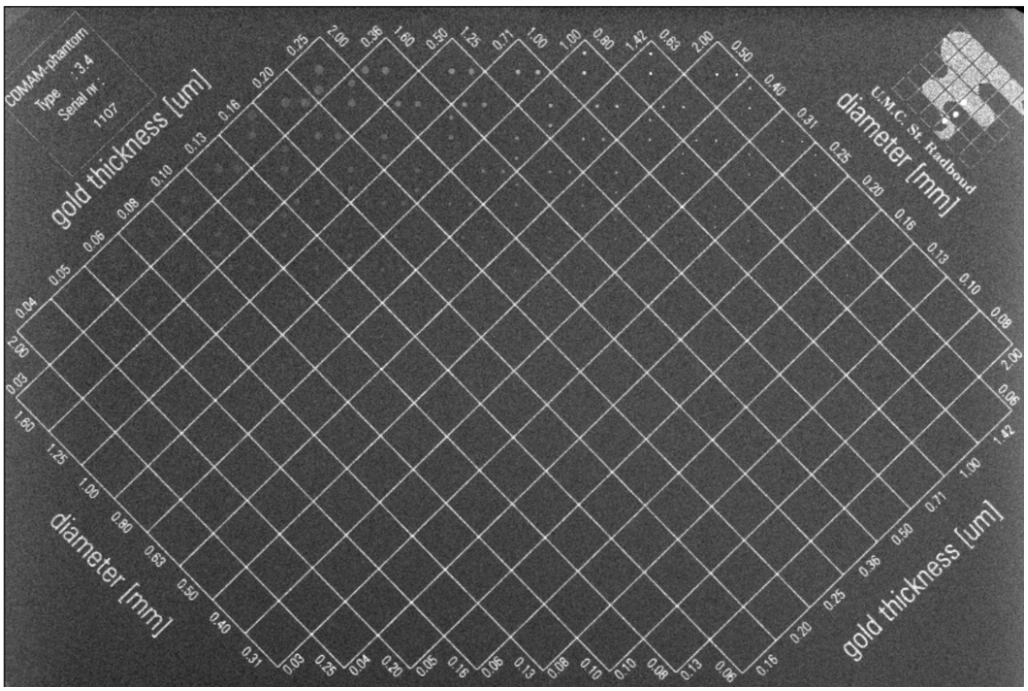

Figure 6.8: X-ray image of the CDMAM phantom.

Table 6.5: Description of the experimental set up, showing the combinations of thicknesses and X-ray settings for the images taken with and without grid.

x8 Images with grid (wG) and without grid (w/oG)			
Thickness (mm) [1]	**X-ray settings** Common settings	AEC wG	AEC w/oG
20	25 kV W/Rh (HVL = 0.490 mmAl)	47 mAs	N/A
30	26 kV W/Rh (HVL = 0.500 mmAl)	70 mAs	42 mAs
40	28 kV W/Rh (HVL = 0.520 mmAl)	95 mAs	50 mAs
50	31 kV W/Rh (HVL = 0.590 mmAl)	100 mAs	60 mAs
70	34 kV W/Ag (HVL = 0.500 mmAl)	120 mAs	55 mAs

[1] Equivalent PMMA thickness.

Both the CDMAM and the PMMA plates were rectangular in shape, of constant thickness and covered the detector active area. In consequence, only one kernel per thickness was needed. The kernel was simulated by including the phantom into the geometry and the processed scatter image was obtained by simply convolving the entire grid-less output image by the simulated kernel, as seen in Section 5.5.1. In the simulations, the phantom was simplified to a homogeneous aluminium base encased at the bottom of a 5 mm PMMA plate; the gold discs were not included.

The outcome of the CDCOM is a table that gives the minimum thickness that the gold discs need to have, as a function of the diameter, in order to be detected by a human reader. The values are compared with the achievable and acceptable threshold thickness, upper limits given by the CDMAM protocol. The processed images, i.e. scatter reduced, have been compared first with the grid-less unprocessed images (Figure 6.9) and then with the grid images, (Figures 6.10 and 6.11). Tables with the results are displayed in Appendix A (Tables A.2 to A.6).

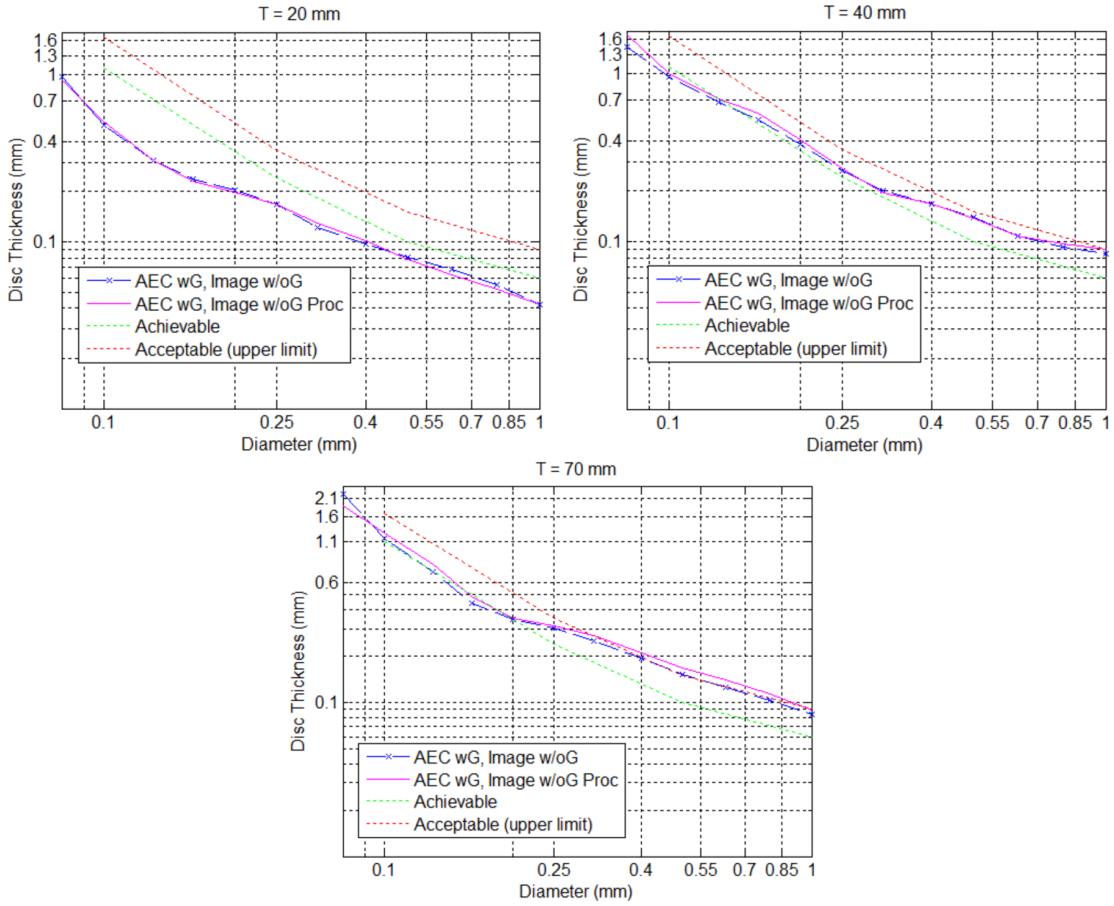

Figure 6.9: Representative examples of the CDCOM results obtained with the grid-less images before and after processing. The thickness/energy combinations of the top-left, top-right and bottom plots are 20 mm/AEC wG, 40 mm/AEC w/oG and 70 mm AEC wG respectively.

When comparing the unprocessed and processed grid-less images at different thickness levels, the results do not show any improvement by applying the scatter correction. As shown in the plots of Figure 6.9, there is no apparent dependency with the phantom thickness or the dose delivered. As the results are comparable across the different thickness and energy ranges used, three cases were chosen as representative examples:

- The top-left corner plot shows the results corresponding to the images acquired at the higher dose, selected by the system's AEC when the grid is in (AEC wG), for a

phantom thickness of 20 mm.

- The top-right corner plot shows the results corresponding to the images acquired at the lower dose, selected by the system's AEC when the grid is removed (AEC w/oG), for a phantom thickness of 40 mm.
- The bottom plot shows the results corresponding to the images acquired at the higher dose, AEC wG, for a phantom thickness of 70 mm.

When comparing the processed grid-less images with the grid images, the results show dependency with the thickness and the dose delivered. The data obtained at higher dose generally shows better contrast when the grid is used. However, the results are dependant on the thickness of both the gold disc and the PMMA. Figure 6.10 shows this variation, i.e. for thinner and thicker phantoms as well as for smaller disc diameters the difference is negligible.

When the dose is reduced by 39-54%, the difference between grid and grid-less images practically disappears, see Figure 6.11.

The pronounce fluctuation of the data and dependency with the dose and thickness indicates that contrast thresholding figure is not precise enough to allow the grid vs. grid-less comparison. Therefore, the CDMAM phantom is not a good match for the needs of this study. As previously reported by Bick et al. and Grosjean et al. (Bick and Diekmann, 2007; Grosjean and Muller, 2006), the lack of background structure in contrast-detail phantoms, and the narrow region of interest selected in the analysis, produces an overestimation in the detector's detection performance of larger low-contrast objects. In opposition, for the case of small detail discs (< 0.4 mm), the limitation is in the detector noise instead of the background.

The findings are in agreement with Binst et al.(Binst et al., 2015), who presented inconclusive results. Fieselmann et al. (Fieselmann et al., 2013), on the contrary, do claim to obtain positive results with their scatter-reduction method, when comparing the grid results against the processed grid-less images acquired with reduced doses. There are, however, several factors that need to be taken into account:

- It is not clear the amount of dose that Fieselmann et al. use when acquiring the grid images.
- The dose reduction that they report (11% to 35%) is smaller than the dose differences used in the current study (39% to 54%).
- The results reported by Fieselmann et al. are worse than the results obtained in the current study, see Figure 6.12 comparing the results obtained with grid images in both studies. However, it is not possible to perform a one for one comparison, as

the systems compared are different, i.e. Siemens and Hologic, and the chosen doses may also differ considerably.

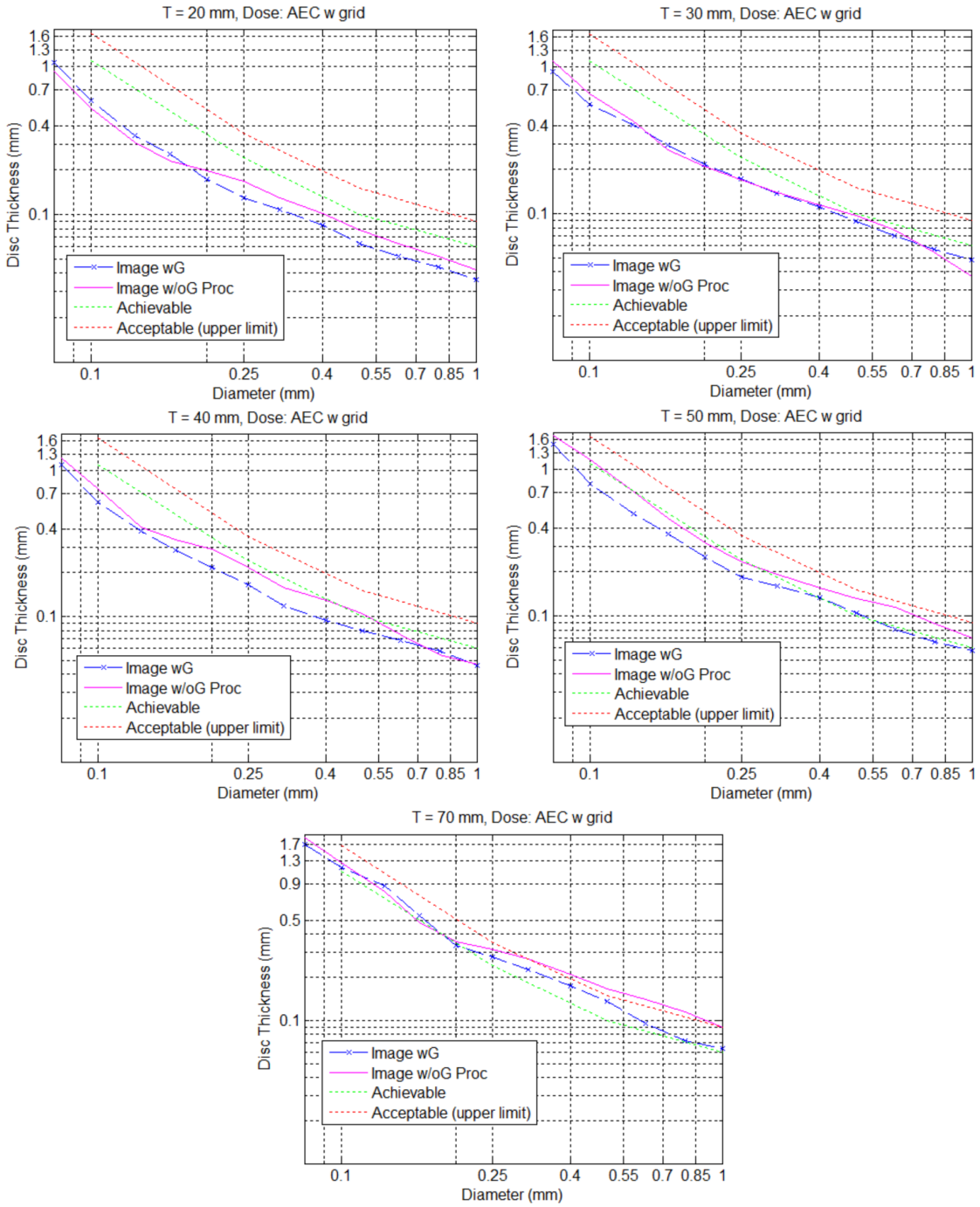

Figure 6.10: CDCOM results from the grid and processed grid-less images acquired with the higher dose settings (AEC wG). Each plot corresponds to one of the five thicknesses selected for this study.

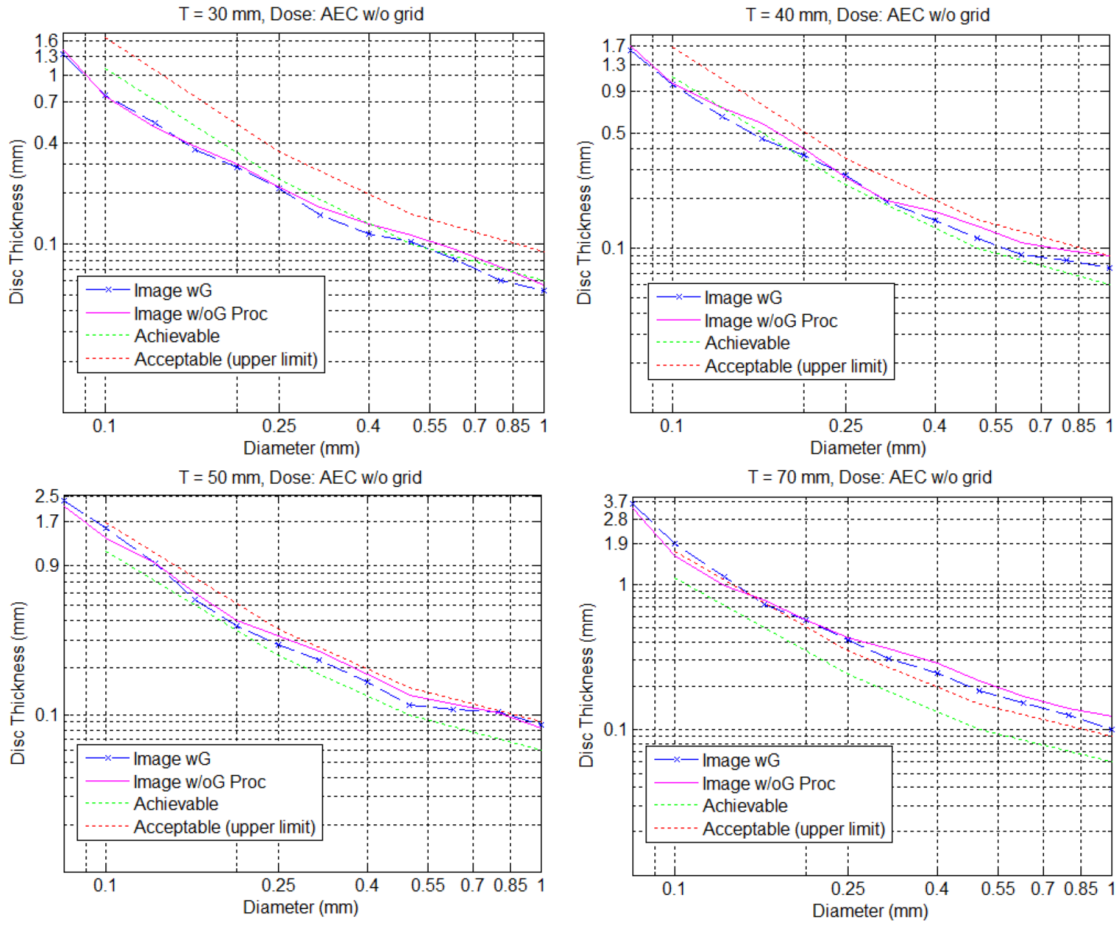

Figure 6.11: CDCOM results from the grid and processed grid-less images acquired with the lower dose settings (AEC w/oG). Each plot corresponds to one of the five phantom thicknesses selected for this study.

Considering the aforementioned differences between the studies, and how little the results change in between cases, the conclusion about the unsuitability of this phantom is still considered valid.

From the results obtained in this study it could be argued that, when comparing the grid performance with the "accepted" and "achievable" upper limits, the dose chosen by the system's AEC when the grid is in use is higher than needed as the values, of phantom thicknesses up to 50 mm, are considerably below the upper limits. This is outside the scope of the experiment and thus the image acquisition method was not optimised to evaluate the percentage of dose reduction, but the findings are in line with data previously published by Binst et al.(Binst et al., 2015) and Fieselmann et al. (Fieselmann et al., 2013).

Due to the inconclusive results obtained with the CDMAM phantom measurements, a different set of phantoms routinely used in the quality control of mammography systems

were included in this study. The phantoms chosen and results obtained are described in the sections below.

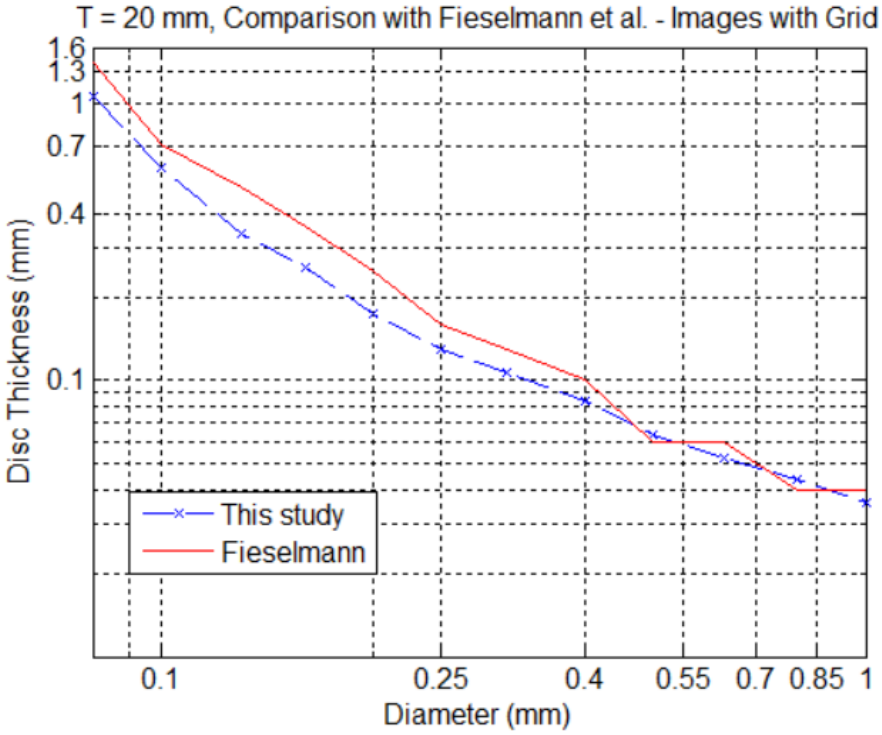

Figure 6.12: Comparison of the CDCOM results obtained in this study against the values presented by Fieselmann et al. (Fieselmann et al., 2013).

6.4.2 TOR-MAS and TOR-MAM phantoms

The TOR-MAS phantom from Leeds Test Objects (*TOR-MAS*) is generally used for routine quality control and aims to provide a quantitative and reproducible image quality test. The test object is an acrylic, i.e. PMMA, semi-circular plate of 11 cm radius and 1 cm thick that contains different types of testers, that allow the evaluation of the sharpness, contrast sensitivity, small detail visibility and noise of the system. The testers included in the phantom are: high-contrast resolution patterns, low-contrast linear and circular details, high-contrast small circular details, grey scale step wedge and micro-particle step wedge, see Figure 6.13-(a).

The aim of the TOR-MAS phantom is to provide quality control for units where the diagnostic effectiveness has already been established. The test images do not necessarily relate to diagnostic performance, as the correlation between technical and diagnostic image quality is not simple to predict. The TOR-MAM phantom complements the information given by the TOR-MAS by including a tester that, even though is more qualitative than quantitative, it is closer to real mammographic images: half of the semi-circle contains a

range of filament, particles and circular details while the other half simulates the appearance of breast tissue, containing micro-calcifications and fibrous and nodular details, see Figure 6.13-(b) (*TOR-MAM*).

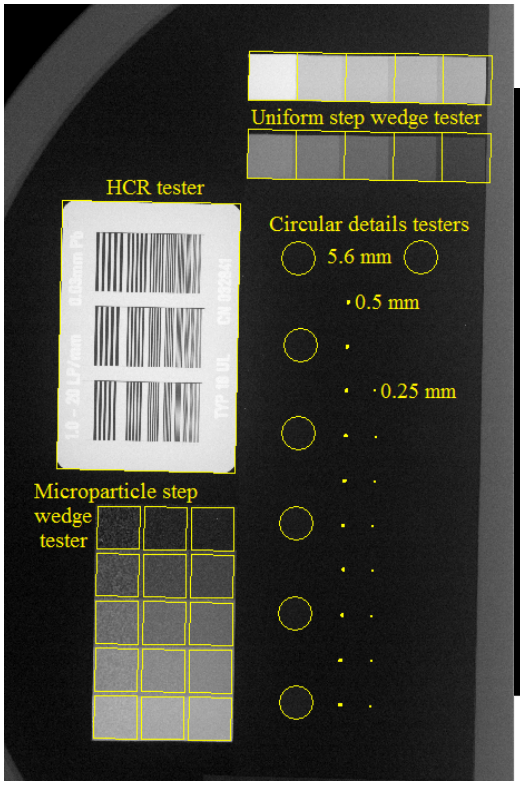

(a) TOR-MAS tester

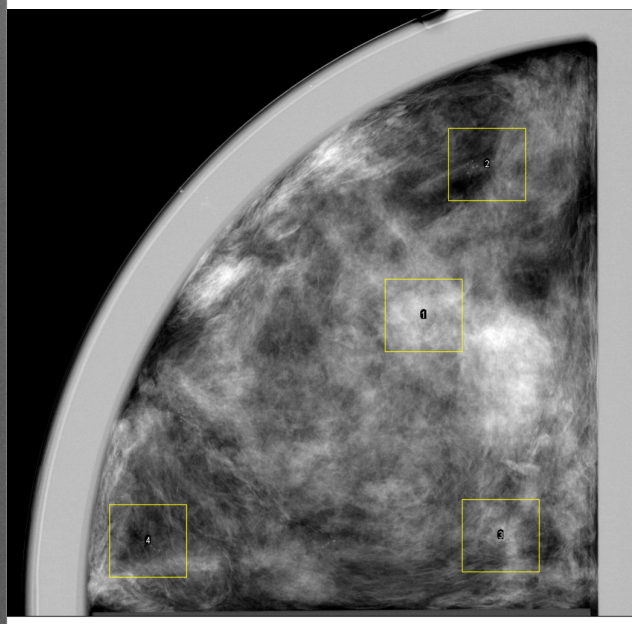

(b) TOR-MAM

Figure 6.13: On the left the figure shows a schematic of the different testers of the TOR-MAS phantom. On the right, the image shows the half of the TOR-MAM phantom that simulates the appearance of breast tissue; the four boxes highlight some of the areas where calcifications are placed.

In this study, both phantoms were used with a series of semi-circular PMMA plates that helped to provide a wider and more realistic range of equivalent breast thicknesses, absorptions and scatter coefficients to the final images. For each thickness, two energies were selected using the system's AEC mode when the grid was in use (AEC wG) and removed (AEC w/oG); the dose obtained when using the grid was 41 to 50% times higher. See Table 6.6 for more details of the thicknesses and X-ray settings chosen.

When applied to this study, the main drawback that these phantoms present is the heterogeneity and unknown composition of the testers' materials. The TOR-MAS phantom has thin metallic objects that considerably increase the scattering, while the half section of the TOR-MAM phantom that is made to simulate the breast tissue is composed by an unknown, not-breast tissue equivalent, polymer material. Due to the lack of information about the thickness and composition of the objects and the additional difficulty of adapting the scattering removal model to the different tester shapes, the analysis was

simplified to the known material that formed the tester backgrounds, i.e. PMMA. For each thickness, phantom and background kernels were simulated according to the needs of the method introduced in Section 5.6, method that was used to calculate the scatter image and, therefore, to obtain the predicted primary image. The geometry of the Hologic Lorad Selenia system was used in these simulations, see Section 5.3. The results obtained are presented below.

Table 6.6: The table shows the different thickness and energy combinations used in the study of the TOR-MAS and TOR-MAM phantoms. Two images were taken for each combination, with and without grid.

Images taken with grid (wG) and without grid (w/oG)			
Phantom	**X-ray settings**		
(Thick. mm)	Common settings	AEC wG	AEC w/oG
TOR-MAS (30)	26 kV W/Rh (HVL = 0.511 mmAl)	55.0 mAs	32.5 mAs
TOR-MAS (50)	28 kV W/Rh (HVL = 0.533 mmAl)	120.0 mAs	65.0 mAs
TOR-MAS (70)	27 kV W/Ag (HVL = 0.530 mmAl)	220.0 mAs	110.0 mAs
TOR-MAM (32)	26 kV W/Rh (HVL = 0.511 mmAl)	50.0 mAs	32.5 mAs
TOR-MAM (52)	28 kV W/Rh (HVL = 0.533 mmAl)	100.0 mAs	55.0 mAs

6.4.2.1 TOR-MAS

The consequences of the simplifications are mainly seen in the TOR-MAS phantom, where the scattering of the metallic structures contribute to the non-uniformity of the image. The general non-uniformity is improved between the unprocessed and the processed grid-less images, but it is worse when compared against the grid image, Figure 6.14 shows X-ray images obtained with a phantom thickness of 50 mm and the higher energy settings, obtained with the AEC when the grid was in use, (see AEC wG in Table 6.6).

Figure 6.15 shows the intensity profile across the central area of the phantom for the three examples presented in Figure 6.14. The grid-less processed image shows non-uniformity around the area where the central testers are, stabilising towards both extremes, while the profile taken with the grid image is completely flat. Although the non-uniformity is present in all the evaluated images, it worsens with the thickness of the phantom as illustrated in Figure 6.16.

The analysis of the TOR-MAS phantom was made using a software provided by Leeds Test Objects, AutoPIA (Automatic Phantom Image Analysis) (CyberQual, 2016; Leeds Test Objects, 2016), that provides reproducible and objective qualitative indices for image quality control. The analysis was made with the three thicknesses under study for both the processed grid-less and the grid images.

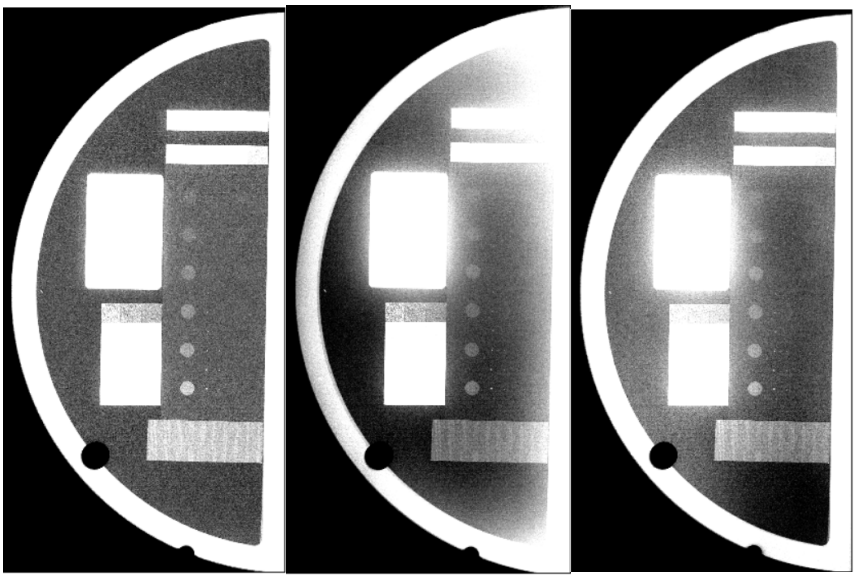

(a) Grid image **(b)** Grid-less image **(c)** Proc. grid-less image

Figure 6.14: Images acquired for a phantom of thickness T=50 mm and a dose given by the system's AEC when the grid was in. From left to right: grid image, grid-less unprocessed image and grid-less processed image.

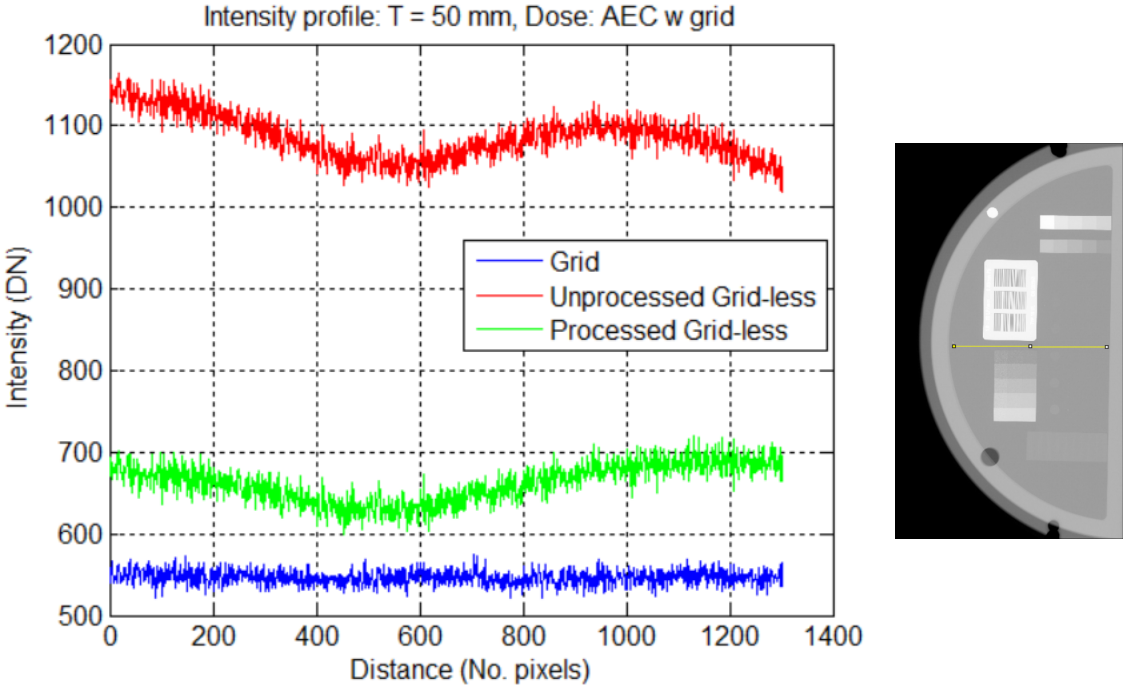

Figure 6.15: Intensity profile plot across the centre of the phantom (see image on the right) comparing the grid image and the grid-less unprocessed and processed images for a phantom thickness T=50 mm and a dose given by the system's AEC when the grid was in.

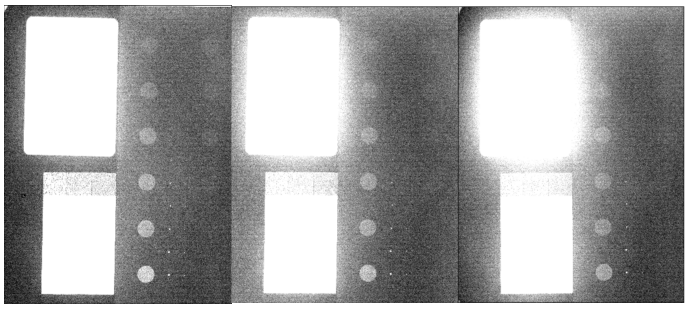

(a) T=30 mm **(b)** T=50 mm **(c)** T=70 mm

Figure 6.16: Processed grid-less images of increasing thickness, from left to right: 30, 50 and 70 mm, using a dose given by the system's AEC when the grid was in. The non-uniformity introduced by the testers worsens with the phantom thickness.

The different testers present in the TOR-MAS phantom and evaluated in this study are shown in Figure 6.13. The circular details were highly affected by the difference in the scattering introduced by the step wedge testers and, mainly, the HCR tester. The latter also affected the wedge testers in a smaller amount. The results obtained with the circular and microparticle step wedge testers, placed in areas that are highly affected by the non-uniformity, are dependent on the phantom thickness. For thinner phantoms, the results were better or comparable in the processed grid-less image case, while the grid images performed better as the thickness increased. The analysis methods and results provided by AutoPIA are:

- Circular detail testers:

  The analysis that AutoPIA provides to evaluate the visibility of the circular detail testers are the Contrast to Noise Ratio (CNR) for the bigger details, i.e. 5.6 mm, and the Detail Compacted Contrast (DCC) for the smaller testers, i.e. 0.5 and 0.25 mm. Figures 6.17 to 6.19 compare the results obtained for images with grid and without grid after processing, using the two chosen energy settings shown in Table 6.6 at two thicknesses levels (30 mm and 70 mm).

  The three circular detail testers show similar dependencies with the thickness. As expected by the thickness dependent non-uniformity explained above, see Figure 6.16. Thinner phantoms show comparable or improved results for the grid-less processed image. However, as the thickness increases the results show better performance when the grid is in use. The plots show the two extreme cases (T = 30 mm and T = 70 mm), at a 50 mm thickness the results already favour the grid images over the processed grid-less.

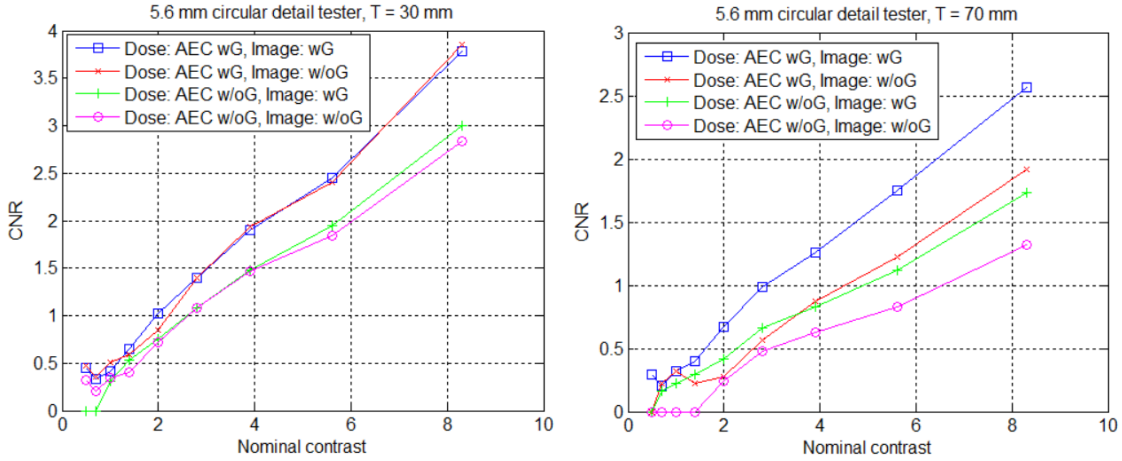

Figure 6.17: Analysis of the 5.6 mm circular detail tester. The plots show the CNR versus the nominal contrast for the grid and processed grid-less images acquired with the two dose settings at thicknesses 30 and 70 mm (left and right respectively).

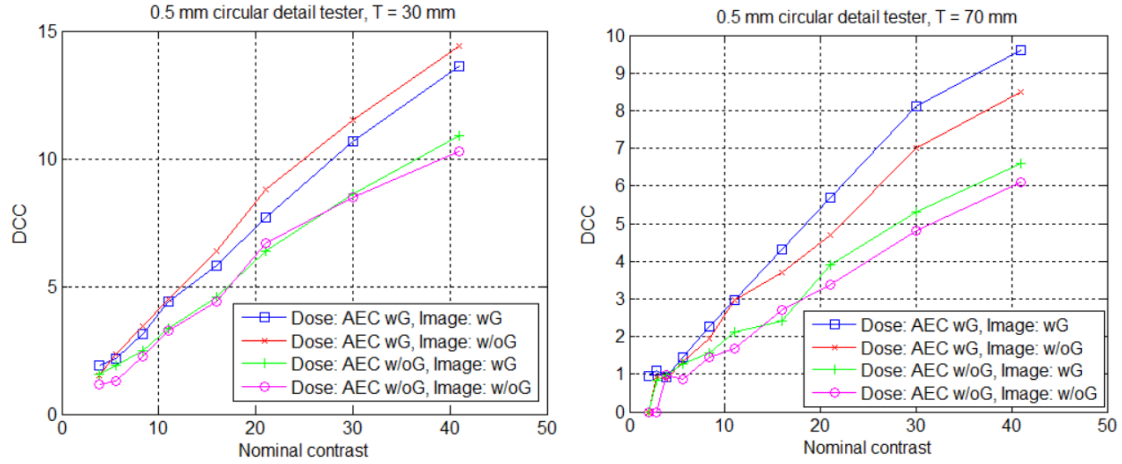

Figure 6.18: Analysis of the 0.5 mm circular detail tester. The plots show the DCC versus the nominal contrast for the grid and processed grid-less images acquired with the two dose settings at thicknesses 30 and 70 mm (left and right respectively).

- Microparticle step wedge tester:

  AutoPIA's analysis of the microparticle step wedge tester is performed by calculating the variance ratio between each step and a reference value that is always kept constant (taken from the uniform step wedge tester). The results comparing the variance ratio versus the tester's nominal contrast for the 30 and 70 mm images are given by Figures 6.20 and 6.21. The former plot refers to the smaller particle size of the tester (125 μm, right column of the tester) and the latter to the bigger particle size (328 μm, left column of the tester).

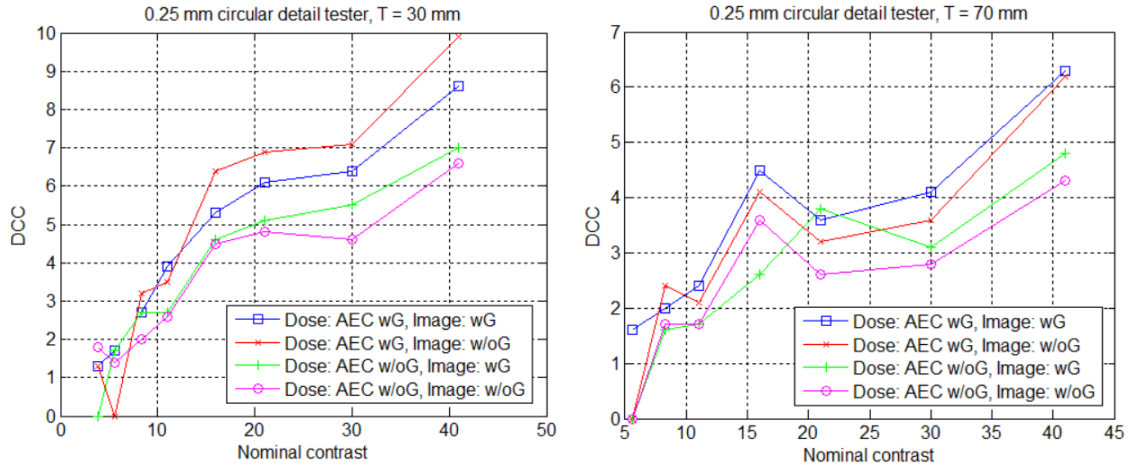

Figure 6.19: Analysis of the 0.25 mm circular detail tester. The plots show the DCC versus the nominal contrast for the grid and processed grid-less images acquired with the two dose settings at thicknesses 30 and 70 mm (left and right respectively).

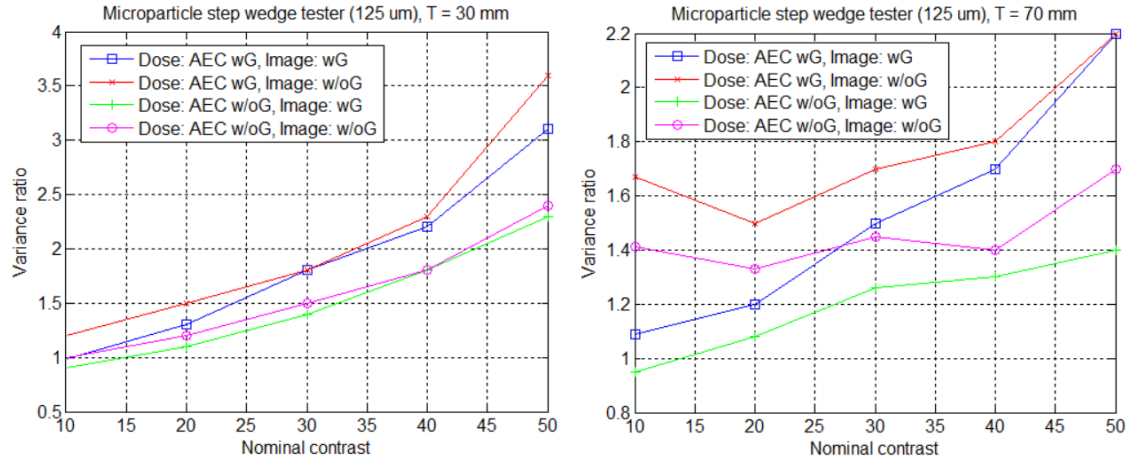

Figure 6.20: Analysis of the microparticle step wedge tester for particle size of 125 µm. The plots show the variance ratio versus the nominal contrast for the grid and processed grid-less images acquired with the two dose settings at thicknesses 30 and 70 mm (left and right respectively).

As shown in the plots, the processed grid-less image performs better than the grid image for the smaller particle size in the tester, independently of the phantom's thickness. As the particle size increases, the results become thickness dependent, similarly to the circular detail tester: thinner breasts perform better with the processed grid-less image while thicker breasts favour the grid images. The processed image improves in response at smaller nominal contrast, the area that is further away from the HCR tester and is, therefore, less affected by the non-uniformity. For lower doses, i.e. dose given by the AEC when the grid is removed, the results become comparable and do not show dependency with the thickness.

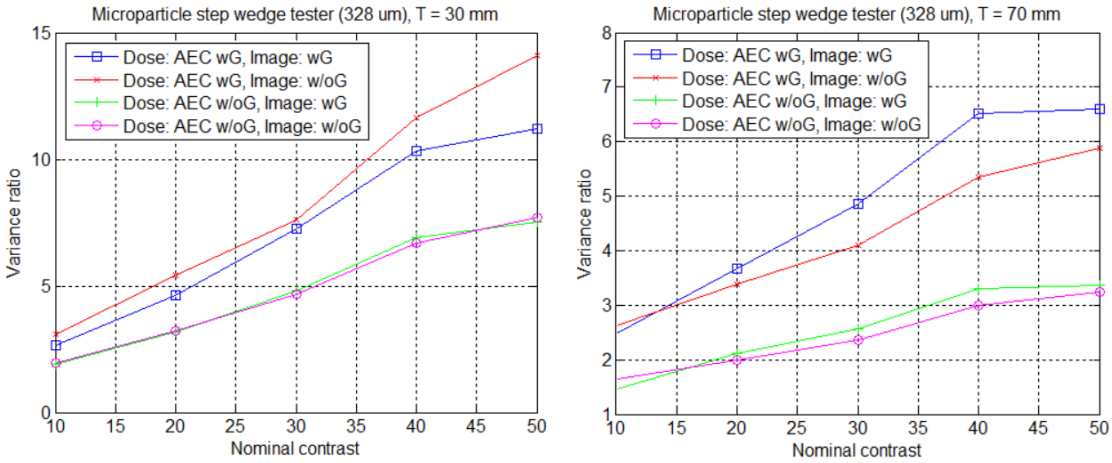

Figure 6.21: Analysis of the microparticle step wedge tester for particle size of 328 µm. The plots show the variance ratio versus the nominal contrast for the grid and processed grid-less images acquired with the two dose settings at thicknesses 30 and 70 mm (left and right respectively).

- Uniform step wedge tester:

  The uniform step wedge tester is analysed by measuring the relative contrast between the steps and the background, taken from the area surrounding the tester. The results obtained are consistent for the three thicknesses and two energies tested (see Table 6.6): the processed grid-less image performs better than the grid image. Figure 6.22 shows the results of T=50 mm as an example. The curves correspondent to the processed grid-less images acquired with high and low doses, have higher relative contrast at all points than the curves obtained with the grid images.

  It can be seen in the plot that the relative contrast decreases with the dose. This degradation is specially pronounced when using the grid, showing a maximum discrepancy of 36%, when comparing the two doses. In the processed grid-less images however, the maximum discrepancy is not bigger than 8%.

- High contrast resolution grid (HCR) tester:

  The HCR tester allows to measure the modulation transfer function (MTF) of the system. The results obtained are again in favour of the processed grid-less images and consistent for all thicknesses and energies used. Figure 6.23 shows the results of the 50 mm thick phantom, as an example.

  The small improvement seen in the spatial resolution of the processed images is in line with the theoretical expected results. The simulations used in the calculation of the kernels include different layers of the detector itself, accounting for some of the scattering produced after the surface of the detector. An improvement that cannot be achieved by only the use of the grid.

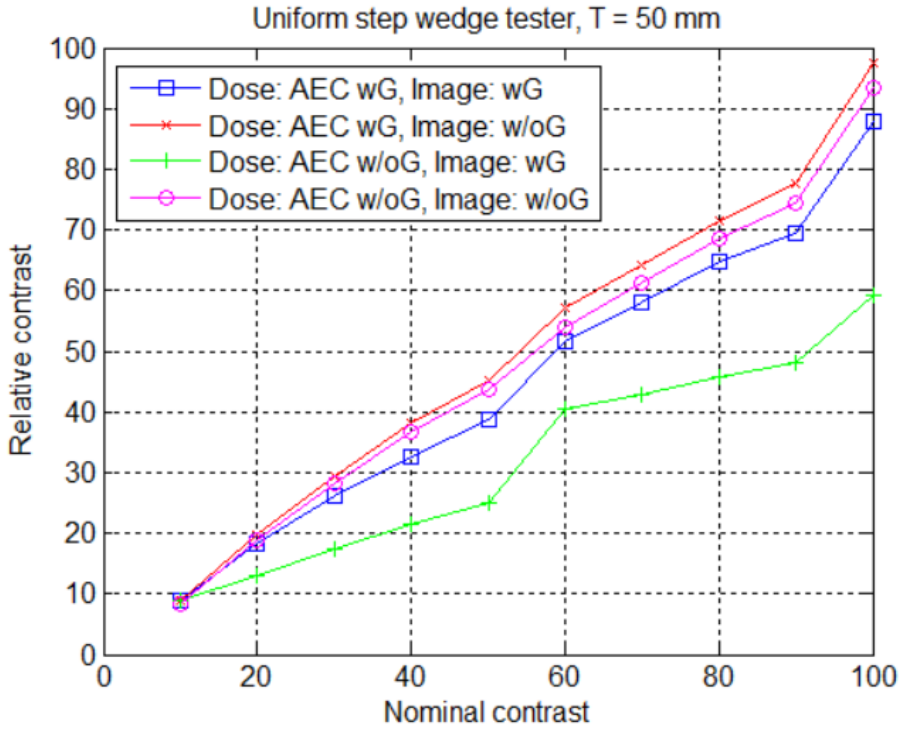

Figure 6.22: Analysis of the uniform step wedge tester. The plot show the relative contrast versus nominal contrast for the grid and processed grid-less images acquired with the two dose settings at thickness T=50 mm.

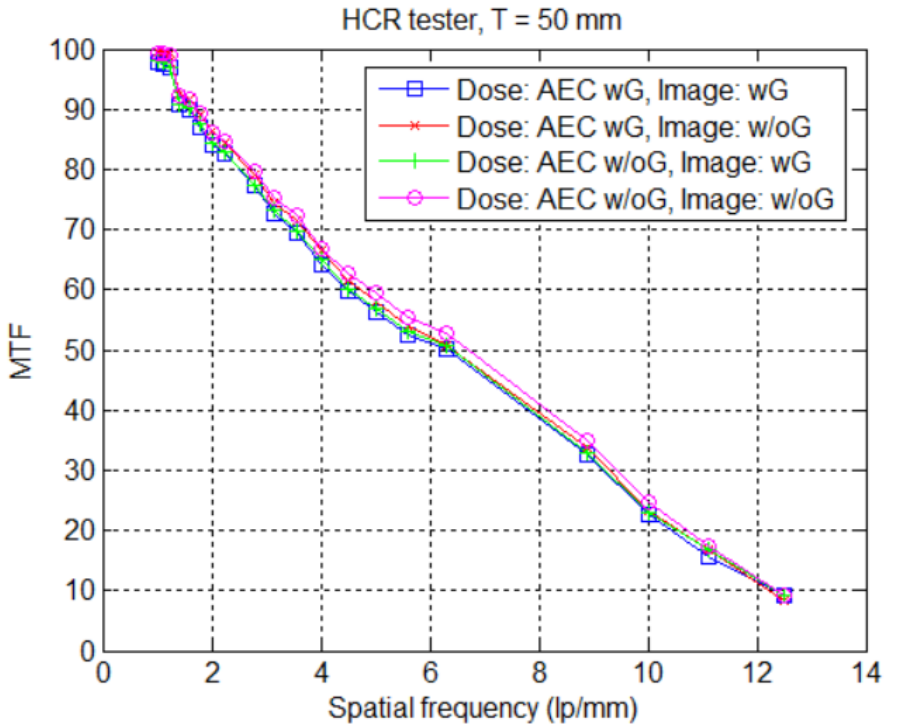

Figure 6.23: Analysis of the HCR tester. The plot show the MTF versus spatial frequency for the grid and processed grid-less images acquired with the two dose settings at thickness T=50 mm.

For more information refer to Appendix A, where Tables A.7 to A.24 show the data that has been illustrated in this section.

6.4.2.2 TOR-MAM

The visually realistic area of the TOR-MAM phantom adapted better to the needs of this study. Even though the composition of the phantom does not correspond to equivalent breast tissue values and the simulations were made by simplifying the phantom to a PMMA block, the unknown material did not present abrupt changes in the scattering as it covered the whole area of the phantom, contributing to a more homogeneous response.

The AutoPIA software does not include analysis tools for the visually realistic area of this phantom. Therefore, the analysis in this study has been made using the Contrast to Noise Ratio value, see equation 6.1.

$$\mathrm{CNR} = \frac{\bar{x}_D - \bar{x}_{Bckg}}{\sigma_{Bckg}} \tag{6.1}$$

where,

$\bar{x}_D$ = mean pixel value of the detail ROI

$\bar{x}_{Bckg}$ = mean pixel value of the background ROI

σ_{Bckg} = standard deviation of the background ROI

The chosen analysis method also faced challenges that were related to the phantom texture, as it was not possible to find a homogeneous area to take as a reference background value. In consequence, an area close to the calcifications was chosen and kept constant among the grid and processed grid-less images to obtain a fair comparison. The chosen calcifications are the ones highlighted in yellow boxes of Figure 6.13-right. The CNRs obtained for each one of the settings chosen in this study (refer to Table 6.6) are shown in Table 6.7. Negative CNR values indicate a ROI signal level lower than the background, they appear as whiter areas in the images. Figure 6.24 shows a zoom of the TOR-MAM calcifications for the grid and processed grid-less X-ray images, acquired at the higher dose (AEC wG) with the 32 mm phantom. On the right side of the image, the Region of Interest (ROI) chosen for the sensitive area (calcifications) and background area are shown in each of the four examples selected.

The results obtained were consistently in favour of the processed grid-less procedure. As seen in Table 6.7, the only example that favoured the use of the grid is ROI 4 with the 52 mm thick phantom. All the remaining combinations had higher CNR with the processed grid-less image. However, the fluctuation found was too high to be able to

choose between methods. If several backgrounds areas are taken around the object in order to perform a Student's T-test (to compare the grid vs. processed grid-less CNR results), the p-values obtained show that the results are not statistically significant (p-value > 10% for every one of the cases).

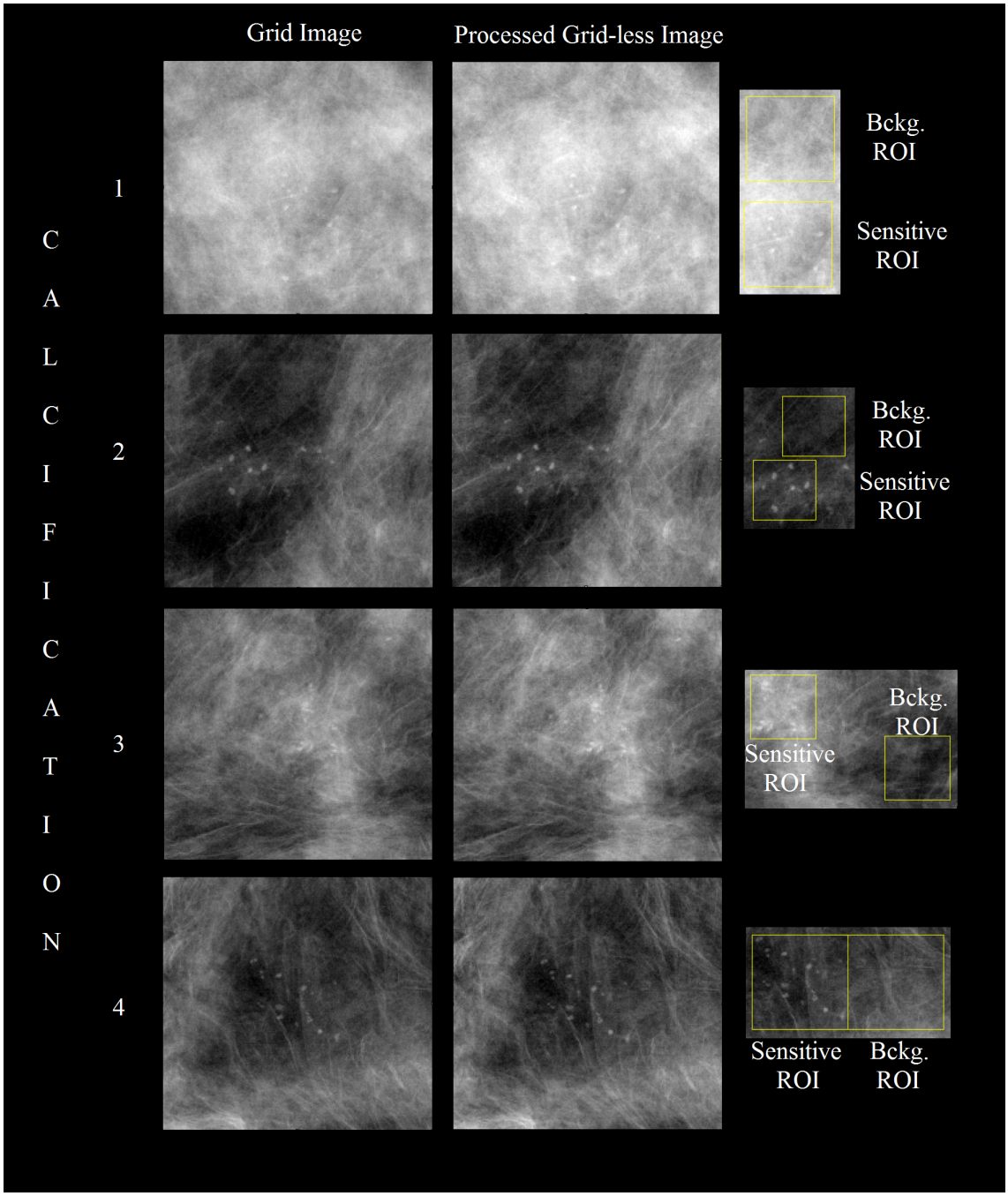

Figure 6.24: The figure shows the calcification areas of the 32 mm TORMAM phantom comparing the grid and processed grid-less images acquired at the higher dose (AEC wG). Highlighted on the right are the ROI areas chosen for the CNR calculations.

Table 6.7: The table gives a comparison of the contrast to noise ratio values of four ROI areas of the images acquired with the grid, grid-less and processed grid-less methods. The values shown include all the combinations described in Table 6.6.

CNR							
Calc.	**Thick. (mm)**	**AEC without grid**			**AEC with grid**		
		Grid	Without grid		Grid	Without grid	
			Unproc.	Proc.		Unproc.	Proc.
1	**32**	-0.88	-0.86	**-0.92**	-0.85	-0.81	**-0.88**
	52	-0.60	-0.50	**-0.64**	-0.58	-0.48	**-0.64**
2	**32**	-1.49	-1.20	**-1.53**	-1.37	-1.12	**-1.43**
	52	-1.23	-0.88	**-1.50**	-1.08	-0.69	**-1.22**
3	**32**	-6.23	-5.86	**-6.25**	-6.02	-5.64	**-6.04**
	52	-5.37	-4.49	**-5.50**	-5.08	-4.23	**-5.19**
4	**32**	1.25	1.20	**1.36**	1.20	1.14	**1.30**
	52	**1.16**	1.08	1.11	**1.11**	0.99	1.05

6.4.3 CIRS phantom

The CIRS object is a tissue-equivalent anthropomorphic breast phantom from CIRS Inc - Tissue Simulation and Phantom Technology (*CIRS*). The model used, 010A, simulates the shape of a compressed 50 mm thick breast, composed by a 5 mm thick adipose tissue-equivalent layer, i.e. skin, that surrounds a 40 mm thick block made of 30% / 70% Glandular/Adipose equivalent tissue. There are different test objects simulating calcifications, fibrous ducts and tumour masses embedded in the phantom. Except one of the test objects, a line pair target for measuring spatial resolution, the rest of the testers are breast tissue equivalent, either imitating calcifications or varying the percentage of glandular-adipose tissue, see Figure 6.25 and Table 6.8 for more information. In the phantom simulation, the testers were not taken into account, approximating the object to an homogeneous background of 30% glandularity.

Table 6.8: Information of the composition and size of the CIRS testers used in this study: Step wedge, circular details and calcifications testers.

Tester	Detail no.	Composition	Size (mm)
Step wedge	1 to 5	Glandular (%): 0, 30, 50, 70, 100	N/A
Circular details	1 to 7	55% Glandular 45% adipose	4.76, 3.16, 2.38, 1.98, 1.59, 1.19, 0.90
Calcifications	1 to 12	N/A	0.130, 0.165, 0.196, 0.230, 0.275, 0.400, 0.230, 0.196, 0.165, 0.230, 0.196, 0.165

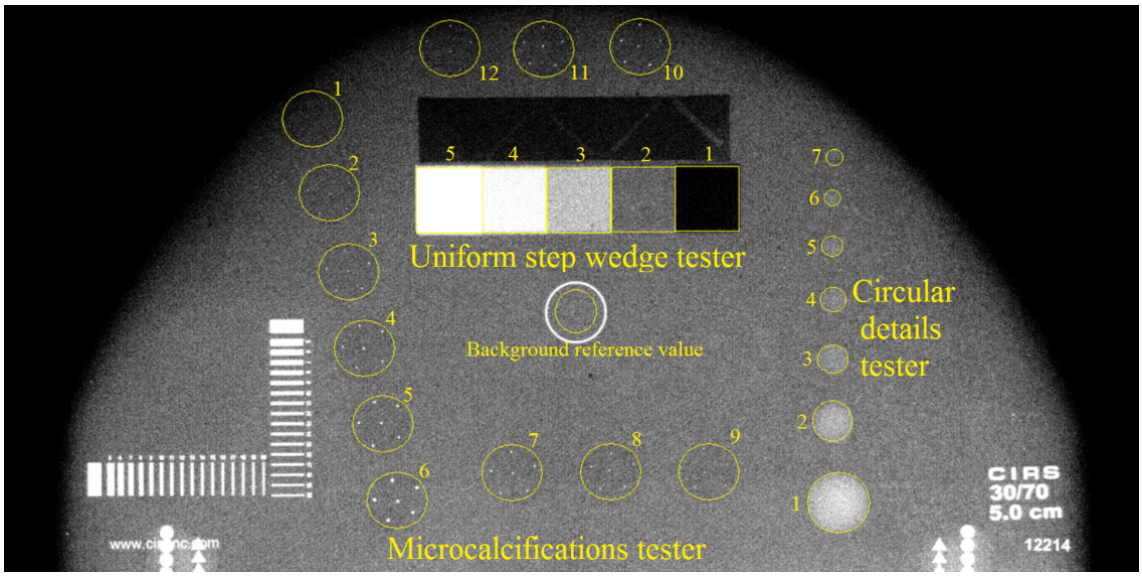

Figure 6.25: X-ray image of the CIRS phantom. The testers used in the analysis of this study are highlighted in the image: Uniform step wedge tester, circular details tester and microcalcifications tester.

This phantom is not intended to be used in combination with PMMA plates, so only one thickness, 50 mm, was evaluated at two different doses, selected by the system's AEC when the grid was in place (AEC wG) and removed (AEC w/oG): 28 kV W/Rh (HVL=0.533 mmAl) 100 and 55 mAs respectively. Two images were acquired for both doses, with and without grid. The latter was post-processed to remove the estimated scatter produced in the system. The geometry of the Hologic Lorad Selenia, as described in Section 5.3 and illustrated in Figure 5.6-right, was simulated with and without the presence of the phantom, to obtain the phantom and background kernels, according to the needs of the method introduced in Section 5.6.

The uniformity, Contrast to Noise Ratio (CNR) and variance ratio were the methods used for the analysis of the three testers chosen, see equations 6.1 and 6.2. The results obtained are shown and compared below.

$$\text{VarianceRatio} = \frac{\sigma_D^2}{\sigma_{Bckg}^2} \tag{6.2}$$

where,

σ_D^2 = variance of the detail ROI

σ_{Bckg}^2 = variance of the background ROI

6.4.3.1 Uniformity

The main non-uniformity, introduced by the absence of grid in the system, is located in the horizontal direction of the phantom, i.e. from the chest-wall to the breast edge. The post-processing scattering correction suggested in this study allows to recover the uniformity of the image in this direction. Figure 6.27 shows the intensity profile across the horizontal direction of the phantom, comparing the grid image with the unprocessed and processed grid-less images, for the two energies tested. Figure 6.26-left indicates the area of the phantom where the horizontal and vertical profiles were taken.

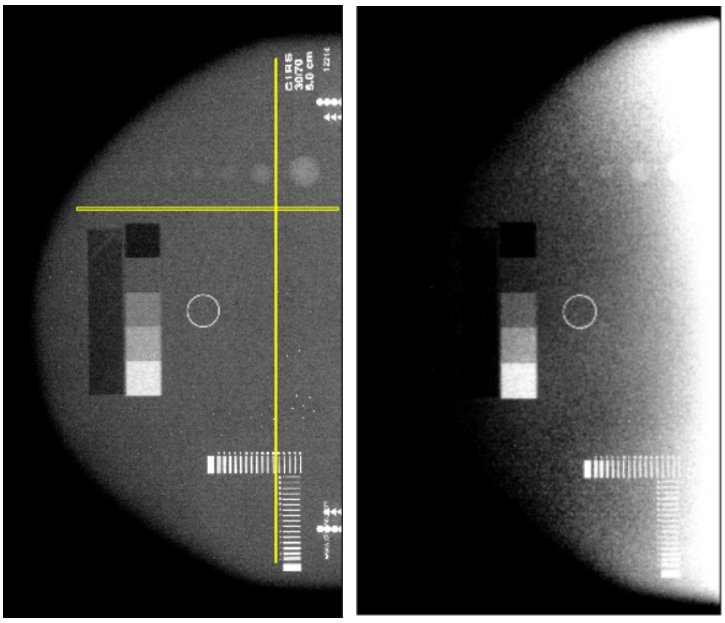

Figure 6.26: The image on the left highlights in yellow the areas used for the analysis of the phantom uniformity in the vertical and horizontal directions. On the right, the image shows an asymmetry of the scatter distribution seen in those images acquired without a grid.

The total non-uniformity is comparable for both cases, even though the shape of the processed grid-less image seems more variable in the profile plot. Using the peak to peak variation as a definition of the non-uniformity, the difference between grid and grid-less images (for both doses analysed) is of 2 Digital Numbers (DN), value that is below the noise floor.

The intensity profile of the unprocessed grid-less images in the vertical direction is almost as flat as the grid image. However, the images acquired without the grid show an asymmetry in the intensity level on the top area of the image, as illustrated in Figure 6.26-right and in the plots of Figure 6.28. This is likely to be linked to a problem in the grid-less gain correction (the gain correction was applied when the images were acquired at the hospital). The scatter correction model applied in this study assumes that changes in the scattering are linked to physical variations of the phantom. Therefore

the predicted grid-less image did not correct completely for this artificial non-uniformity, as it can be appreciated in Figure 6.28, where an additional 20 DN is introduced to the overall non-uniformity.

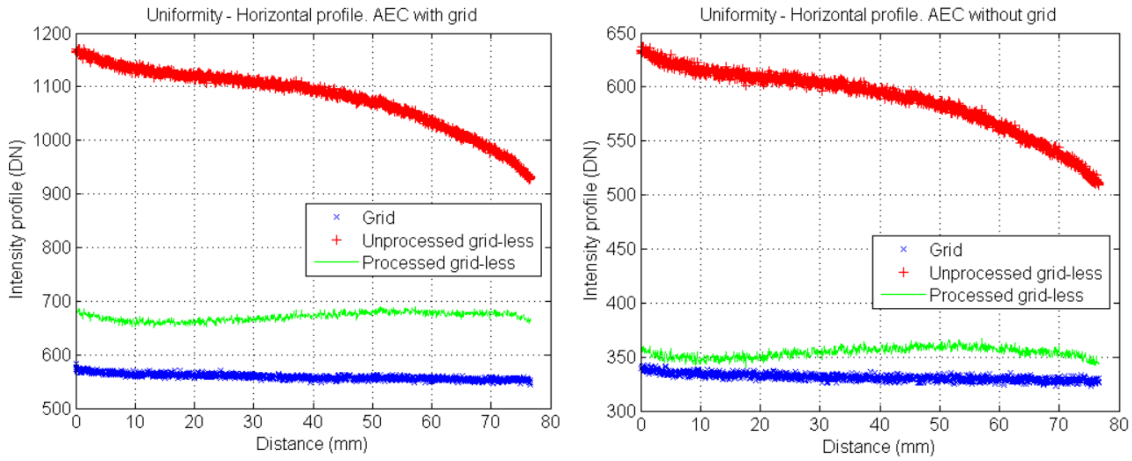

Figure 6.27: Intensity profiles in the horizontal direction of the phantom, comparing grid images against processed and unprocessed grid-less images at the two energies studied (AEC wG on the left and AEC w/oG on the right).

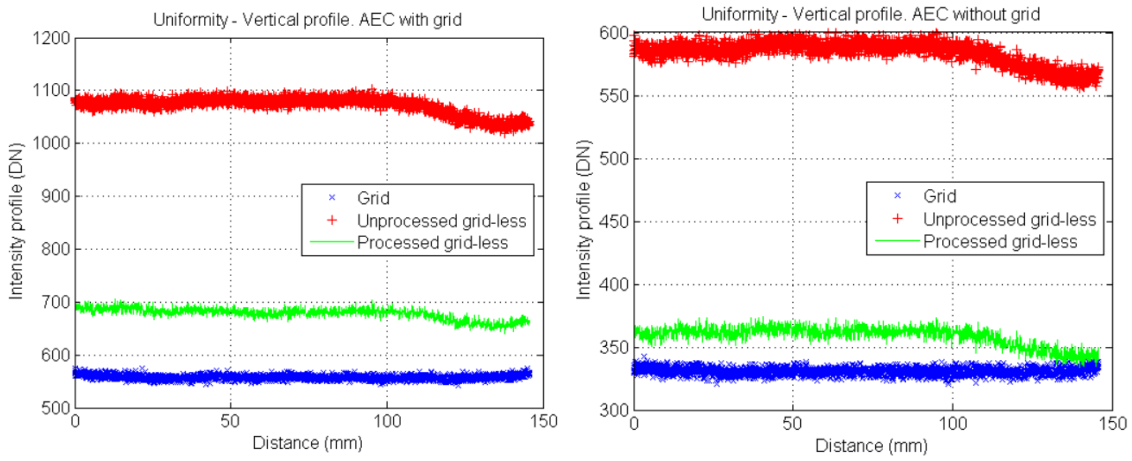

Figure 6.28: Intensity profiles in the vertical direction of the phantom, comparing grid images against processed and unprocessed grid-less images at the two energies studied (AEC wG on the left and AEC w/oG on the right).

6.4.3.2 Uniform step wedge tester

The evaluation of the uniform step wedge tester was performed by calculating the CNR of each detail, see equation 6.1. The background values were taken from the background reference point highlighted in Figure 6.25.

The results obtained are shown in Table 6.9 and Figure 6.29. The processed grid-less image performs worse than the grid image for the detail that has higher percentage of

adipose tissue than the background, i.e step number 1 in Figure 6.25, where the change in material introduces an area with more scattering, more absorption and higher signal than the background (positive CNR). In this case, the model does not reproduce the total amount of scattering, leading to smaller CNR values. When the proportion of glandular tissue increases, step numbers 3 to 5, the process is inverted (negative CNR). The model performs better than the grid for these cases. The glandularity used in the simulation of the phantom, 30%, is equivalent to the step number 2, so the CNR in this case should be close to zero. The grid example gives more accurate results in this case, this is likely related to the difference in scattering that arrives from the neighbouring testers.

Table 6.9: Average CNR values calculated in each step of the step wedge tester for grid and processed grid-less images acquired at two energies. The standard deviation of the measurements is shown in brackets (σ).

CNR - Step wedge tester						
Step no.	**AEC with grid**			**AEC without grid**		
	Grid (σ)	Proc. (σ)	<p> (%)	Grid (σ)	Proc. (σ)	<p> (%)
1	3.66 (0.02)	3.01 (0.09)	0.28	2.69 (0.01)	2.19 (0.01)	0.01
2	0.06 (0.01)	-0.24 (0.08)	1.07	0.08 (0.01)	-0.17 (0.01)	0.01
3	-2.32 (0.01)	-2.49 (0.08)	3.62	-1.70 (0.01)	-1.72 (0.01)	0.98
4	-4.71 (0.02)	-5.10 (0.10)	0.87	-3.45 (0.01)	-3.68 (0.01)	0.01
5	-8.56 (0.03)	-8.86 (0.08)	0.57	-6.27 (0.03)	-6.50 (0.04)	0.13

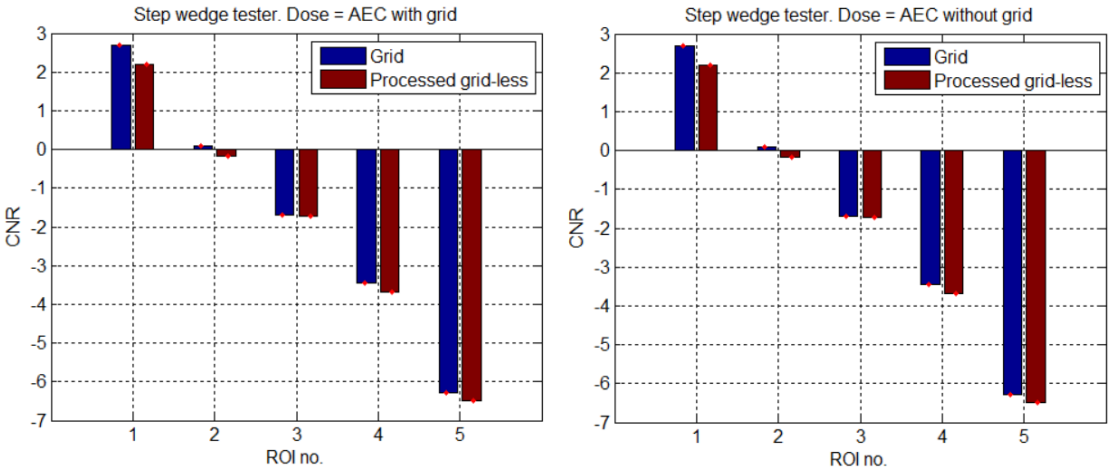

Figure 6.29: Bar plot of the CNR results of Table 6.9. The grid images are compared against the processed grid-less images at a higher (left plot) and lower (right plot) doses. The standard deviation of the measurements is shown in the error bars.

The results obtained are reproducible at both energies. For each case, the analysis was repeated three times to gain statistics, by selecting different ROI sizes inside the details of the testers, i.e. one as big as the tester, a medium ROI and a smaller one, all centred in the tester. The results presented are an average of the measurements, the errors

were obtained by calculating the standard deviation of the three measurements. In addition, a Student's T-test was performed to study the statistical significance of the grid vs. processed grid-less comparison. The null hypothesis considered was that the two measurements were not differentiable and a 5% significance level was chosen. The p-values obtained are all below the chosen limit, as shown in Table 6.9, indicating that the comparison is statistically significant.

6.4.3.3 Circular details tester

The circular details tester was evaluated using the CNR measurements, in a similar way to the step wedge tester. Table 6.10 and Figure 6.30 show the results obtained in the analysis.

Table 6.10: Average CNR values calculated in each detail of the circular detail tester for grid and processed grid-less images acquired at two energies. The standard deviation of the measurements is shown in brackets (σ).

CNR - Circular detail tester						
Detail no.	**AEC with grid**			**AEC without grid**		
	Grid (σ)	Proc. (σ)	<p> (%)	Grid (σ)	Proc. (σ)	<p> (%)
1	-2.64 (0.09)	**-2.69** (0.03)	21.61	**-1.96** (0.04)	-1.90 (0.04)	9.01
2	**-1.62** (0.04)	-1.41 (0.01)	0.26	**-1.16** (0.03)	**-1.16** (0.03)	46.38
3	**-0.77** (0.01)	-0.62 (0.01)	0.07	-0.60 (0.01)	**-0.69** (0.01)	0.01
4	-0.47 (0.03)	**-0.59** (0.06)	2.71	-0.36 (0.02)	**-0.72** (0.02)	0.01
5	-0.29 (0.03)	**-0.77** (0.02)	0.01	-0.30 (0.03)	**-1.11** (0.01)	0.02
6	-0.10 (0.05)	**-0.64** (0.03)	0.02	0.02 (0.04)	**-1.30** (0.06)	0.01
7	0.43 (0.01)	**-0.40** (0.04)	0.04	0.15 (0.03)	**-1.25** (0.02)	0.01

The higher CNR values obtained with the biggest details, numbers 1 to 3 in Figure 6.25, oscillate between the grid and the processed grid-less image, leaning in favour of the grid image. For the smaller and more difficult to detect details, the processed grid-less image gives higher CNR values for all details and doses. However, the results obtained with the two last details, numbers 6 and 7, are unrealistically high in the processed image. These details are placed closer to the edge of the phantom where the non-uniformity increases, making the CNR measurement less precise. The results presented are the average of three separate measurements, where the ROIs were re-defined each time. The errors shown correspond to the standard deviation of the three measurements. A Student's T-test was performed, again considering as a null hypothesis that the two values were not differentiable and a 5% of significance level. The p-values obtained show that that the CNR differences between grid and processed grid-less images are statistically significant, except in the first (and second in the lower dose case) detail, where the CNR values are therefore comparable.

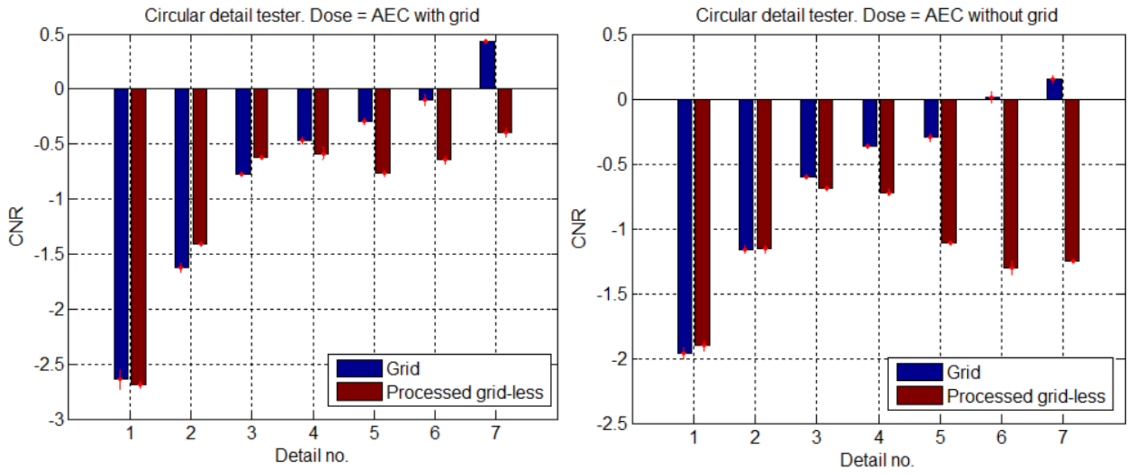

Figure 6.30: Bar plot of the CNR results of Table 6.10. The grid images are compared against the processed grid-less images at a higher (left plot) and lower (right plot) doses. The standard deviation of the measurements is shown in the error bars.

This tester is placed in the area affected by the vertical non-uniformity of the phantom. The CNR results are likely to be considerably affected by this issue leading to an unreliable comparison.

6.4.3.4 Microcalcifications tester

For this last tester it was not possible to use the CNR metric, as the fluctuations in the results made this measurement unreliable. The variance ratio was chosen instead, see equation 6.2. The results obtained, shown in Table 6.11 and Figure 6.31, were less noisy and more stable.

Each detail of the microcalcification tester has 6 dots of the same thickness, 5 concentric microparticles and an additional one in the centre, as shown in Figure 6.25. To gain statistics, the detail variance (σ_D^2 in the equation) was measured for the six microparticles. The results presented were obtained from the average of the six measurements. The error was calculated from their standard deviation and a Student's T-test was performed, assuming as a null hypothesis the no differentiation of the measurements and choosing the significance level for values smaller than the 5%.

At the higher dose, i.e. AEC with grid, the results were comparable for both cases, grid and processed grid-less images. The higher variance ratio fluctuates between both images, independently of the size of the microparticles. The p-value indicates that the differences are not statistically significant. The performance at lower doses, although close together and within the measurement error, is in favour of the grid images. The higher

background noise of the processed images seems to affect the variance ratio evaluation in this case as the detection of microcalcifications is noise limited.

Table 6.11: The table gives the values of the variance ratio for the different details of the calcifications tester, for the grid and processed grid-less images acquired at two different doses; the standard deviation of the six measurements is stated inside the brackets (σ).

Variance ratio - Microcalcifications tester						
Detail no.	**AEC with grid**			**AEC without grid**		
	Grid (σ)	Proc. (σ)	<p> (%)	Grid (σ)	Proc. (σ)	<p> (%)
1	Not visible					
2	**2.38** (0.38)	2.34 (0.42)	43.3	**1.89** (0.32)	1.78 (0.33)	1.2
3	3.40 (0.36)	**3.47** (0.25)	36.2	**2.05** (0.35)	1.91 (0.34)	0.8
4	**5.82** (2.19)	5.53 (2.25)	41.6	**3.59** (1.50)	3.57 (1.16)	0.5
5	**10.51** (1.98)	10.25 (1.93)	41.4	**6.04** (1.32)	5.67 (1.13)	0.1
6	**18.77** (5.03)	18.23 (4.89)	42.6	**10.99** (2.63)	9.94 (2.59)	0.1
7	5.66 (1.43)	**5.73** (1.33)	47.4	**3.61** (0.89)	3.32 (0.80)	0.3
8	3.26 (0.47)	**3.28** (0.55)	46.8	**2.32** (0.50)	1.97 (0.29)	0.5
9	**1.84** (0.54)	1.83 (0.52)	48.8	**1.54** (0.41)	1.32 (0.29)	25.0
10	4.10 (1.57)	**4.25** (1.28)	44.8	**2.88** (0.67)	2.69 (0.73)	0.8
11	3.02 (0.64)	**3.14** (0.86)	38.3	**2.28** (0.32)	2.15 (0.55)	1.8
12	**2.08** (0.52)	2.00 (0.56)	41.9	**1.66** (0.39)	1.36 (0.30)	26.3

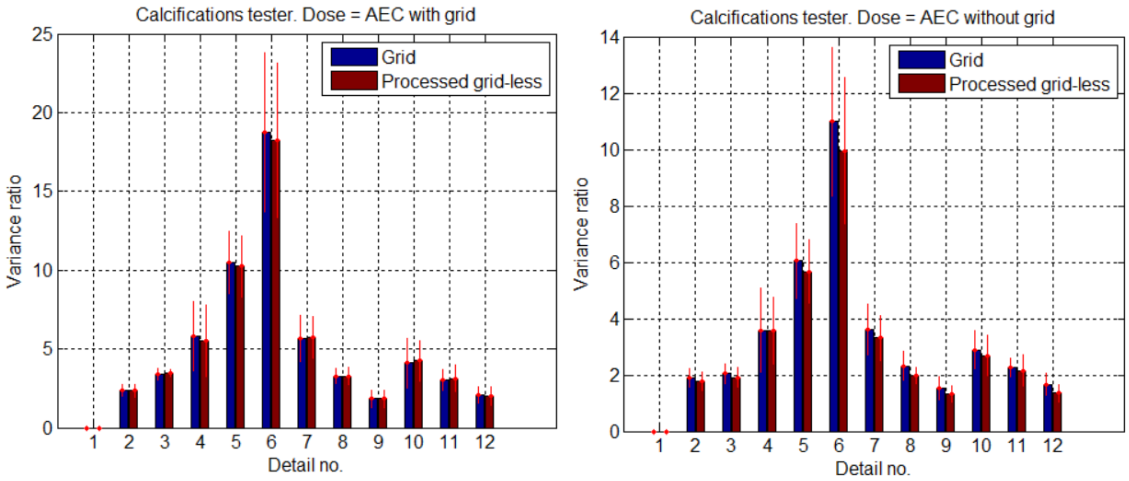

Figure 6.31: Bar plot of the variance ratio results of Table 6.11. The grid images are compared against the processed grid-less images at a higher (left plot) and lower (right plot) doses. The standard deviation of the measurements is shown in the error bars.

6.5 Realistic clinical images

The method evaluation that has been used so far involved the validation with Monte Carlo simulations and different types of phantoms available for mammography applications. Despite the large variety of simulated phantoms that can be generated with the aid of MC simulations, the study also needed to evaluate the performance of the method in a realistic environment. However, the phantoms at our disposal presented a series of drawbacks when applied to this study. These phantoms are aimed to be used for quality control, to check for damage or degradation of the detector or the X-ray tube. Therefore, they have embedded testers of unknown materials and unrealistic shapes that allow to accurately quantify the system performance but hinders the performance of the scattering removal method presented in this study, as the analysis of the phantoms has to be made by simplifying their structure to a single material and homogeneous shape. Although the overall results observed so far are positive, as seen in the previous sections, these simplifications introduced some uncertainties that complicated the analysis process, worsening the results of the processed grid-less images. These shortcomings, in combination with the need to evaluate the stability of the suggested method in a more realistic clinical environment, led to the use of organic phantoms as a final stage of this study.

The ideal solution would have been to use real mammograms of patients. However, two images would have been required for comparison purposes, one with grid and the other one without a grid, resulting in an unnecessary double irradiation that goes against the ALARP (As Low As Reasonably Practicable) principle and hospital ethics. The possibility of using the images of women that are called back for a DBT scan (without grid) after a first 2D mammogram (with grid) was considered, but the dose delivered at 0 degrees angle in DBT is considerably lower than in the 2D scan, compromising the comparison. After discarding human cadavers as an option, for logistic reasons and time constraints, the possibility of using mammary glands of farm animals was taken into consideration. After a study of the different possibilities, sheep were selected as the better option for this study, for their similarity to human breast (i.e. in terms of size, structure and composition) and their availability.

6.5.1 Sheep mammary glands

The reason sheep were selected as the best option for this study are multiple:

- **Ethics and availability:** From the range of mammals available, farm animals that were slaughter for food were the only possible option. Typically, the udders are disposed with the skin and the rest of the carcass that is not processed into food, so no animal has been slaughtered to carry this study.

Government regulations classify them in the "Category 3 Animal By-Product (ABP) waste" and it is considered to be low risk and low value to the industry, (Gov.uk, 2014).

- **Disposal:** According to the government regulations, category 3 ABP waste has to undergo food screening in the abattoir before they are disposed or re-used. For this reason they can be disposed of in landfill as common uncooked food waste once they have been used.
- **Size:** From the available options, pig mammary glands would have adapted better to the study for their similarity with humans. However, the size and structure of the glands did not match the needs of the study. Sheep, goats or cows were the best option size-wise.
- **Structure:** Cow udders are formed by four individual glands, or quarters. Each side of the udder is independent of the other, but the two quarters of each half share the vasculature, nerve supply and lymphatic drainage, reducing the similitude with human breasts. Goats and sheep udders on the other hand, are divided into two individual and independent sections, each of them formed by only one teat, streak canal, teat cistern and gland cistern, resembling slightly more the human breast. (Frandson, Wilke, and Fails, 2013).

Internal structure

The sheep udder is composed of two independent mammary glands, each wrapped by a bag of fibroelastic connective tissue and contained under a single skin bag. The glands are separated by a ligament wall of connective tissue that is essential to maintain the udder tightly attached to the abdominal wall.

Each half of the udder is formed by the parenchyma and the stroma. The parenchyma is a tubule-alveolar epithelial structure formed by a cistern (composed at the same time by the glandular and teat cisterns) and secretory lobes (consisting of branched intralobular ducts and alveoli). The alveolus is in charge of the secretion and initial storage of the milk while the glandular and teat cisterns drain the milk from the alveoli and stores it in its ducts. The storma is formed by the complementary tissue, such as blood and lymph vessels, and adipose, connective and nervous tissues. (Gerado Caja, Xavier Such, 1981; Frandson, Wilke, and Fails, 2013).

When compared with human breasts, each mammary gland is composed of similar elements, Figure 6.32 compares the internal structure of the udder and the human female breast. See Section 4.1.1 for the detail explanation of the composition of human breasts. The main differences are in terms of the size of the ducts and the percentage of glandular and adipose tissue.

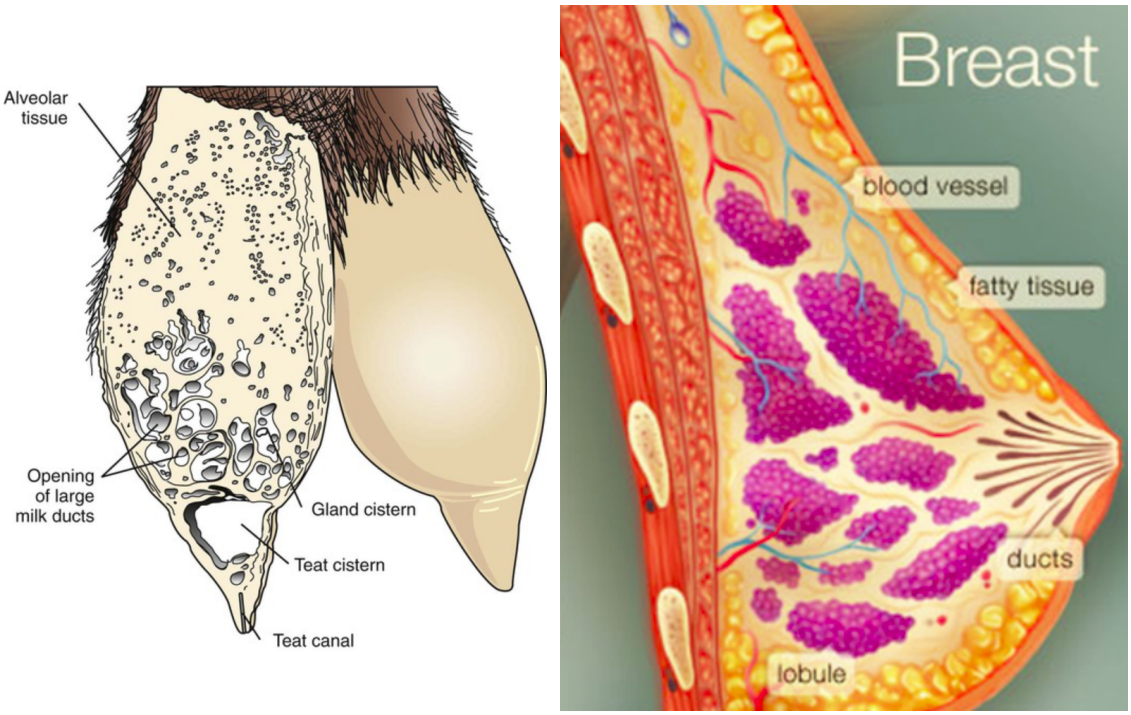

Figure 6.32: Internal structure of an udder and a human breast (Key, 2016; WebMed, 2014).

6.5.2 Experimental set up

Before the experiment was started, Bournemouth University's ethical department (see Appendix B) and Barts NHS trust gave their approval for acquiring the udders and perform the measurements. The hospital's condition was to seal completely the udders from the exterior to avoid the animal parts touching the mammography system. PMMA boxes were designed for this purpose, the udders were placed in the middle of each box and the area was collimated excluding the edges of the box, to reduce the scattering. Figure 6.33 shows the experimental set up and photographies of the three udders inside the acrylic boxes.

In addition to their isolation function, the boxes were designed to be used as a compression paddle, so the compression paddle was removed from the system. Three udders, equivalent to a small size breast, were used in this experiment: the smaller and medium udders were compressed into a 20 mm thick box and the bigger into a 30 mm thick one. The top and bottom covers were 5 mm thick, so the total thickness was 25 and 35 mm plus a 5 mm thick compression paddle. Ideally, the small udder should have been placed in a 10 or 15 mm thick box, leaving the 20 mm box to the large udder. However, the boxes were designed and manufactured before the udders were delivered and the design was planned for larger sizes. Although the box did allow to compress the glands, some areas of the small and the large udders could have been compressed better.

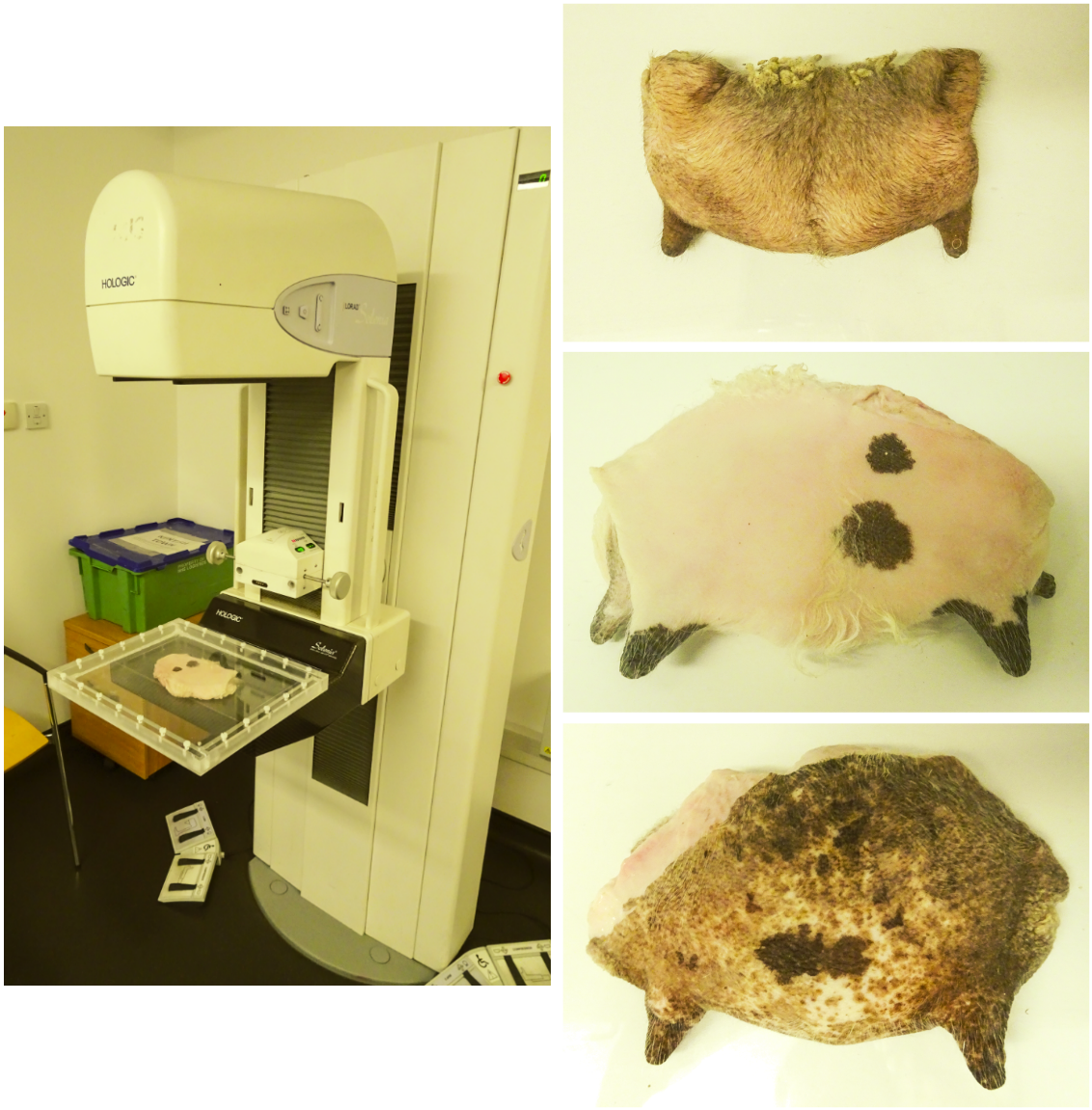

Figure 6.33: The picture of the left shows the experimental set up at Barts NHS trust, the udder is sealed from the exterior with a PMMA box. The three udders used in this study are displayed on the right side of the figure. The sizes from top to bottom are: small, medium and large.

Images with and without grid were acquired for each of the udders at three doses: high dose (selected by the system's AEC when the grid was in use), medium dose (selected by the system's AEC without the grid) and a low dose measurement, 50% of the medium dose. All the measurements were performed at Barts NHS trust, following the geometry introduced in Section 5.3 and illustrated in Figure 5.6-right. The simulations were done with and without the presence of the phantom, to obtain the phantom and background kernels, according to the needs of the method introduced in Section 5.6. Table 6.12 gives more details about the experimental set up.

Table 6.12: The table shows details of the thicknesses and X-ray settings chosen for each of the three sheep mammary glands used in this study.

Udders	**Thickness (mm)**		**X-ray settings**			
	Udder	PMMA	General settings	AEC wG	AEC w/oG	
					100%	50%
Small	20	5	25 kV W/Rh (HVL=0.501 mmAl)	60 mAs	35 mAs	16 mAs
Mediun	20	5	25 kV W/Rh (HVL =0.501 mmAl)	85 mAs	47 mAs	24 mAs
Large	30	5	26 kV W/Rh (HVL=0.511 mmAl)	140 mAs	70 mAs	35 mAs

The skin was approximated to 1.5 mm thick. For the selection of the percentage of glandular and adipose tissue, the mammograms were classified in terms of density with the BI-RADS atlas (Sickles, 2013). It was considered by visual inspection that the udders were closer to the classification C, i.e. heterogeneously dense brest, corresponding to a glandular percentage between 51 and 75%. The glandularity was approximated to 60% in this study.

To ensure that the udders presented at least one area of interest for the study, the udders were injected with powder talcum paste to mimic the presence of calcifications (Andersen et al., 2006). This can be seen as white spots in Figure 6.34.

Once the scatter was estimated and removed from the grid-less mammogram, the grid and processed grid-less images were compared. To help in the analysis, both set of raw images were enhanced with the aid of the DexView software (Varex Imaging), which simulates the final post-processing step of the hospital systems. DexView is an image processing library which converts mammograms, and other X-Ray images, from "For-Processing" to "For-Presentation" images. It enhances the image contrast in such a way that no further adjustment for viewing is needed. In a mammogram, overexposure occurs on the periphery of the breast due to the reduced thickness, resulting in poor visualization of the periphery. DexView performs techniques like histogram equalization, contrast stretching along with other noise reduction operations to output an image which has better visual quality across the complete object. This ensures that image quality is preserved for both thin and thicker regions in the mammogram. DexView is a C++ library which can be used with a command line executable to call specific functions. It provides a set of parameters that can adjust the contrast and sharpness of the image. All the parameters were set to default in this study. The results are shown in Figure 6.34 for the three udders.

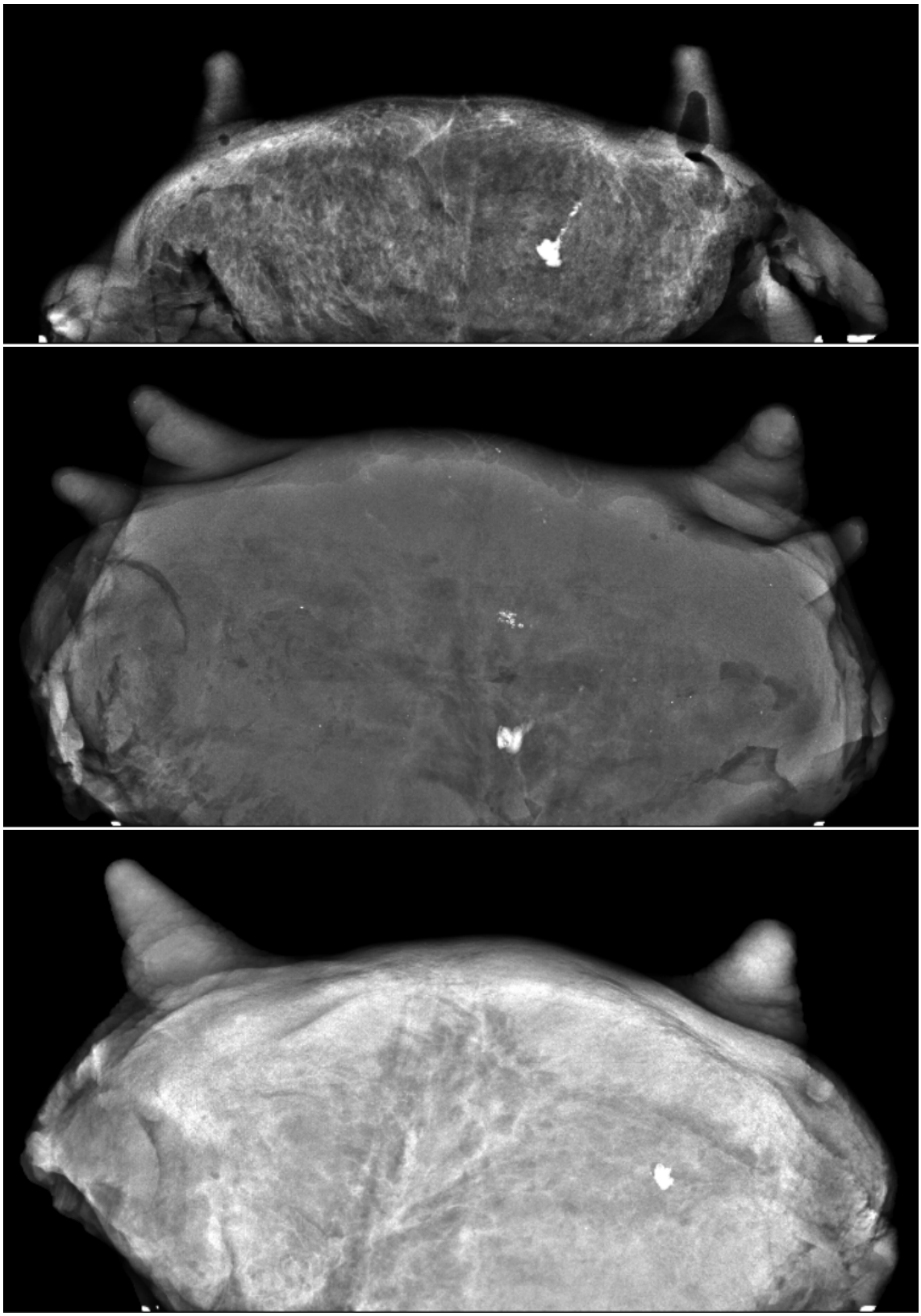

Figure 6.34: Mammograms of sheep mammary glands, corresponding to processed grid-less images acquired at the higher dose (AEC wG). From top to bottom: small, medium and large udders. The images were enhanced with the aid of DexView software (property of Dexela Ltd. a Varex Imaging company).

6.5.3 Results

The quality of the final processed images obtained with and without the grid did not differ enough to be able to distinguish any difference by visual inspection with untrained eyes. For comparison purposes, and to avoid the possibility of introducing biased results, both images were analysed quantitatively. The two figures of merit chosen to perform the analysis were the CNR and the variance ratio (Vr), figures that were previously used in the analysis of the commercial breast phantoms.

The measurements were performed in significant areas of the mammograms, choosing a varied selection of regions of interest in order to cover a wider analysis range. The background areas were selected in nearby areas of each of the ROIs, a total of four background areas were chosen for each of the six cases. The locations of the selected regions were kept constant across the different configurations, i.e. grid and grid-less images at the three doses used to help in the comparison. Figure 6.35 shows the six ROIs chosen for each case and one of the background ROIs (four visualization purposes the other three background ROIs were excluded). The regions chosen for the study presented either microcalcifications or non-homogeneous areas that were considered of interest.

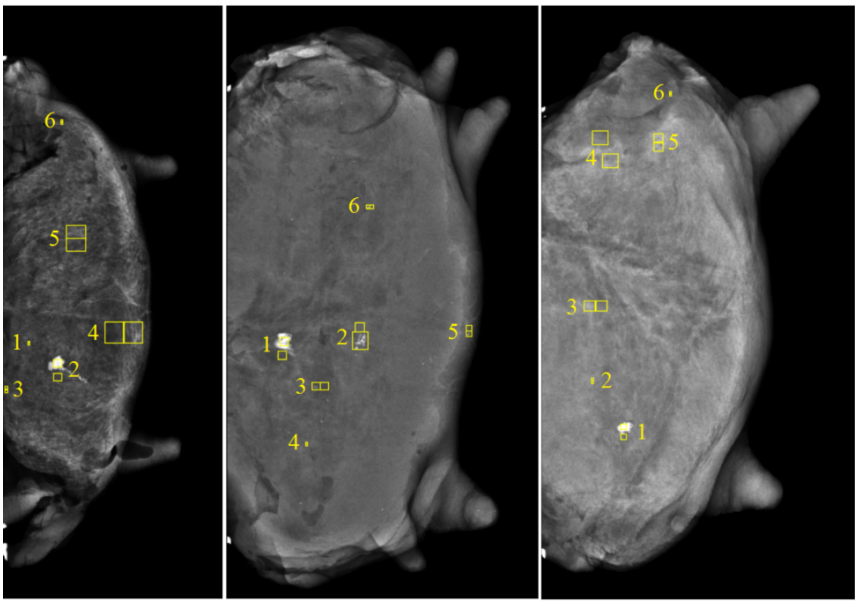

Figure 6.35: The figure shows the six ROIs selected for each udder: smaller on the left, medium in the middle and larger on the right.

The CNR and variance ratio values of the six selected ROIs were compared for each case, i.e. grid vs. processed grid-less at the three selected doses, for each one of the mammary glands. The results for the small, medium and large udder are shown in Figures 6.36 to 6.38 respectively. Each one of the figures features one plot per X-ray setting (showing the CNR on the left y-axis and the variance ratio on the right y-axis) and a table with the values, placed next to each plot.

Small Udder: High dose				
ROI no.	**CNR**		**Vr.**	
	Grid	Proc.	Grid	Proc.
1	2.17	**2.31**	10.14	**11.65**
2	17.00	**17.26**	**8.34**	7.90
3	1.45	**1.89**	12.25	**13.84**
4	5.59	**5.72**	10.38	**12.32**
5	1.76	**1.86**	2.32	**2.45**
6	2.69	**3.29**	16.94	**19.98**

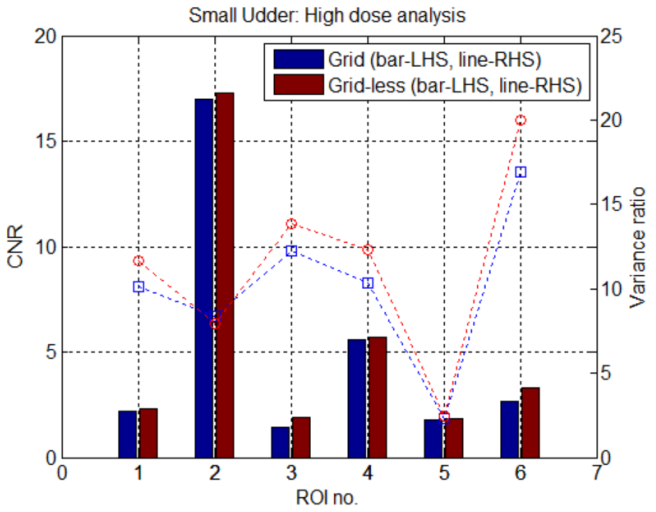

Small Udder: Medium dose				
ROI no.	**CNR**		**Vr.**	
	Grid	Proc.	Grid	Proc.
1	1.48	**1.82**	**8.06**	8.04
2	**15.76**	15.47	7.61	**7.74**
3	1.23	**1.32**	9.17	**10.35**
4	**4.88**	4.86	8.34	**9.40**
5	**1.58**	1.55	2.11	**2.25**
6	2.21	**2.81**	12.77	**14.30**

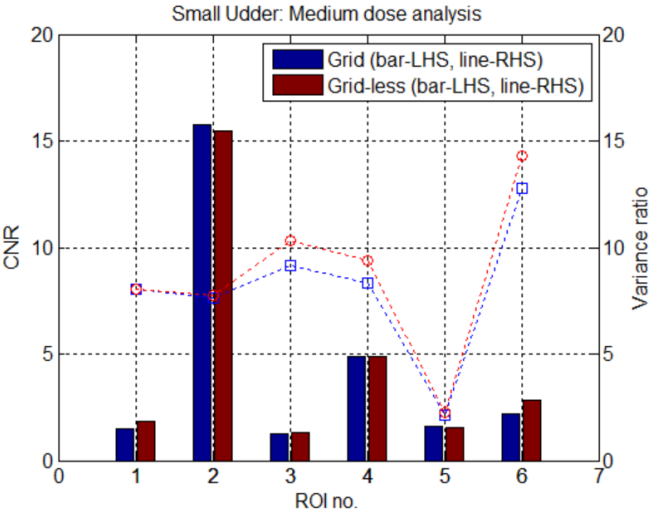

Small Udder: Low dose				
ROI no.	**CNR**		**Vr.**	
	Grid	Proc.	Grid	Proc.
1	0.92	**1.48**	3.69	**6.08**
2	12.28	**13.03**	6.80	**6.92**
3	0.95	**1.08**	4.52	**5.92**
4	3.44	**3.82**	4.88	**6.64**
5	1.16	**1.25**	1.75	**1.95**
6	1.75	**1.99**	6.99	**8.58**

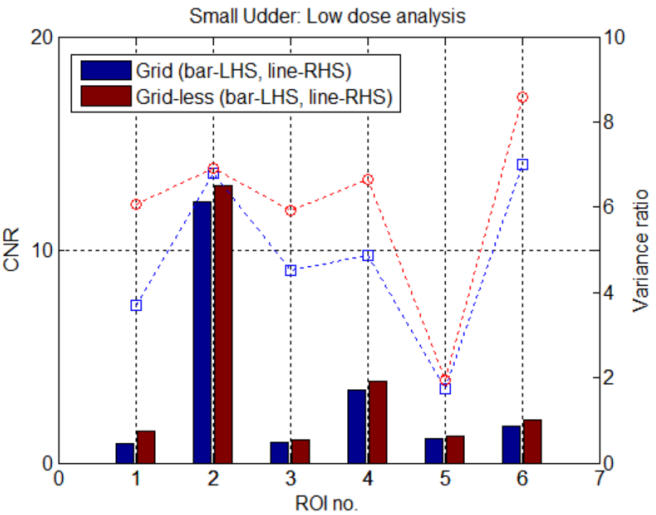

Figure 6.36: The figure shows the plots and tables of results of the averaged CNR and variance ratio results for the six ROIs selected in the small udder. From top to bottom the figure features the high, medium and low doses. LHS and RHS stands for left hand side and right hand side respectively.

Medium Udder: High dose				
ROI no.	**CNR**		**Vr.**	
	Grid	Proc.	Grid	Proc.
1	18.90	**20.29**	26.44	**35.41**
2	2.48	**2.71**	26.77	**33.42**
3	1.09	**1.19**	5.08	**6.08**
4	3.95	**5.03**	128.58	**214.11**
5	0.90	**1.11**	8.74	**11.18**
6	1.95	**2.07**	27.46	**36.04**

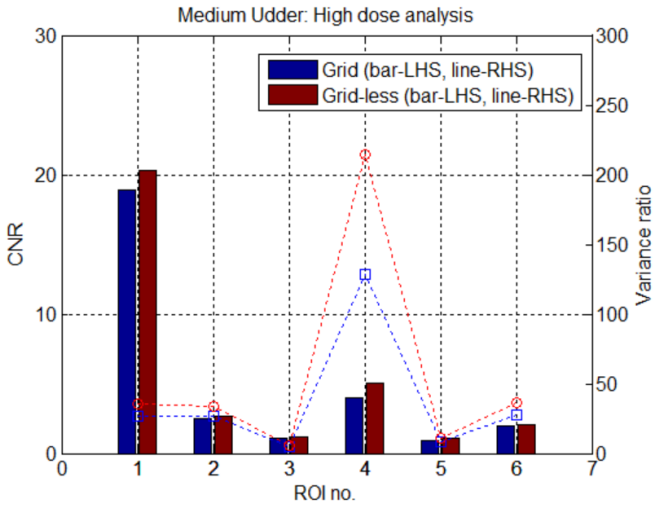

Medium Udder: Medium dose				
ROI no.	**CNR**		**Vr.**	
	Grid	Proc.	Grid	Proc.
1	16.12	**17.76**	19.76	**26.47**
2	2.11	**2.13**	19.31	**19.84**
3	**0.98**	0.93	**4.18**	4.17
4	3.01	**3.57**	69.18	**97.33**
5	0.97	**1.07**	7.37	**9.15**
6	1.44	**1.53**	16.48	**19.97**

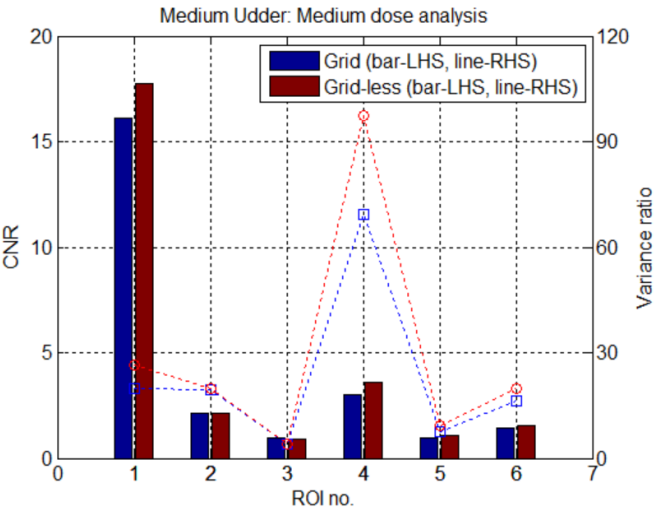

Medium Udder: Low dose				
ROI no.	**CNR**		**Vr.**	
	Grid	Proc.	Grid	Proc.
1	11.91	**14.25**	11.27	**19.41**
2	1.41	**1.53**	9.13	**11.67**
3	0.63	**0.77**	2.74	**3.14**
4	1.86	**2.60**	30.88	**62.72**
5	0.77	**1.05**	5.64	**6.97**
6	1.15	**1.19**	8.36	**12.24**

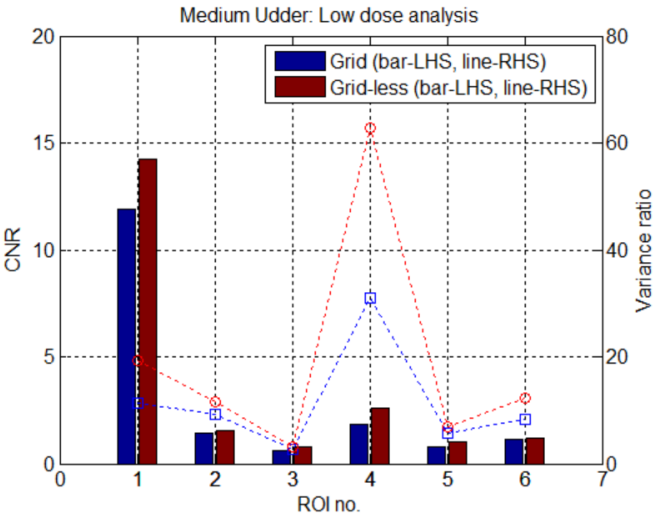

Figure 6.37: The figure shows the plots and tables of results of the averaged CNR and variance ratio results for the six ROIs selected in the medium udder. From top to bottom the figure features the high, medium and low doses. LHS and RHS stands for left hand side and right hand side respectively.

Large Udder: High dose				
ROI no.	**CNR**		**Vr.**	
	Grid	Proc.	Grid	Proc.
1	54.08	**65.07**	417.53	**660.22**
2	1.85	**2.13**	8.44	**10.51**
3	3.49	**3.64**	3.46	**3.75**
4	2.19	**2.36**	2.30	**2.37**
5	0.27	**0.40**	0.97	**1.02**
6	0.70	**0.89**	**6.03**	6.02

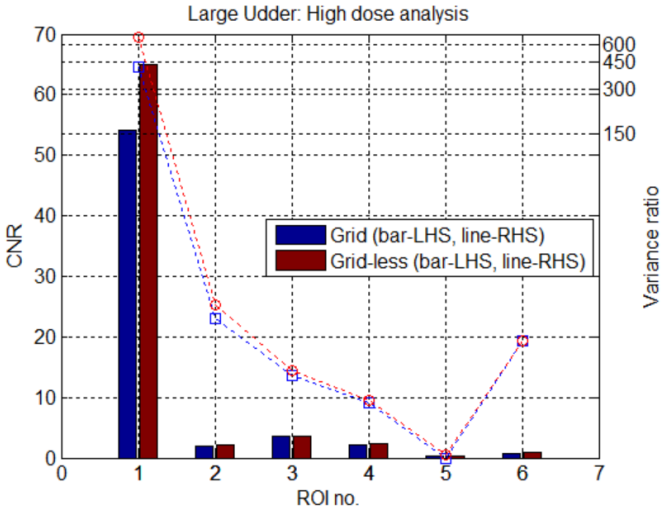

Large Udder: Medium dose				
ROI no.	**CNR**		**Vr.**	
	Grid	Proc.	Grid	Proc.
1	41.50	**48.16**	229.67	**373.30**
2	1.40	**1.54**	**7.21**	6.21
3	3.01	**3.02**	**2.89**	2.83
4	1.79	**1.97**	1.79	**1.94**
5	**0.27**	0.24	0.91	**0.93**
6	0.55	**0.66**	**4.48**	3.56

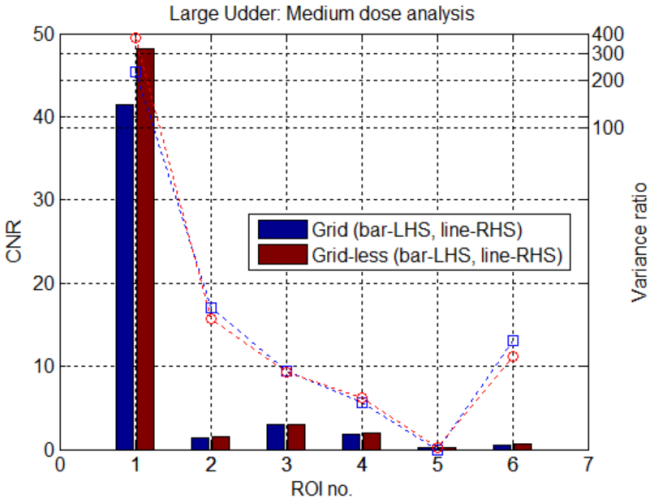

Large Udder: High dose				
ROI no.	**CNR**		**Vr.**	
	Grid	Proc.	Grid	Proc.
1	26.32	**35.17**	80.87	**178.17**
2	0.76	**0.89**	2.55	**2.93**
3	2.06	**2.34**	2.08	**2.44**
4	1.23	**1.49**	1.47	**1.62**
5	0.17	**0.27**	0.98	**1.11**
6	**0.57**	0.44	2.24	**2.38**

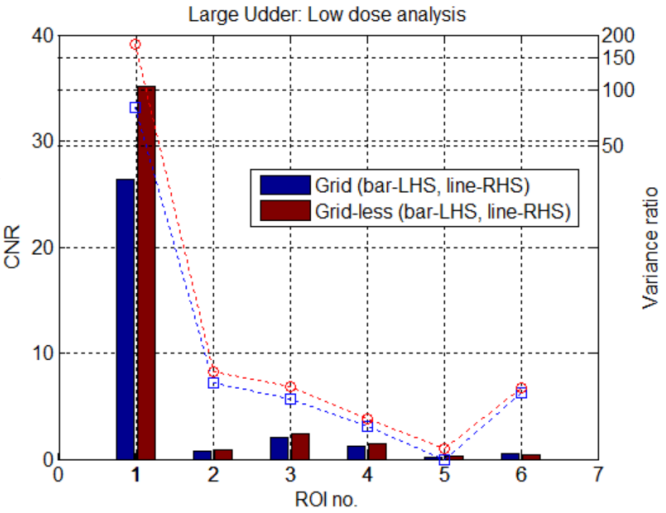

Figure 6.38: The figure shows the plots and tables of results of the averaged CNR and variance ratio results for the six ROIs selected in the large udder. From top to bottom the figure features the high, medium and low doses. LHS and RHS stands for left hand side and right hand side respectively.

6.5.4 Discussion

The results shown in Figures 6.36 to 6.38 are summarised in Table 6.13, where it is stated which of the images (grid vs. grid-less) has the better performance for each case, in terms of the CNR and Vr. The table color code shows green when the processed grid-less image (P) gave better results, yellow when the images were comparable or the test was inconclusive (C) and red when the grid image (G) was better. To ensure that the measurements were statistically relevant, a Student's T-test was performed, choosing 5% as the significance level (the results obtained with this test are shown in Tables A.25 and A.26 of the Appendix A). A measurement was considered comparable or inconclusive when the p-values for both, the CNR and the Vr, were higher than 5% or when both p-values were significant but the results contradicted each other.

Table 6.13: The table summarises the results obtained with the three realistic phantoms analysed in this section. The table highlights which image performs better for each of the ROIs and energies analysed.

	Dose								
	Small udder			Medium udder			Large udder		
ROI no.	H.	M.	L.	H.	M.	L	H.	M.	L
1	C	P	P	P	P	P	P	P	P
2	C	G	P	P	C	P	P	C	P
3	P	C	P	P	C	P	C	C	P
4	P	P	P	P	P	P	C	C	P
5	P	P	P	P	P	C	P	C	P
6	P	C	P	P	P	P	C	C	C

P = Processed grid-less image.
G = Grid image.
C = Comparable results.

As shown in Table 6.13 the overall results obtained are very positive. The best outcome was obtained with the medium sized udder, followed by the smaller one, with the larger udder presenting the higher amount of comparable results. This dependency with the type of udder seems to be in line with the insufficient compression in the small and large udders, reported in the "Experimental set up" section.

As per the energies chosen, the highest and lowest doses produce better results than the middle dose:

- At a very low energy, the signal detected by the panel when the grid is in use is too low to give good results. The increased signal detected as a consequence of the grid removal is essential in the performance, as it has been seen in the results.

- The medium dose presents the higher amount of comparable results and a negative one in the case of the smaller udder. This indicates that the energy reduction, given by the system's AEC when the grid was not used, was too large.
- The results obtained with the higher dose are very positive, indicating that the removal of the grid would contribute to an overall improvement of the image quality, at least for the thicknesses tested.

6.6 Chapter summary and discussion

In this chapter, the post-process scattered radiation reduction method that had been previously defined was evaluated and its robustness tested using a mammography system.

Prior to this evaluation, an initial study was performed to decide on the level of simplifications that could be implemented in the simulations. The results showed that it was important to add the detector information, as the implementation of an idealised geometry underestimated the SPR up to 14%. Consequently, it was decided that the following experiments would include all the detector information up to the sensor layer, for the direct conversion X-ray systems, and up to the scintillator layer, for indirect detection X-ray systems, unless otherwise specified.

The first study with phantoms focused in the restoration of the low frequency spatial resolution when using a phantom highly affected by scattering. For logistical reasons, a CMOS X-ray detector placed in a radiography system was chosen for this experiment set up. The scattering reduction post-processing technique successfully recovered the total spatial resolution lost. Moreover, the post-processed images were artefact free.

The rest of the evaluation was performed with a real mammography system, using the α-Se technology. With the aid of several mammography QC phantoms, the performance of the post-processing scattering reduction technique was challenged by making a one to one comparison between processed grid-less images and grid images. Overall, it was found that these phantoms were not fit to purpose. Due to the structure of the phantoms it was necessary to introduce a large amount of assumptions and simplifications in the simulations used for the grid-less image processing. Therefore, the results obtained, although generally comparable with grid's results, did not suggest a performance as good as it was initially expected. It was made clear that a more clinical realistic phantom was needed for performing a fair comparison. For this reason, sheep mammary glands were chosen for the last study.

The results obtained in this last experiment were very encouraging and indicated that the scattering reduction technique (suggested in this study for processing the grid-less images) outperforms the performance of the anti-scatter grids when the measurements

are taken under the same conditions. Due to lack of resources and time constraints, only thin udders were tested. Although the performance is not expected to degrade much for thicknesses below 70 mm, another round of testing would be advisable. Suggestions for future research are introduced in the next chapter.

Chapter 7

Conclusions and future work

The work presented in this thesis covers two topics within the two main areas of digital radiography applications:

- Image acquisition: the design cycle of new CMOS X-ray detectors has been challenged in terms of their image quality.
- Image processing: a method for image scattering reduction using post-processing techniques for grid-less mammography applications has been proposed.

A summary of the results obtained for each section is described below.

7.1 CMOS X-ray detector characterization and qualification

The main goal of this study was to contribute, with the aid of image characterisation techniques, to the development of new CMOS X-ray detectors. Shortcomings in the design cycle ultimately present themselves as image artefacts that compromise the quality of the product. For that reason, the use of image characterization to challenge the design during the development process is essential to ensure the final quality of the detectors. To that end, well-known image analysis techniques were adapted, extended and optimized to qualify and debug the product at different stages of development.

The novelty in this exercise was to take the architecture of a state-of-the-art active pixel sensor CMOS imager and to develop a set of image processing tools to test it to its limit, during the design cycle. In the course of this thesis, image artefacts and performance issues were found and addressed as a result of iterative image quality evaluation. The project has involved a close collaboration with a multinational team of engineers, whose input was required to investigate the root cause of the issues found and to address the problems consequently. The teams involved depended on the nature of the problem, which could affect the electronics, firmware, software or sensor designs.

Issues encountered during the image characterization exercise have been, among others, high and low frequency noise, noise flickering, bit errors, image clipping, non-linearity, glowing rows or columns, image artefacts due to scintillator afterglow and gain hysteresis, pixel cross-talk and unrealistic DQE values. The group of tests suggested in this thesis have been integrated in the company routine testing and detector validation and verification exercises. This study was key for the successful release of final CMOS flat panel detectors designed and built at Dexela Ltd. (Varex Imaging Corporation - London).

7.2 Scatter removal by image processing in digital mammography

The scatter removal method that has been proposed in this thesis is based in image convolution with point spread function (PSF) kernels, obtained with a simplified Monte Carlo simulation using a narrow pencil beam in a symmetric environment. The simulations were performed using the Geant4 simulation tool-kit.

The method uses a semi-empirical approach to correct the breast-edge area for the scatter originated outside the breast, i.e. background contribution mainly coming from the compression paddle, and, in case of breasts of thicknesses greater than 50 mm, for the thickness variations caused by the angle of the X-ray beam at the edge of the breast and the thickness reduction of the breast edge itself. Two additional kernels needed to be simulated for performing the background correction and an additional one for the correction of thickness reductions in the breast-edge. The novelty of the proposed method consists in the interpolation between kernels using a semi-empirical equation. This accounts for the impact that a change in the absorption coefficients has in the simulated scatter, e.g. background scatter contribution to the breast is affected by the change between background and breast absorption and it is dependent on the distance to the breast edge.

The optimization of the semi-empirical equation and the final testing of the method was made by comparing, for a range of thicknesses, the results against the primary image generated with full MC simulations. The uncertainty introduced by the correction was found to be dependent on the thickness, improving for thin breasts. The results are very positive, showing a maximum discrepancy of 10% for a breast thickness of 70 mm, value that is reduced down to 3% for a 35 mm breast. For breasts that are thicker than 70 mm the uncertainties found were too large, i.e. > 20%, showing a limitation of the method for very thick breasts. As an alternative, an asymmetric kernel approach could reduce the uncertainties for these cases; otherwise, additional research resources would be needed to solve this issue in the method (see the "Future work" section below).

After the definition and validation of the method was completed, its robustness was tested against real images. The first step was to decide the level of detail needed in the

geometry of the simulations. In previous published studies the geometry of the detector and compression/support paddles had not been handled with care, either for lack of knowledge of the geometry or for simplification purposes. However, the study indicated that any simplification in the geometry affects the final results, as the scatter underestimation in the PSF kernels was found to be considerable. The underestimation goes from 3-6% for a detector that is simplified to a scintillator plate to 10-14% for an ideal detector simplification.

The ability to recover the spatial resolution, that had been reduced by the effect of the scatter in the system, was then evaluated. Two test devices were used for this purpose: a benchmark phantom ("ground truth") that was an IEC approved edge test device designed to evaluate the MTF of the system and another edge test device that was embedded in a PMMA block (DMam from Leeds Test Objects). The PMMA increases the scattering produced in the surroundings of the edge, reducing the low frequency spatial resolution. The images acquired with the second phantom were processed with the method followed in this study and the MTF obtained was compared with the "ground truth" results. The extreme conditions of this test, where the correction focuses in the boundary between two materials with very different scatter and absorption properties, allowed not only to evaluate the quality of the method but also to ensure that the processing did not insert any artefacts to the image. The resulting images were clear of artefacts, as shown in the smooth MTF curves obtained, and the low frequency spatial resolution was restored, slightly improving the results shown by the benchmark images. As proven later on, an additional benefit of including in the simulations the scatter that is produced in the detector layers is an improvement in the overall spatial resolution, giving post-processing scatter removal methods an advantage over anti-scatter grids.

The final goal of this study was to obtain an image quality comparable or better than the one obtained with the use of anti-scatter grids. Therefore, grid and grid-less images were acquired under the same conditions and a one to one comparison study was made. The measurements from this moment onwards were made with a clinical mammography system. Due to the reduced number of mammography systems that used CMOS technology, the rest of the measurements were performed with a Hologic Lorad Selenia α-Se system. The range of phantoms chosen were: CDMAM, TOR-MAS and TOR-MAM from Leeds Test Objects, 010A from CIRS and sheep mammary glands.

The results obtained with the QA phantoms, i.e. CDMAM, TOR-MAS, TOR-MAM and 010A CIRS, were mostly inconclusive:

- The CDMAM phantom was seen to be inaccurate for the type of measurements and comparisons performed in this study, this was in agreement with previous publications.

- The unknown materials and random structure of the testers inside the TOR-MAS and TOR-MAM phantoms leaded to the introduction of big uncertainties, due to the simplifications that had to be made in the simulations. The results obtained were, however, comparable with the grid application.

  In the TOR-MAS phantom, those testers affected by the scattering of the neighbouring testers favoured the grid images, specially for thicker phantoms. However, the step wedge and high contrast resolution grid testers gave better results in the grid-less cases. Results that were in line with the previous MTF experiment, indicating that the post-processing improves the overall spatial resolution of the system.

  The calcifications of the visually realistic area of the TOR-MAM phantom generally had higher contrast to noise ratio in the processed grid-less images, across the different energies and thicknesses tested. Although consistent, the difference was very small to be considered statistically relevant, pointing to comparable results.

- Similar results were obtained with the CIRS phantom. The materials were known in this case, so the uncertainty introduced in the simulations was lower. The grid-less images showed a non-uniformity in one of the extremes of the phantom, likely introduced during the gain and offset correction step at the hospital. Therefore, the results obtained with the tester placed in that area, i.e. circular detail tester, were affected. The step wedge tester favoured the processed grid-less measurements for those steps with higher glandularity percentage and the grid measurements when the percentage of adipose tissue was higher. The results with the microcalcifications tester, on the other hand, were inconclusive. The errors in the measurements were too large and the results varied across the details.

The phantoms used up to this point required the use of simplifications in the scatter estimation method, undermining the results obtained. It became clear the need of a more realistic clinical phantom that allowed a fair one to one grid vs. processed grid-less comparison, while challenging the method in real-life applications. Sheep mammary glands were chosen as a good trade-off between synthetic phantoms and female breasts.

The results obtained with the udders were in clear favour of the processed grid-less images. Looking at the higher air kerma used (chosen by the AEC system when the grid was in use) the percentage of results in favour of the grid-less methodology was 67%, 100% and 50% for the small, medium and large udders respectively, with two inconclusive results in the small udder case (33%) and three in the larger udder (50%). During the experimental set up it was found that the compression of the small and large udders was poorer, explaining the better results obtained with the well-compressed gland.

7.3 Future work

The test procedure implemented in Dexela Ltd. to evaluate CMOS X-ray detector prototypes has evolved and adapted along with the development process. The re-defined test methods have been successfully employed across a varied range of detectors and applications. However, with the design of new products, or with a change in the product application, new features can be found that might highlight the need of a new test or the modification of the current ones. In that case, the testing procedure will need to be adapted. A future interesting route to pursue would be to apply this study to additional technologies, i.e. α-Si detectors or photon-counting detectors.

For the proposed scatter reduction technique, future work could involve research in the optimization of the model, such as binning the images to speed up the convolution step and then un-bin the estimated scatter image to apply the final correction. Some additional effort could be made to improve the model for thicker breast cases, i.e. T > 70 mm, that currently suffer from large errors. Finally, further validations should be performed with clinically realistic phantoms, i.e. animal mammary glands, 3D printed phantoms or similar, specially focusing in thicker samples. QC phantoms have proven to be source of large uncertainties, so more relevant phantoms could be tested in order to gain statistics. Furthermore, the improvement in the image quality seen in the last test, i.e. with the sheep mammary glands, indicates that the dose could be reduced without compromising the image quality that the grid applications give. The dose reduction would be in between the higher and medium doses tested. Further efforts would be needed to identify the exact percentage of reduction, this could be done for example with the set of phantom slabs provided by CIRS (014 series). A qualitative analysis from qualified radiographers would also be required to ensure that the dose reduction and image post-processing do not affect their diagnosis.

Appendix A

Complementary information

A.1 Chapter 5: Additional data

Table A.1 provides the data obtained in the validation against the AAPM task group 195 - Case 3 report, introduced in Section 5.2.3.

Table A.1: Validation against AAPM TG195 - Case 3, data corresponding to Section 5.2.3 of this thesis.

		V1		V2		V3		V4	
		Result (%Error)	AAPM (%Error)	Result (%Error)	AAPM (%Error)	Result (%Error)	AAPM (%Error)	Result (%Error)	AAPM (%Error)
ROI 1	P	109.689(0.035)	110.342(0.001)	105.146(0.037)	105.806(0.001)	-	-	-	-
	C	0.904(0.388)	0.898(0.001)	0.954(0.395)	0.949(0.001)	0.107(0.692)	0.106(0.004)	0.393(0.517)	0.391(0.002)
	R	2.202(0.250)	2.210(0.001)	2.090(0.262)	2.099(0.001)	0.059(0.937)	0.059(0.005)	0.139(0.850)	0.139(0.004)
	M	0.223(0.772)	0.230(0.003)	0.278(0.737)	0.280(0.003)	0.159(0.566)	0.157(0.003)	0.559(0.425)	0.549(0.002)
ROI 2	P	1.486(0.304)	1.489(0.001)	3.188(0.233)	3.209(0.001)	-	-	-	-
	C	0.189(0.847)	0.185(0.003)	0.433(0.633)	0.429(0.002)	1.037(0.223)	1.036(0.001)	2.702(0.194)	2.691(0.001)
	R	0.355(0.622)	0.355(0.002)	0.614(0.521)	0.615(0.002)	1.138(0.214)	1.138(0.001)	1.925(0.224)	1.921(0.001)
	M	0.191(0.839)	0.184(0.003)	0.435(0.621)	0.420(0.002)	1.188(0.207)	1.184(0.001)	2.695(0.190)	2.688(0.001)
ROI 3	P	1.452(0.308)	1.461(0.001)	3.135(0.235)	3.156(0.001)	-	-	-	-
	C	0.354(0.617)	0.346(0.002)	0.660(0.505)	0.649(0.002)	0.449(0.338)	0.446(0.002)	1.289(0.282)	1.285(0.001)
	R	0.467(0.543)	0.466(0.002)	0.771(0.464)	0.773(0.002)	0.317(0.406)	0.316(0.002)	0.595(0.406)	0.595(0.002)
	M	0.264(0.713)	0.258(0.003)	0.551(0.550)	0.542(0.002)	0.569(0.300)	0.565(0.002)	1.492(0.257)	1.480(0.001)
ROI 4	P	1.531(0.300)	1.540(0.001)	3.274(0.230)	3.290(0.001)	-	-	-	-
	C	0.172(0.888)	0.170(0.003)	0.438(0.633)	0.437(0.002)	1.937(0.163)	1.932(0.001)	4.798(0.146)	4.787(0.001)
	R	0.359(0.618)	0.362(0.002)	0.628(0.516)	0.633(0.002)	3.265(0.126)	3.261(0.001)	5.310(0.134)	5.306(0.001)
	M	0.197(0.827)	0.191(0.003)	0.475(0.597)	0.461(0.002)	2.102(0.156)	2.097(0.001)	4.347(0.149)	4.334(0.001)
ROI 5	P	1.521(0.301)	1.528(0.001)	3.254(0.231)	3.280(0.001)	131.362(0.20)	131.251(0.001)	282.885(0.019)	282.831(0.001)
	C	0.232(0.764)	0.228(0.003)	0.580(0.550)	0.576(0.002)	2.603(0.414)	2.602(0.001)	6.737(0.124)	6.740(0.001)
	R	0.439(0.559)	0.440(0.002)	0.763(0.468)	0.761(0.002)	18.454(0.053)	18.432(0.001)	33.056(0.054)	33.041(0.001)
	M	0.258(0.722)	0.254(0.003)	0.607(0.527)	0.598(0.002)	3.811(0.116)	3.825(0.001)	7.325(0.114)	7.353(0.001)
ROI 6	P	1.468(0.306)	1.476(0.001)	3.161(0.234)	3.178(0.001)	-	-	-	-
	C	0.306(0.665)	0.297(0.002)	0.647(0.515)	0.639(0.002)	1.038(0.223)	1.033(0.001)	2.701(0.194)	2.692(0.001)
	R	0.454(0.550)	0.453(0.002)	0.771(0.465)	0.773(0.002)	1.137(0.214)	1.135(0.001)	1.925(0.224)	1.923(0.001)
	M	0.271(0.704)	0.267(0.002)	0.602(0.528)	0.599(0.02)	1.189(0.207)	1.185(0.001)	2.696(0.190)	2.686(0.001)
ROI 7	P	1.486(0.304)	1.491(0.001)	3.193(0.233)	3.211(0.001)	-	-	-	-
	C	0.189(0.847)	0.184(0.003)	0.433(0.633)	0.429(0.002)	0.107(0.693)	0.106(0.004)	0.392(0.518)	0.391(0.002)
	R	0.355(0.623)	0.355(0.002)	0.616(0.521)	0.616(0.002)	0.060(0.934)	0.060(0.005)	0.139(0.853)	0.139(0.004)
	M	0.191(0.838)	0.184(0.003)	0.434(0.623)	0.420(0.002)	0.161(0.563)	0.158(0.003)	0.558(0.426)	0.549(0.002)

A.2 Chapter 6: Additional data

A.2.1 CDMAM

Tables A.2 to A.6 provide the data obtained in the study of the CDMAM phantom, introduced in Section 6.4.1.

A.2.1.1 Thickness = 20 mm

Table A.2: Data obtained with the CDCOM software in the analysis of the T=20 mm thick CDMAM phantom, corresponding to Figure 6.9 of this thesis.

Diameter (mm)	**Predicted human gold thickness (µm)**		
		AEC with grid	
	wG	w/oG Unproc.	w/oG Proc.
0.08	1.07	0.97	0.93
0.10	0.59	0.50	0.52
0.13	0.34	0.30	0.31
0.16	0.25	0.24	0.23
0.20	0.17	0.20	0.20
0.25	0.13	0.17	0.17
0.31	0.11	0.12	0.13
0.40	0.08	0.10	0.10
0.50	0.06	0.08	0.08
0.63	0.05	0.07	0.06
0.80	0.04	0.05	0.05
1.00	0.04	0.04	0.04

A.2.1.2 Thickness = 30 mm

Table A.3: Data obtained with the CDCOM software in the analysis of the T=30 mm thick CDMAM phantom.

Diameter (mm)	Predicted human gold thickness (µm)					
	AEC with grid			AEC without grid		
	wG	w/oG Unproc.	w/oG Proc.	wG	w/oG Unproc.	w/oG Proc.
0.08	0.92	1.09	1.10	1.34	1.40	1.42
0.10	0.56	0.67	0.65	0.77	0.77	0.75
0.13	0.41	0.43	0.43	0.52	0.55	0.49
0.16	0.30	0.29	0.27	0.36	0.39	0.38
0.20	0.22	0.21	0.21	0.28	0.30	0.30
0.25	0.17	0.16	0.17	0.21	0.22	0.22
0.31	0.14	0.13	0.14	0.15	0.16	0.16
0.40	0.11	0.11	0.11	0.12	0.13	0.13
0.50	0.09	0.10	0.10	0.10	0.11	0.11
0.63	0.07	0.08	0.08	0.08	0.09	0.09
0.80	0.06	0.06	0.05	0.06	0.07	0.07
1.00	0.05	0.04	0.04	0.05	0.05	0.06

A.2.1.3 Thickness = 40 mm

Table A.4: Data obtained with the CDCOM software in the analysis of the T=40 mm thick CDMAM phantom, corresponding to Figure 6.9 of this thesis.

Diameter (mm)	Predicted human gold thickness (µm)					
	AEC with grid			AEC without grid		
	wG	w/oG Unproc.	w/oG Proc.	wG	w/oG Unproc.	w/oG Proc.
0.08	1.10	1.16	1.22	1.60	1.44	1.70
0.10	0.61	0.72	0.75	0.99	0.96	1.00
0.13	0.39	0.40	0.41	0.63	0.67	0.71
0.16	0.28	0.33	0.34	0.46	0.53	0.58
0.20	0.22	0.28	0.29	0.36	0.38	0.40
0.25	0.16	0.21	0.22	0.28	0.26	0.27
0.31	0.12	0.15	0.16	0.19	0.20	0.19
0.40	0.09	0.11	0.13	0.15	0.17	0.17
0.50	0.08	0.10	0.10	0.11	0.14	0.14
0.63	0.07	0.08	0.08	0.09	0.11	0.11
0.80	0.06	0.06	0.05	0.08	0.09	0.10
1.00	0.05	0.04	0.05	0.08	0.08	0.09

A.2.1.4 Thickness = 50 mm

Table A.5: Data obtained with the CDCOM software in the analysis of the T=50 mm thick CDMAM phantom.

Diameter (mm)	Predicted human gold thickness (µm)					
	AEC with grid			AEC without grid		
	wG	w/oG Unproc.	w/oG Proc.	wG	w/oG Unproc.	w/oG Proc.
0.08	1.49	1.71	1.72	2.33	2.38	2.16
0.10	0.80	1.11	1.17	1.54	1.47	1.35
0.13	0.50	0.67	0.71	0.92	0.90	0.92
0.16	0.36	0.47	0.47	0.55	0.56	0.59
0.20	0.25	0.33	0.31	0.37	0.37	0.40
0.25	0.18	0.25	0.23	0.28	0.28	0.32
0.31	0.16	0.20	0.19	0.23	0.23	0.25
0.40	0.13	0.16	0.15	0.16	0.16	0.18
0.50	0.10	0.13	0.13	0.12	0.11	0.13
0.63	0.08	0.11	0.11	0.11	0.10	0.12
0.80	0.07	0.09	0.09	0.11	0.09	0.10
1.00	0.06	0.07	0.07	0.09	0.08	0.08

A.2.1.5 Thickness = 70 mm

Table A.6: Data obtained with the CDCOM software in the analysis of the T=70 mm thick CDMAM phantom, corresponding to Figure 6.9 of this thesis.

Diameter (mm)	Predicted human gold thickness (µm)					
	AEC with grid			AEC without grid		
	wG	w/oG Unproc.	w/oG Proc.	wG	w/oG Unproc.	w/oG Proc.
0.08	1.71	2.26	1.89	3.59	2.32	3.32
0.10	1.17	1.16	1.26	1.90	1.47	1.57
0.13	0.87	0.70	0.79	1.11	1.00	0.98
0.16	0.54	0.44	0.49	0.73	0.81	0.78
0.20	0.33	0.35	0.35	0.57	0.62	0.57
0.25	0.28	0.31	0.32	0.41	0.44	0.43
0.31	0.23	0.25	0.27	0.31	0.35	0.36
0.40	0.17	0.19	0.21	0.24	0.26	0.28
0.50	0.14	0.15	0.17	0.19	0.20	0.22
0.63	0.09	0.13	0.14	0.15	0.15	0.17
0.80	0.07	0.10	0.11	0.13	0.12	0.14
1.00	0.06	0.08	0.09	0.10	0.11	0.12

A.2.2 TOR-MAS

Tables A.7 to A.24 provide the data obtained in the study of the TOR-MAS phantom, introduced in Section 6.4.2.1.

A.2.2.1 5.6 mm circular detail tester

Table A.7: Data obtained with the AutoPIA software in the analysis of the 5.6 mm circular detail tester of the T=30 mm thick TOR-MAS phantom, corresponding to Figure 6.17 of this thesis. Values in gray indicate the details that the software consider non-visible.

Thickness = 30 mm					
		CNR			
Detail (no.)	**Nominal Contrast**	**AEC with grid**		**AEC without grid**	
		wG	w/oG Proc.	wG	w/oG Proc.
1	**8.30**	3.78	3.85	3.00	2.84
2	**5.60**	2.45	2.40	1.95	1.84
3	**3.90**	1.90	1.93	1.48	1.47
4	**2.80**	1.40	1.40	1.08	1.08
5	**2.00**	1.02	0.85	0.75	0.72
6	**1.40**	0.65	0.59	0.53	0.40
7	**1.00**	0.41	0.51	0.31	0.35
8	**0.70**	0.33	0.36	0.00	0.21
9	**0.50**	0.45	0.47	0.31	0.32
10	**0.35**	0.17	0.22	0.18	0.00
11	**0.25**	0.00	0.00	0.10	0.00

Table A.8: Data obtained with the AutoPIA software in the analysis of the 5.6 mm circular detail tester of the T=50 mm thick TOR-MAS phantom. Values in gray indicate the details that the software consider non-visible.

Thickness = 50 mm					
		CNR			
Detail (no.)	**Nominal Contrast**	**AEC with grid**		**AEC without grid**	
		wG	w/oG Proc.	wG	w/oG Proc.
1	**8.30**	3.27	3.68	2.16	1.98
2	**5.60**	2.15	1.71	1.36	1.28
3	**3.90**	1.64	1.37	1.00	1.02
4	**2.80**	1.18	0.91	0.67	1.67
5	**2.00**	0.80	0.51	0.38	0.48
6	**1.40**	0.51	0.38	0.28	0.33
7	**1.00**	0.34	0.25	0.09	0.14
8	**0.70**	0.30	0.19	0.07	0.00
9	**0.50**	0.25	0.20	0.10	0.00
10	**0.35**	0.15	0.15	0.00	0.00
11	**0.25**	0.00	0.00	0.03	0.00

Table A.9: Data obtained with the AutoPIA software in the analysis of the 5.6 mm circular detail tester of the T=70 mm thick TOR-MAS phantom, corresponding to Figure 6.17 of this thesis. Values in gray indicate the details that the software consider non-visible.

Thickness = 70 mm					
		CNR			
Detail (no.)	**Nominal Contrast**	**AEC with grid**		**AEC without grid**	
		wG	w/oG Proc.	wG	w/oG Proc.
1	**8.30**	2.57	1.92	1.73	1.32
2	**5.60**	1.75	1.22	1.12	1.83
3	**3.90**	1.26	0.87	0.83	1.63
4	**2.80**	0.99	0.57	0.66	1.48
5	**2.00**	0.67	0.28	0.42	0.24
6	**1.40**	0.40	0.22	0.29	0.00
7	**1.00**	0.32	0.32	0.22	0.19
8	**0.70**	0.21	0.22	0.16	0.00
9	**0.50**	0.29	0.00	0.00	0.00
10	**0.35**	0.00	0.00	0.00	0.00
11	**0.25**	0.00	0.00	0.00	0.00

A.2.2.2 0.5 mm circular detail tester

Table A.10: Data obtained with the AutoPIA software in the analysis of the 0.5 mm circular detail tester of the T=30 mm thick TOR-MAS phantom, corresponding to Figure 6.18 of this thesis. Values in gray indicate the details that the software consider non-visible.

Thickness = 30 mm					
		DCC			
Detail (no.)	Nominal Contrast	AEC with grid		AEC without grid	
		wG	w/oG Proc.	wG	w/oG Proc.
1	**41.0**	13.6	14.4	10.9	10.3
2	**30.0**	10.7	11.5	8.60	8.5
3	**21.0**	7.7	8.8	6.4	6.7
4	**16.0**	5.8	6.4	4.6	4.4
5	**11.0**	4.4	4.5	3.4	3.3
6	**8.3**	3.1	3.4	2.5	2.3
7	**5.6**	2.7	2.4	1.9	1.3
8	**3.9**	1.9	1.5	1.6	1.2
9	**2.8**	1.7	3.4	0.9	0.7
10	**2.0**	1.0	0.7	0.8	0.6
11	**1.4**	0.0	0.0	0.8	0.0

Table A.11: Data obtained with the AutoPIA software in the analysis of the 0.5 mm circular detail tester of the T=50 mm thick TOR-MAS phantom. Values in gray indicate the details that the software consider non-visible.

Thickness = 50 mm					
		DCC			
Detail (no.)	Nominal Contrast	AEC with grid		AEC without grid	
		wG	w/oG Proc.	wG	w/oG Proc.
1	**41.0**	11.4	10.8	8.1	7.6
2	**30.0**	9.0	8.5	6.3	6.1
3	**21.0**	6.5	6.0	4.9	4.7
4	**16.0**	5.1	5.0	3.6	3.1
5	**11.0**	3.6	3.2	2.6	2.5
6	**8.3**	2.8	2.3	2.1	1.5
7	**5.6**	2.1	2.1	1.4	1.7
8	**3.9**	1.8	1.3	1.1	1.1
9	**2.8**	0.7	1.0	0.9	0.8
10	**2.0**	0.9	0.0	0.0	0.0
11	**1.4**	0.0	0.0	0.0	0.0

Table A.12: Data obtained with the AutoPIA software in the analysis of the 0.5 mm circular detail tester of the T=70 mm thick TOR-MAS phantom, corresponding to Figure 6.18 of this thesis. Values in gray indicate the details that the software consider non-visible.

Thickness = 70 mm					
		DCC			
Detail (no.)	Nominal Contrast	AEC with grid		AEC without grid	
		wG	w/oG Proc.	wG	w/oG Proc.
1	**41.0**	9.6	8.5	6.6	6.1
2	**30.0**	8.1	7.0	5.3	4.8
3	**21.0**	5.7	4.7	3.9	3.4
4	**16.0**	4.3	3.7	2.4	2.7
5	**11.0**	3.0	3.0	2.6	1.7
6	**8.3**	2.3	1.9	1.6	1.4
7	**5.6**	1.4	1.3	1.3	0.9
8	**3.9**	0.9	0.9	1.0	1.0
9	**2.8**	1.1	0.9	0.8	0.0
10	**2.0**	1.0	0.0	0.0	0.0
11	**1.4**	0.0	0.0	0.0	0.0

A.2.2.3 0.25 mm circular detail tester

Table A.13: Data obtained with the AutoPIA software in the analysis of the 0.25 mm circular detail tester of the T=30 mm thick TOR-MAS phantom, corresponding to Figure 6.19 of this thesis. Values in gray indicate the details that the software consider non-visible.

Thickness = 30 mm					
		DCC			
Detail (no.)	Nominal Contrast	AEC with grid		AEC without grid	
		wG	w/oG Proc.	wG	w/oG Proc.
1	**41.0**	8.6	9.9	7.0	6.6
2	**30.0**	6.4	7.1	5.5	4.6
3	**21.0**	6.1	6.9	5.1	4.8
4	**16.0**	5.3	6.4	4.6	4.5
5	**11.0**	3.9	3.5	2.7	2.6
6	**8.3**	2.7	3.2	2.7	2.0
7	**5.6**	1.7	0.0	1.7	1.4
8	**3.9**	1.3	1.3	0.0	1.8
9	**2.8**	0.0	1.4	0.0	0.0
10	**2.0**	0.0	1.4	1.8	0.0
11	**1.4**	0.0	0.0	0.0	0.0

Table A.14: Data obtained with the AutoPIA software in the analysis of the 0.25 mm circular detail tester of the T=30 mm thick TOR-MAS phantom. Values in gray indicate the details that the software consider non-visible.

Thickness = 50 mm					
		DCC			
Detail (no.)	**Nominal Contrast**	**AEC with grid**		**AEC without grid**	
		wG	w/oG Proc.	wG	w/oG Proc.
1	**41.0**	7.8	7.0	6.1	5.2
2	**30.0**	5.2	4.7	4.2	3.6
3	**21.0**	5.1	4.8	3.6	3.9
4	**16.0**	4.2	4.6	4.1	2.9
5	**11.0**	3.8	3.5	2.3	1.7
6	**8.3**	1.8	2.2	1.6	1.6
7	**5.6**	1.6	1.7	0.0	1.5
8	**3.9**	1.6	1.7	0.0	0.0
9	**2.8**	0.0	0.0	0.0	0.0
10	**2.0**	0.0	0.0	1.2	0.0
11	**1.4**	0.0	0.0	0.0	0.0

Table A.15: Data obtained with the AutoPIA software in the analysis of the 0.25 mm circular detail tester of the T=70 mm thick TOR-MAS phantom, corresponding to Figure 6.19 of this thesis. Values in gray indicate the details that the software consider non-visible.

Thickness = 70 mm					
		DCC			
Detail (no.)	**Nominal Contrast**	**AEC with grid**		**AEC without grid**	
		wG	w/oG Proc.	wG	w/oG Proc.
1	**41.0**	6.3	6.2	4.8	4.3
2	**30.0**	4.1	3.6	3.1	2.8
3	**21.0**	3.6	43.2	3.8	2.6
4	**16.0**	4.5	4.1	2.6	3.6
5	**11.0**	2.4	2.1	1.7	1.7
6	**8.3**	2.0	2.4	1.6	1.7
7	**5.6**	1.6	0.0	0.0	0.0
8	**3.9**	0.0	0.0	0.0	0.0
9	**2.8**	0.0	0.0	0.0	0.0
10	**2.0**	0.0	0.0	1.3	0.0
11	**1.4**	0.0	0.0	0.0	0.0

A.2.2.4 Microparticle step wedge tester

Table A.16: Data obtained with the AutoPIA software in the analysis of the microparticle step wedge tester of the T=30 mm thick TOR-MAS phantom, corresponding to Figures 6.20 and 6.21 of this thesis.

Thickness = 30 mm					
		Variance ratio			
Size (µm)	**Nominal Contrast**	**AEC with grid**		**AEC without grid**	
		wG	w/oG Proc.	wG	w/oG Proc.
125	**50**	3.1	3.6	2.3	2.4
	40	2.2	2.3	1.8	1.8
	30	1.8	1.8	1.4	1.5
	20	1.3	1.5	1.1	1.2
	10	1.0	1.2	0.9	1.0
234	**50**	4.8	5.8	3.5	3.5
	40	4.0	4.6	3.1	3.0
	30	3.2	3.3	2.4	2.3
	20	2.3	2.4	1.7	1.7
	10	1.3	1.5	1.1	1.2
328	**50**	11.2	14.1	7.5	7.7
	40	10.3	11.6	6.9	6.7
	30	7.3	7.6	4.8	4.7
	20	4.6	5.4	3.2	3.2
	10	2.7	3.1	1.9	1.9

Table A.17: Data obtained with the AutoPIA software in the analysis of the microparticle step wedge tester of the T=50 mm thick TOR-MAS phantom.

Thickness = 50 mm					
		Variance ratio			
Size (µm)	**Nominal Contrast**	**AEC with grid**		**AEC without grid**	
		wG	w/oG Proc.	wG	w/oG Proc.
125	**50**	2.5	2.7	1.6	1.9
	40	1.8	1.9	1.3	1.5
	30	1.7	1.7	1.3	1.4
	20	1.3	1.6	1.3	1.3
	10	1.0	1.5	1.2	1.1
234	**50**	3.8	3.9	2.2	2.4
	40	3.3	3.2	2.0	2.1
	30	2.6	2.3	1.7	1.8
	20	1.9	2.0	1.5	1.5
	10	1.3	1.5	1.2	1.2
328	**50**	8.4	8.6	4.2	4.7
	40	7.7	7.5	4.1	4.2
	30	5.8	5.2	3.2	3.2
	20	4.0	4.0	2.7	2.5
	10	2.5	2.6	1.8	1.6

Table A.18: Data obtained with the AutoPIA software in the analysis of the microparticle step wedge tester of the T=70 mm thick TOR-MAS phantom, corresponding to Figures 6.20 and 6.21 of this thesis.

Thickness = 70 mm					
		Variance ratio			
Size (µm)	**Nominal Contrast**	**AEC with grid**		**AEC without grid**	
		wG	w/oG Proc.	wG	w/oG Proc.
125	**50**	2.2	2.2	1.4	1.7
	40	1.7	1.8	1.3	1.4
	30	1.5	1.7	1.3	1.5
	20	1.2	1.5	1.1	1.3
	10	1.1	1.7	1.0	1.4
234	**50**	3.0	2.8	1.9	1.9
	40	2.8	2.5	1.8	1.7
	30	2.2	2.0	1.6	1.6
	20	1.8	1.7	1.3	1.3
	10	1.2	1.5	1.0	1.2
328	**50**	6.6	5.9	3.4	3.3
	40	6.5	5.4	3.3	3.0
	30	4.9	4.1	2.6	2.4
	20	3.7	3.4	2.1	2.0
	10	2.5	2.6	1.5	1.7

A.2.2.5 Uniform step wedge tester

Table A.19: Data obtained with the AutoPIA software in the analysis of the uniform step wedge tester of the T=30 mm thick TOR-MAS phantom.

Thickness = 30 mm					
		Relative contrast			
Detail (no.)	Nominal Contrast	AEC with grid		AEC without grid	
		wG	w/oG Proc.	wG	w/oG Proc.
1	**100**	98.2	97.4	84.8	93.4
2	**90**	73.2	80.3	69.7	77.2
3	**80**	68.3	74.7	65.0	72.1
4	**70**	62.1	67.5	59.1	65.6
5	**60**	55.5	60.0	52.8	59.0
6	**50**	44.6	48.8	42.4	46.5
7	**40**	38.1	41.7	36.3	40.0
8	**30**	30.4	32.9	28.9	31.9
9	**20**	21.2	22.5	20.2	22.3
10	**10**	10.4	10.2	9.9	11.0

Table A.20: Data obtained with the AutoPIA software in the analysis of the uniform step wedge tester of the T=50 mm thick TOR-MAS phantom, corresponding to Figure 6.22 of this thesis.

Thickness = 50 mm					
		Relative contrast			
Detail (no.)	Nominal Contrast	AEC with grid		AEC without grid	
		wG	w/oG Proc.	wG	w/oG Proc.
1	**100**	87.8	97.5	59.2	93.5
2	**90**	69.6	77.7	48.1	74.5
3	**80**	64.7	71.6	45.7	68.5
4	**70**	58.1	64.3	42.8	61.2
5	**60**	51.6	57.0	40.5	54.1
6	**50**	38.8	45.3	24.9	43.7
7	**40**	32.6	38.2	21.6	36.7
8	**30**	26.1	29.4	17.5	28.4
9	**20**	18.4	19.7	13.1	18.9
10	**10**	8.9	9.0	8.9	8.3

Table A.21: Data obtained with the AutoPIA software in the analysis of the uniform step wedge tester of the T=70 mm thick TOR-MAS phantom.

Thickness = 70 mm					
		Relative contrast			
Detail (no.)	**Nominal Contrast**	**AEC with grid**		**AEC without grid**	
		wG	w/oG Proc.	wG	w/oG Proc.
1	**100**	86.3	92.0	79.0	90.3
2	**90**	63.6	68.5	58.1	66.3
3	**80**	58.2	62.2	53.2	59.4
4	**70**	51.8	54.9	47.3	51.3
5	**60**	45.4	47.6	41.6	43.4
6	**50**	34.5	37.4	30.2	37.9
7	**40**	29.1	31.3	25.3	30.7
8	**30**	22.8	23.4	20.1	22.2
9	**20**	15.2	14.7	13.9	12.9
10	**10**	6.9	5.0	6.4	2.7

A.2.2.6 High contrast resolution tester

Table A.22: Data obtained with the AutoPIA software in the analysis of the HCR tester of the T=30 mm thick TOR-MAS phantom.

Thickness = 30 mm				
Spatial freq. (lp/mm)	**MTF**			
	AEC with grid		**AEC without grid**	
	wG	w/oG Proc.	wG	w/oG Proc.
1.00	97.4	98.1	97.5	98.5
1.12	97.0	97.9	97.2	98.3
1.25	95.2	96.5	95.4	96.8
1.40	90.4	91.0	90.5	91.6
1.60	88.7	89.6	89.0	90.0
1.80	86.1	87.3	86.4	88.0
2.00	84.0	84.7	84.1	85.4
2.24	81.0	81.9	81.3	82.4
2.50	78.4	79.5	78.5	80.2
2.80	75.3	76.2	75.4	76.8
3.15	71.6	72.3	71.7	73.1
3.55	67.6	68.6	67.7	69.5
4.00	62.9	63.8	63.2	64.9
4.50	57.8	58.8	58.3	59.8
5.00	54.0	55.5	54.7	56.1
5.60	49.2	50.2	49.5	51.0
6.30	44.8	45.5	45.2	46.4
7.10	37.3	38.4	37.5	39.0
8.00	32.6	33.2	32.9	34.4
8.90	27.8	28.5	28.5	29.4
10.00	20.8	21.5	21.4	22.1
11.10	14.9	15.3	15.6	15.9
12.50	8.2	8.5	8.0	8.5

Table A.23: Data obtained with the AutoPIA software in the analysis of the HCR tester of the T=50 mm thick TOR-MAS phantom, corresponding to Figure 6.23 of this thesis.

Thickness = 50 mm				
	MTF			
Spatial freq. (lp/mm)	**AEC with grid**		**AEC without grid**	
	wG	w/oG Proc.	wG	w/oG Proc.
1.00	96.6	98.4	96.7	98.7
1.12	96.2	97.3	96.6	98.5
1.25	94.5	97.3	95.4	97.1
1.40	89.7	97.3	89.9	91.6
1.60	88.0	91.7	88.4	90.1
1.80	85.6	90.0	86.4	88.2
2.00	83.6	88.3	83.7	85.7
2.24	80.1	85.8	80.7	82.3
2.50	77.9	82.6	79.0	80.7
2.80	74.6	77.3	75.3	77.1
3.15	71.0	73.5	71.8	73.7
3.55	67.1	70.1	68.4	70.2
4.00	62.6	65.6	63.5	65.4
4.50	57.5	60.2	58.3	60.2
5.00	53.7	56.8	55.0	56.6
5.60	48.1	50.6	49.2	50.8
6.30	44.3	46.4	44.8	46.7
7.10	39.1	41.7	40.7	41.7
8.00	33.0	35.3	34.7	35.2
8.90	27.5	29.6	28.1	29.3
10.00	20.0	22.3	21.0	21.9
11.10	14.6	16.0	15.9	15.7
12.50	8.4	8.6	8.3	8.6

Table A.24: Data obtained with the AutoPIA software in the analysis of the HCR tester of the T=70 mm thick TOR-MAS phantom.

Thickness = 70 mm				
	MTF			
Spatial freq. (lp/mm)	**AEC with grid**		**AEC without grid**	
	wG	w/oG Proc.	wG	w/oG Proc.
1.00	97.9	99.7	98.0	99.2
1.12	97.6	99.6	97.8	99.2
1.25	97.0	99.4	97.0	99.1
1.40	90.9	92.5	90.9	92.2
1.60	90.0	91.8	90.1	91.7
1.80	87.1	89.1	87.6	89.3
2.00	84.2	86.3	84.3	86.2
2.24	82.6	84.4	82.9	84.6
2.80	77.3	79.2	77.4	79.7
3.15	72.7	74.6	73.3	75.3
3.55	69.3	71.5	69.8	72.5
4.00	64.1	66.6	65.1	66.9
4.50	59.7	61.5	60.0	62.6
5.00	56.4	58.0	57.0	59.6
5.60	52.4	54.0	53.1	55.4
6.30	50.2	50.6	50.8	52.7
8.90	32.6	33.8	32.9	34.8
10.00	22.6	23.2	23.0	24.7
11.10	15.7	16.7	16.9	17.3
12.50	9.1	8.2	9.3	9.3

A.2.3 Realistic clinical images

Tables A.25 and A.26 provide the p-value data obtained with the Student T-test in the study of the realistic clinical phantoms, introduced in Section 6.5.

Table A.25: P-values obtained during the study of the CNR of three sheep udder phantoms at three doses, high (H), medium (M) and low (L) and for six ROIs. Data shown and summarised in Figures 6.36 to 6.38 and Table 6.13 of this thesis.

CNR study: Student T-test, p-value (%)									
ROI no.	**Small udder**			**Medium udder**			**Large udder**		
	H.	M.	L.	H.	M.	L	H.	M.	L
1	48.1	0.6	0.6	8.6	1.3	0.9	1.2	1.1	0.1
2	15.5	3.0	1.2	0.1	36.5	4.0	0.2	24.7	1.5
3	9.6	15.2	15.1	4.9	10.5	2.7	11.7	39.6	2.9
4	0.5	41.1	1.5	0.6	7.1	0.9	7.5	6.5	2.7
5	0.2	6.8	1.4	10.9	9.1	8.7	1.1	31.8	4.6
6	18.7	9.6	13.5	12.1	6.3	14.1	5.7	28.8	7.9

Table A.26: P-values obtained during the study of the variance ratio of three sheep udder phantoms at three doses, high (H), medium (M) and low (L) and for six ROIs. Data shown and summarised in Figures 6.36 to 6.38 and Table 6.13 of this thesis.

Vr. study: Student T-test, p-value (%)									
ROI no.	**Small udder**			**Medium udder**			**Large udder**		
	H.	M.	L.	H.	M.	L	H.	M.	L
1	15.5	48.1	0.5	4.1	1.5	0.6	0.8	0.5	0.1
2	16.9	15.5	29.3	0.7	24.5	0.6	1.3	6.4	2.4
3	6.0	9.6	4.4	2.3	47.7	0.9	17.9	25.0	4.0
4	2.4	0.5	0.7	0.9	4.7	0.5	30.2	5.8	4.3
5	1.6	0.2	0.6	0.1	1.7	6.4	10.8	11.5	1.1
6	8.7	18.7	1.6	0.6	1.0	0.1	49.5	10.7	36.3

Appendix B

Research Ethics Checklist

Bournemouth University

Research Ethics Checklist

Reference Id	16495
Status	Approved
Date Approved	18/05/2017

Researcher Details

Name	Elena Marimon Munoz
Faculty	Business School
Status	Postgraduate Research (MRes, MPhil, PhD, DProf, DEng)
Course	Postgraduate Research - Business
Have you received external funding to support this research project?	No
Please list any persons or institutions that you will be conducting joint research with, both internal to BU as well as external collaborators.	Oliver Diaz - ViCOROB research institute, University of Girona, Spain. Philip A. Marsden - UDA, UK.

Project Details

Title	Digital radiography: Image Acquisition and Scattering Reduction in X-ray Imaging
Proposed Start Date of Data Collection	25/05/2017
Proposed End Date of Project	30/06/2017
Original Supervisor	Hammadi Nait-Charif
Approver	Research Ethics Panel

Summary - no more than 500 words (including detail on background methodology, sample, outcomes, etc.)
My project focuses on the study of grid-less scattering reduction methods in X-ray Mammography. Scatter radiation degrades the quality of the image and complicated the diagnosis process. Anti-scatter grids are currently used in planar mammography examinations as the standard physical scattering reduction technique. However, this method has been found to be inefficient. It increases the dose delivered to the patient and does not remove all the scattered radiation. Alternative methods based on post-processing algorithms are under investigation to substitute anti-scatter grids. The method used in this study is a convolution-based scatter estimation. It is based on the premise that the scatter in the system is spatially diffuse, thus it can be approximated by a two-dimensional low-pass convolution filter of the primary image. To obtain the scatter kernel this algorithm uses the narrow pencil beam method. The kernel is then used to convolve an image, acquired without anti-scatter grid.The results obtained show an image quality comparable, in the worst case, to the grid image, in terms of uniformity and contrast to noise ratio. Further improvement is expected when using clinically-representative phantoms. For this reason, we are carrying out additional measurements involving more realistic phantoms. Oliver Diaz has borrowed one of the phantoms needed, CDMAM. The measurements will be carried out in a hospital in Sabadell, hospital Parc Tauli. The hospital is borrowing their facilities, there will be no contact with patients or animals and we will not be needing access to sensible information.

External Ethics Review

Does your research require external review through the NHS National Research Ethics Service (NRES) or through another external Ethics Committee?	No

Research Literature

Is your research solely literature based?	No

Human Participants

Will your research project involve interaction with human participants as primary sources of data (e.g. interview, observation, original survey)?	No

Final Review

Will you have access to personal data that allows you to identify individuals OR access to confidential corporate or company data (that is not covered by confidentiality terms within an agreement or by a separate confidentiality agreement)?	No
Will your research involve experimentation on any of the following: animals, animal tissue, genetically modified organisms?	No
Will your research take place outside the UK (including any and all stages of research: collection, storage, analysis, etc.)?	Yes

Does the country in which you are conducting research require that you obtain internal ethical approval (i.e. beyond that required by Bournemouth University)?	No

Please use the below text box to highlight any other ethical concerns or risks that may arise during your research that have not been covered in this form.

Bournemouth University

University Research Ethics Committee
Science, Technology & Health Research Ethics Panel
Bournemouth University
Melbury House 402
1-3 Oxford Rd
Bournemouth
BH8 8ES

Amendments to Ethics ID 16495
Approved by Chairs Action: 5 July 2017

1) Research details

Institutions that I will be conducting joint research: The Barts Health NHS trust will allow me access to a Mammography system.

2) Project details - summary updated:

My project focuses on the study of grid-less scattering reduction methods in X-ray Mammography. Scatter radiation degrades the quality of the image and complicated the diagnosis process. Anti-scatter grids are currently used in planar mammography examinations as the standard physical scattering reduction technique. However, this method has been found to be inefficient. It increases the dose delivered to the patient and does not remove all the scattered radiation. Alternative methods based on post-processing algorithms are under investigation to substitute anti-scatter grids. The method used in this study is a convolution-based scatter estimation. It is based on the premise that the scatter in the system is spatially diffuse, thus it can be approximated by a two-dimensional low-pass convolution filter of the primary image. To obtain the scatter kernel this algorithm uses the narrow pencil beam method. The kernel is then used to convolve an image, acquired without anti-scatter grid.The results obtained show an image quality comparable, in the worst case, to the grid image, in terms of uniformity and contrast to noise ratio. Further improvement is expected when using clinically-representative phantoms.

For this reason, we are carrying out additional measurements involving more realistic phantoms. Oliver Diaz has borrowed one of the phantoms needed, CDMAM. The measurements will be carried out in a hospital in Sabadell, hospital Parc Tauli. The hospital is borrowing their facilities, there will be no contact with patients or animals and we will not be needing access to sensible information.

Due to the impossibility of doing the final study with women, as it would imply to do two consecutive mammograms, and go therefore against the ALARP principle, we propose to finalise the study using udders from dead goats or sheep.

3) Final review:

Will your research involve experimentation on any of the following: animals, animal tissue, genetically modified organisms? Yes, animal tissue.

pp Prof Holger Schutkowski
Chair
Science, Technology & Health Research Ethics Panel

Bibliography

AAPM, TG195 (2015). *Monte Carlo Reference Data Sets for Imaging Research*. Tech. rep. 195.

Agostinelli, S et al. (2003). "Geant4—a simulation toolkit". In: *Nuclear Instruments and Methods in Physics Research Section A: Accelerators, Spectrometers, Detectors and Associated Equipment* 506.3, pp. 250–303.

Ahn, S. K., G. Cho, and H. Jeon (2006). "A scatter correction using thickness iteration in dual-energy radiography". In: *IEEE Transactions on Nuclear Science* 53.1, pp. 133–138.

Allison, J. et al. (2006). "Geant4 developments and applications". In: *IEEE Transactions on Nuclear Science* 53.1, pp. 270–278.

Andersen, A et al. (2006). "Calcification or artefact? A case study examining potential products which can mimic calcification in mammography". In: *Breast Cancer Research : BCR* 8.Suppl 1, P39.

Bansal, G J (2006). "Digital radiography. A comparison with modern conventional imaging". In: *Postgraduate Medical Journal* 82.969, pp. 425–428.

Barnes, Gary and Donald G. Frey (1993). "Screen film mammography: Imaging considerations and medical physics responsabilities". In: *Investigative Radiology* 28.5, p. 464.

Bick, Ulrich and Felix Diekmann (2007). "Digital mammography: what do we and what don't we know?" In: *European radiology* 17.8, pp. 1931–1942.

Bigas, M. et al. (2006). "Review of CMOS image sensors". In: *Microelectronics Journal* 37.5, pp. 433–451.

Binst, J et al. (2015). "Evaluation of automated CDMAM readings for non-standard CDMAM imaging conditions : grid-less acquisitions and scatter correction". In: *Radiation Protection Dosimetry*, pp. 1–4.

Boone, J M, T R Fewell, and R J Jennings (1997). "Molybdenum, rhodium, and tungsten anode spectral models using interpolating polynomials with application to mammography." In: *Medical physics* 24.12, pp. 1863–1874.

Boone, J M and J A Seibert (1988). "An analytical model of the scattered radiation distribution in diagnostic radiology." In: *Medical physics* 15.5, pp. 721–725.

Boone, J M et al. (2000). "Scatter/primary in mammography: comprehensive results." In: *Medical physics* 27.10, pp. 2408–2416.

Boone, John M. and Virgil N. Cooper (2000). "Scatter/primary in mammography: Monte Carlo validation." In: *Medical Physics* 27.8, pp. 1818–31.

Buhr, Egbert, Susanne Guenther-Kohfahl, and Ulrich Neitzel (2003). "Simple method for modulation transfer function determination of digital imaging detectors from edge images". In: *Proceedings of SPIE, Medical Imaging* 5030, p. 877.

Bushberg, J. T. et al. (2012). "The Essential Physics of the Medical Imaging, 3rd ed". In: *Lippincott Williams & Wilkins*, p. 1048.

CERN, [online] (2016). *Geant4 User Documentation*. URL: http://geant4.cern.ch/support/userdocuments.shtml (visited on 06/08/2016).

– (2017). *Geant4 physics list*. URL: http://geant4.cern.ch/collaboration/working{_}groups/electromagnetic/physlist10.1.shtml{\#}opt4 (visited on 06/08/2016).

CIRS, Tissue Simulation & Phantom Technology [online]. *CIRS*. URL: http://www.cirsinc.com/products/all/6/tissue-equivalent-phantom-for-mammography/ (visited on 01/25/2018).

collaboration, Geant4 (2016). "Geant4 User's Guide for Application Developers". In: *CERN* December.

Cooper, V N et al. (2000). "An edge spread technique for measurement of the scatter-to-primary ratio in mammography." In: *Medical physics* 27.5, pp. 845–853.

CyberQual, [online] (2016). *AutoPIA*. URL: autopia.cyberqual.it (visited on 03/20/2018).

Dance, D R et al. (2000). "Additional factors for the estimation of mean glandular breast dose using the UK mammography dosimetry protocol." In: *Physics in medicine and biology* 45.11, pp. 3225–3240. ISSN: 0031-9155. DOI: 10.1088/0031-9155/45/11/308.

Demchik, Vadim (2011). "Pseudo-random number generators for Monte Carlo simulations on ATI Graphics Processing Units". In: *Computer Physics Communications* 182.3, pp. 692–705.

Díaz, O et al. (2014). "Estimation of scattered radiation in digital breast tomosynthesis." In: *Physics in medicine and biology* 59, pp. 4375–4390.

Díaz, Oliver (2013). "Scattered radiation in projection X-ray mammography and digital breast tomosynthesis". PhD thesis. University of Surrey.

Díaz, Oliver et al. (2012). "A fast scatter field estimator for digital breast tomosynthesis". In: *SPIE, Medical Imaging* 8313, pp. 831305–831305–9.

Diffey, J.L. (2015). "A comparison of digital mammography detectors and emerging technology". In: *Radiography* 21.4, pp. 1–9.

Dixon, J M (2012). *ABC of Breast Diseases*. ABC Series. Wiley.

Dobbins, J T et al. (1995). "DQE(f) of four generations of computed radiography acquisition devices." In: *Medical physics* 22.10, pp. 1581–1593.

Dowsett, D, P A Kenny, and R E Johnston (2006). *The Physics of Diagnostic Imaging*. 2nd. A Hodder Arnold Publication. Taylor & Francis.

Ducote, J L and S Molloi (2010). "Scatter correction in digital mammography based on image deconvolution." In: *Physics in medicine and biology* 55, pp. 1295–1309.

Evans, D S, A Workman, and M Payne (2002). "A comparison of the imaging properties of CCD-based devices used for small field digital mammography". In: *Physics in Medicine & Biology* 47.1, p. 117.

Farman, Allan G. and Taeko T. Farman (2005). "A comparison of 18 different x-ray detectors currently used in dentistry". In: *Oral Surgery, Oral Medicine, Oral Pathology, Oral Radiology and Endodontology* 99.4, pp. 485–489.

Farman, Taeko T et al. (2005). "Effects of scintillator on the modulation transfer function (MTF) of a digital imaging system." In: *Oral surgery, oral medicine, oral pathology, oral radiology, and endodontics* 99.5, pp. 608–613.

– (2006). "Effects of scintillator on the detective quantum efficiency (DQE) of a digital imaging system". In: *Oral Surgery, Oral Medicine, Oral Pathology, Oral Radiology, and Endodontology* 101.2, pp. 219–223.

Feijó Pery, Vidal and Gabriela Hoff (2008). "Geant4 validation on mammography applications". In: *IEEE Nuclear Science Symposium Conference Record*, pp. 3497–3498.

Feng, Steve Si Jia and Ioannis Sechopoulos (2011). "A software-based x-ray scatter correction method for breast tomosynthesis". In: *Medical Physics* 38.12, pp. 6643–6653.

Feng, Steve Si Jia et al. (2014). "X-ray scatter correction in breast tomosynthesis with a precomputed scatter map library." In: *Medical physics* 41.3, p. 31912.

Fieselmann, Andreas et al. (2013). "Full-field digital mammography with grid-less acquisition and software-based scatter correction: investigation of dose saving and image quality". In: *SPIE Medical Imaging: Physics of Medical Imaging* 8668, 86685Y.

Fossum, Eric R and Senior Member (1997). "CMOS Image Sensors : Electronic Camera-On-A-Chip". In: 44.10, pp. 1689–1698.

Frandson, R D, W L Wilke, and A D Fails (2013). *Anatomy and Physiology of Farm Animals*. Wiley.

Gerado Caja, Xavier Such, Maristela Rovai (1981). "Udder Morphology and Machine Milking Ability in Dairy Sheep". In: *Proceedings of the 6th Great Lakes Dairy Sheep Symposium*.

Gonzalez Trotter, Dinko E et al. (2002). *Thickness-dependent scatter correction algorithm for digital mammography*.

Gov.uk, [online] (2014). *ABP waste*. URL: https://www.gov.uk/guidance/animal-by-product-categories-site-approval-hygiene-and-disposal (visited on 07/15/2017).

Granfors, Paul and Richard Aufrichtig (2000). "DQE(f) of an amorphous-silicon flat-panel x-ray detector: detector parameter influences and measurement methodology". In: *Proceedings of SPIE, Medical Imaging*.

Grosjean, Bénédicte and Serge Muller (2006). "Impact of Textured Background on Scoring of Simulated CDMAM Phantom". In: *Proceeding of IWDM Digital Mammography*. Ed. by Susan M Astley et al. Berlin, Heidelberg: Springer Berlin Heidelberg, pp. 460–467.

Hamamatsu, [online]. *Scintillator plates - Hamamatsu photonics*. URL: http://www.hamamatsu.com/jp/en/product/category/3100/3010/index.html (visited on 03/23/2016).

Hammerstein, G Richard et al. (1979). "Absorbed Radiation Dose in Mammography". In: *Radiology* 130.2, pp. 485–491.

Hendee, William R. and E. Russell Ritenour (2002). *Medical Imaging Physics*. 4th ed. Wiley-Liss.

Highnam, R. P., J. M. Brady, and B. J. Shepstone (1998). "Estimation of compressed breast thickness during mammography". In: *British Journal of Radiology* 71.June, pp. 646–653.

Highnam, Ralph et al. (2010). "Robust Breast Composition Measurement - VolparaTM". In: *Digital Mammography: 10th International Workshop, IWDM 2010, Girona, Catalonia, Spain, June 16-18, 2010. Proceedings*. Ed. by Joan Martí et al. Berlin, Heidelberg: Springer Berlin Heidelberg, pp. 342–349.

Hoheisel, Martin (2006). "Review of medical imaging with emphasis on X-ray detectors". In: *Nuclear Instruments and Methods in Physics Research Section A: Accelerators, Spectrometers, Detectors and Associated Equipment* 563.1, pp. 215–224.

IECP (2007a). *IEC 62220-1-2 Medical electrical equipment - Characteristics of digital X-ray imaging devices - Part 1-2: Determination of the detective quantum efficiency - Detectors used in mammography*. Tech. rep. Geneva.

– (2007b). *IEC 62220-1 Medical electrical equipment - Characteristics of digital X-ray imaging devices - Part 1: Determination of the detective quantum efficiency*. Tech. rep. Geneva.

James, J.J (2004). "The current status of digital mammography". English. In: *Clinical Radiology* 59.1, pp. 1–10.

Key, Veterian [online] (2016). *Udder structure*. URL: https://veteriankey.com/the-mammary-gland-2/ (visited on 06/25/2017).

Knoll, Glenn F. (2010). *Radiation detection and measurement*. 4th ed. New York: Wiley.

Konstantinidis, Anastasios C. (2011). "Evaluation of digital X-ray detectors for medical imaging applications". PhD thesis. UCL.

Konstantinidis, Anastasios C et al. (2012). "The Dexela 2923 CMOS X-ray detector A flat panel detector based on CMOS active pixel sensors for medical imaging applications". In: *Nuclear Inst. and Methods in Physics Research, A* 689.C, pp. 12–21.

Konstantinidis, Anastasios C. et al. (2013). "X-ray Performance Evaluation of the Dexela CMOS APS X-ray Detector Using Monochromatic Synchrotron Radiation in the Mammographic Energy Range". In: *IEEE Transactions on Nuclear Science* 60.5, pp. 3969–3980.

Kopans, D B (2007). *Breast Imaging*. Lippincott Williams & Wilkins.

Krol, A et al. (1996). "Scatter reduction in mammography with air gap." In: *Medical physics* 23.7, pp. 1263–1270.

Leeds Test Objects, [online]. *AutoPIA Leeds Test Objects*. URL: https://www.leedstestobjects.com/index.php/phantom/autopia-software/ (visited on 02/05/2018).

– *TOR-MAM*. URL: http://www.leedstestobjects.com/index.php/phantom/tor-mam/ (visited on 01/25/2018).

– *TOR-MAS*. URL: http://www.leedstestobjects.com/index.php/phantom/tor-mas/ (visited on 01/25/2018).

Leon, Stephanie M, Libby F Brateman, and Louis K Wagner (2014). "Characterization of scatter in digital mammography from physical measurements." In: *Medical physics* 41.6, p. 061901.

Love, L. Alan (1987). "Scatter estimation for a digital radiographic system using convolution filtering". In: *Medical Physics* 14.2, p. 178.

Marimon, Elena et al. (2016). "Detailed Analysis of Scatter Contribution from Different Simulated Geometries of X-ray Detectors". In: *IWDM proceedings*, pp. 203–210.

Mawdsley, Gordon E. et al. (2009). "Accurate estimation of compressed breast thickness in mammography." In: *Medical physics* 36.2009, pp. 577–586.

McPherson, K, C M Steel, and J M Dixon (2000). "Breast cancer-epidemiology, risk factors, and genetics". In: *British Medical Journal* 321.7261, pp. 624–628.

Miller, Scott T et al. (2012). "Summary of the evidence of breast cancer service screening outcomes in Europe and first estimate of". In: *Journal of Medical Screening* 19, pp. 5–13.

Monnin, P et al. (2007). "A comparison of the performance of digital mammography systems." In: *Medical physics* 34.3, pp. 906–914.

Moy, Jean-Pierre (1998). "Image quality of scintillator-based x-ray electronic imagers". In: *Proceedings of SPIE* 3336.February, pp. 187–194.

Muller, Serge (1999). "Full-field digital mammography designed as a complete system". In: *European Journal of Radiology* 31.1, pp. 25–34.

NASA, [online] (2015). *The electromagnetic spectrum*. URL: http://imagine.gsfc.nasa.gov/science/toolbox/emspectrum1.html (visited on 09/11/2015).

National Cancer Institute, [online] (2015). *Cancer screening*. URL: https://www.cancer.gov/about-cancer/screening (visited on 07/20/2017).

NHS, [online] (2016). *Breast Cancer NHS*. URL: http://www.nhs.uk/Conditions/Cancer-of-the-breast-female/Pages/Introduction.aspx (visited on 07/05/2017).

Nikola, Biller-Andorno and Jüni Peter (2014). "Abolishing Mammography Screening Programs? A View from the Swiss Medical Board". In: *New England Journal of Medicine* 370.21, pp. 1965–1967.

NIST. *NIST material composition [online]*. URL: https://physics.nist.gov/cgi-bin/Star/compos.pl (visited on 05/25/2015).

NIST, [online] (2004). *NIST Linear attenuation coefficients*. URL: https://www.nist.gov/pml/x-ray-mass-attenuation-coefficients (visited on 10/12/2016).

Noel, A. and Fabienne Thibault (2004). "Digital detectors for mammography: The technical challenges". In: *European Radiology* 14, pp. 1990–1998.

Peters, Inge M. et al. (2016). "High dynamic range CMOS-based mammography detector for FFDM and DBT". In: *SPIE Medical Imaging. International Society for Optics and Photonics* 9783, p. 978316.

Pisano, Etta D et al. (2005). "Diagnostic Performance of Digital versus Film Mammography for Breast-Cancer Screening". In: *The New England Journal of Medicine* 353.17, pp. 1773–1783.

Rangayyan, Rangaraj M and Thanh M Nguyen (2005). "Pattern classification of breast masses via fractal analysis of their contours". In: *International Congress Series* 1281, pp. 1041–1046.

Reed, Amy B. (2011). "The history of radiation use in medicine". In: *Journal of Vascular Surgery* 53.1 SUPPL. Pp. 3–5.

Rodríguez-Ruiz, Alejandro, Greeshma A Agasthya, and Ioannis Sechopoulos (2017). "The compressed breast during mammography and breast tomosynthesis: in vivo shape characterization and modeling". In: *Physics in Medicine & Biology* 62.17, pp. 6920–6937.

Samei, E, M J Flynn, and D a Reimann (1998). "A method for measuring the presampled MTF of digital radiographic systems using an edge test device." In: *Medical physics* 25.1, pp. 102–113.

Samei, Ehsan et al. (2006). "Intercomparison of methods for image quality characterization. I. Modulation transfer function." In: *Medical physics* 33.5, pp. 1454–1465.

Sechopoulos, Ioannis (2007). "Investigation of physical processes in digital x-ray tomosynthesis imaging of the breast". PhD thesis. Georgia Institute of Technology.

Sechopoulos, Ioannis et al. (2007a). "Computation of the glandular radiation dose in digital tomosynthesis of the breast Ioannis". In: *Medical Physics* 34.1, pp. 221–232.

Sechopoulos, Ioannis et al. (2007b). "Scatter radiation in digital tomosynthesis of the breast". In: *Medical physics* 34.1, pp. 221–32.

Sechopoulos, Ioannis et al. (2015). "Monte Carlo reference data sets for imaging research: Executive summary of the report of AAPM Research Committee Task Group 195". In: *Medical physics* 3834.195.

Seeley, R R, T D Stephens, and P Tate (1998). *Anatomy & Physiology*. WCB/McGraw-Hill.

Seibert, J a and J M Boone (2006). "X-ray scatter removal by deconvolution." In: *Medical physics* 15.1988, pp. 567–575.

Sempau, J et al. (2001). "Monte Carlo simulation of electron beams from an accelerator head using PENELOPE." In: *Physics in medicine and biology* 46.4, pp. 1163–1186.

Sickles, EA [online] (2013). *ACR BI-RADS® Mammography*. URL: https://www.acr.org/Quality-Safety/Resources/BIRADS/About-BIRADS/How-to-Cite-BIRADS (visited on 06/23/2017).

Siemens, [online] (2018). *Simulation of X-ray Spectra*. URL: https://www.oem-xray-components.siemens.com/x-ray-spectra-simulation (visited on 05/03/2018).

Smith, A P (2003). "Fundamentals of digital mammograhpy: physiscs, technology and practical considerations." In: *Radiology Management* 25(5), pp. 18–31.

Tan, Jiaming (2013). "4T CMOS Active Pixel Sensors under Ionizing Radiation". PhD thesis, p. 147.

Timmers, J M H et al. (2012). "The Breast Imaging Reporting and Data System (BI-RADS) in the Dutch breast cancer screening programme: its role as an assessment and stratification tool". In: *European Radiology* 22.8, pp. 1717–1723.

Tobias, J S and D Hochhauser (2009). *Cancer and its Management*. Wiley.

Torre, Lindsey A et al. (2016). "Global Cancer Incidence and Mortality Rates and Trends — An Update". In: *Cancer, Epidemiology, Biomarkers & Prevention* 25.January, pp. 16–28.

Turner, James E. (1995). *Atoms, radiation and radiation protection*. 2nd. New York, NY: Wiley.

Wang, Adam et al. (2015). *Asymmetric scatter kernels for software-based scatter correction of gridless mammography*.

Waugh, Anne et al. (2014). *Ross and Wilson anatomy and physiology in health and illness.* 12th. Edinburgh : Churchill Livingstone, 2014.

WebMed, [online] (2014). *WebMD - Picture of the Breasts*. URL: http://www.webmd.com/women/picture-of-the-breasts{\#}1 (visited on 07/17/2017).

Welch, H and H.J. Passow (2014). "Quantifying the benefits and harms of screening mammography". In: *JAMA Internal Medicine* 174.3, pp. 448–454.

White, D R, R J Martin, and R Darlison (1977). "Epoxy resin based tissue substitutes." eng. In: *The British journal of radiology* 50.599, pp. 814–821.

Whitman, Gary J. et al. (2006). "Breast Cancer Staging". In: *Seminars in Roentgenology* 41.2, pp. 91–104.

WHO (2014). *WHO Position Paper on Mammography Screening*. Tech. rep.

World Cancer Research Fund International, [online] (2015). *Breast cancer statistics*. URL: https://www.wcrf.org/int/cancer-facts-figures/data-specific-cancers/breast-cancer-statistics (visited on 05/03/2018).

Yaffe, M. J. et al. (2009). "The myth of the 50-50 breast". In: *Medical Physics* 36.12, p. 5437. ISSN: 00942405. DOI: 10.1118/1.3250863. URL: http://scitation.aip.org/content/aapm/journal/medphys/36/12/10.1118/1.3250863.

Yaffe, Martin J and James G Mainprize (2004). "Detectors for Digital Mammography". In: *Technology in Cancer Research & Treatment* 3.4, pp. 309–324.

Zanella, G (2002). "Gray levels, dynamic range, contrast and DQE in imaging detectors". In: *Nuclear Instruments and Methods in Physics Research Section A: Accelerators, Spectrometers, Detectors and Associated Equipment* 481, pp. 691–695.